

**A Thesis Submitted for the Degree of PhD at the University of Warwick**

**Permanent WRAP URL:**

<http://wrap.warwick.ac.uk/144874>

**Copyright and reuse:**

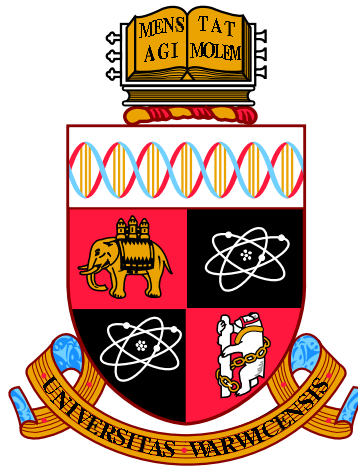
This thesis is made available online and is protected by original copyright.

Please scroll down to view the document itself.

Please refer to the repository record for this item for information to help you to cite it.

Our policy information is available from the repository home page.

For more information, please contact the WRAP Team at: [wrap@warwick.ac.uk](mailto:wrap@warwick.ac.uk)



**Particle-in-cell Simulations of Laser-Plasma  
Instabilities in Shock-Ignition**

by

**Alexander George Seaton**

**Thesis**

Submitted to the University of Warwick

for the degree of

**Doctor of Philosophy**

**Department of Physics**

September 2019

THE UNIVERSITY OF  
**WARWICK**



# Contents

<b>List of Tables</b>	<b>iv</b>
<b>List of Figures</b>	<b>v</b>
<b>Acknowledgments</b>	<b>xxi</b>
<b>Declarations</b>	<b>xxii</b>
<b>Abstract</b>	<b>xxiii</b>
<b>Abbreviations</b>	<b>xxiv</b>
<b>Chapter 1 Introduction</b>	<b>1</b>
1.1 Inertial Confinement Fusion . . . . .	1
1.1.1 Fundamental Principles . . . . .	1
1.1.2 Direct & Indirect-drive . . . . .	5
1.1.3 Current Status . . . . .	6
1.1.4 Shock Ignition . . . . .	7
1.2 Previous Work . . . . .	8
1.2.1 Experiments . . . . .	8
1.2.2 Theory & Simulation . . . . .	10
1.3 Normalisations . . . . .	11
<b>Chapter 2 Theory</b>	<b>12</b>
2.1 Fundamental Equations . . . . .	12
2.2 Plasma Waves . . . . .	15
2.3 Landau Damping . . . . .	17
2.4 Particle Trapping . . . . .	20
2.5 Parametric Instabilities . . . . .	21
2.5.1 Temporal Growth in an Infinite Homogeneous System . . . . .	22

2.5.2	Growth in a Homogeneous System . . . . .	25
2.5.3	Growth in an Inhomogeneous System . . . . .	30
2.5.4	Stimulated Raman Scattering . . . . .	31
2.5.5	Two-Plasmon Decay . . . . .	34
2.5.6	Stimulated Brillouin Scattering . . . . .	37
<b>Chapter 3</b>	<b>Methods</b>	<b>40</b>
3.1	EPOCH & The Particle-in-cell Method . . . . .	40
3.1.1	Code Overview . . . . .	42
3.1.2	Field Solver . . . . .	42
3.1.3	Particle Push . . . . .	43
3.1.4	Particle Weighting . . . . .	44
3.2	Simulations of SRS in a 1D Periodic Box . . . . .	45
3.2.1	Simulation Setup . . . . .	45
3.2.2	Resonant Undamped Growth . . . . .	47
3.2.3	Off-resonant Undamped Growth . . . . .	53
3.3	2D Simulation Diagnostics . . . . .	55
3.3.1	Outgoing Flux Diagnostics . . . . .	57
3.3.2	Bulk Plasma Diagnostics . . . . .	60
<b>Chapter 4</b>	<b>Effect of Ion Waves on TPD Linear Growth</b>	<b>62</b>
4.1	Derivation of The Coupled Equations . . . . .	63
4.2	Transverse Density Perturbations ( $\mathbf{k}_i = 2k_y\hat{\mathbf{y}}$ ) . . . . .	68
4.3	Oblique Density Perturbations . . . . .	70
4.4	Summary . . . . .	75
<b>Chapter 5</b>	<b>Small-scale Simulation</b>	<b>77</b>
5.1	Simulation Setup . . . . .	78
5.2	Initial Behaviour . . . . .	80
5.2.1	Linear Growth . . . . .	81
5.2.2	Initial Saturation Effects . . . . .	81
5.3	Long-term Behaviour . . . . .	85
5.3.1	Cavitation . . . . .	86
5.3.2	Pump Depletion & Wave Propagation . . . . .	89
5.3.3	Ion Density Perturbations . . . . .	90
5.3.4	Summary . . . . .	95
5.4	Hot Electron Production . . . . .	95
5.4.1	Angular Distribution . . . . .	95

5.4.2	Hot Electron Sources . . . . .	98
5.4.3	Conversion Efficiency & Energy Distribution . . . . .	100
5.5	Summary . . . . .	103
<b>Chapter 6 Ignition-scale Simulation</b>		<b>105</b>
6.1	Simulation Setup . . . . .	106
6.2	Initial Behaviour . . . . .	107
6.2.1	Linear Growth . . . . .	107
6.2.2	Initial Saturation Effects . . . . .	110
6.3	Long-term Behaviour . . . . .	112
6.3.1	Two-plasmon Decay . . . . .	112
6.3.2	Stimulated Brillouin Scattering & Filamentation . . . . .	116
6.3.3	Kinetic Inflation of SRS . . . . .	119
6.4	Hot Electrons . . . . .	125
6.4.1	SRS Hot Electron Production . . . . .	125
6.4.2	TPD Hot Electron Production . . . . .	128
6.5	Summary . . . . .	130
<b>Chapter 7 Conclusion</b>		<b>132</b>
<b>Appendix A The Coupled Mode Equations</b>		<b>137</b>
A.1	Derivation of The General Solution . . . . .	137
A.2	Solution for Delta Function Initial Conditions . . . . .	140

# List of Tables

- 1.1 Summary of laser and plasma parameters used in experiments investigating shock-ignition, ordered by date. Results are published in: (1): [Batani et al., 2019], (2): [Trela et al., 2018], (3): [Cristoforetti et al., 2017, 2018], (4): [Baton et al., 2017], (5): [Theobald et al., 2015; Nora et al., 2015], (6): [Hohenberger et al., 2014], (7): [Theobald et al., 2012], (8): [Batani et al., 2012, 2014], (9), [Baton et al., 2012], and (10): [Theobald et al., 2008]. In experiments where conditions were varied significantly between shots (e.g. phase plates on or off) entries are split into multiple rows. Intensities are identified as single beam (‘S’) or the sum of the multiple beam intensities (‘M’). The beam count refers to the quantity on during the intensity spike. Under smoothing, ‘PP’ refers to phase plates, ‘SSD’ to smoothing by spectral dispersion and ‘PS’ to polarisation smoothing. Under geometry, ‘HS’ refers to hemispherical targets. Question marks under parameters indicate that the quantity was either not diagnosed or that this data could not be found in the associated publication. Finally, the scatter and hot-electron fractions are as a percentage of delivered laser energy. . . . . 9

# List of Figures

1.1	Binding energy per nucleon for selected nuclei with atomic number $Z$ and neutron count $N$ . Grey line connects nuclei with the highest binding energy per nucleon for given nucleon count $A$ . These are not always the most stable nuclei; for example the ${}^8\text{Be}$ nucleus is extremely unstable and decays to ${}^9\text{Be}$ immediately. ${}^{56}\text{Fe}$ , marked in red, is the nucleus with the highest binding energy per nucleon. Data from [Huang et al., 2017]. . . . .	2
1.2	Thermal reactivities of various fusion reactions as a function of temperature, calculated using the parameterisations of [Bosch and Hale, 1992]. A temperature of 1keV is equivalent to $1.16 \times 10^7\text{K}$ . The D-D reaction has two branches which occur with almost equal likelihood. Their reaction rates are indistinguishable in this figure. . . . .	2
1.3	Illustration of the two main laser drive configurations, direct and indirect-drive. In the former the target is illuminated directly by the laser, while in the latter a radiation enclosure formed of a high- $Z$ material such as gold is used to convert laser photons to X-rays. Lower inset panels show snapshots in time illustrating an implosion. Reprinted by permission from Nature Physics [Betti and Hurricane, 2016]. . . . .	5
2.1	Dispersion relations of the three waves supported by an unmagnetised plasma with Maxwellian distribution function: electromagnetic, electron-plasma and ion-acoustic waves. Plasma parameters used are: $n_e = 0.15n_{\text{cr}}$ , $T_e = 3.5\text{keV}$ , $T_i = 1.7\text{keV}$ and $Z = 1$ , which aside from $Z = 1$ are typical for this thesis. Left and right panels differ only in the frequency scale used. Frequency and wavenumber normalisations are the frequency and vacuum wavenumber of light from a frequency-tripled Nd:Glass laser. . . . .	15

2.2	Derivative of the plasma dispersion function plotted in the complex plane of its argument. Blue and red colour scales in left two plots indicate positive and negative values respectively, each on a logarithmic scale. The dashed lines in the two left hand plots indicate paths along which $\text{Re}(Z'(z)) = 0$ while along the solid lines $\text{Im}(Z'(z)) = 0$ . The contour lines in the right hand plot indicate where $ Z'(z)  = 10^n$ , with the highest contour at $10^8$ . Solutions to the warm plasma dispersion relation (equation 2.25) lie along the black solid lines in the two left-hand plots where $\text{Re}(Z'(z)) \geq 0$ . . . . .	18
2.3	Frequency and damping rates of the solutions to the the warm plasma dispersion relation. The blue line corresponds to electron plasma waves while the green, red and turquoise lines are strongly damped modes which are not usually observed. . . . .	19
2.4	From left to right: parametric instability growth rate as a function of pump strength $\gamma_0$ , total damping rate $\Gamma_T \equiv (\Gamma_1 + \Gamma_2)/2$ and frequency mismatch $\Delta\omega$ . In the left two plots the ratio of the two waves' damping rates ( $\Gamma_R \equiv \Gamma_2/\Gamma_1$ ) is varied, with $\Gamma_R = 1, 10$ and $100$ in blue, green and red respectively. . . . .	24
2.5	Transient behaviour of the explicit solution to the coupled mode equations for a homogeneous initial disturbance. $a_1(t)$ is the amplification predicted by equation 2.58 and $\gamma$ is given by equation 2.43. Parameters used are $\Gamma_T = 0.8\gamma_0$ and $\Gamma_R \equiv \Gamma_2/\Gamma_1 = 10^0, 10^1, 10^2$ and $10^{10}$ in blue, green red and black respectively. This illustrates that the transient behaviour has very little effect and can be approximated by the asymptotic solution in most cases. . . . .	27
2.6	Spatiotemporal evolution of the wave envelope $a_1$ in response to an initial disturbance of form $a_1(x, 0) = \delta(x)$ . <b>Left &amp; centre:</b> amplitude plotted on a logarithmic colour scale with $V_T/V_D = 1.5$ and $-0.75$ . The two wave characteristics are shown as green and blue dashed lines while $x = V_T t$ , the mean trajectory of the pulse, is shown as a black dashed line. <b>Right:</b> amplitude versus time either at fixed points corresponding to previous two plots (solid lines) or along $x = V_T t$ (dashed line). . . . .	29

- 2.7 **Top:** Solution of the SRS frequency and wavenumber matching conditions using the fluid EPW dispersion relation at  $T_e = 3.5\text{keV}$  (coloured lines). In both panels black lines indicate the zero-temperature limit. The laser wave-vector is parallel to the  $k_x$  axis. **Left:**  $k_x$  component of the EPW wavenumber as a function of electron density for SRS forward, back and 90-degree side-scatter in blue, green and red respectively. **Right:**  $k_y$  and  $k_x$  components of EM (green) and EPW (blue) wavenumbers at  $0.05n_{\text{cr}}$  (solid) and  $0.20n_{\text{cr}}$  (dashed). **Bottom:** Frequency & wavenumber matching for SRS back (blue) and forward-scatter (green) daughter waves at  $T_e = 3.5\text{keV}$  &  $n_e = 0.2n_{\text{cr}}$ . Considering each vector  $(k, \omega)$ , it can be seen that the sum of vectors for the two daughter-waves gives the laser vector (black). . . . . 32
- 2.8 Homogeneous coupling constant ( $\gamma_0$ ) for SRS as a function of density and scattered light propagation angle  $\theta$  (angle with respect to the laser wavenumber) for a laser intensity of  $2 \times 10^{15}\text{Wcm}^{-2}$  at  $T_e = 3.5\text{keV}$  (coloured lines). In both panels black lines indicate the zero temperature limit. **Left:**  $\gamma_0$  versus electron density for SRS back, forward and 90-degree side-scatter in green, blue and red respectively including the Landau damping rate. **Right:**  $\gamma_0$  versus scattered light propagation angle at  $0.05n_{\text{cr}}$  (solid) and  $0.20n_{\text{cr}}$  (dashed). Landau damping rate included for red lines, neglected for green lines. . . . . 33
- 2.9 Solution of the TPD frequency and wavenumber matching conditions using the fluid EPW dispersion relation at  $T_e = 3.5\text{keV}$ . **Left:** circle indicates wavenumbers permitted by the TPD matching conditions at  $0.22n_{\text{cr}}$ . The circle's radius increases monotonically with decreasing density. The colour scale indicates the relative linear growth rate of TPD for a given wavevector, scale in arbitrary units. Maximum growth is achieved along the hyperbolae marked by white dashed lines. Black arrows mark the EPW wavenumbers at  $0.22n_{\text{cr}}$  that would produce maximum growth, with the laser wavevector shown in blue. **Right:** variation with density of the TPD EPW wavenumbers with largest linear growth rates. Lines plotted are the parallel ( $k_x$ ) and perpendicular ( $k_y$ ) components of the longer EPW wavevector ( $\mathbf{k}_1$ ), along with magnitudes of the two wavenumbers. . . . . 35

- 2.10 Homogeneous coupling constant ( $\gamma_0$ ) for TPD as a function of wavenumber and density for a laser intensity of  $2 \times 10^{15} \text{Wcm}^{-2}$  at  $T_e = 3.5 \text{keV}$ . **Left:**  $\gamma$  versus wavenumber, as in figure 2.9 but including the Landau damping rate of the EPWs. Values are in arbitrary units. Note that density is not fixed in this plot. The location of the Landau cutoff ( $|\mathbf{k}|\lambda_D = 0.3$ ) is marked by a blue circle, assuming a density of  $0.2n_{\text{cr}}$ . **Right:**  $\gamma$  versus density at three different temperatures including Landau damping (solid lines) and excluding it (dashed line). Due to the small variation in  $\gamma_0$  and exponential behaviour of the damping rate this closely resembles the left panel of figure 2.4. . . . 37
- 2.11 Solution of the SBS frequency and wavenumber matching conditions using the fluid IAW dispersion relation with  $T_e = 3.5 \text{keV}$ ,  $T_i = T_e/2$ , and for a hydrogen plasma. **Left:** circles indicate wavenumbers permitted by the SBS matching conditions at  $0.2n_{\text{cr}}$ . The circle's radius increases monotonically with decreasing density. The colour scale shows the linear growth rate of SBS for a given scattered light wavevector (neglecting Landau damping), with an arbitrary normalisation. Maximum growth is achieved for direct backscatter. Black arrows mark a possible triad of wavenumbers at  $0.2n_{\text{cr}}$ , with the laser wavevector shown with a dashed line. **Right:** Growth rate as a function of scatter angle for  $T_e = 3.5 \text{keV}$ ,  $T_i = 1.7 \text{keV}$ ,  $I = 2 \times 10^{15} \text{Wcm}^{-2}$  (solid lines) and the same parameters but with halved temperatures (dashed lines). The densities used are  $0.2n_{\text{cr}}$  (green),  $0.1n_{\text{cr}}$  (blue) and  $0.4n_{\text{cr}}$  (red). . . . . 38
- 3.1 Points in density-temperature parameter space where the SRS daughter wave wavelengths exactly fit a domain of size  $L_x = 6\lambda_0$  where  $\lambda_0$  is the local laser wavelength. Blue solid lines represent SRS backscatter; green solid lines forward-scatter. The dashed black line corresponds to the maximum density at which SRS can occur. For this case back and forward-scatter are indistinguishable and the daughter wavenumbers become  $k = k_0$  and  $k_s = 0$ . . . . . 46



- 3.2 Spatiotemporal discrete Fourier transform (DFT) of the electrostatic field component  $E_x$ . The narrow curve at  $\omega/\omega_0 \simeq 0.5$  corresponds to the dispersion relation for EPWs, excited by thermal noise fluctuations. Fluctuations are also responsible for the triangular features extending from  $k_x = 0$  at low frequency. These features are not resonant modes of the plasma but are caused by the thermal motion of the electrons and hence have phase velocities  $\omega/k \lesssim 4.5v_{th}$ . Locations where the EPW dispersion relation intersects with this region indicate significant Landau damping of those waves would occur. A large-amplitude EPW is excited by SRS in this simulation and appears as a peak in the Fourier transform at  $k = 1.19\omega_0/c$  (Fourier mode  $j = 8$ ). A further peak of smaller amplitude can be seen at  $k = 2.38\omega_0/c$  ( $j = 16$ ) which corresponds to the second harmonic of the SRS EPW, driven by nonlinear fluid effects. . . . . 48
- 3.3 Spatiotemporal discrete Fourier transform (DFT) of the electromagnetic field component  $E_y$ . The hyperbolic curve that is visible corresponds to the dispersion relation for EM waves in a plasma, traced out by thermal fluctuations. Two peaks are visible with amplitude significantly larger than the thermal noise background. The peak of largest amplitude at  $k = 0.89\omega_0/c$  corresponds to the laser, while the smaller peak at  $k = -0.30\omega_0/c$  corresponds to the backscattered EM wave driven by SRS. The low-amplitude curve that extends out from the backscatter peak is caused by Thomson scattering of the laser off electron plasma waves. . . . . 49
- 3.4 Amplitude of spatial modes corresponding to the laser (left, blue), backscattered EM (left, green) and EPW (right, green) as a function of time. The electric field is normalised by  $e/(m_e\omega_0c)$ . The solid black lines are the time-envelopes of these signals, calculated by applying a complex bandpass filter and taking the modulus of the resulting signal. This isolates the waves corresponding to backscatter SRS (the forward-SRS scattered light would occur at the same spatial mode in the simulation) and reduces noise. The dashed black line in the left panel is the equivalent envelope for forward-scatter SRS and demonstrates that this is sufficiently detuned as not to undergo any significant growth. . . . . 51

- 3.5 Measured growth rates for varying frequency mismatch in a periodic simulation for SRS backscatter (blue points) and forward scatter (green points). The frequency mismatch is varied by changing the simulation density. Over the range of densities considered both forward and back-scatter are present (left pane). In the left figure dashed lines indicate the infinite homogeneous growth rates ( $\gamma_0$ ) while solid lines are linear interpolations between points to guide the eye. In the right hand figure the growth rates, normalised to the theoretical infinite homogeneous growth rate ( $\gamma_0$ ), are plotted as a function of the theoretical mismatch ( $\Delta\omega$ ). This would be expected to give peak growth at  $\Delta\omega = 0$  which the data do not follow, indicating that there is an unexpected frequency shift to the SRS daughter wave dispersion relations. The data are fitted by the theoretical model (eq. 3.17) which includes an arbitrary frequency shift and scaled maximum growth rate (solid lines, right). This gives  $\Delta\omega_f = -1.6 \times 10^{-3}\omega_0$  and  $\Delta\omega_b = -2.1 \times 10^{-3}\omega_0$  for the frequency shift. . . . . 54
- 3.6 Same as figure 3.5 but with simulation data from a non-relativistic version of the simulation code. The fitted curves in the right hand figure give frequency shifts of  $\Delta\omega_f = -0.48 \times 10^{-3}\omega_0$  and  $\Delta\omega_b = -3.1 \times 10^{-5}\omega_0$ , considerably smaller than for the relativistic case. This indicates that the bulk of the frequency shift is due to relativistic effects. . . . . 56
- 3.7 2D simulation domain (not to scale), illustrating geometry and location of diagnostics. Blue dashed lines indicate locations where measurements of outgoing particle and field fluxes are measured. High frequency field measurements are also made along red dashed line at  $y = 0$ . Laser enters from the left hand boundary as indicated by cyan arrow. In all simulations the cell sizes  $\Delta x, \Delta y$  are equal. . . . . 57

- 4.1 **Upper left:** Wavenumber matching of transverse density perturbations. Laser wavenumber shown as black arrow, while black solid curve marks wave-vectors where TPD matching conditions are satisfied at  $n_e = 0.22n_{\text{cr}}$  and  $T_e = 3.5\text{keV}$ . TPD growth rates for a homogeneous, unperturbed background density are shown on the colour scale for varying density, with maximum growth occurring along dashed lines. Two symmetric pairs of TPD daughter waves are indicated by blue and green arrows. The two forward (or backward) propagating waves have the same frequency and can be coupled by a density perturbation with  $\mathbf{k}_i = \pm 2k_y\hat{\mathbf{y}}$  (cyan). **Upper right:** growth as a function of background density  $n_e$  for TPD maximum growth wavenumbers (dashed lines in left panel), with density perturbation of  $\delta n/n_e = 0$  (black), 0.02 (blue) and 0.04 (green). Dashed lines neglect Landau damping, solid lines include it. Approximate solution for  $\delta n/n_e = 0.04$  shown in red. **Lower centre:** Growth rate as a function of transverse density perturbation amplitude for TPD at electron densities indicated. Solid lines show numerical solution while the dashed lines use equation 4.18. Each curve's growth rates are normalised to the numerically calculated  $\gamma$  with no density perturbation. . . . . 69
- 4.2 Wavenumber matching of oblique density modes. Laser wavenumber shown as black arrow, while black solid curve marks wave-vectors where TPD matching conditions are satisfied at  $n_e = 0.22n_{\text{cr}}$  and  $T_e = 3.5\text{keV}$ . TPD growth rates for a homogeneous, unperturbed background density are shown on the colour scale for varying density, with maximum growth occurring along dashed lines. Two pairs of TPD daughter waves with similar  $k_y$  are indicated by blue and green arrows. The two forward (or backward) propagating waves have similar frequency and can be coupled by a density perturbation with wave vector indicated by cyan arrows. . . . . 71

4.3	Dependence of the TPD growth rate on the location of a second TPD EPW pair coupled by density perturbations, with $T_e = 3.5\text{keV}$ , $I = 2 \times 10^{15}\text{Wcm}^{-2}$ and background density indicated in the figure. The EPW pairs are parameterised by an angle made by one of their wavevectors, defined $\tan(\theta) \equiv k_y/(k_x - \frac{k_0}{2})$ . Here the first TPD pair is located at the angle marked $\theta_1$ , which is where peak TPD growth occurs with no density perturbation. Two growth rates are obtained, one for each pair, shown as blue and red curves corresponding to $\mathbf{k}(\theta_1)$ and $\mathbf{k}(\theta_2)$ respectively. Density perturbation amplitudes of $\delta n/n_e = 0$ (black), 0.01 (solid colour) and 0.02 (dashed colour) are used. A green dot marks the growth rates corresponding to transverse density perturbations. . . . .	72
4.4	Dependence of the TPD growth rate on the separation of two TPD EPW pairs that are coupled by oblique density perturbations, with $T_e = 3.5\text{keV}$ , $I = 2 \times 10^{15}\text{Wcm}^{-2}$ and background density indicated in the figure. The EPW pairs are parameterised by an angle made by one of their wavevectors, defined $\tan(\theta) \equiv k_y/(k_x - \frac{k_0}{2})$ . Here the wavevectors are symmetrically distributed about a central angle, $\theta_0$ , which is where peak growth occurs when no density perturbations are included. The two angles are given by $\theta_1 = \theta_0 - \Delta\theta/2$ and $\theta_2 = \theta_0 + \Delta\theta/2$ so that their angular separation is $\Delta\theta$ . The growth rates of the pairs are degenerate and indicated by blue lines for $\delta n/n_e = 0.02$ . Black lines mark the growth rates at $\theta_1$ and $\theta_2$ for $\delta n = 0$ . Growth rates are also shown for equivalent transverse density perturbations (green dashed lines) where the wavevectors are located at $\theta_1 = \theta_0 + \Delta\theta/2$ and $\theta_2 = -\theta_1$ . . . . .	73
5.1	Density profiles used for the simulations presented in this and the next chapter. The large-scale profile is purely exponential (see chapter 6) while the small-scale profile, used for the simulation in this chapter, is given in [Yan et al., 2014]. The small-scale profile is a fit to the output of a hydrodynamic simulation of an experiment on the OMEGA laser [Theobald et al., 2012]. . . . .	78

- 5.2 **Left:** Instantaneous  $k_y$  energy spectrum of the  $E_x$  field component during initial instability growth at  $t = 2.1\text{ps}$ . The laser wave-vector and  $\nabla n_e$  are parallel to the  $x$  axis while the laser polarisation is along the  $y$  axis. The white curve indicates where maximal linear growth of TPD is expected at each density, while the white dashed line marks TPD Landau cutoff ( $|\mathbf{k}|\lambda_D = 0.3$ ). The feature with small  $k_y$  near  $n_{\text{cr}}/4$  corresponds to absolute SRS backscatter. **Right:** Measured TPD linear growth rate (blue). Solid black and red lines indicate the theoretical convective growth rate at  $2 \times 10^{15}\text{Wcm}^{-2}$  and  $1.2 \times 10^{15}\text{Wcm}^{-2}$  [Yan et al., 2010], including Landau damping. Dashed line shows theoretical absolute growth rate [Simon, 1983]. . . . . 80
- 5.3 Diagnostics of initial LPI growth. **Left column:** Poynting flux diagnostics, filtered to include only waves at the laser frequency (a) or SRS scattered light frequency (c). Differing colour scales are used to allow scattered light to be seen. Positive values denote flux in the  $+\hat{\mathbf{x}}$  direction. Striations visible in (c) correspond to the SRS backscattered light wavelength. **(b):** Transverse-averaged electrostatic wave energy. **(d):** Transverse standard deviation of carbon density fluctuations. Dashed vertical lines on all plots mark the TPD Landau cutoff ( $|\mathbf{k}|\lambda_D = 0.3$ ). . . . . 82
- 5.4 Energy spectra of electrostatic field ( $E_x$ , top) and carbon density perturbations ( $\delta n_C$ , bottom) at 2.2ps (left), and 2.5ps (right). The data used covers the entire domain. In the  $E_x$  spectra a dashed line marks the Landau cutoff ( $|\mathbf{k}|\lambda_D = 0.3$ ), the solid circle bounds possible SRS EPW wavenumbers, and solid curved lines mark the wavenumbers where TPD has its maximum linear growth rate in a homogeneous plasma. Since these spectra are calculated using instantaneous snapshots the sign of  $\mathbf{k}$  is ambiguous; forward-propagating TPD daughter waves at  $\mathbf{k} = \mathbf{k}_+$  also appear at  $\mathbf{k} = -\mathbf{k}_+$ . . . . . 84

5.5	<p><b>Left:</b> Scattered light time-history. Green and olive lines measure SRS and SBS back-scatter detected at the laser entrance boundary, while SRS forward-scatter measured at the laser exit boundary is shown by the blue line. The SBS curve is calculated by subtracting the laser's maximum power from the signal measured at the laser entrance boundary and negating the result. This does not account for the laser rise, leading to the apparent 100% SBS scattering before 2ps. <b>Right:</b> Transmitted light time-history. In both panels, the vertical scale is normalised to the maximum incident laser power, and a Gaussian filter has been applied to all signals to remove high-frequency noise with period shorter than 25fs. . . . .</p>	86
5.6	<p><b>Left:</b> Threshold EPW field amplitude as a function of density for TPD. The wavenumber used in the calculation is that of the backwards-propagating daughter wave as this produces the lowest threshold. <b>Right:</b> Transverse-averaged cavitation correlator as a function of space and time. Vertical dashed line marks the TPD Landau cutoff. Following initial growth, TPD EPWs cause cavitation in the region closest <math>n_{cr}/4</math>, as predicted by threshold calculation in left panel. . .</p>	87
5.7	<p>(a): Poynting flux, filtered to include only EM waves at the laser frequency. (c): Poynting flux filtered to include only EM waves at frequency of SRS scattered light. (b): Transverse-averaged electrostatic wave energy in the <math>E_x</math> field component. (d): Transverse standard deviation of carbon ion density perturbations. See main text for an explanation of these figures. . . . .</p>	88
5.8	<p>Spectra of electrostatic field (<math>E_x^2</math>, left) and carbon density perturbations (<math>\delta n_C</math>, right) at 3.8ps (top), 6.3ps (middle), and 7.3ps (bottom). Data from 0.17-0.23<math>n_{cr}</math>. In the EPW spectra, the dashed line marks the Landau cutoff (<math> \mathbf{k} \lambda_D = 0.3</math>), solid circles bound possible SRS EPW wavenumbers, and solid lines mark location of maximum TPD linear growth rate. Dashed boxes in (a) and (b) indicate the integration regions for figure 5.9. . . . .</p>	91

- 5.9 Diagnostics of ‘bursty’ TPD activity as time series. Upper panel: Coloured lines show spectral amplitude of TPD EPWs of different handedness, averaged over regions bounded by dashed lines in first  $E_x$  spectrum of fig. 5.8. Black line is the sum of coloured lines. Vertical grey lines mark the peak of each burst. Second panel: Mean spectral amplitude of density perturbations, averaged over corresponding regions of first  $\delta n$  spectrum in fig. 5.8. Third panel: Lineouts of laser intensity from laser Poynting flux diagnostic of figure 5.7 at locations indicated in legend. Final panel: Differences between the lineouts of the previous panel, indicating absorbed intensity over the respective intervals. . . . . 93
- 5.10 Inferred time-integrated distribution functions, calculated from outgoing hot electron data. Time integration is performed over the period indicated in each panel. Particle counts in each momentum bin have been weighted according to the energy of the bin. Histograms are each normalised to maximum of the binned values, and colour scales are shared. White dashed lines show the momenta expected of TPD-accelerated hot electrons, while the white circles indicate the particle energy at a given  $|\mathbf{p}|$ . . . . . 96
- 5.11 All panels from  $t = 4.5\text{ps}$ . **(a)**: Distribution of forward-propagating electrons with kinetic energy  $E_k > 50\text{keV}$  in  $x$ - $p_y$  phase space. Large  $|p_y|$  population due to Landau damping of TPD EPWs. **(b)**: Spatial distribution of small  $|p_y|$  ( $|p_y| < 0.1m_e c$ ) electrons from (a) in subsection of simulation domain, featuring striations corresponding to potential wells of EPWs, along with de-phased (uniformly distributed) electrons. **(c)**:  $k_x$ - $k_y$  spectrum of spatial modes of hot electron density (same population as in (b), but calculated over entire domain). Bright features identify EPW wavenumbers causing trapping. **(d)**: EPW spectrum from  $E_x$  field component, showing EPWs responsible for trapped electron populations in (c). Note that spectra in (c) and (d) are from static snapshots so the sign of  $\mathbf{k}$  is ambiguous. In (c) & (d) dashed circle indicates approximate Landau cutoff ( $|\mathbf{k}|\lambda_D = 0.3$ ), small solid circle indicates wavenumbers of SRS EPWs and two curved lines denote TPD wavenumbers. . . . . 99

5.12 Flux of particles travelling through the laser exit boundary. **Left:** Instantaneous flux distribution integrated over different energy bins to produce time-histories of the power carried within these bins, normalised to the laser power. Flux from the bulk plasma in the lowest energy bin has been subtracted, and is negligible in higher-energy bins. **Right:** Flux distribution, time integrated over the whole simulation and weighted according to the energy of each bin. The  $y$ -axis normalisation is the total delivered laser energy. Curves plotted are simulation data (black), the expected thermal distribution (blue) and components of a multi-temperature fit to the hot-electron distribution (green, red and cyan). **Bottom:** Same as right, but showing low-energy range. Green line shows an energy-equivalent single-temperature fit to the multi-component version above. . . . . 101

6.1 **Left:** Instantaneous  $k_y$  energy spectrum of the  $E_x$  field component during initial instability growth at 2.3ps. The laser wave-vector and  $\nabla n_e$  are parallel to the  $x$  axis while laser polarisation is along the  $y$  axis. The solid white curve indicates where maximal linear growth of TPD is expected at each density, while the dashed white curve indicates wavenumbers required for absolute 90°SRS side-scatter. The SRS observed has lower  $k_y$  and is therefore convective and at lower scatter angles. Dashed white and green lines mark the Landau cut-offs of TPD and SRS backscatter respectively. Both are in reasonable agreement with the data. **Right:** Instantaneous  $k_y$ - $k_x$  energy spectrum of  $B_z$  field component calculated from the same snapshot but using only data from between  $x = 350$ - $400\mu\text{m}$ . Arcs are EM waves from SRS back and side-scatter at angles of up to 60° from direct backscatter. Overlaid solid white curves mark bounds on the possible SRS backscatter wavenumbers for the relevant range of densities. . . . . 108



6.2	Measured TPD linear growth rate for NIF-scale simulation (blue). The solid black line indicates the theoretical inhomogeneous convective growth rate [Yan et al., 2010] including Landau damping, while the dashed black line indicates the theoretical absolute growth rates [Simon, 1983]. The observed growth shows better agreement with the range of wavenumbers where convective growth is expected to occur, but there is a large discrepancy in the values which is currently unexplained. . . . .	109
6.3	Diagnostics of initial LPI growth. <b>(a)</b> : Poynting flux filtered to include only waves at the laser frequency. <b>(c)</b> : Same, but for SRS scattered light frequencies. <b>(b)</b> : Transverse-averaged electrostatic wave energy. <b>(d)</b> : Transverse standard deviation of carbon density fluctuations. . . . .	111
6.4	Diagnostics of initial LPI growth. <b>(a)</b> : Poynting flux along $y = 0$ , filtered to include only waves at the laser frequency. <b>(c)</b> : Same, but for SRS scattered light frequencies. <b>(b)</b> : Transverse-averaged electrostatic wave energy. <b>(d)</b> : Transverse standard deviation of carbon density fluctuations. . . . .	113
6.5	Lineouts from figure 6.4 (a) at the densities indicated. These show the incident intensity available to TPD ( $0.19n_{\text{cr}}$ ) and the remaining intensity at $n_{\text{cr}}/4$ . Note that these intensities are measured at $y = 0$ and so may not be representative of the intensity where $y \neq 0$ . . . .	114
6.6	Transverse-averaged cavitation correlator. The white vertical line marks the TPD Landau cutoff. Values of the statistic that are above 0.5 indicate probable cavitation activity. Note that in this figure only a subset of the domain is shown; cavitation does not occur in the lower density plasma. . . . .	115
6.7	Carbon density perturbation spectra. <b>Left</b> : Evaluated between $x = 50\text{-}100\mu\text{m}$ at 5.0ps. Arc visible at $k_x \sim 1.8\omega_0/c$ is due to SRS backscatter. <b>Right</b> : Evaluated between $x = 350\text{-}400\mu\text{m}$ at 14.0ps. Arc at $\mathbf{k} \simeq \mathbf{0}$ is due to the filamentation instability; this is also visible at lower amplitude in the left panel. . . . .	116

6.8	<b>Left:</b> Scattered light time-history. Green and olive lines measure SRS and SBS back-scatter detected at the laser entrance boundary. SRS forward-scatter measured at the laser exit boundary is shown by a blue line, however this remains at $\sim 1\%$ for the duration of the simulation. <b>Right:</b> Transmitted light time-history. In both panels, the vertical scale is normalised to the maximum incident laser power, and a Gaussian filter has been applied to all signals to remove high-frequency noise with period shorter than 25fs. . . . .	118
6.9	(a) and (b): $E_x$ field energy spectra, calculated along $y = 0$ between 1.5-2.5ps and 5-6ps for the region $x = 300\text{-}350\mu\text{m}$ . Colour scales are shared. White dashed lines indicate bounds on EPW wave frequencies possible within this region, while green dashed lines show the Stokes line. Instability occurs at the intersection of the Stokes line with electrostatic waves. (c) and (d): spatially averaged electron distribution functions corresponding to each spectrum (blue lines). Range of EPW phase velocities marked by black dashed lines, distribution function at $t = 0$ in green. . . . .	120
6.10	$E_x$ (left column) and $B_z$ (right column) field energy spectra, calculated along $y = 0$ between 1.5-2.5ps (upper row) and 4-5ps (lower row). Colour scales are common on each row. White and black dashed lines indicate expected frequencies of EM and ES waves from back and forward-scatter SRS. Red dashed line corresponds to side-scatter at $60^\circ$ from direct backscatter, the largest angle of scattered light relative to direct backscatter observed in the simulation. Solid black line in (a) and (c) marks $\omega_{pe}$ . At 1.5-2.5ps, wave growth occurs between red and white dashed lines as expected. At 4-5ps, SRS electrostatic waves trap electrons leading to downshifted electrostatic waves and upshifted scattered light. Bright feature at $x \simeq 400\mu\text{m}$ in (c) is backwards propagating TPD mode. . . . .	122

- 6.11 **(a)**:  $E_x$  energy spectrum along  $y = 0$  between  $t = 5$ -6ps and  $x = 50$ - $100\mu\text{m}$ . **(b)**: Electron distribution function spatially averaged over the same region at 5.5ps. Waves visible in (a) are driven by the beating of the laser and SRS backscattered light. Beat frequencies are not natural frequencies of any electrostatic mode so are not driven to large amplitude, but are sufficient to produce the suprathermal electron population seen in (b). Black dashed lines in (b) bound possible phase velocities of SRS EPWs. Red dashed line marks largest phase velocity of waves visible in (a). . . . . 123
- 6.12 Inferred time-integrated distribution function, calculated from outgoing hot electron data using the method described in section 5.4.1. Time integration is performed over the entire simulation. Particle counts in each momentum bin have been weighted according to the energy of the bin. White dashed lines show the momenta expected of TPD-accelerated hot electrons, while the white circles indicate the particle energy at a given  $|\mathbf{p}|$ . . . . . 126
- 6.13 Flux of particles travelling in the forwards ( $+\hat{\mathbf{x}}$ ) direction through a surface at  $x = 350\mu\text{m}$  ( $\sim 0.18n_{\text{cr}}$ ), inferred from snapshots of high-energy electrons in the bulk plasma. These must be produced by SRS as TPD does not occur left of this surface. **Left**: Instantaneous flux distribution integrated over different energy bins to produce time-histories of the power carried within these bins, normalised to the laser power. Flux from the bulk plasma in the lowest energy bin has been subtracted, and is negligible in higher-energy bins. **Right**: Flux distribution, time integrated over the simulation and weighted according to the energy of each bin. The  $y$ -axis normalisation is the total delivered laser energy. Curves plotted are simulation data (black), the expected thermal distribution (blue) and a single-temperature fit to the hot-electron distribution (green). . . . . 127

6.14 Flux of particles through the laser exit boundary. **Left:** Instantaneous flux distribution integrated over different energy bins to produce time-histories of the power carried within these bins, normalised to the laser power. Flux from the thermal component in the lowest energy bin has been subtracted, and is negligible in higher-energy bins. **Right:** Flux distribution, time integrated over the simulation duration and weighted according to the energy of each bin. The  $y$ -axis normalisation is the total delivered laser energy. Curves plotted are simulation data (black), the expected thermal distribution (blue) and a three-temperature fit to the suprathermal distribution (purple), along with the three separate components (green, red and cyan). **Bottom:** Same as right panel, but with a single-temperature fit used instead. . . . . 129

# Acknowledgments

I would like to thank Tony Arber, my supervisor, for his support and enduring patience throughout the degree. I would also like to thank the EPOCH developer team (Keith Bennett, Chris Brady, Tom Goffrey and Heather Ratcliffe) for their assistance in fixing bugs in the simulation code. My family, friends, and girlfriend have provided unconditional support throughout the PhD, and it has been a pleasure working alongside the talented members of the CFSA at Warwick.

Computational resources for simulations and post-processing were provided by EPCC via ARCHER and Cirrus, HPC Midlands Plus via Athena, and the University of Warwick's Centre for Scientific Computing. Finally, I acknowledge the financial support of EPSRC and CCPP in funding my studentship.

# Declarations

This thesis is submitted to the University of Warwick in support of my application for the degree of Doctor of Philosophy. It has been composed by myself and has not been submitted in any previous application for any degree. The work presented (including data generated and data analysis) was carried out by the author except in the cases outlined below:

- The derivation presented in the appendix was performed in collaboration with B. C. G. Reman.

Parts of this thesis have been published by the author:

- A. G. Seaton & T. D. Arber, *Particle-in-Cell Simulations of Laser-plasma Instabilities in Long Scale-Length Plasmas Relevant to Shock-ignition*, submitted to Physics of Plasmas.

# Abstract

In the shock-ignition (SI) approach to direct-drive inertial confinement fusion (ICF) a high-intensity laser pulse ( $10^{15}$ - $10^{16}$ Wcm $^{-2}$ ) is used to drive a converging shock through a pre-compressed fuel pellet to trigger its ignition [Betti et al., 2007]. Studies over the last decade have indicated that laser-plasma instabilities (LPIs) play a key role in determining the effectiveness of this ignitor shock [Theobald et al., 2012; Nora et al., 2015]. In particular, the hot electron distribution produced by LPIs is vital [Betti et al., 2008]. Electrons below a threshold energy, usually taken to be around 100keV, may be stopped in the dense fuel behind the shock and strengthen it, while above this threshold the electrons can pre-heat the fuel ahead of the shock and reduce its strength.

Previous simulation work has investigated SI for short density scale-length plasmas [Yan et al., 2014] relevant to experiments with targets of a smaller scale than required for ignition [Theobald et al., 2012]. In this project a series of 2D particle-in-cell simulations was performed of coronal plasmas with a variety of scale-lengths. Of these, two are presented in this thesis. In the first simulation the small-scale regime of [Yan et al., 2014] is revisited, while the second has initial conditions chosen to represent a full-scale ignition design. It is found that the two-plasmon decay (TPD) dominates the dynamics and hot-electron production in the small-scale case, while stimulated Raman scattering (SRS) plays a more prominent role in larger-scale coronas. In the sub-scale case the spectrum of IAWs that is ponderomotively driven by TPD is found to be important. Growth rates are derived to treat this, and offer a possible explanation for the dynamics observed. In the ignition-scale case SRS is found to exhibit kinetic inflation [Montgomery et al., 2002; Vu et al., 2002], and two mechanisms are proposed to describe the long-term behaviour observed. In both cases the hot-electron distribution can be characterised by a relatively low temperature of around 30keV, which is promising for the SI scheme.

# Abbreviations

BAM	Beam-acoustic mode
CBET	Cross-beam energy transfer
FIR	Finite impulse response
EM	Electromagnetic
EOS	Equation of state
EPW	Electron-plasma wave
IAW	Ion-acoustic wave
ICF	Inertial confinement fusion
LPI	Laser-plasma instability
NIF	National ignition facility
PIC	Particle-in-cell
PP	Phase plate
PS	Polarisation smoothing
RPIC	Reduced particle-in-cell
SBS	Stimulated Brillouin scattering
SI	Shock ignition
SRS	Stimulated Raman scattering
SSD	Smoothing by spectral dispersion
TPD	Two-plasmon decay
TPMI	Trapped particle modulational instability



# Chapter 1

## Introduction

### 1.1 Inertial Confinement Fusion

Inertial Confinement Fusion (ICF) is one of the two major approaches to achieving self-sustaining thermonuclear fusion that are currently being pursued, the other being Magnetic Confinement Fusion (MCF). In both, the challenge is to confine the fuel over a sufficient period of time that fusion reactions result in net energy gain. In the inertial approach, as the name suggests, the inertia of the fuel itself is used to maintain this confinement.

#### 1.1.1 Fundamental Principles

Nuclear fusion refers to the joining of two atomic nuclei. This occurs when the Coulomb repulsion between their positively charged protons is overcome by the attractive force of the strong nuclear interaction. Nuclear reactions result in a change in potential energy, which can be calculated by considering the mean energy gain per nucleon that is achieved when assembling a given nucleus. This is shown in figure 1.1. A reaction in which the total binding energy of the reactants is greater than that of the products is energetically favourable and results in the energy difference being delivered as the kinetic energy of the products. Considering figure 1.1, one can deduce that fusion reactions producing nuclei lighter than  $^{56}\text{Fe}$  are energetically favourable. In contrast, producing nuclei heavier than  $^{56}\text{Fe}$  is not. Furthermore for nuclei heavier than  $^{56}\text{Fe}$ , energy can only be extracted by their splitting, or fission.

In order to achieve fusion for the purposes of exploiting this energy gain, the primary difficulty lies in the environment required for the reactions to take place at an appreciable rate. Due to the short range of the strong nuclear force, the reactants must reach very short separation before the reaction will take place.

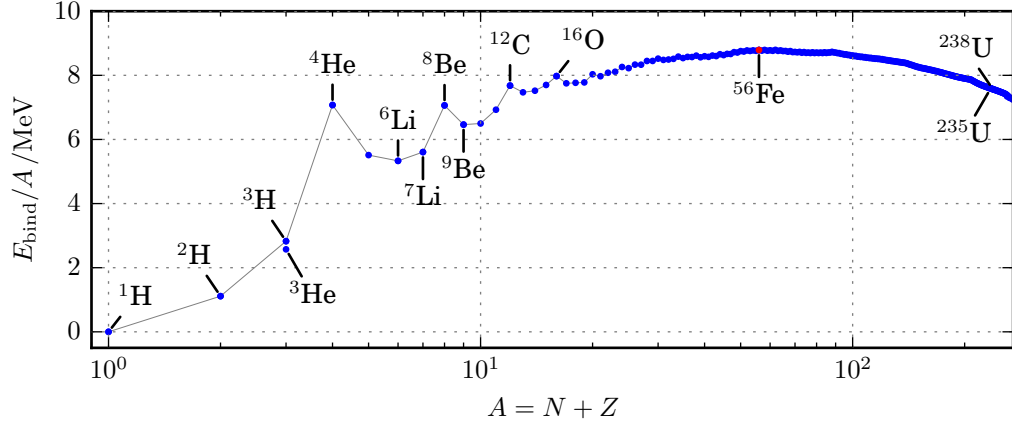


Figure 1.1: Binding energy per nucleon for selected nuclei with atomic number  $Z$  and neutron count  $N$ . Grey line connects nuclei with the highest binding energy per nucleon for given nucleon count  $A$ . These are not always the most stable nuclei; for example the  $^8\text{Be}$  nucleus is extremely unstable and decays to  $^9\text{Be}$  immediately.  $^{56}\text{Fe}$ , marked in red, is the nucleus with the highest binding energy per nucleon. Data from [Huang et al., 2017].

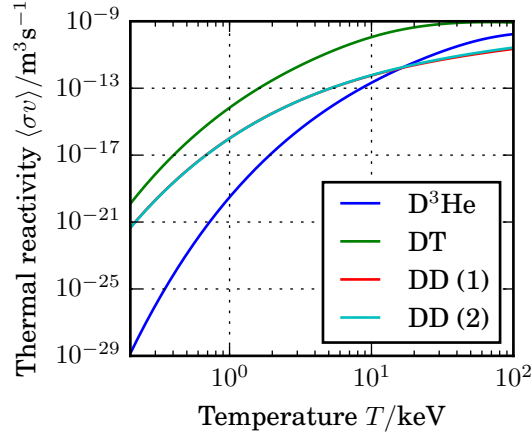
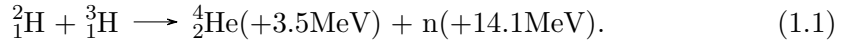


Figure 1.2: Thermal reactivities of various fusion reactions as a function of temperature, calculated using the parameterisations of [Bosch and Hale, 1992]. A temperature of 1keV is equivalent to  $1.16 \times 10^7\text{K}$ . The D-D reaction has two branches which occur with almost equal likelihood. Their reaction rates are indistinguishable in this figure.

Forcing two nuclei so close together requires a significant amount of energy due to the Coulomb repulsion, and so is referred to as the ‘Coulomb barrier’. For the reaction between Deuterium and Tritium, this energy barrier is on the order of 0.4MeV. If this were the average energy of each reacting particle a temperature of around  $5 \times 10^9\text{K}$  would be required. Fortunately, by considering the reaction rate averaged over a material with thermally distributed particle energies, a significantly lower required temperature can be calculated. This is because such a distribution contains small numbers of particles with energies much larger than the mean particle energy, and these may be capable of overcoming the Coulomb barrier. Furthermore, quantum tunnelling lowers the required energy to an extent. Figure 1.2 shows the fusion reaction rate, averaged over a thermal distribution of reactant velocities, as a function of temperature for several important fusion reactions. The reaction with the highest rates at low temperatures is that between deuterium and tritium, isotopes of hydrogen with one and two neutrons respectively. The reaction may be written



As shown in figure 1.2, this requires temperatures on the order of 10keV ( $\sim 10^8\text{K}$ ) to achieve an appreciable reaction rate; two orders of magnitude less than the Coulomb barrier’s effective temperature. Assuming such a temperature can be achieved, a simple inequality can be derived for achieving net energy gain in a fusion device. This is called the Lawson criterion, and balances heating of plasma due to fusion reactions against energy losses, which are assumed to occur over some confinement time  $\tau_E$ . For DT fuel at a temperature of  $T = 10\text{keV}$ , the condition may be written as

$$n\tau_E \gtrsim 10^{21}\text{s/m}^3 \quad (1.2)$$

where  $n$  is the electron number density.

In ICF, confinement is provided by the fuel’s inertia and so  $\tau_E$  is very small. A more useful criterion for ICF can be produced by assuming that the confinement time is given by the time necessary for a rarefaction wave to travel from the edge of the fuel to its centre over a distance  $R$ . The Lawson criterion can then be reformulated in terms of an ‘areal density’  $\rho R$

$$\rho R \gtrsim 1\text{g/cm}^2, \quad (1.3)$$

where  $\rho$  is the mass density of the fuel. This mass of fuel must be heated to 10keV,

with the energy required to do so scaling with mass as  $E \propto \rho R^3 = (\rho R)^3 / \rho^2$ . Constructing a driver capable of delivering greater amounts of energy is generally very costly so, since the numerator in this expression is fixed by the Lawson criterion, it is highly advantageous to maximise the final density of the fuel. A target density on the order of  $300\text{g/cm}^{-3}$  or 1000 times the density of the solid fuel is typically considered necessary [Atzeni and Meyer-ter Vehn, 2004]. The largest ICF driver currently delivers an energy of 1.9MJ, while high-performing experiments reach fuel densities of around  $500\text{g/cm}^{-3}$  with areal densities of up to  $0.3\text{g/cm}^{-2}$  [Meezan et al., 2017; Hurricane et al., 2019].

In a fusion reactor designed for electricity generation, so as to outweigh inefficiencies and make such a reactor economical, it would be necessary for the fusion reactions to produce a much greater quantity of energy than supplied for target compression and heating. This ratio of output to input energy is referred to as the gain. It was realised early on in the ICF programme that high gain cannot be achieved if the drive energy is used to uniformly heat the compressed fuel. Instead, laser-driven ICF designs attempt to achieve what is known as ‘hot-spot ignition’ [Nuckolls et al., 1972], through which high gain is thought possible. This is illustrated in the four inset panels of figure 1.3. In this scheme, the target is a spherically symmetric pellet formed of three components. The outer layer is a solid shell called an ‘ablator’, typically composed of plastic. Within this lies a second shell of solid DT fuel, while the centre of the target is filled with DT gas. To compress the target the outer layer is progressively ablated by illuminating it with a powerful radiation source. The resulting pressure on the remainder of the target causes it to implode and become compressed. On reaching peak compression, the work done by the dense DT fuel on the central gas fill raises its temperature to the point where it ignites and therefore heats the remaining fuel to ignition. This scheme can achieve high gain since only a small mass of fuel (the gas fill) needs to be heated to temperatures at which it ignites, and acts as a spark to trigger ignition of a much larger fuel mass.

In order for hot-spot ignition to be successful, the compression of the fuel must be close to isentropic; heating before the stagnation phase would necessitate a considerably greater drive energy. In early hot-spot ignition designs, smooth, carefully shaped laser pulses were proposed to achieve almost perfectly isentropic implosions [Nuckolls et al., 1972]. Unfortunately, since compression occurs so rapidly, these pulse shapes are liable to introduce shocks that are less effective at compressing the target. Rather than attempt to avoid the inevitable, modern designs purposefully drive a series of shocks that are timed to arrive in the hotspot at the same

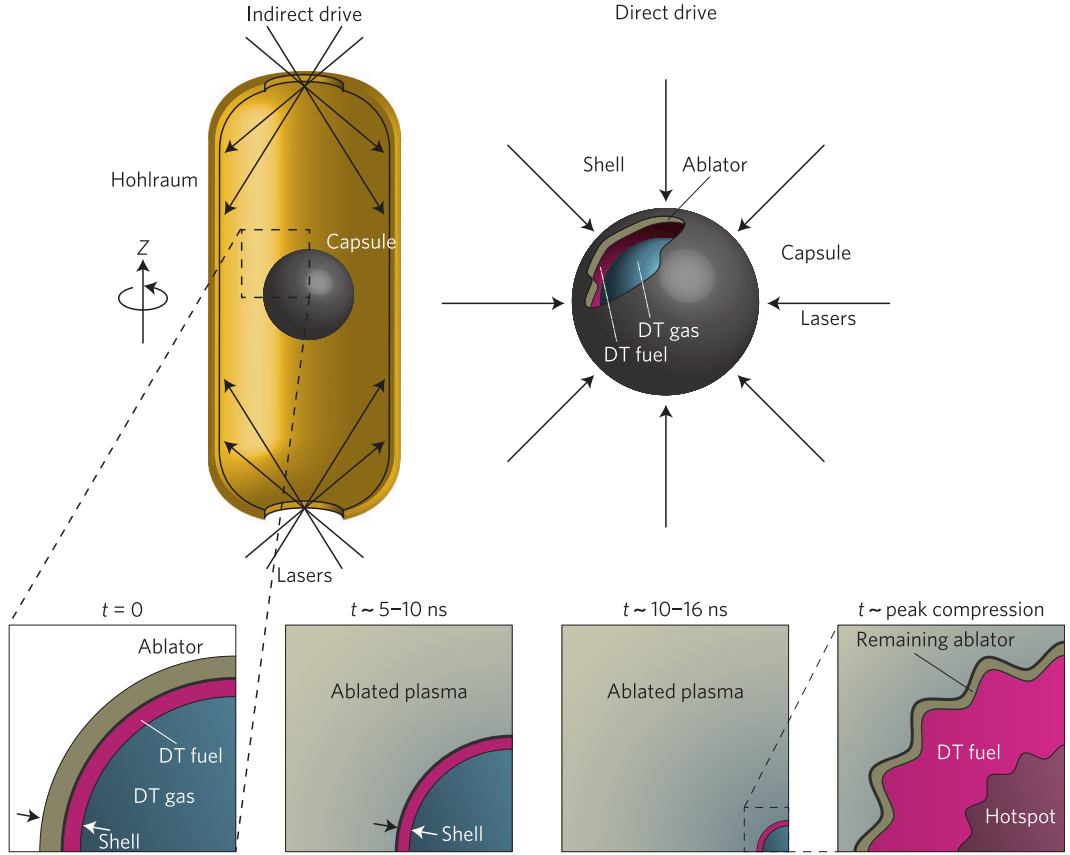


Figure 1.3: Illustration of the two main laser drive configurations, direct and indirect-drive. In the former the target is illuminated directly by the laser, while in the latter a radiation enclosure formed of a high-Z material such as gold is used to convert laser photons to X-rays. Lower inset panels show snapshots in time illustrating an implosion. Reprinted by permission from Nature Physics [Betti and Hurricane, 2016].

time. By driving multiple small shocks in this manner it can be shown that the implosion can be made close to isentropic.

### 1.1.2 Direct & Indirect-drive

Two drive configurations have generally been used for laser-driven ICF. These are shown schematically in figure 1.3. In the direct-drive scheme the laser beams are used to directly illuminate the target, and enter from ports that are distributed uniformly about the (spherical) target chamber. Historically, this approach has been hindered by poor beam uniformity. This leads to ‘imprint’ of the laser beam’s spatial intensity profile on the target surface [Peebles et al., 2019] which seeds hy-

hydrodynamic instabilities, primarily the Rayleigh-Taylor instability. More recently, various techniques have been developed to smooth the intensity distribution on target. These techniques include spatial smoothing (random phase plates or RPPs) [Kato et al., 1984], temporal smoothing (smoothing by spatial dispersion or SSD) [Skupsky et al., 1989] and polarisation smoothing [Boehly et al., 1999]. Along with the lack of progress with the indirect-drive approach, this has renewed interest in the direct-drive scheme.

In the indirect-drive approach the fuel pellet is placed at the centre of a cylindrical radiation enclosure constructed from a high-Z material, called a ‘hohlraum’. The lasers are arranged in two circular clusters at opposing sides of the target chamber and focused through two holes in the end of the hohlraum at its inner surface. This leads to their conversion into X-rays which drive the implosion of the target. The indirect-drive approach leads to a considerable improvement in drive uniformity by comparison to direct-drive which, among other reasons, is why this approach has generally been favoured in the past. This method of increasing drive uniformity comes at a significant price however as the conversion to X-rays is inefficient and results in loss of roughly two thirds of the laser energy.

### 1.1.3 Current Status

Since the beginning of the laser-driven ICF programme a succession of facilities have been built with progressively larger delivered laser energy and beam counts. Presently the largest laser systems configured for direct and indirect-drive are OMEGA and the National Ignition Facility (NIF) respectively. Both of these are infrared Nd:glass lasers, frequency tripled into the UV with an output wavelength of 351nm. The OMEGA laser facility is a 60-beam system based at the University of Rochester’s Laboratory for Laser Energetics that delivers 30kJ (UV). The NIF is based at the Lawrence Livermore National Laboratory and is currently the world’s largest laser system by delivered energy at 1.9MJ (UV). It is a 192-beam system, though these are grouped into 48 ‘quads’ that each occupy a single port in the target chamber.

Due to the much larger drive energy available at the NIF for indirect-drive, this approach currently produces the highest-performing shots. It had been envisaged that after construction of the facility in 2009, ignition would be achieved rapidly within a few years [Moses et al., 2009]. Unfortunately progress was considerably slower than anticipated and as of 2019 ignition has yet to be reached. Nevertheless certain milestones have been achieved. Perhaps most notable was the attainment in 2013 of so-called ‘fuel gain’ greater than unity [Hurricane et al., 2014], where energy delivered to the fuel is exceeded by that produced from fusion reac-

tions. More recent designs achieve fuel gains greater than two, with a fusion yield of around 55kJ [Pape, 2018].

Several factors have limited the performance of these experiments. Time-dependent drive asymmetries, due in part to laser-plasma instabilities, led to many experiments producing hot-spots with low-mode asymmetries [Kritcher et al., 2016]. These asymmetries cause inefficient transfer of kinetic energy to the hotspot and present a higher surface area through which it can be cooled. Additionally, hydrodynamic instabilities seeded by engineering features such as the gas fill tube or the plastic film (‘tent’) used to fix the target in place, may cause mixing of high-Z ablator material into the fuel [Clark et al., 2016]. This leads to considerable loss of energy through bremsstrahlung X-ray emission and thermal conduction. Strategies to mitigate these effects have produced higher performing implosions [Dittrich et al., 2014; Park et al., 2014; Hinkel et al., 2016], but involve sacrifices that limit the performance that can ultimately be reached. The performance of these experiments can potentially be increased to the point where ignition will occur, and several potential routes to this are being actively pursued [Hurricane et al., 2019]. However at this stage it is unclear whether indirect drive ICF will ever be capable of high gain, at least without radical improvements in the laser driver.

#### 1.1.4 Shock Ignition

With the slow progress made with conventional ICF approaches, there has been consideration of potential alternative ignition schemes that can leverage modern technology, such as high-power lasers [Strickland and Mourou, 1985]. Of these alternative schemes, one which has emerged as a promising approach is the shock ignition (SI) scheme [Betti et al., 2007]. In this direct-drive concept a short, high intensity ‘spike’ is appended to the conventional laser pulse. This launches an additional shock, which is timed to collide with the rebound compression shock in the central hotspot at peak convergence of the capsule. The converging shock is amplified through this collision, and subsequently raises the hotspot pressure above the threshold for ignition. Like other alternative ignition schemes, this arrangement can be thought of as separating ICF into two phases: creation of a dense fuel assembly (compression), and delivery of the energy needed to ignite the hotspot (ignition).

There are several advantages to this scheme over conventional direct-drive ICF. First, it has potential to achieve higher energy gain. This is because the pressure reached in the central hotspot is higher than that of the surrounding cold fuel, in contrast with conventional schemes where an isobaric fuel assembly is created [Betti et al., 2007]. Consequently, for the same yield, the shell implosion velocity

and therefore laser intensity may be lower than a conventional direct-drive implosion. While this is beneficial in terms of reducing the required driver energy, it also reduces the risk of detrimental effects caused by both hydrodynamic and laser-plasma instabilities (LPIs). However, during the ‘spike’ in laser power, intensities of  $10^{15}$ - $10^{16}$  Wcm $^{-2}$  are required in order to generate a shock of sufficient strength for ignition of the hotspot. These intensities are considerably larger than those typically used for direct-drive, which are typically  $10^{14}$ - $10^{15}$  Wcm $^{-2}$ . This places this portion of the pulse in an intensity regime that has not received much attention in a direct-drive ICF context.

Laser-plasma instabilities (LPIs) can scatter significant fractions of laser energy or, indirectly, divert it into supra-thermal (‘hot’) electron populations via Landau damping of the resulting electron plasma waves (EPWs). The main instabilities involved are stimulated Brillouin scattering (SBS), stimulated Raman scattering (SRS) and the two-plasmon decay (TPD). In general LPIs are considered detrimental to ICF schemes and conventionally it has been important to minimise their activity. With regard to SI however, it is possible that the hot electrons produced by these instabilities could be beneficial. Depending on their energy, these may either be stopped in the dense shell behind the ignitor shock and enhance its pressure, or deposit energy ahead of the shock and inhibit efficient compression. The threshold energy above which these electrons are considered detrimental is thought to be around  $\sim 100$  keV [Betti et al., 2007]. This has led to some SI designs in which the production of moderate energy ( $< 100$  keV) electrons is maximised - so called ‘electron shock ignition’ [Shang et al., 2017; Theobald et al., 2017]. Naturally these issues make an understanding of the behaviour of LPIs under relevant conditions important to the success of SI.

## 1.2 Previous Work

### 1.2.1 Experiments

Experiments investigating SI have typically focused on sub-scale target designs as the laser facilities that were available could not deliver sufficiently energetic pulses to drive full ignition-scale implosions. This has resulted in most experiments having plasma conditions near  $n_{cr}/4$  of  $T_e = 1$ - $3.5$  keV and density scale-length  $L_n < 350 \mu\text{m}$  [Cristoforetti et al., 2017, 2018; Baton et al., 2017; Theobald et al., 2012, 2015; Nora et al., 2015; Hohenberger et al., 2014; Batani et al., 2012, 2014; Baton et al., 2012; Theobald et al., 2008] (see table 1.1 for a summary of key information from the associated publications). The results of these have been varied, however there are



Key	$I/10^{15}$ $\text{Wcm}^{-2}$	Laser system	Beams	Smoothing	Target Geometry	Parameters at $n_{\text{cr}}/4$			LPI Measurements			
						Ions	$T_e$ /keV	$L_n$ / $\mu\text{m}$	SBS /%	SRS /%	$T_{\text{hot}}$ /keV	$f_{\text{hot}}$ /%
(1)	$3^{\text{S}}$ $10^{\text{S}}$	PALS ( $1\omega$ ) PALS ( $3\omega$ )	1	PP	Planar	CH	3-4 1.5	? 50-100	? ?	0.5-5 < 0.2	$38^{+57}_{-12}$ $20^{+15}_{-8}$	$5.32^{+6.90}_{-0.26}$ $0.28^{+0.28}_{-0.06}$
(2)	$1.5^{\text{S}}$	OMEGA	20	-	Spherical	CD	?	?	?	?	$38\pm3.5$	$1.8\pm0.4$
(3)	2-6	PALS	1	PP	Planar	C <sub>8</sub> H <sub>7</sub> Cl	1.5	20-80	3-15	0.02-0.2	$20\pm10$	?
(4)	$1.5$	LIL	4	PP, SSD	Planar, HS	CH	?	?	2.5	1.2	?	?
(5)	$1.3\text{-}3^{\text{M}}$ $1.5\text{-}2.1^{\text{M}}$	OMEGA	60	PP, PS PP, PS, SSD	Spherical	CH	3.5	120S	7	?	60-80	$5.5\text{-}9$ $1\text{-}4$
(6)	$0.6\text{-}1.4^{\text{M}}$	OMEGA	12	PP, PS	Planar	CH	2.0-2.9	350	<1-3	<1-3	25-70	$0.1\text{-}1.8$
(7)	$0.5\text{-}8^{\text{S}}$ $0.5\text{-}3^{\text{S}}$ $1.5^{\text{S}}$	OMEGA	20	- - PP	Spherical	CD	1.8	170	5-12 6-9 4-5	3-24 1.2-7 0.5-0.8	30 30 40	? ? ?
(8)	$2\text{?}\text{-}30^{\text{S}}$	PALS	1	PP	Planar	CH	1-2	?	?	?	50	?
(9)	$0.07\text{-}1.0^{\text{S}}$	LULI	1	-	Planar	CH	?	10-200	7-11	<5	?	?
(10)	$\sim 1.4^{\text{S}}$	OMEGA	60	PP, SSD, PS	Spherical	CH/CD	?	?	?	?	?	?

Table 1.1: Summary of laser and plasma parameters used in experiments investigating shock-ignition, ordered by date. Results are published in: (1): [Batani et al., 2019], (2): [Trela et al., 2018], (3): [Cristoforetti et al., 2017, 2018], (4): [Baton et al., 2017], (5): [Theobald et al., 2015; Nora et al., 2015], (6): [Hohenberger et al., 2014], (7): [Theobald et al., 2012], (8): [Batani et al., 2012, 2014], (9), [Baton et al., 2012], and (10): [Theobald et al., 2008]. In experiments where conditions were varied significantly between shots (e.g. phase plates on or off) entries are split into multiple rows. Intensities are identified as single beam ('S') or the sum of the multiple beam intensities ('M'). The beam count refers to the quantity on during the intensity spike. Under smoothing, 'PP' refers to phase plates, 'SSD' to smoothing by spectral dispersion and 'PS' to polarisation smoothing. Under geometry, 'HS' refers to hemispherical targets. Question marks under parameters indicate that the quantity was either not diagnosed or that this data could not be found in the associated publication. Finally, the scatter and hot-electron fractions are as a percentage of delivered laser energy.

some features of note. In cases where beams were stacked in order to reach high intensities, common-wave TPD [Myatt et al., 2014] (where beams share a decay wave) resulted in a hot electron temperature ( $T_{\text{hot}}$ ) that increased with laser intensity [Hohenberger et al., 2014]. This poses a potentially serious preheat risk for shock ignition. It was therefore suggested that this could be mitigated in future designs where common-wave TPD occurs by minimising beam overlap [Hohenberger et al., 2014]. In contrast, other experiments identified SRS as the dominant source of hot electrons and found weaker dependence of  $T_{\text{hot}}$  on laser intensity [Theobald et al., 2012, 2015, 2017]. In these cases SRS was thought to be triggered by filamentation of the laser beams at a relatively low density, which prevented large intensities from reaching  $n_{\text{cr}}/4$  [Theobald et al., 2012, 2015, 2017]. The most recent of these studies examined the effect of ablator material on LPI, finding CH to produce most hot electrons due to relatively high ion acoustic wave (IAW) damping rates. This is because IAWs act to limit the saturation amplitude of the LPIs [Theobald et al., 2017].

### 1.2.2 Theory & Simulation

At shock ignition intensities, many of the approximations that are made to simplify modelling of direct-drive experiments are not applicable. For example it is necessary to model the loss of energy of the laser (pump depletion), and self-consistent modelling of kinetic effects may become more important due to larger suprathermal electron populations. Prior simulations have therefore resorted to computationally expensive self-consistent 2D particle-in-cell (PIC) simulations. Like the experiments described above, these have considered plasmas with short scale-lengths. Simulations with  $L_n \simeq 50\mu\text{m}$ ,  $T_e = 5\text{keV}$  and a laser intensity  $I_L = 40\text{--}50 \times 10^{15}\text{Wcm}^{-2}$  found that both SRS and TPD were largely suppressed by cavitation near  $n_{\text{cr}}/4$  [Weber et al., 2012; Klimo et al., 2014]. More recently, collisional simulations modelled the OMEGA experiments of [Theobald et al., 2012] with coronal plasma parameters of  $L_n \simeq 170\mu\text{m}$  and  $T_e = 1.6\text{--}3.5\text{keV}$  [Yan et al., 2014]. These indicated that, at an intensity of  $2 \times 10^{15}\text{Wcm}^{-2}$ , both TPD and absolute SRS were active near  $n_{\text{cr}}/4$ . A moderate hot electron temperature of  $T_{\text{hot}} = 30\text{keV}$  was measured, consistent with the experiments, and was attributed to SRS. Finally, it was found that TPD occurred in bursts, with a mechanism proposed of the interaction of high and low density modes via pump-depletion [Yan et al., 2014].

With the construction of megajoule-class laser facilities such as the NIF, initial experiments have been performed to examine laser-plasma instabilities under shock-ignition relevant conditions, though results are yet to be published. Targets

shot on MJ-class facilities are expected to have coronal plasma parameters on the order of  $T_e \simeq 4\text{-}8\text{keV}$  and  $L_n \simeq 400\text{-}750\mu\text{m}$ . At conventional direct-drive intensities these parameters favour the SRS instability over TPD [Rosenberg et al., 2018; Michel et al., 2019], in contrast with sub-scale experiments where TPD has generally been dominant [Seka et al., 2009; Froula et al., 2012]. There has so far however been little modelling of LPI under these conditions, and none at SI intensities. The main aim of this project is therefore to address the lack of modelling by performing an initial study examining how LPI activity differs between the sub-scale design space and the ignition or NIF-scale regime.

### 1.3 Normalisations

Here the normalisations used in the remainder of the thesis are defined. Unless another normalisation is explicitly specified, equations are all written in SI units. For plots and when quoting values of quantities, the unit system chosen is based on the customary units of the laser-plasma literature. These are summarised in the table below.

Quantity	Symbol	Unit	Unit Name	Unit value (SI)
Time	$t$	ps	Picosecond	$10^{-12}\text{s}$
Frequency	$\omega$	$\omega_0$	3 <sup>rd</sup> harmonic of Nd:Glass laser	$2\pi c/(351\text{nm})$
Length		$\mu\text{m}$	Micron	$10^{-6}\text{m}$
Wavenumber	$k$	$\omega_0/c$	Vacuum wavenumber, Nd:Glass @ $3\omega$	$2\pi/(351\text{nm})$
Temperature	$T$	keV	kilo-electron volt	$1000e/k_B$
Density	$n$	$n_{\text{cr}}$	Critical density, Nd:Glass @ $3\omega$	$\omega_0^2 m_e \epsilon_0 / e^2$
Electric field	$E$	$m_e \omega_0 c / e$		$m_e \omega_0 c / e$
Magnetic field	$B$	$m_e \omega_0 / e$		$m_e \omega_0 / e$
Intensity	$I$	$\text{Wcm}^{-2}$		$10^{-4}\text{Wm}^{-2}$
Kinetic energy	$E_k$	keV	kilo-electron volt	$1000e$

# Chapter 2

## Theory

In this chapter theoretical descriptions of key phenomena are summarised that will be invoked to explain the results presented in later chapters. First, in section 2.1 we begin by discussing the systems of equations that are the foundation for modelling weakly coupled plasmas, and which underpin all of the subsequent theory. In section 2.2 the linear waves supported by these equations in an unmagnetised plasma are introduced and their basic properties described. The collisionless damping of the electrostatic waves and nonlinear effects which affect them are then discussed in sections 2.3 and 2.4. Finally, in section 2.5 the theory of three-wave parametric instabilities is introduced, beginning with general theory and subsequently specialising to the specific instabilities that are encountered in our simulations.

### 2.1 Fundamental Equations

The simulations in this thesis model the corona of a directly-driven ICF target. This is formed by the explosion of the target's ablator in response to its illumination by multiple UV laser beams. The laser is typically a frequency-tripled Nd:Glass laser with vacuum wavelength 351nm. The ablator is usually composed of plastic (CH) and forms a plasma characterised by a spatially uniform electron temperature of 1-10keV ( $\sim 10^7$ - $10^8$ K) depending on the experiment and, compared with the bulk of the target, a low density ranging from vacuum to  $n_e \simeq 10^{28}\text{m}^{-3}$ . Under these conditions the plasma is weakly collisional with an electron-ion collision frequency much lower than the plasma frequency  $\nu_{ei}/\omega_{pe} \sim 10^{-5}$ - $10^{-3}$ . As a result the ions are not in thermal equilibrium with the electrons and usually have a temperature that is smaller than that of the electrons by a factor of two or more. Since this plasma is being ablated from the main target its density decreases (usually exponentially)

with distance from the target’s ablation surface and has a large bulk velocity on the order of the ion sound speed. Finally, the plasma is usually not magnetised.

In the study of this system we aim to understand the self-consistent motion of ions and unbound electrons in the electromagnetic fields. Due to the high temperature we can neglect ionisation (assuming a CH plasma). With this assumption one may derive an equation for the evolution of the single-particle probability density function in phase-space for each species  $\alpha$ <sup>1</sup>:

$$\frac{\partial f_\alpha}{\partial t} + \mathbf{v} \cdot \nabla f_\alpha + \frac{q_\alpha}{m_\alpha} [\mathbf{E} + \mathbf{v} \times \mathbf{B}] \cdot \frac{\partial f_\alpha}{\partial \mathbf{v}} = \sum_\beta C_{\alpha\beta}(f_\alpha, f_\beta) \quad (2.1)$$

On the left hand side of the equation are terms describing the so-called ‘collective behaviour’ of particles in response to the electromagnetic fields. The term on the right hand side of the equation accounts for interactions between particles on length-scales  $\Delta x \lesssim \lambda_D$ , which are referred to as collisions [Braginskii, 1965]. These in general act to relax the distribution function towards a thermal equilibrium. Due to the low collision frequency in the system under consideration, this term is typically small and plays a relatively minor role in the evolution of the plasma. When the term is neglected and set to zero, the equation is referred to as the Vlasov equation.

Aside from through the collision term, the equations above are coupled via the electromagnetic fields whose evolution is described by Maxwell’s equations:

$$\nabla \cdot \mathbf{E} = \frac{\rho}{\epsilon_0}, \quad (2.2)$$

$$\nabla \cdot \mathbf{B} = 0, \quad (2.3)$$

$$\nabla \times \mathbf{B} = \mu_0 \mathbf{J} + \mu_0 \epsilon_0 \frac{\partial \mathbf{E}}{\partial t}, \quad (2.4)$$

$$\nabla \times \mathbf{E} = -\frac{\partial \mathbf{B}}{\partial t}. \quad (2.5)$$

It is important to note that the fields  $\mathbf{E}$  and  $\mathbf{B}$  in equation 2.1 refer to averaged quantities which neglect microscopic fluctuations arising due to particle collisions.

The Vlasov-Maxwell system including a collision term represents a ‘gold-standard’ description for the regime of plasma parameters important to laser-plasma instabilities in ICF. Unfortunately this description is often prohibitively complex and so it is often necessary to use a less detailed fluid formulation. This may be derived

---

<sup>1</sup>The equation shown is for the non-relativistic case, but may easily be generalised by replacing the velocity  $\mathbf{v}$  by the Lorentz boosted velocity  $\mathbf{u} \equiv \gamma \mathbf{v}$  everywhere other than in the 2nd term and Lorentz force expression.

by taking moments of the Vlasov equation and leads to the following equations, referred to as the ‘two-fluid equations’:

$$\frac{\partial n_\alpha}{\partial t} + \nabla \cdot (n_\alpha \mathbf{u}_\alpha) = 0, \quad (2.6)$$

$$m_\alpha \frac{\partial \mathbf{u}_\alpha}{\partial t} + m_\alpha (\mathbf{u}_\alpha \cdot \nabla) \mathbf{u}_\alpha = q_\alpha (\mathbf{E} + \mathbf{u}_\alpha \times \mathbf{B}) - \frac{1}{n_\alpha} \nabla P_\alpha, \quad (2.7)$$

where:

$$n_\alpha(\mathbf{x}, t) \equiv \int_{\mathbb{R}^3} f(\mathbf{x}, \mathbf{v}, t) d^3 \mathbf{v}, \quad (2.8)$$

$$\mathbf{u}_\alpha(\mathbf{x}, t) \equiv \int_{\mathbb{R}^3} \mathbf{v} f(\mathbf{x}, \mathbf{v}, t) d^3 \mathbf{v}, \quad (2.9)$$

$$\mathbf{P}_\alpha(\mathbf{x}, t) \equiv \int_{\mathbb{R}^3} (\mathbf{v} - \mathbf{u})(\mathbf{v} - \mathbf{u}) f(\mathbf{x}, \mathbf{v}, t) d^3 \mathbf{v} \quad (2.10)$$

are the density, bulk velocity and pressure tensor of species  $\alpha$ .

Formally, the moment equations continue indefinitely and include successive higher order moments. In order to be tractable they must be truncated at some order. This is normally done by defining an equation of state that relates the thermal pressure  $P_\alpha$  to lower order moments and the plasma temperature. This avoids the need for an equation to model heat transfer. Two common choices are made here, the first being the ideal gas equation of state

$$P_\alpha = n_\alpha k_B T_\alpha, \quad (2.11)$$

and second the adiabatic equation

$$P_\alpha \propto n_\alpha^\gamma. \quad (2.12)$$

where  $\gamma \equiv (N_d + 2)/N_d$  and  $N_d$  is the number of degrees of freedom. In fact, the adiabatic relation is not an equation of state, and so the ideal gas EOS is usually used to calculate a proportionality constant at a reference temperature. The ideal gas EOS is applicable for processes with characteristic velocity  $\omega/k \ll v_{\text{th},\alpha}$  while the adiabatic EOS is applicable where  $\omega/k \gg v_{\text{th},\alpha}$ . The intermediate case requires a fully kinetic description as per the Vlasov equation [Kruer, 2003].

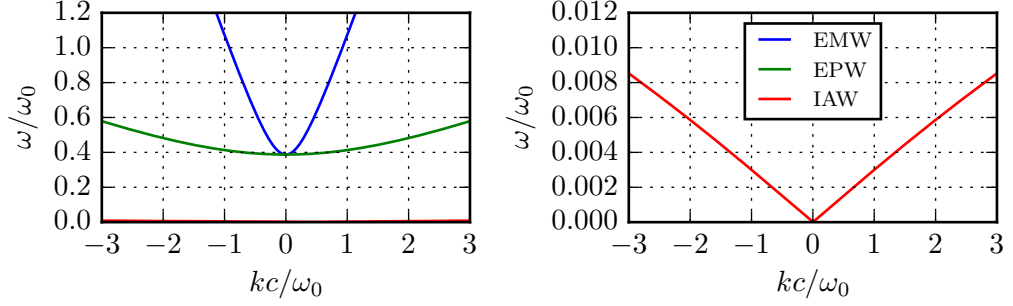


Figure 2.1: Dispersion relations of the three waves supported by an unmagnetised plasma with Maxwellian distribution function: electromagnetic, electron-plasma and ion-acoustic waves. Plasma parameters used are:  $n_e = 0.15n_{\text{cr}}$ ,  $T_e = 3.5\text{keV}$ ,  $T_i = 1.7\text{keV}$  and  $Z = 1$ , which aside from  $Z = 1$  are typical for this thesis. Left and right panels differ only in the frequency scale used. Frequency and wavenumber normalisations are the frequency and vacuum wavenumber of light from a frequency-tripled Nd:Glass laser.

## 2.2 Plasma Waves

In an unmagnetised plasma with Maxwellian distribution functions three wave modes are supported: electromagnetic, electron-plasma and ion-acoustic waves. The dispersion relations for these three wave types are plotted in figure 2.1 for representative plasma conditions.

Beginning with electromagnetic (EM) waves, a linearised fluid or kinetic derivation for these waves produces a dispersion relation given by

$$\omega_{\text{EM}} = \sqrt{\omega_{\text{pe}}^2 + c^2|\mathbf{k}|^2}. \quad (2.13)$$

where  $\omega_{\text{pe}}$  is the electron plasma frequency, defined

$$\omega_{\text{pe}} = \left( \frac{n_e e^2}{m_e \epsilon_0} \right)^{\frac{1}{2}} \quad (2.14)$$

Since the plasma frequency increases with density, the above relation demonstrates that EM waves propagating through a plasma have a maximum density above which they cannot propagate. This is known as the critical density and is given by

$$n_{\text{cr}} = \frac{m_e \epsilon_0}{e^2} \omega_0^2, \quad (2.15)$$

where  $\omega_0$  is the EM wave frequency. As the wave propagates its electric field induces

oscillations of the electrons in the plasma. This is referred to as the electron quiver, with the amplitude of the oscillations in electron velocity referred to as the quiver velocity  $\mathbf{v}_{\text{os}}$ . In terms of the electric field amplitude this is given by

$$\mathbf{v}_{\text{os}} = \frac{e\mathbf{E}_0}{m_e\omega_0}. \quad (2.16)$$

The quiver velocity normalised to the speed of light is denoted  $a_0$ . Values  $a_0 \ll 1$  indicate a non-relativistic intensity, while for larger values the above dispersion relation would need a relativistic correction. In this thesis the maximum laser intensity considered is on the order of  $10^{16} \text{Wcm}^{-2}$ , or  $a_0 = 0.03$ .

The second supported mode is the electron-plasma wave (EPW) which is an electrostatic wave. Linearising the two-fluid equations, its dispersion relation may be derived:

$$\omega_{\text{EPW}} \simeq \sqrt{\omega_{\text{pe}}^2 + 3v_{\text{th}}^2|\mathbf{k}|^2}. \quad (2.17)$$

Since the electron temperature is on the order 1-10keV, the thermal velocity ( $v_{\text{th}} \equiv \sqrt{k_{\text{B}}T_e/m_e}$ ) is  $\sim 0.04\text{-}0.14c$ . This means that the group velocity of these waves is considerably smaller than EM waves. A kinetic treatment of these waves produces a similar dispersion relation, however with the addition of a damping coefficient. The above dispersion relation is accurate for  $k\lambda_{\text{D}} \ll 1$ , while for  $k\lambda_{\text{D}} \gtrsim 0.25$  the waves are strongly damped. This is discussed in detail in section 2.3.

The final plasma wave is the ion-acoustic wave (IAW), also an electrostatic wave. Using a linearised kinetic description and considering a single ion species, a dispersion relation of the form

$$\omega_{\text{IAW}} \simeq |\mathbf{k}| \sqrt{Z \frac{m_e}{m_i} \frac{v_{\text{th}}^2}{1 + |\mathbf{k}|^2 \lambda_{\text{D}}^2} + 3v_{\text{th},i}^2} \quad (2.18)$$

may be derived. Here  $Z$  is the ion charge state,  $m_i$  its mass and  $v_{\text{th},i} \equiv \sqrt{k_{\text{B}}T_i/m_i}$  the ion thermal velocity. The kinetic treatment also indicates that these waves are damped unless  $T_i \ll T_e$ . In order for an IAW to be able to propagate distances in excess of its wavelength requires  $T_e/T_i \gtrsim 5\text{-}10$  [Cairns, 1985]. For small  $k\lambda_{\text{D}}$  the dispersion relation may be simplified to

$$\omega_{\text{IAW}} \simeq c_s |\mathbf{k}|, \quad (2.19)$$

where  $c_s$  is the ion sound speed



$$c_s = \sqrt{Z \frac{m_e}{m_i} v_{\text{th}}^2 + 3v_{\text{th},i}^2}. \quad (2.20)$$

In-depth discussion of the IAW dispersion relation and its damping for a plasma with multiple ion species may be found in [Williams et al., 1995].

Finally it should be noted that as the phase velocity of IAWs is much smaller than  $v_{\text{th}}$ , the wave's frequency can be significantly Doppler shifted. In particular since the coronal plasma of an ICF target usually has supersonic bulk flow velocities  $\mathbf{u}$  this effect is relevant here. Thus the dispersion relation above becomes

$$\omega_{\text{IAW}} \simeq c_s |\mathbf{k}| + \mathbf{u} \cdot \mathbf{k}. \quad (2.21)$$

## 2.3 Landau Damping

A key result of kinetic theory is that of Landau damping. Here, electrostatic waves transfer their energy to particles travelling near the wave phase velocity  $v_{\text{ph}} = \omega/k$ . Electrons travelling at velocity slightly below  $v_{\text{ph}}$  will gain energy by being accelerated in the potential wells of the wave, while the opposite occurs for those with velocity slightly higher. If the distribution function has negative gradient with respect to velocity at  $v = v_{\text{ph}}$  this will lead to net transfer of energy to the electron population.

This may be described theoretically by considering the case of a small-amplitude sinusoidal electrostatic wave supported by a perturbed Maxwellian electron distribution. Application of the linearised Vlasov equation to this scenario leads to the following dispersion relation

$$1 + \frac{1}{k} \frac{e^2}{m_e \varepsilon_0} \int_{\mathbb{R}^3} \frac{\partial f_0 / \partial v_z}{\omega - k v_z} d\mathbf{v} = 0, \quad (2.22)$$

where  $f_0$  is the initial electron distribution function and the coordinate system is chosen such that  $\hat{\mathbf{z}}$  is parallel to  $\mathbf{k}$  so that  $k \equiv |\mathbf{k}|$ . The second term on the left may be identified as the electron susceptibility  $\chi_e(\omega, k)$  which can be written as

$$\chi_e(\omega, k) = -\frac{1}{2(k\lambda_D)^2} Z' \left( \frac{1}{\sqrt{2}} \frac{\omega}{v_{\text{th}}} \frac{\omega}{k} \right). \quad (2.23)$$

Here  $Z'(\zeta)$  is the derivative of the plasma dispersion function  $Z(\zeta)$  [Fried and Conte, 1961] defined

$$Z(\zeta) = \frac{1}{\sqrt{\pi}} \int_{-\infty}^{\infty} \frac{e^{-x^2}}{x - \zeta} dx. \quad (2.24)$$

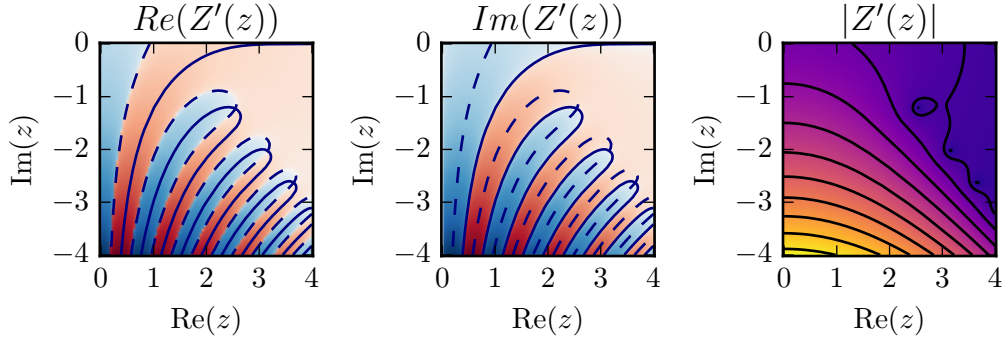


Figure 2.2: Derivative of the plasma dispersion function plotted in the complex plane of its argument. Blue and red colour scales in left two plots indicate positive and negative values respectively, each on a logarithmic scale. The dashed lines in the two left hand plots indicate paths along which  $\text{Re}(Z'(z)) = 0$  while along the solid lines  $\text{Im}(Z'(z)) = 0$ . The contour lines in the right hand plot indicate where  $|Z'(z)| = 10^n$ , with the highest contour at  $10^8$ . Solutions to the warm plasma dispersion relation (equation 2.25) lie along the black solid lines in the two left-hand plots where  $\text{Re}(Z'(z)) \geq 0$ .

This integral must be treated correctly; in its first analysis it was treated by taking the principal value [Vlasov, 1945] which results in a dispersion relation for undamped waves. The problem was later revisited, where it was correctly treated via a contour integration [Landau, 1946] resulting in a dispersion relation with no purely real roots. This indicates that electron plasma waves are in fact damped. In the following discussion the plasma dispersion function is evaluated numerically using routines found in standard libraries [Jones et al., 2001].

The plasma dispersion function has an infinite number of zeros and so the dispersion relation above has an infinite number of branches. These can be found by writing the dispersion relation as

$$Z'(\zeta) = 2(k\lambda_D)^2, \quad (2.25)$$

and plotting  $Z'(\zeta)$ , with  $\zeta = (\sqrt{2}v_{th})^{-1}\omega/k$ . Branches of the dispersion relation lie along the set of paths where  $\text{Im}(Z') = 0$  (solid lines in fig. 2.2) and  $\text{Re}(Z') \geq 0$  (red regions of the left hand panel in fig. 2.2).

Writing the  $i$ th branch of roots as  $\omega_i(k)$  gives the complex frequency of the resulting modes, whose real and imaginary components are shown in fig. 2.3. The real part corresponds to the wave frequency while the imaginary part corresponds

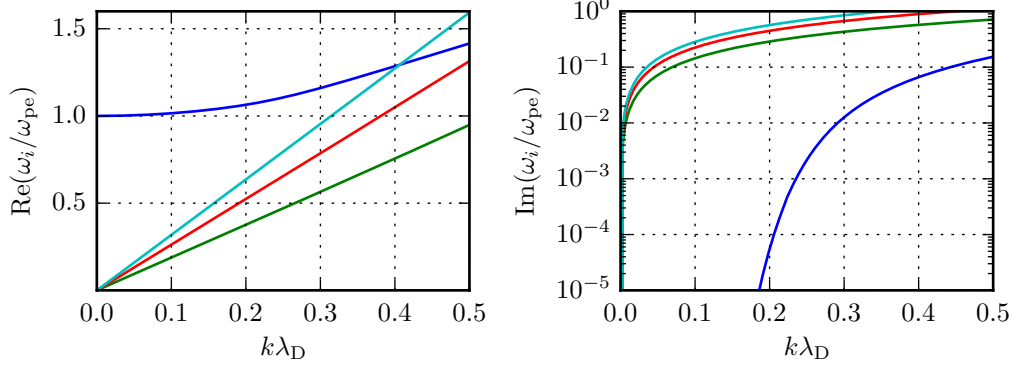


Figure 2.3: Frequency and damping rates of the solutions to the warm plasma dispersion relation. The blue line corresponds to electron plasma waves while the green, red and turquoise lines are strongly damped modes which are not usually observed.

to the damping rate. Branch  $i = 0$  represents electron-plasma waves (EPWs) while branches  $i > 0$  are strongly damped modes that consequently are not observed under normal circumstances.

The frequency and damping rate of EPWs may be approximated by the simple expressions

$$\omega_{\text{Re}} = \sqrt{\omega_{\text{pe}}^2 + 3v_{\text{th}}^2 k^2}, \quad (2.26)$$

$$\omega_{\text{Im}} = -\sqrt{\frac{\pi}{8}} \frac{\omega_{\text{pe}}}{(k\lambda_D)^3} e^{-((k\lambda_D)^2+3)/2}, \quad (2.27)$$

which are calculated by expanding the integrand in the plasma dispersion function. These break down for  $k\lambda_D \gtrsim 0.25$ , with the damping rate in particular producing incorrect asymptotic behaviour. Throughout this thesis, unless otherwise stated, numerical solutions of the dispersion relation above will be used to calculate the EPW frequency and damping rate.

To calculate these solutions numerically, the function  $f(\zeta, K) \equiv Z'(\zeta) - 2K^2$  is defined (with  $K \equiv k\lambda_D$ ). The solutions are zeros of this function. Applying the implicit function theorem gives

$$\frac{d\zeta}{dK} = \frac{\partial f}{\partial K} \left( \frac{\partial f}{\partial \zeta} \right)^{-1}, \quad (2.28)$$

and evaluating the right hand side results in

$$\frac{d\zeta}{dK} = -2K/Z''(\zeta). \quad (2.29)$$

This is an ordinary differential equation and so given a known initial solution  $\zeta(K_0)$  (tabulated in [Fettis et al., 1973]) the standard algorithms for solving ODEs may be applied to find solutions at other values of  $K$ . This method is advantageous compared to the naive approach of numerically minimising  $f(\zeta, K)$  at fixed  $K$  since it ensures that the desired root is found.

It is important to note that the above dispersion relation does not represent the only way of approaching this problem. Following Landau's initial work it was subsequently shown that for each  $k$ , there exist stable wave solutions at all real values of  $\omega$  [Van Kampen, 1955]. These undamped solutions form a complete orthogonal set which can be used to construct the damped solutions of Landau [Case, 1959], meaning that the 'damping' can be interpreted as the result of phase mixing of the Van Kampen modes.

## 2.4 Particle Trapping

The analysis above is strictly only valid during the initial phase of damping before the distribution function changes significantly. Considering the rest frame of the wave, electrons initially at  $v = v_{ph}$  appear stationary in the wave's potential wells. In the initial linear 'Landau damping' phase, electrons at positions where  $d\phi/dx \neq 0$  ( $\phi$  is the wave potential) are accelerated by the wave's electrical potential and gain kinetic energy. At some point they cross the bottom of the potential well where  $d\phi/dx$  changes sign and the particles begin to accelerate in the opposite direction. Naturally, this situation leads to oscillatory motion within the wells with characteristic frequency  $\omega_B = \sqrt{eEk/m_e}$ , referred to as the bounce frequency. Therefore after the initial phase of wave damping the energy of the wave may undergo oscillations as particles trapped in its potential wells gain and lose energy.

This was the subject of research during the 1960's where several important results were obtained. It was shown by O'Neil that while trapping of particles initially leads to oscillation between periods of wave growth and damping, the wave ultimately settles into an undamped state [O'Neil, 1965]. It was subsequently demonstrated that this process also results in oscillations in the wave's frequency, which settles on a steady state shift whose value is [Morales and O'Neil, 1972]

$$\delta\omega = -1.63 \sqrt{\frac{eE_0}{m_e k}} \left( \frac{\omega_{pe}}{k} \right)^2 \frac{\partial^2 f_0}{\partial v^2} \bigg|_{v_\phi} \frac{\partial \varepsilon}{\partial \omega} \bigg|_{\omega_0}^{-1}. \quad (2.30)$$

The above results depend on the amplitude of the wave not varying significantly on timescales of order  $\omega_B^{-1}$ , which in effect requires that  $k\lambda_D \lesssim 0.25$  [Dawson and Shanny, 1968]. Despite this constraint they are solutions of the nonlinear equation and so the undamped final state represents the nonlinear analogue of the Van Kampen modes described above, which are solutions of the linearised problem. The existence of nonlinear, undamped solutions to the Vlasov equation was demonstrated by Bernstein, Greene and Kruskal [Bernstein et al., 1957].

Another consequence of the harmonic motion of the trapped particles is that their motion within the wells may be coherent, leading to a two-stream type instability with respect to the bulk plasma. The process leads to the growth of side-bands about the wave’s central frequency, referred to as the Trapped Particle Modulational Instability (TPMI) and first modelled by Kruer and Dawson [Kruer et al., 1969]. An approximate dispersion relation for this instability is given in that work and may be used to numerically calculate its growth rate.

Finally, even when the wave’s phase velocity is significantly greater than the thermal velocity, it remains possible for wave-particle effects to become prominent. This may occur when the amplitude of the EPW becomes sufficiently large that the oscillation velocity of the electrons supporting it becomes comparable with the wave’s phase velocity. When this occurs, a large fraction of the distribution may come into resonance with the wave and it will collapse - a process referred to as ‘wave-breaking’. This was first treated in the limiting case of a cold plasma [Dawson, 1959], with extension to a waterbag distribution made later by Coffey [Coffey, 1971]. In the latter work a simple expression is given for the field amplitude required for wave-breaking,

$$E_{\text{WB}} = \frac{m_e v_\phi \omega_{\text{pe}}}{e} \sqrt{1 - \frac{1}{3}\beta - \frac{8}{3}\beta^{\frac{1}{4}} + 2\beta^{\frac{1}{2}}}, \quad (2.31)$$

where  $\beta \equiv 3v_{\text{th}}^2/v_\phi^2$ . For a Maxwellian distribution there is no well-defined equivalent amplitude limit since the distribution is not strictly zero anywhere. Nevertheless the above expression serves as a good indication of the amplitude at which wave-breaking will become important.

## 2.5 Parametric Instabilities

The primary instabilities of interest for this thesis fall under the general category of parametric instabilities. These are the result of nonlinear interactions between multiple (typically three) waves. Here the general theory of these instabilities is

presented, followed by results for the three specific instabilities that will be encountered: Stimulated Raman Scattering; Stimulated Brillouin Scattering and the Two-Plasmon Decay.

The concept of a parametric instability is closely related to that of a parametric oscillator. The latter is a generalisation of the harmonic oscillator in which some property of the oscillator, such as its resonant frequency  $\omega_0$  or damping rate  $\Gamma_0$ , is varied by a small amount in a sinusoidal manner. If the frequency  $\Omega$  at which this parameter is varied satisfies a resonance condition  $\Omega \simeq 2\omega_0$ , then the oscillation at  $\omega_0$  can be amplified. A similar process occurs for a parametric instability. Here a nonlinearity of the host medium permits amplification of waves that satisfy a resonance condition.

### 2.5.1 Temporal Growth in an Infinite Homogeneous System

To illustrate this process, we follow the formalism of Nishikawa [Nishikawa, 1968]. Beginning with the linear description, the modes of the system are described by a dispersion relation that permits oscillations at frequencies  $\omega(k)$ . Considering arbitrarily three of these frequencies  $\omega_i$  ( $i \in \{0, 1, 2\}$ ), assuming the system has infinite spatial extent, has no spatial dependence, and that there is wavenumber resonance between the waves, the oscillations of these independent modes of the host medium may be described by

$$\left[ \frac{d^2}{dt^2} + 2\Gamma_i \frac{d}{dt} + \omega_i^2 \right] X_i(t) = 0. \quad (2.32)$$

In this equation the coefficient  $\Gamma_i$  is the damping rate of each of the waves. If mode 0 is treated as having large amplitude then the medium's nonlinear response must be included. To lowest order, this will be of form  $X^2$  ( $X \equiv \sum X_i$ ). Assuming mode zero has negligible damping and that the amplitudes of modes 1 and 2 are small, this leads to the following coupled system:

$$\left[ \frac{d^2}{dt^2} + \omega_0^2 \right] X_0(t) = 0 \quad (2.33)$$

$$\left[ \frac{d^2}{dt^2} + 2\Gamma_1 \frac{d}{dt} + \omega_1^2 \right] X_1(t) = 2\alpha X_0(t)X_2(t) \quad (2.34)$$

$$\left[ \frac{d^2}{dt^2} + 2\Gamma_2 \frac{d}{dt} + \omega_2^2 \right] X_2(t) = 2\beta X_0(t)X_1(t). \quad (2.35)$$

The equation for mode 0 has no nonlinear term as we assume  $X_1 X_2$  to be negligible.

This equation is therefore independent of the others and can be solved directly to give oscillation at a constant amplitude  $\bar{X}_0$ . Taking the Fourier transform of the remaining equations gives

$$[\omega^2 + 2i\Gamma_1\omega - \omega_1^2] \hat{X}_1(\omega) = -\alpha\bar{X}_0 [\hat{X}_2(\omega - \omega_0) + \hat{X}_2(\omega + \omega_0)] \quad (2.36)$$

$$[\omega^2 + 2i\Gamma_2\omega - \omega_2^2] \hat{X}_2(\omega) = -\beta\bar{X}_0 [\hat{X}_1(\omega - \omega_0) + \hat{X}_1(\omega + \omega_0)]. \quad (2.37)$$

In order for there to be coupling between the modes it is necessary for the wave frequencies to be resonant. This occurs when the frequency matching condition is satisfied:

$$\omega_0 \simeq \omega_1 + \omega_2. \quad (2.38)$$

If we choose  $|\omega_1| \leq |\omega_2|$  and consider  $\omega \simeq \omega_1$  then the couplings to  $\hat{X}_i(\omega \pm 2\omega_0)$  can be ignored. Then the following equation is obtained [Nishikawa, 1968]

$$D_1(\omega) = \alpha\beta\bar{X}_0^2 \left[ \frac{1}{D_2(\omega - \omega_0)} + \frac{1}{D_2(\omega + \omega_0)} \right]. \quad (2.39)$$

Zeros of the function  $D_n(\omega) \equiv \omega^2 - \omega_n^2 + 2i\Gamma_n\omega$  give the complex frequency of wave  $n$ . Here equation 2.39 is examined for the case where  $\omega_1/\omega_0$  is sufficiently large that the  $D_2(\omega + \omega_0)^{-1}$  term may be neglected. The case of  $\omega_1/\omega_0 \sim 0$  is also treated in [Nishikawa, 1968], however is rarely encountered for the instabilities considered in this thesis and so is not discussed here.

Under the above conditions, equation 2.39 may be separated into equations for the real and imaginary components of  $\omega$ . The equation for the imaginary component, i.e. the exponential growth rate  $\gamma$  is [Nishikawa, 1968]

$$(\gamma + \Gamma_1)(\gamma + \Gamma_2) \left[ 1 + \frac{\Delta\omega^2}{(2\gamma + \Gamma_1 + \Gamma_2)^2} \right] = \gamma_0^2 \quad (2.40)$$

where

$$\Delta\omega \equiv \omega_0 - (\omega_1 + \omega_2) \quad (2.41)$$

is the frequency mismatch and

$$\gamma_0 \equiv \frac{\bar{X}_0}{2} \sqrt{\frac{\alpha\beta}{\omega_1\omega_2}} \quad (2.42)$$

is the maximum growth rate (when  $\Delta\omega = \Gamma_1 = \Gamma_2 = 0$ ) and is also referred to as

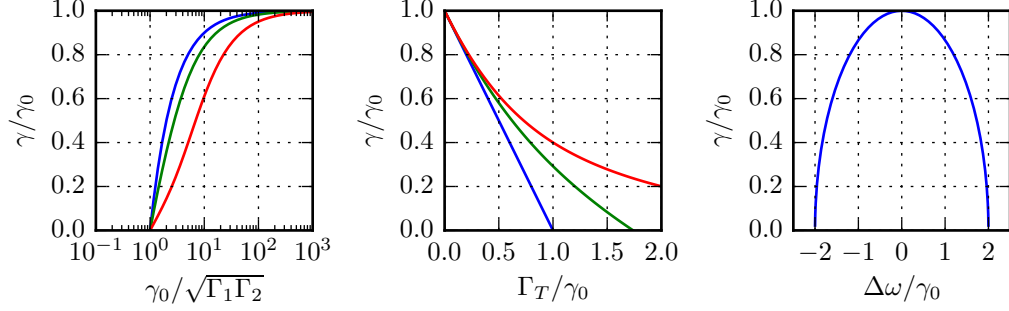


Figure 2.4: From left to right: parametric instability growth rate as a function of pump strength  $\gamma_0$ , total damping rate  $\Gamma_T \equiv (\Gamma_1 + \Gamma_2)/2$  and frequency mismatch  $\Delta\omega$ . In the left two plots the ratio of the two waves' damping rates ( $\Gamma_R \equiv \Gamma_2/\Gamma_1$ ) is varied, with  $\Gamma_R = 1, 10$  and  $100$  in blue, green and red respectively.

the coupling constant.

These equations illustrate several important features of three-wave instabilities. To begin with, ignoring any frequency mismatch or damping it is clear that the growth rate  $\gamma = \gamma_0$  scales with the amplitude of the pump. Allowing non-zero damping rates but again with  $\Delta\omega = 0$  equation 2.40 may be solved to give

$$\gamma = \gamma_0 \sqrt{1 + \left( \frac{\Gamma_2 - \Gamma_1}{2\gamma_0} \right)^2} - \frac{\Gamma_1 + \Gamma_2}{2}. \quad (2.43)$$

A notable feature of this equation is that below a threshold pump amplitude there are no positive solutions for  $\gamma$ , indicating that there is a threshold amplitude for growth (see left panel of figure 2.4). This threshold is given by

$$\gamma_0 > \gamma_{\text{thr},c} \equiv \sqrt{\Gamma_1 \Gamma_2}, \quad (2.44)$$

or alternatively in terms of pump intensity

$$I > I_{\text{thr}} \propto \Gamma_1 \Gamma_2 \quad (2.45)$$

In addition, while intuitively the growth rate decreases linearly with the total damping rate  $\Gamma_T \equiv (\Gamma_1 + \Gamma_2)/2$ , a difference between the damping rates of the two waves  $\Gamma_D \equiv (\Gamma_2 - \Gamma_1)/2$  acts to increase the growth rate (central panel of figure 2.4).

Now considering the opposite case where there is a frequency mismatch  $\Delta\omega$  but negligible damping, equation 2.40 becomes



$$\gamma = \gamma_0 \sqrt{1 - \left(\frac{\Delta\omega}{2\gamma_0}\right)^2} \quad (2.46)$$

which indicates that there is a region of mismatched frequencies of width  $\delta\omega = 4\gamma_0$  that allow growth (right panel of figure 2.4). Of course, for late time the mode with frequency  $\Delta\omega = 0$  will tend to dominate so that in absence of broadening through other mechanisms the spectrum will be narrower than this.

It is important to note at this stage that the daughter wave amplitudes  $X_1$  and  $X_2$  were assumed small. This led to the equation for the pump wave  $X_0$  (2.33) being uncoupled from those of the other oscillators. Since the solutions for  $X_1(t)$  and  $X_2(t)$  are exponential, their amplitudes will rapidly grow leading to the violation of this assumption. At this point the full set of coupled equations are needed instead. Qualitatively this situation develops with a reduction in amplitude of the pump amplitude  $\bar{X}_0$  and a corresponding slowing of instability growth. This is referred to as pump depletion and is one possible mechanism for saturation of the instability. It is also possible that pump depletion never occurs due to some other nonlinear saturation mechanism.

### 2.5.2 Growth in a Homogeneous System

The above analysis considered the temporal evolution of a system and ignored any spatial dependence, calculating its temporal growth rate and demonstrating that there is a threshold pump intensity for this growth to occur. Here the results including spatial dependence are summarised.

As with the temporal analysis the waves must be matched in frequency but, since the spatial dependence is now considered, there must also be wavenumber matching:

$$k_0 \simeq k_1 + k_2. \quad (2.47)$$

With these conditions satisfied, the equations governing coupled waves can often be simplified by using the slow-varying envelope approximation to arrive at the coupled mode equations, which are simply a set of coupled advection equations [Cairns, 1985]:

$$[\partial_t + V_{g,0}\partial_x + \Gamma_0] a_0(x, t) = -K a_1(x, t) a_2(x, t), \quad (2.48)$$

$$[\partial_t + V_{g,1}\partial_x + \Gamma_1] a_1(x, t) = K a_0(x, t) a_2^*(x, t), \quad (2.49)$$

$$[\partial_t + V_{g,2}\partial_x + \Gamma_2] a_2^*(x, t) = K a_0^*(x, t) a_1(x, t). \quad (2.50)$$

Here  $a_i$  is the complex envelope of wave  $i$  and  $V_{g,i}$ ,  $\Gamma_i$  are its group velocity and damping rate. While not included here for brevity, it is straightforward to incorporate phase factors in order to model wave detuning. Note that for the system to be written in the symmetric form above, with equal coefficients on the right hand side of each equation, the amplitudes must be normalised using  $a_i(x, t) \equiv \sqrt{\omega_i} A_i(x, t)$ . Neglecting such normalisation constants, the physical quantities modulated by each wave (e.g. electric field  $E$  or density perturbation  $\delta n$ ) may be related to the amplitudes  $a_i$  by

$$E_i(x, t) = \frac{1}{2} \left[ a_i(x, t) e^{i(k_i x - \omega_i t)} + a_i^*(x, t) e^{-i(k_i x - \omega_i t)} \right]. \quad (2.51)$$

An important result that may be derived from these equations relates to the transfer of energy. In particular, the energy density of each wave  $W_i$  may be calculated as  $W_i = \omega_i |a_i|^2$ . Writing the above system of equations in terms of this energy density and neglecting damping, one may derive the following equations

$$\frac{d}{dt} \left[ \frac{W_0}{\omega_0} + \frac{W_1}{\omega_1} \right] = 0, \quad (2.52)$$

$$\frac{d}{dt} \left[ \frac{W_0}{\omega_0} + \frac{W_2}{\omega_2} \right] = 0, \quad (2.53)$$

$$\frac{d}{dt} \left[ \frac{W_1}{\omega_1} - \frac{W_2}{\omega_2} \right] = 0. \quad (2.54)$$

These are known as the Manley-Rowe relations which follow from energy conservation and describe energy transfer between the waves.

Even with the approximation of slow-varying envelopes, equations 2.48-2.50 are significantly more complex than those previously considered. In order to give an intuitive description of the physics two simple situations are considered here. As before we are primarily interested in early time behaviour before the instabilities cause pump-depletion, meaning that the assumption  $|a_0| \gg |a_1 a_2|$  applies and that the right hand side of equation 2.48 can be neglected. It is also assumed that  $\Gamma_0 = 0$  so that equation for  $a_0$  is simply the advection equation, and we take the

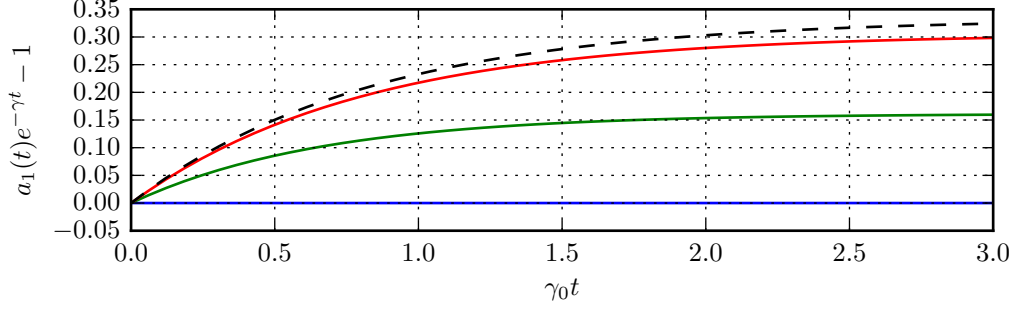


Figure 2.5: Transient behaviour of the explicit solution to the coupled mode equations for a homogeneous initial disturbance.  $a_1(t)$  is the amplification predicted by equation 2.58 and  $\gamma$  is given by equation 2.43. Parameters used are  $\Gamma_T = 0.8\gamma_0$  and  $\Gamma_R \equiv \Gamma_2/\Gamma_1 = 10^0, 10^1, 10^2$  and  $10^{10}$  in blue, green red and black respectively. This illustrates that the transient behaviour has very little effect and can be approximated by the asymptotic solution in most cases.

initial pump amplitude to be  $a_0(x, 0) = a_0$ , meaning that it is constant everywhere and remains so over the time-period of interest. Then the coupling constant from the temporal analysis is recovered by writing  $Ka_0 = \gamma_0$ . The two remaining coupled equations are solved in appendix A using the method of characteristics and result in the following general solution

$$a_1(x, t) = \int_{-\infty}^{\infty} e^{ikx} e^{-ikV_T t} \left[ C(k) \cosh \left( t \sqrt{\gamma_0^2 - k^2 V_D^2} \right) + S(k) \sinh \left( t \sqrt{\gamma_0^2 - k^2 V_D^2} \right) \right] dk, \quad (2.55)$$

where the functions  $C(k)$  and  $S(k)$  are determined by the initial conditions on  $a_1(x, t)$ . Two conditions are required,  $a_1(x, 0) = f(x)$  and  $\partial_t a_1(x, 0) = g(x)$ . Writing their spatial Fourier transforms as  $\hat{f}(k)$  and  $\hat{g}(k)$ ,  $C(k)$  and  $S(k)$  are given by

$$C(k) = \hat{f}(k), \quad (2.56)$$

$$S(k) = \frac{ikV_T \hat{f}(k) + \hat{g}(k)}{\sqrt{\gamma_0^2 - k^2 V_D^2}}. \quad (2.57)$$

### Homogeneous Initial Disturbance

For this first scenario it is imagined that the instability is seeded by an initial disturbance to  $a_1$  that is homogeneous in space and occurs at  $t = 0$ . So  $a_1(x, 0) = A_1 H(t)$  and  $\partial_t a_1(x, 0) = A_1 \delta(t)$  where  $H(t)$  is the Heaviside step function and  $\delta(t)$  its distributional derivative, the Dirac delta-function. These initial conditions make the Fourier integral above trivial, resulting in the solution

$$a_1(x, t) = A_1 e^{-\Gamma_T t} \left[ \cosh \left( t \sqrt{\gamma_0^2 - \Gamma_D^2} \right) + \frac{1}{\sqrt{\gamma_0^2 - \Gamma_D^2}} \sinh \left( t \sqrt{\gamma_0^2 - \Gamma_D^2} \right) \right]. \quad (2.58)$$

Here  $\Gamma_T \equiv \frac{1}{2}(\Gamma_1 + \Gamma_2)$  and  $\Gamma_D \equiv \frac{1}{2}(\Gamma_2 - \Gamma_1)$ . Expanding the hyperbolic functions as exponentials and considering the behaviour when  $t \gg \gamma_0^{-1}$  we find

$$a_1(x, t) \propto \exp \left[ t \left( \sqrt{\gamma_0^2 - \Gamma_D^2} - \Gamma_T \right) \right].$$

This is the same result that was derived in section 2.5.1, except that here an explicit time-dependent solution has been found to the partial-differential equations while previously only the dispersion relation was considered. The transient behaviour of this solution results in a slightly higher initial growth rate than the asymptotic value, as shown in figure 2.5 where it is compared with the time-asymptotic solution.

### Localised Initial Disturbance

In the second case we treat, the initial condition is taken to be an instantaneous disturbance to the first daughter wave occurring at  $x = 0$  and  $t = 0$ , i.e.  $a_1(x, 0) = A_1 \delta(x)$ . While a  $\delta$ -function breaks the assumption of the coupled-mode equations of slowly varying wave envelopes it simplifies the analysis and produces results which are applicable to more complex situations.

The Fourier integrals above are examined in appendix A.2, where it is shown that they may be written in terms of Hankel functions. This is plotted in figure 2.6 with two choices of  $V_T/V_D$ . Assuming without loss of generality that  $V_2 > V_1$ , the solution vanishes where  $x - V_1 t < 0$  and  $x - V_2 t > 0$  while elsewhere there is exponential growth. That the solution vanishes in these regions is a simple consequence of causality and wave propagation, however it has important implications. If  $V_1 V_2 > 0$ , both daughter waves travel in the same direction and therefore there is no fixed point in space where the waves will experience indefinite temporal growth. There may however be indefinite growth in the frame of the pulse. On the other

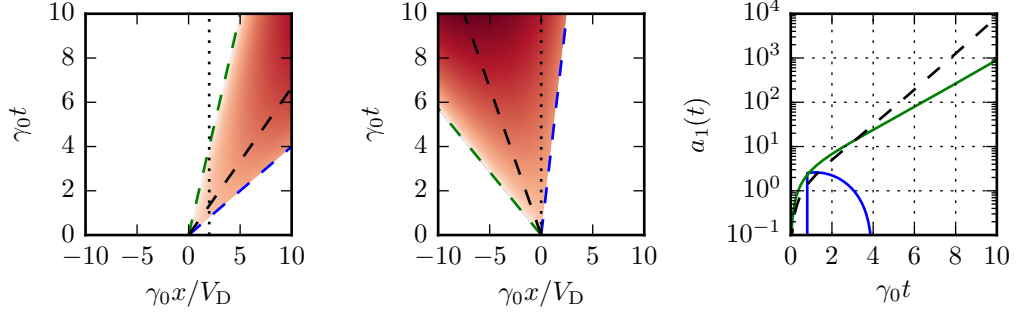


Figure 2.6: Spatiotemporal evolution of the wave envelope  $a_1$  in response to an initial disturbance of form  $a_1(x, 0) = \delta(x)$ . **Left & centre:** amplitude plotted on a logarithmic colour scale with  $V_T/V_D = 1.5$  and  $-0.75$ . The two wave characteristics are shown as green and blue dashed lines while  $x = V_T t$ , the mean trajectory of the pulse, is shown as a black dashed line. **Right:** amplitude versus time either at fixed points corresponding to previous two plots (solid lines) or along  $x = V_T t$  (dashed line).

hand if  $V_1 V_2 < 0$  and the waves propagate in opposite directions there will be indefinite temporal growth at all points in space. This type of behaviour, where local growth occurs indefinitely is referred to as ‘absolute’ growth, while the case where growth occurs in a propagating frame is referred to as ‘convective’ growth.

In the above scenario, damping of the daughter waves was neglected. Re-introducing it leads to several additional possibilities. First, considering the case where  $V_1 V_2 > 0$  and growth can only be convective, it is clear that this is still restricted to occurring when the pump intensity is above the threshold for parametric instability derived in the temporal analysis. In the case where  $V_1 V_2 < 0$  this threshold still applies, however there is now an additional higher threshold above which absolute growth can also occur. This new threshold is exceeded when the following condition is satisfied [Briggs, 1964]

$$\gamma_0 > \gamma_{\text{thr,a}} \equiv \frac{\sqrt{|V_1 V_2|}}{2} \left( \frac{\Gamma_1}{|V_1|} + \frac{\Gamma_2}{|V_2|} \right) \quad (2.59)$$

When the pump intensity is above the threshold for instability, but below the absolute threshold there will simply be convective growth. Considering laser-plasma instabilities in ICF, the threshold for absolute instability is often an important design consideration for experiments as an absolute instability can in principle grow without limit while convective instabilities are limited to amplification over the spa-

tial extent of plasma.

The distinction between convective and absolute growth also motivates discussion of what is meant by a growth rate. In particular, growth rates can either be specified as temporal or spatial rates. Spatial growth rates are typically used for convective instabilities while temporal growth rates may be used for either. This can lead to confusion when the ‘convective growth rate’ is referred to without specifying whether this is respect to time or space. Additionally it is important to note that the absolute growth rate, i.e. the temporal growth rate of the daughter waves at a fixed point in space, is not the maximum possible temporal growth rate. The maximum temporal growth rate occurs along a trajectory  $x = V_{\max}t$  where  $V_1 < V_{\max} < V_2$  and  $V_{\max}$  is determined by the damping rates of the daughter waves. This maximum temporal growth rate corresponds to the growth rate derived in section 2.5.1 and is referred to in this thesis as the ‘convective temporal growth rate’.

### 2.5.3 Growth in an Inhomogeneous System

In direct-drive ICF, the plasma through which the laser propagates is inhomogeneous, meaning that in order to consider theoretically instabilities occurring in this regime the above analysis must be further extended. Unfortunately, general analytic results are difficult to obtain, and much analysis has to be performed either numerically or for very specific cases. There are however several results that should be discussed first before considering specific instabilities.

One of the key results in this area was derived by Rosenbluth in 1972. This particular analysis was performed using an extended version of the coupled mode equations described above, neglecting the response of the pump [Rosenbluth, 1972]:

$$[\partial_t + V_{g,1}\partial_x + \Gamma_1] a_1(x, t) = \gamma_0 a_2^*(x, t) \exp \left[ i \int_{x_0}^x \kappa dx \right] \quad (2.60)$$

$$[\partial_t + V_{g,2}\partial_x + \Gamma_2] a_2^*(x, t) = \gamma_0 a_1(x, t) \exp \left[ -i \int_{x_0}^x \kappa dx \right]. \quad (2.61)$$

The phase factors included on the right hand side integrate over the wavenumber mismatch  $\kappa(x) \equiv k_0 - (k_1 + k_2)$  of the waves. This addition models the loss of resonance of the two daughter waves as they propagate away from a point  $x_0$  where they satisfy the matching conditions perfectly ( $\kappa(x_0) = 0$ ). As they do so, their frequency remains fixed however their wavelengths change so as to satisfy their respective dispersion relations locally, resulting in  $\kappa(x) \neq 0$ . Using these equations in the absence of damping it was shown that there can be no absolute growth when

the mismatch is linear with space,  $\kappa(x) \propto x$ . For this case it was further shown that the convective growth that occurs is limited to the exponential growth factor

$$G = \frac{\pi\gamma_0^2}{V_1 V_2 \kappa'(x)}, \quad (2.62)$$

where  $\kappa'(x)$  is the derivative of the mismatch. Therefore given an initial wave amplitude  $a_1$ , inhomogeneous convective growth will lead to an amplitude of  $a = a_1 e^G$ . This amplification is frequently referred to as the ‘Rosenbluth gain’. This analysis was later extended to include the effects of damping [Rosenbluth et al., 1973].

The initial analysis also considered the case where the mismatch is parabolic ( $\kappa(x) \propto x^2$ ) and therefore has a zero in its derivative. Here it was found that absolute instabilities may occur and their temporal growth rate was calculated [Rosenbluth, 1972]. Later work extended this to include a damping rate [Liu et al., 1974], giving

$$\gamma_{abs} = 2\gamma_0 \left( \frac{\sqrt{|V_1 V_2|}}{V_1 - V_2} \right) (1 - \Delta) - \left( \frac{\Gamma_2 V_1 - \Gamma_1 V_2}{V_1 - V_2} \right), \quad (2.63)$$

where as usual it is required that  $V_1 V_2 < 0$ , we have chosen that  $V_2 < 0$  and it is assumed that  $|\Delta| \ll 1$ , with  $\Delta$  defined

$$\Delta = e^{-i\frac{\pi}{4}} 2^{-\frac{3}{2}} \sqrt{K''} \left( \frac{\gamma_0^2}{|V_1 V_2|} \right)^{-\frac{3}{4}}. \quad (2.64)$$

These are both valuable results, however the WKB methods used to obtain them introduce restrictive conditions on their applicability. Unfortunately, for many instabilities of interest to laser-driven fusion, the regions where the WKB method fails are often the regions that allow for absolute instability. These cases have been treated theoretically via a number of different methods which are not discussed here in detail. For a recent analysis of the problem and a review of previous methods see [Afeyan and Williams, 1997b].

#### 2.5.4 Stimulated Raman Scattering

The Stimulated Raman Scattering (SRS) instability occurs as the decay of an electromagnetic wave to an electron plasma wave and a scattered electromagnetic wave. The bottom panel of figure 2.7 illustrates how frequency and wavenumber matching can be satisfied for the particular cases of forward and back-scatter, using the fluid EPW dispersion relation. More generally, solutions to the frequency and wavenumber matching conditions are shown in the upper two panels of the fig-

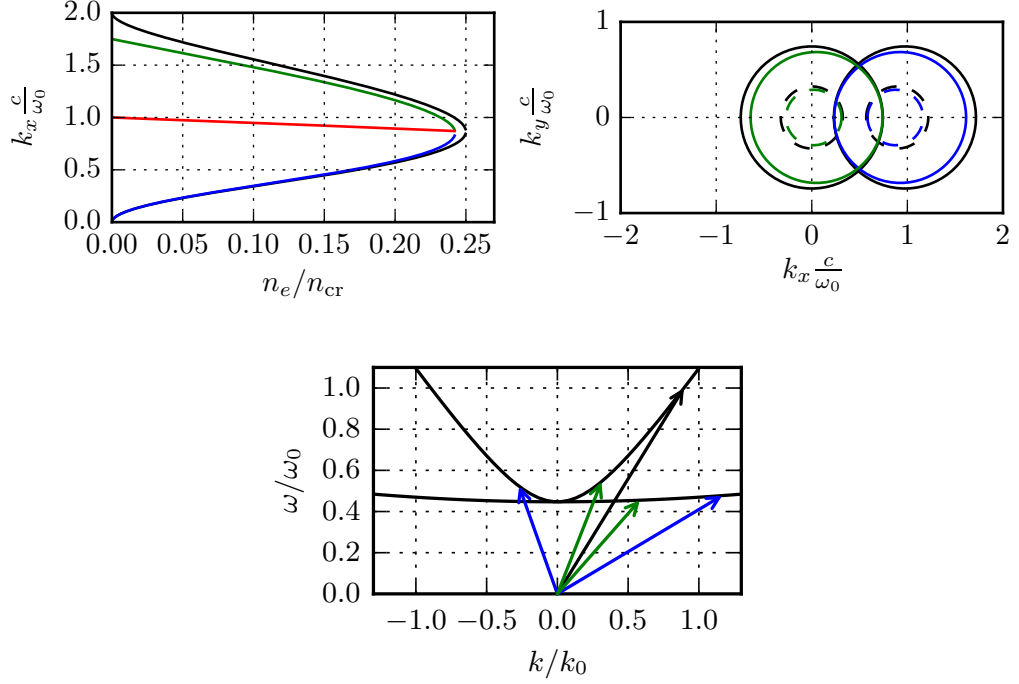


Figure 2.7: **Top:** Solution of the SRS frequency and wavenumber matching conditions using the fluid EPW dispersion relation at  $T_e = 3.5\text{keV}$  (coloured lines). In both panels black lines indicate the zero-temperature limit. The laser wave-vector is parallel to the  $k_x$  axis. **Left:**  $k_x$  component of the EPW wavenumber as a function of electron density for SRS forward, back and 90-degree side-scatter in blue, green and red respectively. **Right:**  $k_y$  and  $k_x$  components of EM (green) and EPW (blue) wavenumbers at  $0.05n_{cr}$  (solid) and  $0.20n_{cr}$  (dashed). **Bottom:** Frequency & wavenumber matching for SRS back (blue) and forward-scatter (green) daughter waves at  $T_e = 3.5\text{keV}$  &  $n_e = 0.2n_{cr}$ . Considering each vector  $(k, \omega)$ , it can be seen that the sum of vectors for the two daughter-waves gives the laser vector (black).

ure at  $T_e = 3.5\text{keV}$ . For comparison solutions are also shown in the limit of  $T_e \rightarrow 0$  (black lines) indicating that there is only a weak dependence on temperature. In this limit the magnitude of the scattered light wavenumber is given by

$$|\mathbf{k}_s| = \frac{\omega_0}{c} \sqrt{1 - 2 \left( \frac{n_e}{n_{cr}} \right)^{\frac{1}{2}}}, \quad (2.65)$$

and its frequency trivially by

$$\omega_s = \omega_0 - \omega_{pe}. \quad (2.66)$$



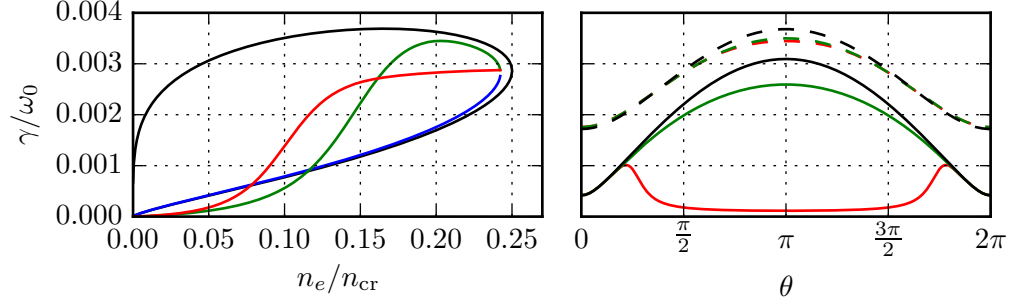


Figure 2.8: Homogeneous coupling constant ( $\gamma_0$ ) for SRS as a function of density and scattered light propagation angle  $\theta$  (angle with respect to the laser wavenumber) for a laser intensity of  $2 \times 10^{15} \text{ Wcm}^{-2}$  at  $T_e = 3.5 \text{ keV}$  (coloured lines). In both panels black lines indicate the zero temperature limit. **Left:**  $\gamma_0$  versus electron density for SRS back, forward and 90-degree side-scatter in green, blue and red respectively including the Landau damping rate. **Right:**  $\gamma_0$  versus scattered light propagation angle at  $0.05n_{\text{cr}}$  (solid) and  $0.20n_{\text{cr}}$  (dashed). Landau damping rate included for red lines, neglected for green lines.

This, along with figure 2.7 illustrates several important features of SRS. Since both decay waves' minimum frequency is the local electron plasma frequency, the frequency matching condition means that the instability cannot occur above the laser's quarter-critical density. In the limit of  $n_e \rightarrow n_{\text{cr}}/4$ , the EPW wavenumber tends to  $k_0$  while the scattered EM wavenumber tends to zero. This leads to scattered light with frequency  $\omega_0/2$ . As the density is reduced  $\omega_s$  increases, and for SRS producing scattered light at angles  $\theta \gtrsim \pi$  to the laser propagation axis, the matching conditions require the EPW wavenumber to increase while the scattered light wavenumber increases.

In a homogeneous plasma, the coupling constant (or undamped temporal convective growth rate) is given by [Kruer, 2003]

$$\gamma_0 = \frac{kv_{\text{os}}}{4} \frac{\omega_{\text{pe}}}{\sqrt{\omega_{\text{ek}}\omega_s}}, \quad (2.67)$$

where  $k$  and  $\omega_{\text{ek}}$  are the wavenumber and frequency of the EPW,  $\omega_s$  is the scattered light frequency, and  $v_{\text{os}}$  is the quiver velocity of electrons in the laser field. Note that as expected this has the same form as equation 2.42. Growth rates calculated using this, equation 2.43, and a numerically evaluated Landau damping rate are shown in figure 2.8 as a function of density and scattered light angle  $\theta$ . In the limit of  $T \rightarrow 0$  the largest growth rates are found for direct backscatter ( $\theta = \pi$ ), however in a warm

plasma Landau damping drastically reduces the growth rate of backscatter at lower density due to the large EPW wavenumbers.

In an inhomogeneous plasma with monotonically increasing density, as would be found in a direct-drive ICF scenario, SRS forward or back-scatter below  $n_{\text{cr}}/4$  can only occur as a convective instability. In these cases the gain is limited to the Rosenbluth factor [Rosenbluth, 1972]. In contrast, when SRS occurs near the turning point of the scattered EM wave it may undergo absolute growth since at this point the wave's velocity directed along  $\nabla n$  is close to zero and energy moves slowly away from the matching point. This occurs at  $n_{\text{cr}}/4$  for backscatter and at successively lower density with increasing  $k_{\perp}$ , where  $k_{\perp}$  is the scattered wave's perpendicular wavevector. This has been the subject of theoretical analyses over a period of several decades using successively less restrictive assumptions. An initial study by Drake & Lee derived the growth rate for backscatter at  $n_{\text{cr}}/4$  assuming normal incidence, a linear density profile, and  $T_e = 0$  [Drake and Lee, 1973]. Liu et al. then generalised this to sidescatter with arbitrary  $k_{\perp}$  [Liu et al., 1974]. It was noted in this study that while sidescatter is absolute in the  $x$  direction (collinear with the laser), the instability is in fact convective in the perpendicular direction. A decade later, a study by Afeyan & Williams removed the restriction of normal laser incidence and zero temperature [Afeyan and Williams, 1985]. Finally, after yet another decade, these authors revisited the topic and extended the theory to power-law density profiles [Afeyan and Williams, 1997b].

In the above studies absolute growth of SRS was found based on the local behaviour of the waves, namely the scattered light's group velocity along  $\nabla n$  vanishing. However, absolute growth may also occur due to behaviour of the waves at distinct points in the plasma. For example it was shown that absolute growth can occur for SRS forward-scatter if the laser and SRS-scattered light are both reflected from their respective critical surfaces and return to the initial point of resonance [Cairns, 1974]. Similar behaviour can be obtained for a parabolic mismatch profile, instead with two resonance regions on either side of the extremum coupled together by scattered light [Williams and Johnston, 1989].

### 2.5.5 Two-Plasmon Decay

The Two-Plasmon Decay (TPD) instability is the parametric decay of an electromagnetic wave to two electron plasma waves, or plasmons. Solutions to the frequency and wavenumber matching conditions using the fluid EPW dispersion relation are shown in figure 2.9 at  $T_e = 3.5\text{keV}$ . The EPW wavenumbers satisfy the matching conditions on the curve described by

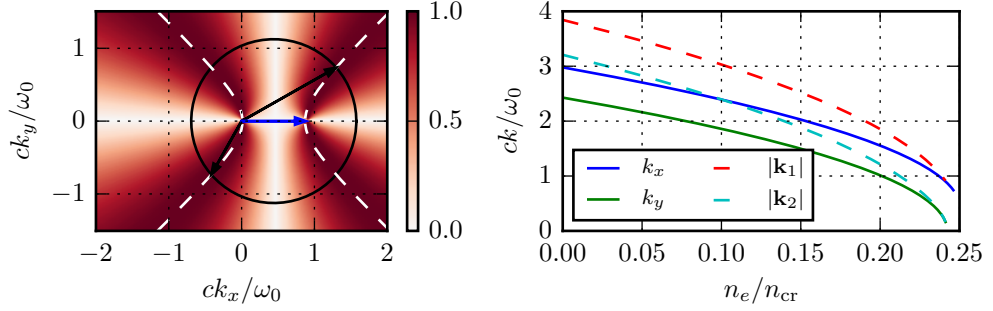


Figure 2.9: Solution of the TPD frequency and wavenumber matching conditions using the fluid EPW dispersion relation at  $T_e = 3.5\text{keV}$ . **Left:** circle indicates wavenumbers permitted by the TPD matching conditions at  $0.22n_{\text{cr}}$ . The circle's radius increases monotonically with decreasing density. The colour scale indicates the relative linear growth rate of TPD for a given wavevector, scale in arbitrary units. Maximum growth is achieved along the hyperbolae marked by white dashed lines. Black arrows mark the EPW wavenumbers at  $0.22n_{\text{cr}}$  that would produce maximum growth, with the laser wavevector shown in blue. **Right:** variation with density of the TPD EPW wavenumbers with largest linear growth rates. Lines plotted are the parallel ( $k_x$ ) and perpendicular ( $k_y$ ) components of the longer EPW wavevector ( $\mathbf{k}_1$ ), along with magnitudes of the two wavenumbers.

$$\left| \mathbf{k} - \frac{1}{2}\mathbf{k}_0 \right|^2 = \frac{\omega_0^2}{c^2} \left[ \frac{c^2}{3v_{\text{th}}^2} \left( \frac{1}{4} - \frac{n_e}{n_{\text{cr}}} \right) - \frac{c^2}{4} \frac{|\mathbf{k}_0|^2}{\omega_0^2} \right] \left[ 1 - 3v_{\text{th}}^2 \frac{|\mathbf{k}_0|^2}{\omega_0^2} \cos^2 \theta \right]^{-1}, \quad (2.68)$$

where  $\theta$  is the angle made by the vector  $\mathbf{k} - \mathbf{k}_0/2$  with  $\mathbf{k}_0$ . This is simply the polar form for an ellipse with centre at  $(|\mathbf{k}_0|/2, 0)$ , minor radius given by the square root of the numerator, and eccentricity  $e = \sqrt{3}v_{\text{th}}|\mathbf{k}_0|/\omega_0$ . At non-relativistic temperatures where  $e \ll 1$  this is well approximated by a circle. The expression for the minor radius also makes it clear that, as with SRS, the instability cannot occur above  $n_{\text{cr}}/4$ . Due to the wavenumber matching condition the EPW wavenumbers must be on opposite sides of this curve as illustrated in figure 2.9. As density decreases, the radius of the circle increases monotonically and the EPW wavevectors lengthen rapidly.

In a homogeneous plasma, the coupling constant for TPD is given approximately by [Kruer, 2003]

$$\gamma_0 = \frac{\mathbf{k} \cdot \mathbf{v}_{\text{os}}}{4} \left| \frac{|\mathbf{k}|^2 - |\mathbf{k}_0 - \mathbf{k}|^2}{|\mathbf{k}||\mathbf{k}_0 - \mathbf{k}|} \right|. \quad (2.69)$$

Due to the  $\mathbf{k} \cdot \mathbf{v}_{\text{os}}$  factor, TPD has largest growth rate in the plane of the laser's polarisation.  $\gamma_0$  is plotted for wavevectors in this plane on the colour scale in the left panel of figure 2.9 and can be seen to have strong dependence on  $\mathbf{k}$ . In particular  $\gamma_0$  vanishes where  $k_x = k_0/2$  or where  $k_y = 0$  and is maximised along the hyperbola given by

$$\left(k_x - \frac{1}{2}k_0\right)^2 = k_y^2 + \frac{1}{4}k_0^2. \quad (2.70)$$

TPD occurring with wavenumbers along this curve always produces EPW pairs in which one is forward propagating and the other backwards propagating. As density increases towards the quarter-critical surface, the backwards-propagating wavevector tends to zero while that of the forwards-propagating wave tends to  $\mathbf{k}_0$ . Since the EPW wavevectors lengthen quickly with decreasing density, TPD is restricted to occurring only close to  $n_{\text{cr}}/4$  by the large Landau damping rates experienced by the EPWs at lower density. This is shown in figure 2.10 where the Landau damping rate of the two EPWs has been included in the growth rate calculation. A laser intensity of  $2 \times 10^{15} \text{ W cm}^{-2}$  used again. At this intensity growth goes to zero below a cutoff density of  $\sim 0.2n_{\text{cr}}$ . Growth rates are shown for three different temperatures, including in the limit of  $T \rightarrow 0$ , with temperature having only a minor effect. This is the case as  $|\mathbf{k}|\lambda_D$  has only a weak dependence on temperature at a fixed density.

In an inhomogeneous plasma with monotonically increasing density, as typically the case for direct-drive ICF, TPD occurs as an absolute instability near  $n_{\text{cr}}/4$  where the daughter waves are both near their turning points [Lee and Kaw, 1974] and becomes convective at lower density. The linear theory of the absolute instability has been investigated by several authors [Goldman, 1966; Jackson, 1967; Lee and Kaw, 1974; Liu and Rosenbluth, 1976; Simon, 1983; Afeyan and Williams, 1997a]. The most recent and comprehensive calculations of these absolute growth rates were performed in [Simon, 1983] and [Afeyan and Williams, 1997a]. At lower density where only convective instability is possible, the coupling constant has been calculated accounting for inhomogeneity in [Yan et al., 2010]. This may be used to investigate the convective growth of TPD via the coupled wave model described above.

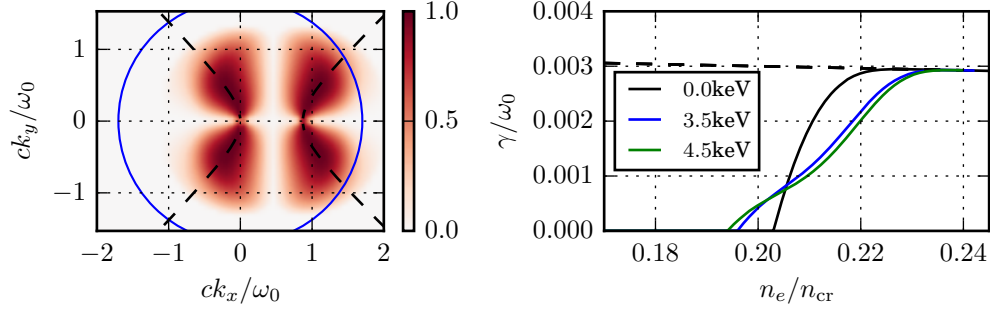


Figure 2.10: Homogeneous coupling constant ( $\gamma_0$ ) for TPD as a function of wavenumber and density for a laser intensity of  $2 \times 10^{15} \text{Wcm}^{-2}$  at  $T_e = 3.5 \text{keV}$ . **Left:**  $\gamma$  versus wavenumber, as in figure 2.9 but including the Landau damping rate of the EPWs. Values are in arbitrary units. Note that density is not fixed in this plot. The location of the Landau cutoff ( $|\mathbf{k}|\lambda_D = 0.3$ ) is marked by a blue circle, assuming a density of  $0.2n_{\text{cr}}$ . **Right:**  $\gamma$  versus density at three different temperatures including Landau damping (solid lines) and excluding it (dashed line). Due to the small variation in  $\gamma_0$  and exponential behaviour of the damping rate this closely resembles the left panel of figure 2.4.

### 2.5.6 Stimulated Brillouin Scattering

The Stimulated Brillouin Scattering (SBS) instability is the decay of an electromagnetic wave to an ion-acoustic wave and a scattered EM wave. Since the ion sound speed is very small by comparison to the group velocity of an EM wave, the wavenumbers satisfying the matching conditions are well approximated by a circle in  $k$  space of radius  $k_0$ . For the scattered light wavevector this is simply

$$|\mathbf{k}_s| \simeq |\mathbf{k}_0|, \quad (2.71)$$

and is plotted in the left panel of figure 2.11. From the frequency matching condition the scattered light has frequency

$$\omega_s \simeq \omega_0 - c_s |\mathbf{k}_{\text{iaw}}| - \mathbf{u} \cdot \mathbf{k}_{\text{iaw}}, \quad (2.72)$$

indicating a very slight shift relative to the laser frequency and that, unlike the prior two instabilities, there is no dependence on density. Consequently SBS can take place anywhere below the laser's critical density.

It should be noted that due to the small IAW frequency, the assumption made in the temporal analysis of section 2.5.1 that  $\omega_1/\omega_0$  is sufficiently far from zero can

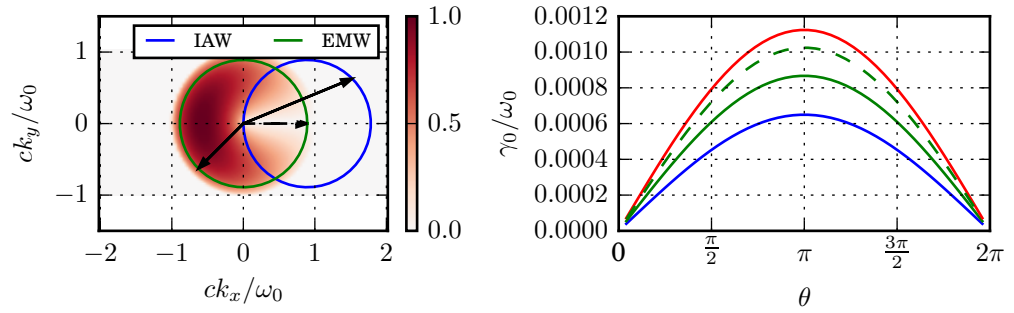


Figure 2.11: Solution of the SBS frequency and wavenumber matching conditions using the fluid IAW dispersion relation with  $T_e = 3.5\text{keV}$ ,  $T_i = T_e/2$ , and for a hydrogen plasma. **Left:** circles indicate wavenumbers permitted by the SBS matching conditions at  $0.2n_{\text{cr}}$ . The circle's radius increases monotonically with decreasing density. The colour scale shows the linear growth rate of SBS for a given scattered light wavevector (neglecting Landau damping), with an arbitrary normalisation. Maximum growth is achieved for direct backscatter. Black arrows mark a possible triad of wavenumbers at  $0.2n_{\text{cr}}$ , with the laser wavevector shown with a dashed line. **Right:** Growth rate as a function of scatter angle for  $T_e = 3.5\text{keV}$ ,  $T_i = 1.7\text{keV}$ ,  $I = 2 \times 10^{15}\text{Wcm}^{-2}$  (solid lines) and the same parameters but with halved temperatures (dashed lines). The densities used are  $0.2n_{\text{cr}}$  (green),  $0.1n_{\text{cr}}$  (blue) and  $0.4n_{\text{cr}}$  (red).

fail when  $\mathbf{k}_{\text{iaw}} \sim 0$ . This occurs for the ‘forward-scatter’ configuration, which is just the filamentation instability. In this situation SBS becomes a strongly coupled instability, with a different growth rate as discussed by Forslund et al. [Forslund et al., 1975].

In a homogeneous plasma the coupling constant of SBS is given by [Forslund et al., 1975]

$$\gamma_0 = \frac{k_{\text{iaw}} v_{\text{os}}}{4} \frac{\omega_{\text{pi}}}{\sqrt{\omega_{\text{iaw}} \omega_{\text{s}}}}, \quad (2.73)$$

where  $\omega_{\text{pi}} = \omega_{\text{pe}} \sqrt{m_e/m_i}$  is the ion plasma frequency. This is shown in figure 2.11 as a function of scattered light wavenumber and angle. The growth rates can be seen to be significantly smaller than those for TPD and SBS in equivalent plasma conditions due to the dependence on slow ion motion. SBS growth is largest for direct backscatter, with growth rates decreasing with the scatter angle. For forward scatter with  $\theta = 0$  the growth rates approach zero as here  $k_{\text{iaw}} \simeq 0$ .

Due to the Doppler frequency term in equation 2.72, one prominent situation in which the instability can take place is where the Doppler shift cancels the natural frequency of the IAW and makes  $\omega_s = \omega_0$ . When this occurs, laser beams with equal frequency crossing in the plasma become coupled by SBS leading to a potentially large transfer of energy between them. This is referred to as Cross-Beam Energy Transfer (CBET) and is a major issue for both indirect and directly-driven ICF schemes.

Finally, in an inhomogeneous plasma SBS can occur as an absolute instability in a similar manner to SRS. Here backscatter is absolute at the critical surface  $n_{\text{cr}}$  and sidescatter is absolute at density that decreases with increasing  $k_y$ . Growth rates for the absolute instability are given in [Liu, 1974].

## Chapter 3

# Methods

This chapter focuses on the simulation code used to perform the modelling presented in subsequent chapters. The code used, EPOCH [Arber et al., 2015], is a particle-in-cell code [Birdsall and Langdon, 1991] and is widely used for the simulation of collisionless and weakly collisional plasmas. In section 3.1 the particle-in-cell method is introduced and its implementation in the EPOCH code described. Then, in section 3.2 the code is tested by using it to model the linear growth of SRS in a 1D, periodic domain. The growth rates are then compared to the results in the previous chapter. Finally, in section 3.3 a description is given of the main diagnostics used in the 2D simulations that are the subject of this thesis.

### 3.1 EPOCH & The Particle-in-cell Method

The particle-in-cell (PIC) approach to simulating a plasma is, by comparison to other simulation techniques, very intuitive. The central concept is to simulate self-consistently the motion of discrete particles in the electric and magnetic fields. Naively, this could be done by directly modelling each electron and ion in the plasma and the pairwise forces between them, an approach known as molecular dynamics. In the coronal plasmas of directly-driven ICF targets, typical plasma parameters are of order  $n_e \sim n_{cr}/4 = 2.26 \times 10^{27} \text{m}^{-3}$  and  $T_e \sim 1 \text{keV}$ . The Debye length is thus  $\lambda_D \sim 5 \text{nm}$ , so in a volume of  $\lambda_D^3$  there would be  $N \sim 300$  particles. This may not seem like many for a modern computer, however at each time-step it would be necessary to compute the pairwise forces between  $N$  particles, requiring  $\mathcal{O}(N^2)$  calculations. Add to this the desire to simulate hundreds or thousands of Debye lengths in each of two or three dimensions, for many thousands of time-steps, and the approach clearly becomes intractable.



The particle-in-cell method drastically reduces these computational requirements by making two key approximations. Firstly, the simulation is divided into a regular grid on which the electromagnetic fields are defined. The cell size of this grid is typically on the order of a Debye length. The behaviour of the fields are then dictated by Maxwell's equations and are solved using standard numerical methods. Secondly particles are grouped into macroparticles or 'particle clouds', and are propagated as a whole under the motion of the gridded fields via the Lorentz force. Along with calculating their motion, the method also records the current or charge at each cell of the EM grid which is then used by the field solver.

These two approximations result in a less computationally expensive algorithm since the particles are no longer directly coupled via the Coulomb force. Instead they only directly interact with the global electromagnetic fields, producing a force calculation that is now  $\mathcal{O}(N)$ . In addition to this, the grouping of physical particles into macroparticles can also dramatically reduce the number simulated relative to a physical plasma. This is because the number of macroparticles required in a Debye volume is now dictated by the need to produce a representative statistical sample of the distribution function rather than by the number of physical particles present.

Inevitably however, these approximations lose aspects of the real-world physics that can be important. In the limit of an infinite number of particles and infinitesimally small cell size it can be shown that the PIC method is equivalent to the collisionless Vlasov equation. This means that collisions are neglected and that the fields modelled are not the true EM fields but smoothed versions. Collisional behaviour can however be re-introduced by employing one of several algorithms which have been developed to calculate the effect of collisions on PIC macroparticles. In addition, since in practice simulations have a finite cell size and number of particles, the fields are not smooth but include statistical noise from the macroparticles. This noise can be problematic if the smoothed fields are desired, and is also not equivalent to the fluctuations that would be introduced by collisions. Finally, additional errors are introduced by the numerical techniques used to propagate the particles and solve Maxwell's equations.

These issues may all prevent meaningful simulation results from being obtained, however they are known and quantifiable effects. Provided they are managed, the PIC method can be a powerful tool in investigating the behaviour of weakly collisional plasmas such as those considered in the subsequent chapters.

### 3.1.1 Code Overview

In pseudocode, the main loop of EPOCH reads as follows:

---

```
loadParticles(); // Initialise particle positions and momenta

for(int i=0; i<nSteps; i++) {
    EBFIELDSHalf(); // Update E & B fields from step i->i+1/2
    pushParticles(); // Particle positions & momenta i->i+1
    depositCurrent(); // Calculate J from particle positions & momenta
    outputRoutines(); // Output required data to disk
    EBFIELDSFinal(); // Update E & B fields from i+1/2->i+1
}
```

---

Here it can be seen that the two main components of the code, the field solver and particle propagation algorithm (referred to as the ‘particle push’), alternate in updating the fields and particle properties. Furthermore, each of the updates uses data for ‘source terms’ from intermediate time-steps. For example the particle push from step  $i \rightarrow i + 1$  uses field data at step  $i + 1/2$  to calculate particle forces. These two components are discussed in further detail in subsections 3.1.2 and 3.1.3. In addition however, since the particles inhabit continuous space while the fields are defined on a discrete grid, a mechanism is needed through which the particles and fields can be coupled. This final component of the code is discussed in subsection 3.1.4.

### 3.1.2 Field Solver

To solve Maxwell’s equations, two regularly spaced grids are defined which are staggered by half a cell-size in each direction. The various field components are assigned to one of these such that, when centred spatial differences are taken, all quantities required to update the fields via Maxwell’s equations are known at the same location. This scheme is due to Yee [Yee, 1966] and is common to most PIC codes.

To update the equations in time a leapfrog-type algorithm is employed. Here the currents from timestep  $n$  are used to update the fields from step  $n$  to  $n + 1/2$ . At this point the particle push is performed which generates currents at step  $n + 1$ , which are then used to complete the field update ( $n + 1/2 \rightarrow n + 1$ ). The scheme is written explicitly as [Arber et al., 2015]:

$$\mathbf{E}^{n+\frac{1}{2}} = \mathbf{E}^n + \frac{1}{2}\Delta t \left[ c^2 \nabla \times \mathbf{B}^n - \frac{1}{\varepsilon_0} \mathbf{J}^n \right], \quad (3.1)$$

$$\mathbf{B}^{n+\frac{1}{2}} = \mathbf{B}^n - \frac{1}{2}\Delta t \left[ \nabla \times \mathbf{E}^{n+\frac{1}{2}} \right], \quad (3.2)$$

for the first half-step, and

$$\mathbf{B}^{n+1} = \mathbf{B}^{n+\frac{1}{2}} - \frac{1}{2}\Delta t \left[ \nabla \times \mathbf{E}^{n+\frac{1}{2}} \right], \quad (3.3)$$

$$\mathbf{E}^{n+1} = \mathbf{E}^{n+\frac{1}{2}} + \frac{1}{2}\Delta t \left[ c^2 \nabla \times \mathbf{B}^{n+1} - \frac{1}{\varepsilon_0} \mathbf{J}^{n+1} \right], \quad (3.4)$$

for the second. When combined and shifted by half a step these equations are identical to the classic leapfrog algorithm. The advantage of performing a split update in this way is that the fields are now known at the same time, rather than at interleaved half timesteps. This is necessary for the particle push and also for the implementation of other physics modules which frequently rely on this. This does come at the cost of additional computational expense, however this is typically not a problem as the field updates usually account for a small fraction of execution time in a PIC simulation.

### 3.1.3 Particle Push

To calculate the force on each particle, the gridded fields must be used to calculate an effective field which the particle experiences. This is discussed in the subsection below, however taking the results of this procedure for particle  $\alpha$  as  $\bar{\mathbf{E}}_\alpha^{n+1/2}$  and  $\bar{\mathbf{B}}_\alpha^{n+1/2}$ , the acceleration experienced by each particle is given by the Lorentz force:

$$\left. \frac{d\mathbf{p}_\alpha}{dt} \right|^{n+\frac{1}{2}} = q_\alpha \left[ \bar{\mathbf{E}}_\alpha^{n+\frac{1}{2}} + \mathbf{v}_\alpha^{n+\frac{1}{2}} \times \bar{\mathbf{B}}_\alpha^{n+\frac{1}{2}} \right]. \quad (3.5)$$

For the particle push, the leapfrog method is again used to update the particle position and momenta. However, as with the field updates this has the disadvantage that both quantities are not known at the same timestep. Consequently the scheme is again split, this time by performing two position updates. The equations then become

$$\mathbf{p}_\alpha^{n+1} = \mathbf{p}_\alpha^n + \Delta t \left. \frac{d\mathbf{p}_\alpha}{dt} \right|^{n+\frac{1}{2}}, \quad (3.6)$$

$$\mathbf{x}_\alpha^{n+\frac{1}{2}} = \mathbf{x}_\alpha^n + \frac{1}{2}\Delta t \mathbf{v}_\alpha^n, \quad (3.7)$$

$$\mathbf{x}_\alpha^{n+1} = \mathbf{x}_\alpha^{n+\frac{1}{2}} + \frac{1}{2}\Delta t \mathbf{v}_\alpha^{n+1}, \quad (3.8)$$

$$\mathbf{x}_\alpha^{n+\frac{3}{2}} = \mathbf{x}_\alpha^{n+1} + \frac{1}{2}\Delta t \mathbf{v}_\alpha^{n+1}, \quad (3.9)$$

In the force calculation above, the particle velocity is required at the half timestep. Various approaches may be taken to handle this, however in most PIC codes (including EPOCH) the momentum update is also split using the Boris rotation algorithm [Boris, 1971]. In EPOCH, following current deposition where  $\mathbf{p}_\alpha^{n+1}$  and  $\mathbf{x}_\alpha^{n+3/2}$  are required, this half-timestep position is discarded and so must be re-calculated from  $\mathbf{x}_\alpha^{n+1}$  at the beginning of the next particle push.

For accurate simulation results large numbers of particles are required in each cell. This is often in the range of tens to thousands depending on the problem under consideration. The particle push is therefore the most computationally expensive component of the core simulation scheme, and usually accounts for the vast majority of execution time.

### 3.1.4 Particle Weighting

To couple the two solvers above an interpolation scheme is required to calculate the effective force of the field on each particle, and the charge or current contributed from each particle to each cell. In modern PIC codes the macroparticles represent a cloud of physical particles distributed over some region of space. The specific form of the distribution is referred to here as its ‘shape function’ and the cell-sized differences of the cumulative distribution function ( $F(x + \Delta x) - F(x)$ ) referred to here as its ‘weight function’ (note that the shape function is sometimes referred to as a weight function in other texts). The weight function is what is used to interpolate quantities to/from each cell that the particle occupies.

The shape functions used in EPOCH and most other PIC codes are successive convolutions of a rectangular function with itself, with each iteration of this procedure producing a closer representation of a Gaussian distribution in accordance with the central limit theorem. Higher orders of convolution act to smooth the response of the fields to the motion of the particles and reduce unphysical ‘self-heating’ of the plasma. The reduction in noise and self-heating from a higher order shape function

means that fewer particles are required for similar level of accuracy. However, they also increase the number of operations required per interpolation as each particle occupies more cells. The choice of shape functions is therefore most commonly first, second or third order (rectangular, triangular etc.).

With the shape functions defined, the effective field components at the particle locations may be calculated via a weighted sum over the weight function and field components. Several methods then exist to calculate the current that is deposited onto the grid, with the method used by EPOCH being Esirkepov’s algorithm [Esirkepov, 2001] which guarantees exact charge conservation.

## 3.2 Simulations of SRS in a 1D Periodic Box

To illustrate agreement between the simulation code and analytic theory, this section is dedicated to an investigation of the Stimulated Raman Scattering (SRS) instability. This was described in the previous chapter so, to ensure agreement between the simulation code and the linear theory of parametric instabilities, several of the results presented in that chapter are verified here.

SRS most commonly occurs as a back or forward-scattering instability, with daughter wave wave-vectors parallel or anti-parallel to that of the pump. For these cases, and only during its linear growth, this provides a physical justification for modelling SRS via a 1D simulation. To further simplify the scenario a homogeneous plasma of infinite extent is considered.

### 3.2.1 Simulation Setup

Since the plasma is homogeneous and of infinite extent it is a reasonable approximation to model it using a periodic simulation box. This has the advantage of reducing computational requirements compared to a large aperiodic domain and avoids any complications at the boundaries. However the periodicity places certain restrictions on the simulation parameters.

For a given domain length the simulation can only support wavenumbers that are integer multiples of the fundamental mode,

$$k_j^{\text{sim}} = j \frac{2\pi}{L_x}, \quad (3.10)$$

where  $j$  is an integer with  $0 \leq j \leq N_x - 1$ ,  $L_x$  is the box length and  $N_x$  is the number of simulation cells. To model forward or back-scatter SRS correctly the simulation domain must accommodate all three SRS wavenumbers. This is not generally pos-

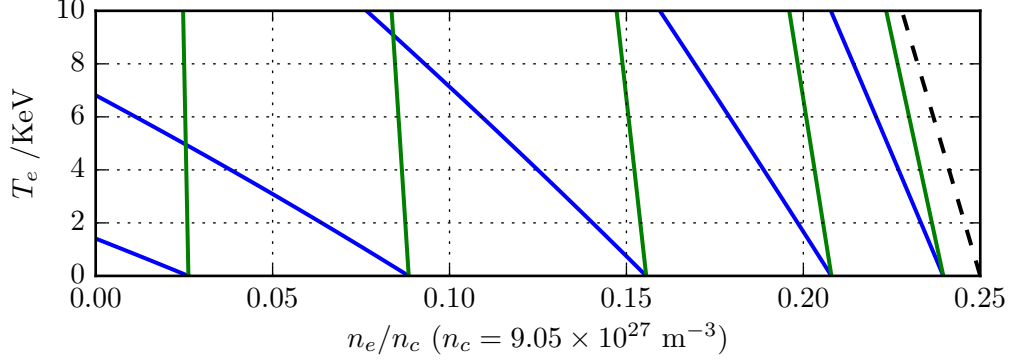


Figure 3.1: Points in density-temperature parameter space where the SRS daughter wave wavelengths exactly fit a domain of size  $L_x = 6\lambda_0$  where  $\lambda_0$  is the local laser wavelength. Blue solid lines represent SRS backscatter; green solid lines forward-scatter. The dashed black line corresponds to the maximum density at which SRS can occur. For this case back and forward-scatter are indistinguishable and the daughter wavenumbers become  $k = k_0$  and  $k_s = 0$ .

sible, however with careful choice of physical parameters the wavenumbers may be tuned such that they match supported modes of the domain.

Figure 3.1 shows the locations in density-temperature parameter space which allow for all three wavenumbers to fit in the domain for back and forward-scatter (blue and green solid lines) respectively with a domain of size  $L_x = 6\lambda_0$ . The dashed black line indicates the upper density boundary for SRS at which back and forward-scatter become indistinguishable and where  $k = k_0$  and  $k_s = 0$ . The wavenumber ratios  $\alpha \equiv k/k_0$  and  $\beta \equiv k_s/k_0$  are given by  $\alpha_i = 1 \pm i/N$  and  $\beta_i = \mp i/N$  where  $N$  is the number of laser wavelengths in the box and  $i \in \mathbb{N}_0 < N$ , with  $i$  increasing with decreasing density. To illustrate why this is the case, consider the frequency matching condition in the limit of  $T_e = 0$ :

$$\begin{aligned}
 \omega_0 &= \omega_{ek} + \omega_s \\
 &= \omega_{pe} + \sqrt{\omega_{pe}^2 + c^2 k_s^2} \\
 &= \omega_{pe} + \sqrt{\omega_{pe}^2 + \beta^2 (\omega_0^2 - \omega_{pe}^2)}.
 \end{aligned}$$

Solving for  $\omega_{pe}$  we find

$$\frac{\omega_{\text{pe}}}{\omega_0} = \frac{1 \pm \sqrt{1 - \beta^2 + \beta^4}}{\beta^2}. \quad (3.11)$$

SRS cannot occur above  $n_{\text{cr}}/4$ , so  $0 < \omega_{\text{pe}}/\omega_0 < 1/2$ . This then means that we must have  $\beta^2 < 1$  and take the negative square root. The domain must fit some multiple  $N$  of the laser wavelength such that  $k_0^{\text{sim}} = k_0/N$ , so all simulation wavenumbers must satisfy  $k_j^{\text{sim}}/k_0 = j/N$ . Therefore  $\beta$  takes on discrete values  $|\beta_i| = i/N < 1$ . Given  $\beta_i$ , the EPW wavenumber ratio  $\alpha_i$  may be found by using the wavenumber matching condition.

While more verbose, the above analysis is easily extended to  $T_e \neq 0$  using the textbook EPW dispersion relation (eq. 2.26), and was used to produce figure 3.1. This more general analysis may also be used to derive a simple approximation for the maximum density at which SRS can occur:

$$\frac{n_e}{n_{\text{cr}}} = \frac{1}{4} \left[ 1 - \left( \frac{3}{2} \frac{v_{\text{th}}}{c} \right)^2 \right]. \quad (3.12)$$

To further reduce computational expense, all simulations shown here have a short domain that is always six times the length of the laser wavelength ( $k_0 = 6k_0^{\text{sim}}$ ). A grid spacing of  $\Delta x = 0.9\lambda_D$  was used such that all wavelengths of interest were well resolved and particle self-heating kept small. Additionally 1000 particles per cell were simulated and particles had triangular shape-functions. To be consistent with the rest of the simulations in this thesis the laser frequency corresponds to that of a frequency-tripled Nd:Glass laser with a vacuum wavelength of 351nm. The laser is modelled as a monochromatic wave that is imposed as an initial condition on the  $E_y$  and  $B_z$  fields and the electron velocity drift in the  $\hat{\mathbf{y}}$  direction. Finally, since we are only considering linear growth of SRS the ions are treated as a fixed neutralising background.

### 3.2.2 Resonant Undamped Growth

As an initial test of consistency, a single simulation was run to see if SRS would occur and behave as predicted. The parameters were chosen to allow SRS backscatter only, with a temperature of 1keV and a density of  $n_e \simeq 0.203$ . A laser intensity of  $I = 10^{15} \text{Wcm}^{-2}$  was used to ensure that SRS was well above the threshold for growth, but also that the intensity not be so high as to induce any relativistic effects ( $a_0 \equiv eE_0/m_e\omega_0c = 9.5 \times 10^{-3} \ll 1$ ). The simulation duration was 0.55ps to allow the instability to grow and reach saturation. This choice of parameters should produce backscatter SRS with EPW wavenumber  $k = 1.19\omega_0/c$  (domain mode  $j = 8$ )

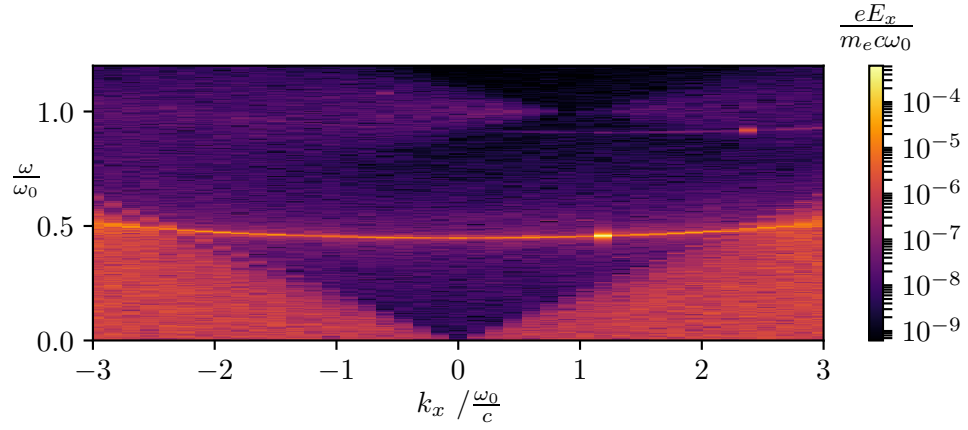


Figure 3.2: Spatiotemporal discrete Fourier transform (DFT) of the electrostatic field component  $E_x$ . The narrow curve at  $\omega/\omega_0 \simeq 0.5$  corresponds to the dispersion relation for EPWs, excited by thermal noise fluctuations. Fluctuations are also responsible for the triangular features extending from  $k_x = 0$  at low frequency. These features are not resonant modes of the plasma but are caused by the thermal motion of the electrons and hence have phase velocities  $\omega/k \lesssim 4.5v_{th}$ . Locations where the EPW dispersion relation intersects with this region indicate significant Landau damping of those waves would occur. A large-amplitude EPW is excited by SRS in this simulation and appears as a peak in the Fourier transform at  $k = 1.19\omega_0/c$  (Fourier mode  $j = 8$ ). A further peak of smaller amplitude can be seen at  $k = 2.38\omega_0/c$  ( $j = 16$ ) which corresponds to the second harmonic of the SRS EPW, driven by nonlinear fluid effects.



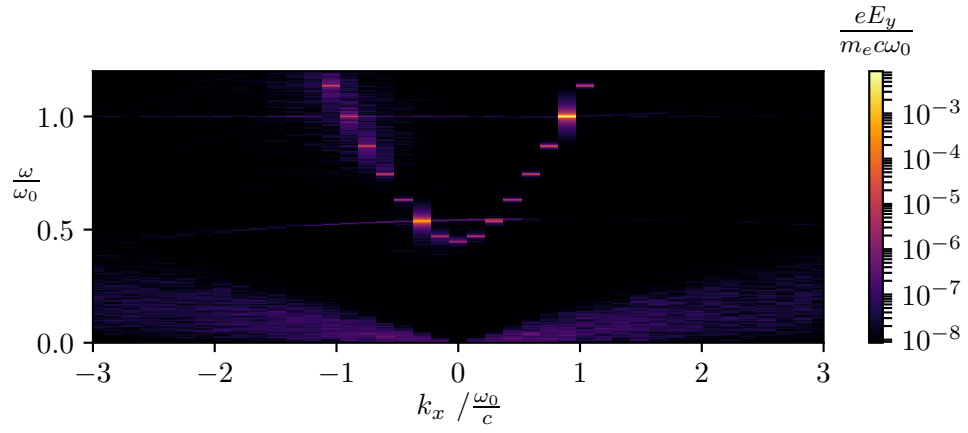


Figure 3.3: Spatiotemporal discrete Fourier transform (DFT) of the electromagnetic field component  $E_y$ . The hyperbolic curve that is visible corresponds to the dispersion relation for EM waves in a plasma, traced out by thermal fluctuations. Two peaks are visible with amplitude significantly larger than the thermal noise background. The peak of largest amplitude at  $k = 0.89\omega_0/c$  corresponds to the laser, while the smaller peak at  $k = -0.30\omega_0/c$  corresponds to the backscattered EM wave driven by SRS. The low-amplitude curve that extends out from the backscatter peak is caused by Thomson scattering of the laser off electron plasma waves.

and scattered EM wavenumber  $k_s = -0.30\omega_0/c$  ( $j = 2$ ). The normalised EPW wavenumber  $k\lambda_D = 0.11 < 0.25$  indicates that Landau damping should be negligible. For a plasma with mean charge state of  $Z = 3.5$ , representative of CH, the electron-ion collision rate would be  $\nu_{ei} = 3.8\text{ps}^{-1}$  [Book, 2018], suggesting that over the duration of the simulation collisions may well be important for a physical plasma. For this initial simulation an undamped system was desired for simplicity so collisional effects were neglected by disabling the collision model in the code. There will still be an effective collision rate brought about by particle noise, but this should be small. Therefore it is reasonable to describe the system here as undamped.

In figures 3.2 & 3.3 the spatiotemporal Fourier transform of the output is shown for the  $E_x$  and  $E_y$  fields, with several notable features visible. In both electrostatic ( $E_x$ ) and electromagnetic ( $E_y$ ) field components the respective linear dispersion relations are traced out by small-amplitude thermal noise fluctuations. In the EM field component a large-amplitude peak is visible at  $(k_0, \omega_0)$  corresponding to the laser, however there is an additional peak with negative  $k$  and lower frequency. The values of  $\omega$  and  $k$  for this peak correspond to those expected for SRS backscatter. A further peak in the electrostatic field component with forward-going wave-vector matches the expected wavenumber and frequency for the SRS EPW. These peaks suggest that SRS has occurred.

To investigate this potential SRS growth, the behaviour of the individual waves was examined. Assuming a given wave's growth or damping is small relative to its frequency ( $|\text{Im}(\omega)| \ll |\text{Re}(\omega)|$ ), the field due to the wave can be written analytically as

$$E_a^T(x, t) = E_a(x, t)e^{i(k_ax - \omega_at)} + E_a^*(x, t)e^{-i(k_ax - \omega_at)}. \quad (3.13)$$

Here  $E_a^T(x, t)$  is the total field from wave  $a$  and  $E_a(x, t)$  is the slowly varying wave envelope, which would be constant for a monochromatic plane wave. Taking a spatial Fourier transform and assuming no spatial dependence of the wave amplitudes gives

$$E_a^T(k, t) = E_a(t)\delta(k - k_a)e^{-i\omega t} + E_a^*(t)\delta(k + k_a)e^{i\omega t}. \quad (3.14)$$

This means that by taking the spatial Fourier transform of the simulation  $E_x$  or  $E_y$  fields, the time-history of a given wave amplitude (i.e. the wave's time-envelope) can be extracted by calculating  $|E(k = k_a, t)|$ , with the modulus necessary to eliminate the rapid oscillation of the complex exponential at  $\omega_a$ . This quantity is plotted in figure 3.4 using the expected wavenumbers of the laser (blue solid line, left panel), scattered light and EPW (green solid lines, left and right panel respectively).

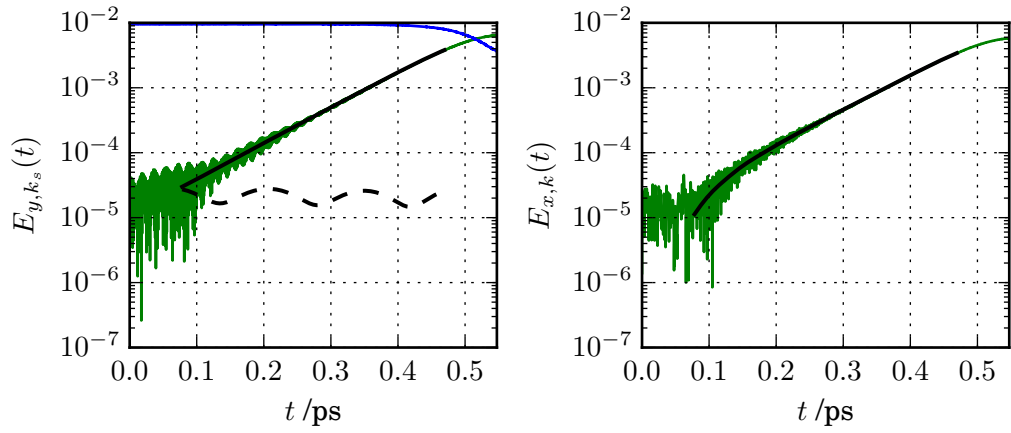


Figure 3.4: Amplitude of spatial modes corresponding to the laser (left, blue), backscattered EM (left, green) and EPW (right, green) as a function of time. The electric field is normalised by  $e/(m_e\omega_0c)$ . The solid black lines are the time-envelopes of these signals, calculated by applying a complex bandpass filter and taking the modulus of the resulting signal. This isolates the waves corresponding to backscatter SRS (the forward-SRS scattered light would occur at the same spatial mode in the simulation) and reduces noise. The dashed black line in the left panel is the equivalent envelope for forward-scatter SRS and demonstrates that this is sufficiently detuned as not to undergo any significant growth.

In figure 3.4 the solid green lines show clear exponential growth though also include significant amounts of simulation noise. In addition, in the case of the amplitude plotted for scattered light it is possible for this to include both forward and back-scatter SRS. This is because for the simulation parameters chosen, the scattered light wavenumber for forward-scatter SRS is similar in magnitude to that of backscatter, though of course opposite in sign. This will appear in the data as a complex exponential oscillating in the opposite direction to that of the backscatter as per eq. 3.14.

To eliminate noise and allow backscatter and forward-scatter to be isolated, the spatially Fourier transformed fields were filtered in time using a complex band-pass filter. These are plotted as the solid black lines in figure 3.4. In both panels the amplitude of the backscatter SRS daughter waves begin to grow exponentially. The dashed black line in the left panel corresponds to the time-envelope for forward-scattered light. Since forward SRS is not resonant for the chosen simulation parameters this does not undergo growth.

The backscatter SRS growth rate in this simulation could be calculated directly from figure 3.4. However since it was anticipated that many simulations would be run, a more methodical approach was taken to performing this measurement. Assuming perfectly linear growth, the growth rate could be measured by numerically evaluating the quantity

$$\gamma = \left\langle \frac{d}{dt} \ln [E_a(t)] \right\rangle_t. \quad (3.15)$$

Where the angle brackets denote a time-average. In practice there is an initial equilibration period in the simulations, followed by a linear growth phase and finally saturation of the instability. This means some method is required to identify where the growth is linear. A simple way to accomplish this is to calculate the time-derivative of the growth rate and require that this is lower than some threshold.

$$\frac{d\gamma}{dt} = \frac{d^2}{dt^2} \ln [E(t)] < \varepsilon. \quad (3.16)$$

Sensible values for this arbitrary threshold can be obtained by considering order of magnitude estimates for the expected growth rate. The growth rate is then measured by taking the longest contiguous sequence of data below this threshold and taking its time-average.

This procedure was applied to the above data and gave an exponential growth rate of  $\gamma_{\text{sim}} = 2.34 \times 10^{-3} \omega_0$  which is close to the theoretical value of  $\gamma_0 = 2.55 \times 10^{-3} \omega_0$ , though this leaves a  $\sim 10\%$  error. This will be explained in the next section.

The laser amplitude is plotted as the solid blue line in the EM field plot (left pane of fig. 3.4). After approximately 0.4ps the laser intensity begins to drop as the daughter waves remove significant fractions of its energy causing pump depletion. This saturates the instability and marks the end of the linear growth phase.

### 3.2.3 Off-resonant Undamped Growth

The above results indicate that for perfectly matched waves, SRS grows at a rate close to that expected by theory. However the theory also predicts growth for unmatched waves. In a physical system or an aperiodic simulation it is usually difficult to observe off-resonant growth. Here the periodic nature of the simulation domain allows a frequency mismatch to be directly imposed and therefore for a measurement of the off-resonant growth rates. This allows for a comparison with equation 2.46, written again here for convenience:

$$\gamma^2 = \gamma_0^2 - \frac{1}{4}\Delta\omega^2.$$

To explore this relationship a series of simulations were run with fixed temperature of 1keV but with density varied by a small amount ( $\pm 7.5 \times 10^{-3} n_{\text{cr}}$ ) about the ‘perfectly matched’ density chosen above. Note that the domain length  $L_x$  is also varied in order to fit the laser wavelength at each density. If SRS is able to grow in one of these ‘off-resonant’ simulations, the wavenumbers for the EPW and EM wave will be forced to be one of the modes of the domain rather than the wavenumbers they would naturally grow at. Provided this shift is small, their mode number  $j$  will remain the same as for the perfectly matched case. This means that they will still satisfy the wavenumber matching condition. However, according to the linear wave dispersion relations, the frequencies of these waves will no longer precisely satisfy the frequency matching condition and this is what results in the deviation from perfect resonance.

Growth rates for this series of simulations are shown in figure 3.5 as a function of density (left) and theoretical frequency shift (right). These were measured following the procedure described in the previous section. In the left panel it can be seen that the range of densities considered spans a region in which both forward and backscatter are able to grow. In the right-hand panel the data have been fitted by the relationship expected from equation 2.46, extended to included an observed frequency shift ( $\Delta\omega_{\text{obs}}$ ) and scaled maximum growth rate ( $a_{\text{obs}}$ ):

$$\gamma^2 = (a_{\text{obs}}\gamma_0)^2 - \frac{1}{4}(\Delta\omega - \Delta\omega_{\text{obs}})^2. \quad (3.17)$$

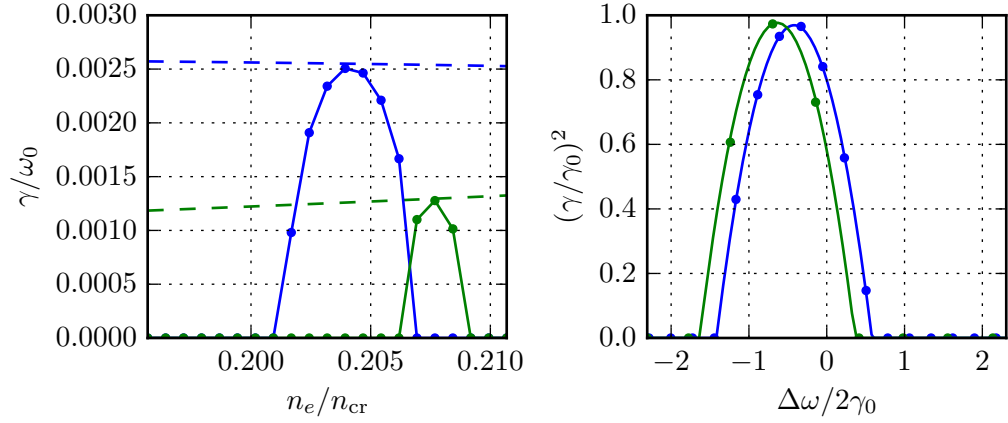


Figure 3.5: Measured growth rates for varying frequency mismatch in a periodic simulation for SRS backscatter (blue points) and forward scatter (green points). The frequency mismatch is varied by changing the simulation density. Over the range of densities considered both forward and back-scatter are present (left pane). In the left figure dashed lines indicate the infinite homogeneous growth rates ( $\gamma_0$ ) while solid lines are linear interpolations between points to guide the eye. In the right hand figure the growth rates, normalised to the theoretical infinite homogeneous growth rate ( $\gamma_0$ ), are plotted as a function of the theoretical mismatch ( $\Delta\omega$ ). This would be expected to give peak growth at  $\Delta\omega = 0$  which the data do not follow, indicating that there is an unexpected frequency shift to the SRS daughter wave dispersion relations. The data are fitted by the theoretical model (eq. 3.17) which includes an arbitrary frequency shift and scaled maximum growth rate (solid lines, right). This gives  $\Delta\omega_f = -1.6 \times 10^{-3}\omega_0$  and  $\Delta\omega_b = -2.1 \times 10^{-3}\omega_0$  for the frequency shift.

As seen in the right hand plot from figure 3.5 this fit closely matches the shape of the measured growth rates and gives good agreement with the maximum growth rate ( $a_{\text{obs,b}} = 0.985$ ,  $a_{\text{obs,f}} = 0.988$ ). However the data clearly indicate that maximum growth occurs some distance from where the frequencies are expected to be matched. This means that the simulated wave dispersion relations differ by some shift relative to the linear relations used for the calculation of the matching plasma parameters. The fitted curves give the value of this shift as  $\Delta\omega_{\text{obs,b}} = -2.13 \times 10^{-3}\omega_0$ ,  $\Delta\omega_{\text{obs,f}} = -1.65 \times 10^{-3}\omega_0$  for back and forward-scatter respectively.

There are several physical effects that are known to produce frequency shifts, however most of these can be ruled out. Such effects include trapping of electrons in the EPW [Morales and O’Neil, 1972], the production of EPW harmonics [Winjum et al., 2007] and shifts due to relativistic effects [Pegoraro and Porcelli, 1984]. In these simulations we do not observe any significant trapping, ruling out the first option. Additionally the predicted shift due to EPW harmonics is in the wrong direction and in any case much smaller than required to explain the observations. The relativistic correction however gives the appropriate direction and order of magnitude for the shift. To lowest order this may be thought of as a modification to the plasma frequency [Pegoraro and Porcelli, 1984], brought about by the relativistic mass increase of high-energy thermal electrons. This is given as

$$\omega_{\text{pe,rel}}^2 = \omega_{\text{pe}}^2 \left( 1 - \frac{5}{2} \frac{v_{\text{th}}^2}{c^2} \right), \quad (3.18)$$

and for these simulations produces a frequency shift  $\Delta\omega_{\text{rel}} \simeq -1.1 \times 10^{-3}\omega_0$ .

To verify that a relativistic correction is indeed responsible for this shift, the simulations were repeated but with the Lorentz factor neglected in the particle push. This allows all relativistic effects to be omitted but will maintain other nonlinear shifts. The resulting growth rates are shown in figure 3.6. Fitting these growth rates results in much smaller frequency shifts relative to linear theory of  $\Delta\omega_{\text{obs,b}} = -0.48 \times 10^{-3}\omega_0$ ,  $\Delta\omega_{\text{obs,f}} = -0.03 \times 10^{-3}\omega_0$  respectively, confirming that the shift observed above is indeed due to relativistic effects.

### 3.3 2D Simulation Diagnostics

Even small particle-in-cell simulations often produce sufficient quantities of data that it is impractical to record their entire output. This means that it is necessary to reduce the output down to some subset which can be used to interpret the behaviour of the system. For the 2D simulations presented in subsequent chapters several

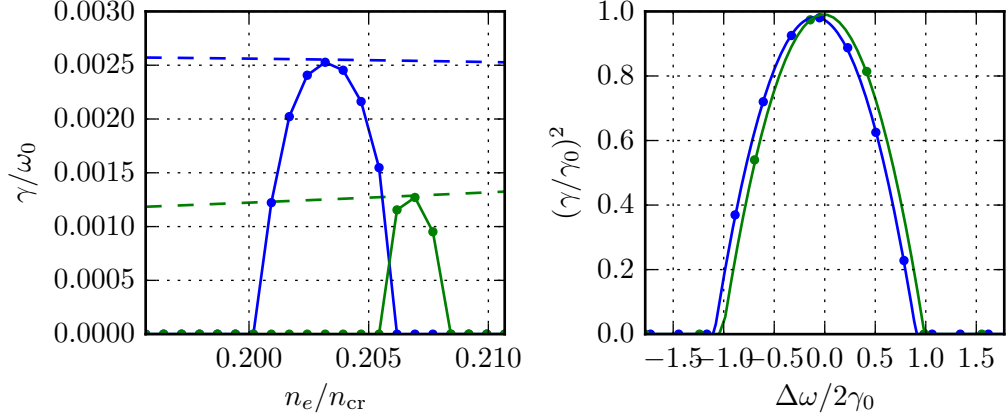


Figure 3.6: Same as figure 3.5 but with simulation data from a non-relativistic version of the simulation code. The fitted curves in the right hand figure give frequency shifts of  $\Delta\omega_f = -0.48 \times 10^{-3}\omega_0$  and  $\Delta\omega_b = -3.1 \times 10^{-5}\omega_0$ , considerably smaller than for the relativistic case. This indicates that the bulk of the frequency shift is due to relativistic effects.

diagnostics have been implemented and were utilised in all of the 2D simulations performed as part of this project. Here an overview of the key diagnostics is given.

A detailed description of the simulation setup can be found in chapter 5, however to aid the discussion below the basic features are described now. The domain (see figure 3.7) is rectangular and divided into a regular Cartesian grid parameterised by  $x$  and  $y$ . The laser enters from the left boundary and propagates along the  $x$  direction, which is also the axis along which plasma density varies.

For the purposes of quantifying the danger posed by laser-plasma instabilities in ICF, two of their products are of interest: scattered light and supra-thermal (‘hot’) electrons. Hot electrons are a concern as they may preheat the fusion fuel, precluding a high compression factor, while scattered light results in redistribution of energy delivered to the target and may lead to an asymmetric drive. The fraction of laser energy diverted into these is therefore one of the key quantities that should be measured in our simulations. To accomplish this, diagnostics were implemented that record outgoing particle and EM-field energy fluxes.

The outgoing energy flux diagnostics give useful information about the system as a whole however, in order to understand the detailed physics involved, additional measurements in the bulk of the domain are required to diagnose instability behaviour. Due to the cost of storing data from the entire domain, this was typi-



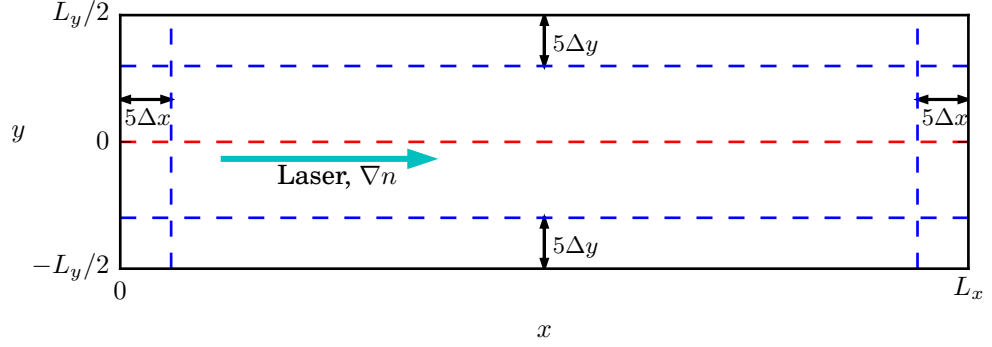


Figure 3.7: 2D simulation domain (not to scale), illustrating geometry and location of diagnostics. Blue dashed lines indicate locations where measurements of outgoing particle and field fluxes are measured. High frequency field measurements are also made along red dashed line at  $y = 0$ . Laser enters from the left hand boundary as indicated by cyan arrow. In all simulations the cell sizes  $\Delta x$ ,  $\Delta y$  are equal.

cally collected infrequently, and includes snapshots of the fields covering the whole domain and further hot-electron data. Finally, an EM field diagnostic was also implemented to allow temporal filtering or calculation of temporal spectra in the bulk domain.

### 3.3.1 Outgoing Flux Diagnostics

#### Hot electrons

To measure outgoing hot electrons, EPOCH's 'probe' diagnostic was used to define surfaces parallel to each of the boundaries which were offset by 5 cell widths into the domain (blue dashed lines in figure 3.7). Simulation electrons whose trajectory crossed one of these surfaces in the outgoing direction and had kinetic energy greater than some threshold had their instantaneous position, velocity and weight recorded in memory. The data from these crossings was accumulated over a period of 0.01ps and then saved to disk, which defines the temporal resolution of this dataset. The use of a threshold kinetic energy was designed to restrict the particle data to only those particles in the tail of the distribution function, since recording information about the core of the outgoing distribution function would be prohibitively expensive in terms of disk space.

In addition to simply measuring the energy diverted into hot electrons, this diagnostic may be used to help determine the specific instabilities taking place. In

particular SRS and TPD, the two main sources of hot electrons, often produce hot electrons with differing energy and angular spread.

## Reflectivity

The measurement of outgoing EM energy flux was made by recording all field components at the same surfaces used to identify outgoing hot electrons (blue dashed lines in figure 3.7). The offsetting of these surfaces from the simulation boundaries reduces the likelihood of boundary artefacts affecting the recorded data. A high sampling frequency was chosen ( $\omega = 8\omega_0$ , where  $\omega_0$  is the laser frequency) so that the laser frequency could be resolved. This allows the outgoing EM flux to be examined spectrally and ensures that the outgoing energy calculated is accurate.

Scattered light generated by instabilities falls into different frequency bands. SRS generates downshifted scattered light with frequency  $\omega_s$  between  $\omega_0/2$  and  $\omega_0$ , with  $\omega_s(n_e)$  in the limit of  $T_e = 0$  given by  $\omega_s \simeq \omega_0(1 - \sqrt{n_e/n_{cr}})$  for backscatter (the downshift increases with  $T_e$ ). Since these simulations do not include a plasma bulk flow, SBS produces backscattered light with a slight downshift relative to the laser of  $\omega_s \simeq \omega_0(1 - 2c_s/c\sqrt{1 - n_e/n_{cr}})$  where  $c_s$  is the ion sound speed. Since this downshift is very small ( $c_s/c < 0.01$ ) in all cases considered here, it is difficult to distinguish SBS-generated light from laser light purely by examining the frequency content of the diagnostic output. TPD does not directly produce scattered light but indirectly, via various secondary processes, produces two characteristic ‘doublet’ features, one about  $\omega_0/2$  and the other about  $3\omega_0/2$  (see for example [Seka et al., 2009]). TPD-scattered light was not considered in the analysis performed in this thesis, however TPD was examined in detail via other diagnostics.

It was desirable to separate out the contributions from SRS, SBS and the laser itself, so the following process was performed. First a bandpass filter about  $\omega_0$ , implemented as a windowed-sinc finite impulse response (FIR) filter, was applied to all EM field components to isolate the laser (and SBS) frequency. The original dataset minus this component gives the component due to SRS. The filtered EM fields were then used to calculate the energy (Poynting) flux in the direction normal to each boundary. The Poynting vector is defined  $\mathbf{P} = 1/\mu_0 \mathbf{E} \times \mathbf{B}$  so the flux leaving in the  $\hat{\mathbf{x}}$  and  $\hat{\mathbf{y}}$  directions is given by

$$\begin{aligned} P_x &= \mathbf{P} \cdot \hat{\mathbf{x}} = \frac{1}{\mu_0} (E_y B_z - E_z B_y), \\ P_y &= \mathbf{P} \cdot \hat{\mathbf{y}} = \frac{1}{\mu_0} (E_z B_x - E_x B_z). \end{aligned}$$

SRS and SBS produce scattered light with the same polarisation as the laser so in each of  $P_x$  and  $P_y$  one of the terms is negligible depending on laser polarisation.

Considering for example backscattered light at frequency  $\omega_s$  with electric and magnetic field components

$$\begin{aligned} E_y &= E_s(t) \cos(-k_s x - \omega_s t), \\ B_z &= -E_s(t) \frac{k_s}{\omega_s} \cos(-k_s x - \omega_s t), \end{aligned}$$

its Poynting flux at the rear boundary is then given by

$$P_x = -\frac{1}{2\mu_0} E_{y,s}(t)^2 (1 + \cos(2\omega_s t)).$$

Here  $E_s(t)$  represents a slow variation of the light's amplitude and is the quantity we wish to calculate. The high frequency oscillation at  $2\omega_s$  is not of interest, so this along with any other high frequency components is filtered out by applying a low-pass filter with a cutoff at the simulation's minimum plasma frequency. The resulting signals are then integrated spatially over each boundary. This results in two energy fluxes for each boundary, one due to light at the laser frequency and the other due to SRS.

These various energy fluxes may be given different interpretations. Beginning with the fluxes at the laser frequency, the flux measured at the laser boundary contains a component due to the laser itself which is precisely known. Subtracting this known component means that the remainder must be the result of backscatter due to SBS. Moving to the boundary on the opposite side of the domain, it was assumed that light at the laser frequency exiting here was purely due to the laser and that there was no forward Brillouin scattered light. This transmitted laser fraction is an important quantity in assessing the efficiency of the various absorption mechanisms.

For the fluxes due to SRS, the flux exiting in the forwards or backwards direction is usually assumed to be purely due to forward or backscatter SRS respectively. The transverse fluxes are somewhat more ambiguous, as the simulation domain is frequently very long and narrow. Therefore SRS scattered light with a small angle from perfect backscatter could be detected at the transverse boundaries and be interpreted as sidescatter. Furthermore, where periodic boundaries are used, any sidescattered light ultimately exits via either the front or rear boundaries and would be interpreted as forward/back scatter. Analysis of diagnostic data from the

bulk plasma is used to resolve these ambiguities.

### 3.3.2 Bulk Plasma Diagnostics

#### Field Snapshots

One of the main diagnostics of instability activity are snapshots taken at regular time intervals of the fields across the entire domain. Unfortunately these are costly in terms of disk space and so it was not feasible to record these at a frequency that would allow resolution of all expected features of the frequency spectrum. Instead the sampling frequency was chosen so that instability growth could be resolved, with typical growth rates of up to  $\gamma_0 \sim 0.005\omega_0$  expected. Samples were therefore taken every 0.01ps (Nyquist frequency  $\sim 0.06\omega_0$ ).

While (temporal) spectral information is therefore severely limited, the spatial information contained in the snapshots in many cases allows the waves produced by different instabilities to be distinguished. To examine electrostatic (ES) waves, the  $E_x$  component of the EM field is typically used since there should be no contribution from the laser. However, as is evident from the Poynting flux expressions above, there may be contributions from EM waves propagating at an angle oblique to the laser (e.g. from SRS sidescatter). Furthermore many of the electrostatic waves examined here, notably those due to TPD, have polarisation at a significant angle relative to the laser propagation axis and so the  $E_x$  field component only captures a fraction of the total wave energy. For electromagnetic waves, the  $B_z$  field component is used. Here the fraction of energy measured is unaffected by the waves' direction of propagation and cannot include electrostatic components, though now includes the laser which may make smaller signals difficult to discern.

Three main approaches are taken to analyse these individual field components, producing distinct and complementary information about the instabilities present. First, taking the Fourier transform of both spatial dimensions allows most instabilities to be distinguished. For example examining the electrostatic field component isolates the various EPWs from TPD and SRS back/forward scatter due to their differing directions of propagation. Second, taking the Fourier transform along only the transverse ( $\hat{y}$ ) direction allows the location of the various instabilities to be determined along the laser axis. Since density in our simulations varies along this axis only, this is typically the direction in which important variation is seen. However, the magnitude of the TPD wavevector's  $k_y$  component is the same for both daughter EPWs and so forwards and backwards propagating waves cannot be distinguished in this way. To separate these, the  $k_x$  component should be examined,

however it is desirable to keep some of the spatial resolution in this direction. Therefore the final method of examining this dataset is to perform a wavelet transform along this direction. Similar analysis could be performed with a short-time Fourier transform (STFT) where the  $x$  direction is divided up into segments which are each individually Fourier transformed.

### Field Strip

Due to the limited sampling frequency and hence spectral resolution of the above dataset, another diagnostic was added to attempt to mitigate this. Here field data from a strip of cells along  $y = 0$  (red dashed line in figure 3.7) is recorded with the same sampling frequency as the reflectivity diagnostic. This data has several important uses. Firstly as with the reflectivity diagnostic, by filtering out the laser or scattered light components, the Poynting flux of laser and scattered light can be measured. This data may then be used to identify locations where the laser is being absorbed or scattered. In addition by taking the  $\omega - k_x$  spectrum, wave properties can be examined in more detail than the domain snapshots allow. This can, for example, shed light on modification of the dispersion relations via kinetic effects.

### Hot Electrons

This final diagnostic aims to examine the electron distribution function in the bulk domain. As with the outgoing particle flux diagnostic, the particle data itself is recorded at intervals of 0.01ps. Since we are primarily interested in the electrons in the tail, only electrons with a  $x$ -directed momentum greater than some threshold  $p_{x,\min}$  are recorded. This threshold was chosen to correspond to the phase velocity of EPWs generated by SRS backscatter at the lowest density in the domain. Since the SRS EPW phase velocity increases with density, this is the lowest phase velocity of SRS-generated electrons possible within the domain. This choice has a clear deficiency in that it neglects hot electron generation at large angles relative to the laser. Information about this component of the distribution function can be examined through the outgoing particle fluxes.

## Chapter 4

# Effect of Ion Waves on TPD Linear Growth

The two-plasmon decay (TPD) instability is saturated as a result of a number of nonlinear effects. Understanding these saturation mechanisms and more generally how they affect the saturation state of the instability is important as this determines how detrimental TPD will be to laser fusion experiments. One mechanism that has frequently been found important in previous numerical studies is the ponderomotive driving of ion density perturbations by the daughter electron-plasma waves (EPWs). In early simulations of TPD in very short scale-length plasmas [Langdon et al., 1979], these were found to cause saturation by scattering EPWs to modes with higher  $|\mathbf{k}|$  that are more strongly damped. This in effect increases the damping rate of the original EPWs. More recently, in simulations representative of direct-drive experiments on the 60-beam OMEGA laser [Yan et al., 2010], transverse density perturbations were instead found to directly prevent TPD growth. It was stated that above some threshold perturbation amplitude the TPD growth rate vanishes. Unfortunately however, while this threshold had been calculated for specific cases, the formulae used for the calculation were not given.

In this chapter the effect of density perturbations on TPD growth is revisited. We begin by deriving the coupled equations that can be used to treat the effect of any density perturbation. These are then applied to two cases. In the first case the perturbations have a wavenumber that is perpendicular to the laser wavenumber; these are the transverse density perturbations of [Yan et al., 2010]. A simple expression is derived for the threshold density perturbation that compares favourably with the values in that prior work. In the second case the effect of density perturbations with an ‘oblique’ wavenumber is considered. These have not previously been

described in the literature and are found to act in a similar way to the transverse perturbations in inhibiting TPD growth, however also break its transverse symmetry. Since these IAW modes are observed in the simulations of later chapters, it is proposed that the resulting asymmetric growth can explain the asymmetric EPW amplitudes found in the simulations.

## 4.1 Derivation of The Coupled Equations

Following [Liu and Rosenbluth, 1976], a fluid model is assumed for the electrons and the ion response is neglected. A coherent EM wave is incident on the plasma and has a fixed electric field given by

$$\mathbf{E} = \frac{\hat{\mathbf{y}}}{2} \left[ E_0 e^{i(k_0 x - \omega_0 t)} + E_0^* e^{-i(k_0 x - \omega_0 t)} \right]. \quad (4.1)$$

This produces an electron quiver velocity  $\mathbf{v}_0$

$$\mathbf{v}_0 = \frac{\hat{\mathbf{y}}}{2} \left[ v_{\text{os}} e^{i(k_0 x - \omega_0 t)} + v_{\text{os}}^* e^{-i(k_0 x - \omega_0 t)} \right] \quad (4.2)$$

where  $v_{\text{os}} \equiv -eE_0/(im_e\omega_0)$ . The electron velocity is split to give  $\mathbf{v}_e = \mathbf{v}_0(\mathbf{r}, t) + \mathbf{v}_1(\mathbf{r}, t)$  where  $\mathbf{v}_1$  is a small perturbation. Finally, this is written as a velocity potential  $\mathbf{v}_1 \equiv \nabla\psi$ .

A homogeneous background plasma density  $n_0$  is assumed. Inhomogeneity could also be introduced as in [Liu and Rosenbluth, 1976], however this would complicate the analysis significantly. The electron density is then also split so that  $n_e(\mathbf{r}, t) = n_0 + n_1(\mathbf{r}, t) + n_i(\mathbf{r}, t)$ , where  $n_1$  is a small perturbation that will include the EPW response and  $n_i$  is a fixed density perturbation due to transverse ion density fluctuations. At this point  $n_i$  is considered large in order to keep the resulting coupling terms, and is given the explicit form

$$n_i = \frac{1}{2} \left[ \delta n e^{i(\mathbf{k}_i \cdot \mathbf{r} - \omega_i t)} + \delta n^* e^{-i(\mathbf{k}_i \cdot \mathbf{r} - \omega_i t)} \right]. \quad (4.3)$$

The electron continuity and momentum equations now become

$$\frac{\partial n_1}{\partial t} + (n_0 + n_i) \nabla^2 \psi + \nabla n_i \cdot \nabla \psi = -\mathbf{v}_0 \cdot \nabla (n_1 + n_i), \quad (4.4)$$

$$\frac{\partial \psi}{\partial t} - \frac{e}{m} \phi + 3v_{\text{th}}^2 \frac{n_1 + n_i}{n_0} = -\mathbf{v}_0 \cdot \nabla \psi, \quad (4.5)$$

and since the waves of interest are electrostatic only Poisson's equation is required

$$\nabla^2 \phi = \frac{e}{\varepsilon_0} n_1.$$

To calculate the linear growth rates these are first Fourier transformed using the convention

$$\hat{f}(\mathbf{k}, \omega) = \iint_{\mathbb{R}^3} f(\mathbf{r}, t) e^{-i(\mathbf{k} \cdot \mathbf{r} - \omega t)} d\mathbf{r} dt, \quad (4.6)$$

so that

$$\begin{aligned} i\omega \hat{n}_1 + n_0 |\mathbf{k}|^2 \hat{\psi} + \frac{1}{2} K^- \delta n \hat{\psi}(\mathbf{k} - \mathbf{k}_i, \omega - \omega_i) + \frac{1}{2} K^+ \delta n^* \hat{\psi}(\mathbf{k} + \mathbf{k}_i, \omega + \omega_i) \\ = \frac{ik_y}{2} [v_{\text{os}} \hat{n}_1(\mathbf{k}_-, \omega_-) + v_{\text{os}}^* \hat{n}_1(\mathbf{k}_+, \omega_+)], \end{aligned} \quad (4.7)$$

$$i\omega \hat{\psi} - \frac{\omega_{\text{ek}}^2}{|\mathbf{k}|^2} \frac{\hat{n}_1}{n_0} = \frac{ik_y}{2} [v_{\text{os}} \hat{\psi}(\mathbf{k}_-, \omega_-) + v_{\text{os}}^* \hat{\psi}(\mathbf{k}_+, \omega_+)]. \quad (4.8)$$

Here Poisson's equation has been used to eliminate  $\phi$  and the non-resonant  $\mathbf{v}_0 \cdot \nabla n_i$  and  $3v_{\text{th}}^2 n_i/n_0$  terms are neglected. For brevity we have defined  $\mathbf{k}_{\pm} \equiv \mathbf{k} \pm \mathbf{k}_0$ ,  $\omega_{\pm} \equiv \omega \pm \omega_0$ ,  $\omega_{\text{ek}}^2 \equiv \omega_{\text{pe}}^2 + 3v_{\text{th}}^2 |\mathbf{k}|^2$ , and

$$K^{\pm} \equiv \mp \mathbf{k}_i \cdot (\mathbf{k} \pm \mathbf{k}_i) + |\mathbf{k} \pm \mathbf{k}_i|^2.$$

Following [Liu and Rosenbluth, 1976] it is assumed that  $\omega \simeq \omega_{\text{pe}}$  and  $\omega_0 \simeq 2\omega_{\text{pe}}$ , meaning that the only Fourier amplitudes that are important are those at  $\omega$  or  $\omega_-$ . In addition  $v_{\text{th}}^2/c^2$ ,  $k_y v_{\text{os}}/\omega_0$  and  $\delta n/n_0$  are small so that terms involving products of them may be neglected [Simon, 1983]. To proceed equation 4.7 is repeatedly substituted into equation 4.8 to eliminate  $\hat{n}_1$ , removing any small terms at each step. A second equation is also obtained by performing the same procedure, this time beginning with equation 4.8 shifted by replacing  $\omega$  with  $\omega_-$  and  $\mathbf{k}$  with  $\mathbf{k}_-$ . This results in the following coupled equations:



$$\begin{aligned}
(\omega^2 - \omega_{\text{ek}}^2) \hat{\psi} = & \frac{\omega_{\text{ek}}^2}{2|\mathbf{k}|^2} \left[ K^- \frac{\delta n}{n_0} \hat{\psi}(\mathbf{k} - \mathbf{k}_i, \omega - \omega_i) + K^+ \frac{\delta n^*}{n_0} \hat{\psi}(\mathbf{k} + \mathbf{k}_i, \omega + \omega_i) \right] \\
& + \frac{k_y v_{\text{os}} \omega}{2} \left[ 1 + \frac{|\mathbf{k}_-|^2}{|\mathbf{k}|^2} \frac{\omega_{\text{ek}}^2}{\omega \omega_-} \right] \hat{\psi}_-,
\end{aligned} \tag{4.9}$$

$$\begin{aligned}
(\omega_-^2 - \omega_{\text{ek},-}^2) \hat{\psi}_- = & \frac{\omega_{\text{ek},-}^2}{2|\mathbf{k}_-|^2} \left[ K_-^- \frac{\delta n}{n_0} \hat{\psi}(\mathbf{k}_- - \mathbf{k}_i, \omega_- - \omega_i) + K_-^+ \frac{\delta n^*}{n_0} \hat{\psi}(\mathbf{k}_- + \mathbf{k}_i, \omega_- + \omega_i) \right] \\
& + \frac{k_y v_{\text{os}}^* \omega_-}{2} \left[ 1 + \frac{|\mathbf{k}|^2}{|\mathbf{k}_-|^2} \frac{\omega_{\text{ek},-}^2}{\omega \omega_-} \right] \hat{\psi},
\end{aligned} \tag{4.10}$$

where  $\hat{\psi}_- \equiv \hat{\psi}(\mathbf{k}_-, \omega_-)$ ,  $\omega_{\text{ek},-} \equiv \omega_{\text{ek}}(\mathbf{k}_-)$  and  $K_{\pm}^{\pm} \equiv K^{\pm}(\mathbf{k}_-)$  have been defined.  $\hat{\psi}$  and  $\hat{\psi}_-$  are the Fourier amplitudes of the two TPD daughter EPWs, and correspond to propagating waves with  $k_y$  (and for maximum growth  $k_x$ ) of opposite sign. Note that since  $\omega_-$  is negative, the wave represented by  $\hat{\psi}_-$  would more conventionally be described by a frequency  $-\omega_-$  and wavenumber  $-\mathbf{k}_-$ .

If no background density perturbation is included ( $|\delta n| = 0$ ) and the laser amplitude is also set to zero ( $|v_{\text{os}}| = 0$ ), the equations are no longer coupled and each reduce to the dispersion relation of an EPW. Keeping  $|\delta n| = 0$  but making the laser amplitude non-zero, the coupled equations can be solved to produce a modified dispersion relation that may be used to calculate the homogeneous TPD growth rate. Note also that in this dispersion relation  $k_y$  always appears in even powers, so the sign of  $k_y$  has no effect on growth. This means that for every pair of growing TPD waves  $\hat{\psi}(\mathbf{k}), \hat{\psi}_-(\mathbf{k})$ , an additional symmetric pair of waves will grow at the same rate with  $k'_y = -k_y$ .

If the background density perturbation is instead retained, coupling can now be induced with a second pair of TPD EPWs. Since ion density perturbations are limited to a frequency comparable to the ion-acoustic wave frequency ( $\omega_i \simeq \omega_{\text{IAW}} \lesssim 5 \times 10^{-3} \omega_0$ ), they may only couple pairs of EPWs with a small frequency difference. Furthermore, the EPWs would not be able to effectively drive a mode with a large frequency shift relative to the IAW dispersion relation. The possible pairings allowed by this restriction on  $\omega_i$  will be considered later, however for the moment it is assumed that  $\omega_i$  can take an arbitrary value so as to develop the general equations. In particular, two additional equations are required to treat the Fourier amplitudes coupled by the density perturbation. These are assumed to also satisfy the TPD frequency and matching conditions, with the forward-propagating wave

having Fourier amplitude  $\hat{\psi}(\omega + \omega_i, \mathbf{k} + \mathbf{k}_i)$ . It is not possible for a third TPD pair to be coupled with forward-propagating wave amplitude at  $\hat{\psi}(\omega - \omega_i, \mathbf{k} - \mathbf{k}_i)$ . To find the two further equations required the same procedure is followed as before, but with  $\omega$  and  $\mathbf{k}$  shifted to the respective values of the new EPWs. The full system of equations becomes

$$\left(\frac{\omega^2 - \omega_{\text{ek}}^2}{\omega_{\text{pe}}^2}\right) \hat{\psi} = Q \frac{\delta n^*}{n_0} \hat{\psi}^\dagger + \frac{k_y v_{\text{os}}}{\omega_{\text{pe}}} P \hat{\psi}_-, \quad (4.11)$$

$$\left(\frac{\omega_-^2 - \omega_{\text{ek},-}^2}{\omega_{\text{pe}}^2}\right) \hat{\psi}_- = Q_- \frac{\delta n^*}{n_0} \hat{\psi}_-^\dagger + \frac{k_y v_{\text{os}}^*}{\omega_{\text{pe}}} P_- \hat{\psi}, \quad (4.12)$$

$$\left(\frac{\omega^\dagger{}^2 - \omega_{\text{ek}}^{\dagger 2}}{\omega_{\text{pe}}^2}\right) \hat{\psi}^\dagger = Q^\dagger \frac{\delta n}{n_0} \hat{\psi} + \frac{k_y^\dagger v_{\text{os}}}{\omega_{\text{pe}}} P^\dagger \hat{\psi}_-^\dagger, \quad (4.13)$$

$$\left(\frac{\omega_-^\dagger{}^2 - \omega_{\text{ek},-}^{\dagger 2}}{\omega_{\text{pe}}^2}\right) \hat{\psi}_-^\dagger = Q_-^\dagger \frac{\delta n}{n_0} \hat{\psi}_- + \frac{k_y^\dagger v_{\text{os}}^*}{\omega_{\text{pe}}} P_-^\dagger \hat{\psi}^\dagger. \quad (4.14)$$

Here the  $X^\dagger$  notation has been introduced to indicate that the frequency and wavenumbers used in quantity  $X$  are shifted by  $\omega_i$  and  $\mathbf{k}_i$ ; for example  $\mathbf{k}^\dagger \equiv \mathbf{k} + \mathbf{k}_i$ . Deviating slightly from this convention, the  $P$ ,  $P_-$ ,  $Q$  and  $Q^\dagger$  factors are defined

$$\begin{aligned} P &\equiv \frac{1}{2} \left[ \frac{|\mathbf{k}|^2 - |\mathbf{k}_-|^2}{|\mathbf{k}|^2} \right], & Q &\equiv \frac{1}{2} \frac{\mathbf{k}^\dagger \cdot \mathbf{k}}{|\mathbf{k}|^2}, \\ P_- &\equiv \frac{1}{2} \left[ \frac{|\mathbf{k}|^2 - |\mathbf{k}_-|^2}{|\mathbf{k}_-|^2} \right], & Q^\dagger &\equiv \frac{1}{2} \frac{\mathbf{k}^\dagger \cdot \mathbf{k}}{|\mathbf{k}^\dagger|^2}, \end{aligned}$$

with the ‘ $\dagger$ ’ superscript and ‘ $-$ ’ subscript and otherwise having their usual meaning when applied to  $P, P_-$  and  $Q, Q^\dagger$  respectively. Additionally, coupling terms on the right hand side have been simplified by approximating  $\omega_{\text{ek}}$  and  $\omega$  as  $\omega_{\text{pe}}$  and using  $\omega_0 \simeq 2\omega_{\text{pe}}$ . It has been verified numerically that this has negligible effect on the accuracy of the solution.

To produce the dispersion relation, the coefficients of the Fourier amplitudes are packed into a  $4 \times 4$  matrix to produce a linear equation of form

$$\mathbf{A} \mathbf{x} = \mathbf{0},$$

with

$$\mathbf{x} = \begin{bmatrix} \hat{\psi} & \hat{\psi}_- & \hat{\psi}^\dagger & \hat{\psi}_-^\dagger \end{bmatrix}^{\mathbf{T}}.$$

Then as usual we are interested in the non-trivial solution such that  $\det \mathbf{A} = 0$ . Using the full system above, an 8<sup>th</sup> order polynomial in  $\omega$  is obtained, which may be solved numerically using standard techniques. The numerical solution is used to produce the plotted growth rates shown later in this section.

In order to instead obtain simple expressions for the growth rates, further approximations must be made. The left hand side of the system of equations above may be simplified by observing that the instability does not significantly shift the EPW frequencies and assuming that  $|\text{Im}(\omega)/\text{Re}(\omega)| \ll 1$ . Provided the matching conditions are satisfied and introducing a transformed variable  $\gamma = -i(\omega - \omega_{\text{ek}})$  means that  $\omega^2 - \omega_{\text{ek}}^2 \simeq 2i\omega_{\text{ek}}\gamma$  and  $\omega_-^2 - \omega_{\text{ek},-}^2 \simeq -2i\omega_{\text{ek},-}\gamma$ . This is an excellent approximation for non-relativistic laser intensities. Additionally, the remaining  $\omega_{\text{ek}}$  and  $\omega_{\text{ek},-}$  factors can be replaced by  $\omega_0 - \omega_{\text{pe}}$  and  $\omega_{\text{pe}}$  respectively<sup>1</sup>, which introduces a small error in the growth rates at lower densities or a larger error if  $\omega_{\text{pe}}$  is used for both.

Now applying all of these approximations and calculating the determinant results in a 4<sup>th</sup> order polynomial in  $\gamma$ :

$$\begin{aligned} \gamma^4 - \frac{1}{4} \left( v_{\text{os}}^2 (k_y^2 P P_- + k_y^{\dagger 2} P^\dagger P_-^\dagger) - \frac{\delta n^2}{n_0^2} \omega_{\text{pe}}^2 (Q Q^\dagger + Q_- Q_-^\dagger) \right) \gamma^2 \\ + \frac{1}{16} \left( v_{\text{os}}^2 k_y k_y^\dagger P^\dagger P_- - \frac{\delta n^2}{n_0^2} \omega_{\text{pe}}^2 Q^\dagger Q_- \right) \left( v_{\text{os}}^2 k_y k_y^\dagger P P_-^\dagger - \frac{\delta n^2}{n_0^2} \omega_{\text{pe}}^2 Q Q_-^\dagger \right) = 0. \end{aligned} \quad (4.15)$$

where  $\delta n$  and  $v_{\text{os}}$  are now taken to be the modulus of the complex amplitudes. While this is a quartic equation, its form is quadratic so that two of the roots are given by  $\gamma_3 = -\gamma_1$  and  $\gamma_4 = -\gamma_2$  and are redundant. The four roots are in general complex, with the growth rate given by  $\text{Re}(\gamma)$  and frequency shift by  $\Delta\omega = \text{Im}(\gamma)$ .

As discussed previously, only small  $\omega_i$  is supported by the density fluctuations, which limits the set of possible couplings to those where the two pairs of TPD EPWs have similar frequency. In the following sections two potential configurations are examined. These are of particular interest since they are observed in the simulations presented later. Other configurations are possible, particularly when considering a full three-dimensional system, but are not treated here.

---

<sup>1</sup> $\omega_{\text{pe}}$  is a better approximation for the backwards-propagating EPW as  $|\mathbf{k}_-| < |\mathbf{k}|$  so its frequency needs a smaller thermal correction. For the forwards-propagating wave this correction is given by  $\omega_0 - \omega$  if the matching conditions are satisfied. In the analysis here swapping the two would make no difference due to the symmetry of the equations.

## 4.2 Transverse Density Perturbations ( $\mathbf{k}_i = 2k_y\hat{\mathbf{y}}$ )

The first coupling examined is between symmetric sets of TPD waves. This configuration is shown in the left panel of figure 4.1. In this case the waves coupled by the density fluctuations have exactly equal frequencies implying a static density fluctuation ( $\omega_i = 0$ ). The wave-vector of the density fluctuation is therefore given by  $\mathbf{k}_i = -2k_y\hat{\mathbf{y}}$ . This choice means that  $P = P^\dagger$ ,  $P_- = P_-^\dagger$ , and  $Q = Q^\dagger$ , with the latter given by

$$Q \equiv \frac{1}{2} \frac{k_x^2 - k_y^2}{|\mathbf{k}|^2}.$$

These symmetries considerably simplify the polynomial in the growth rate  $\gamma$ , which now reduces to

$$\begin{aligned} \gamma^4 - \frac{1}{4} \left( 2k_y^2 v_{\text{os}}^2 P P_- - \frac{\delta n^2}{n_0^2} \omega_{\text{pe}}^2 (Q^2 + Q_-^2) \right) \gamma^2 \\ + \frac{1}{16} \left( k_y^2 v_{\text{os}}^2 P P_- + \frac{\delta n^2}{n_0^2} \omega_{\text{pe}}^2 Q Q_- \right)^2 = 0. \end{aligned} \quad (4.16)$$

Further progress can be made by making an additional specialisation. In the absence of damping, TPD undergoes maximum growth when the wavenumbers satisfy the relation  $(k_x - k_0/2)^2 = k_y^2 + k_0^2/4$ . Choosing those wavenumbers means that  $Q = -Q_-$  so that the equation becomes

$$\gamma^4 - \frac{1}{2} \left( k_y^2 v_{\text{os}}^2 P P_- - \frac{\delta n^2}{n_0^2} \omega_{\text{pe}}^2 Q^2 \right) \gamma^2 + \frac{1}{16} \left( k_y^2 v_{\text{os}}^2 P P_- - \frac{\delta n^2}{n_0^2} \omega_{\text{pe}}^2 Q^2 \right)^2 = 0. \quad (4.17)$$

The growth rate is then given by

$$\gamma = \frac{1}{2} \sqrt{k_y^2 v_{\text{os}}^2 P P_- - \frac{\delta n^2}{n_0^2} \omega_{\text{pe}}^2 Q^2}, \quad (4.18)$$

so that the threshold density perturbation is

$$\frac{\delta n_{\text{thr}}}{n_0} = |k_y| \frac{v_{\text{os}}}{\omega_{\text{pe}}} \sqrt{\frac{P P_-}{Q^2}}. \quad (4.19)$$

We can verify that these results are consistent with those of [Yan et al. \[2010\]](#) by calculating the threshold density perturbation for the two cases described there. In their ‘small-scale’ case the relevant parameters are  $I = 2 \times 10^{15}$ ,  $T_e = 1\text{keV}$

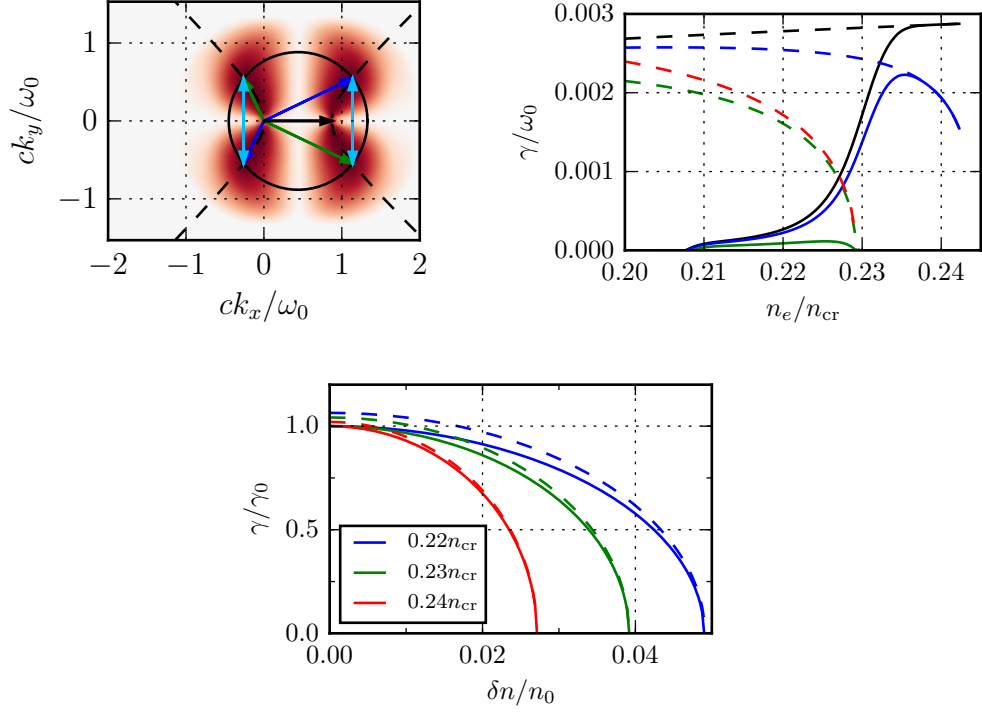


Figure 4.1: **Upper left:** Wavenumber matching of transverse density perturbations. Laser wavenumber shown as black arrow, while black solid curve marks wave-vectors where TPD matching conditions are satisfied at  $n_e = 0.22n_{cr}$  and  $T_e = 3.5\text{keV}$ . TPD growth rates for a homogeneous, unperturbed background density are shown on the colour scale for varying density, with maximum growth occurring along dashed lines. Two symmetric pairs of TPD daughter waves are indicated by blue and green arrows. The two forward (or backward) propagating waves have the same frequency and can be coupled by a density perturbation with  $\mathbf{k}_i = \pm 2k_y\hat{\mathbf{y}}$  (cyan). **Upper right:** growth as a function of background density  $n_e$  for TPD maximum growth wavenumbers (dashed lines in left panel), with density perturbation of  $\delta n/n_e = 0$  (black), 0.02 (blue) and 0.04 (green). Dashed lines neglect Landau damping, solid lines include it. Approximate solution for  $\delta n/n_e = 0.04$  shown in red. **Lower centre:** Growth rate as a function of transverse density perturbation amplitude for TPD at electron densities indicated. Solid lines show numerical solution while the dashed lines use equation 4.18. Each curve's growth rates are normalised to the numerically calculated  $\gamma$  with no density perturbation.

and  $k_y \simeq 1.2\omega_0/c$  for the largest IAWs. Assuming that this acts on the TPD pairs with  $k_y \simeq 0.6\omega_0/c$  gives a plasma density of  $n \simeq 0.244n_{\text{cr}}$ . Equation 4.19 then predicts a threshold of  $0.0098n_{\text{cr}}$  while  $0.0095n_{\text{cr}}$  is predicted in the paper and the saturation amplitude in the simulation is approximately  $0.013n_{\text{cr}}$ . For the second case the parameters are  $I = 1 \times 10^{15} \text{Wcm}^{-2}$ ,  $T_e = 2 \text{keV}$  and  $k_y \simeq 0.35\omega_0/c$  for the TPD waves (so density of around  $n_e \simeq 0.246n_{\text{cr}}$ ). We then predict the threshold to be  $0.0053n_{\text{cr}}$ , which compares favourably with the value given of  $0.005n_{\text{cr}}$  and the measured value of  $0.003n_{\text{cr}}$ .

To illustrate the effect of the transverse density perturbations on growth, the right hand panel of figure 4.1 shows the numerically calculated growth rate plotted as a function of background plasma density for  $T_e = 3.5 \text{keV}$  and  $I = 2 \times 10^{15} \text{Wcm}^{-2}$ . The black, blue and green lines are calculated with  $\delta n/n_0$  equal to 0.0, 0.02 and 0.04, and growth rates are calculated with and without damping (solid and dashed lines respectively). The red dashed line is the approximate solution given by equation 4.18 for the damped  $\delta n = 0.04n_0$  case, and is in good agreement with the numerical solution. Two effects are of note here. First,  $\delta n$  produces a larger reduction in growth at high background density. This is because  $Q^2$  increases rapidly as  $n_{\text{cr}}/4$  is approached from below. At lower densities  $Q^2$  decays slowly to zero and reduces the effectiveness of the density perturbations in lowering growth. Secondly, since  $|\delta n|$  is squared in equation 4.18 there is a sharp transition between it having little effect on TPD and completely suppressing it. This is also apparent in the lower panel of figure 4.1 where the growth rates at three different densities are shown as a function of density perturbation amplitude for the numerical (solid) and approximate (dashed) solutions. This latter plot also confirms that while there is a small error in the value of the growth rate, the approximate solution preserves the location of the threshold.

### 4.3 Oblique Density Perturbations

Another way in which TPD EPWs can be coupled is shown in figure 4.2. Here two pairs of waves are chosen with wavevectors (blue and green arrows) on the matching curve (black circle) with a small wavevector difference. This small wavenumber difference means that the frequency separation of the waves will also be small and therefore they can be coupled by, and drive effectively, IAWs with the wavevectors indicated by the cyan arrows. Furthermore, the fastest growing TPD EPWs (dashed black lines) will be coupled by IAWs which have a wavenumber that is roughly perpendicular to the EPW wavenumbers. These are oblique to the laser and hence will be referred to as ‘oblique’ density perturbations. Unlike the transverse density

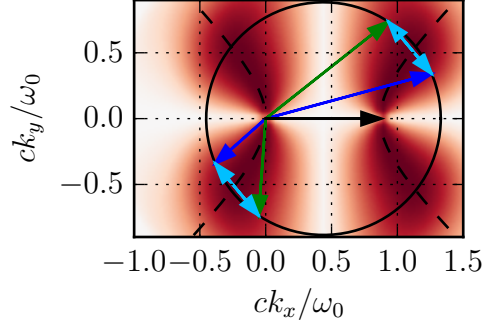


Figure 4.2: Wavenumber matching of oblique density modes. Laser wavenumber shown as black arrow, while black solid curve marks wave-vectors where TPD matching conditions are satisfied at  $n_e = 0.22n_{\text{cr}}$  and  $T_e = 3.5\text{keV}$ . TPD growth rates for a homogeneous, unperturbed background density are shown on the colour scale for varying density, with maximum growth occurring along dashed lines. Two pairs of TPD daughter waves with similar  $k_y$  are indicated by blue and green arrows. The two forward (or backward) propagating waves have similar frequency and can be coupled by a density perturbation with wave vector indicated by cyan arrows.

perturbations described in the previous section, oblique density perturbations have no effect on the symmetric pair of TPD waves (those with  $k_y$  of opposite sign). They therefore allow for the  $k_y$  symmetry of the instability to be broken; this symmetry breaking is a prominent effect in the simulations presented later.

Unfortunately, the lack of symmetry in this case makes proceeding with the analysis somewhat complicated. In principle it should be possible to simplify equation 4.15 by exploiting the fact that the difference of the two EPW wavenumbers is small. Rather than attempting such a scheme, the growth rates are instead discussed here by examining the numerical solution. A further complication is that it is not immediately clear for the oblique case which pairs of TPD EPWs should have the largest growth rates. In the discussion of the transverse density perturbations it was assumed that the EPW wavenumbers leading to maximum growth in the unperturbed case would also have the largest growth rates when  $\delta n$  is included. This assumption will now be verified. Since there are now two waves whose wavenumbers can be chosen there is an additional degree of freedom to explore. To aid in this, the EPW wavenumbers are parameterised in terms of an angle corresponding to their location on the matching curve. This may be defined

$$\tan(\theta) \equiv \frac{k_y}{k_x - \frac{k_0}{2}}. \quad (4.20)$$

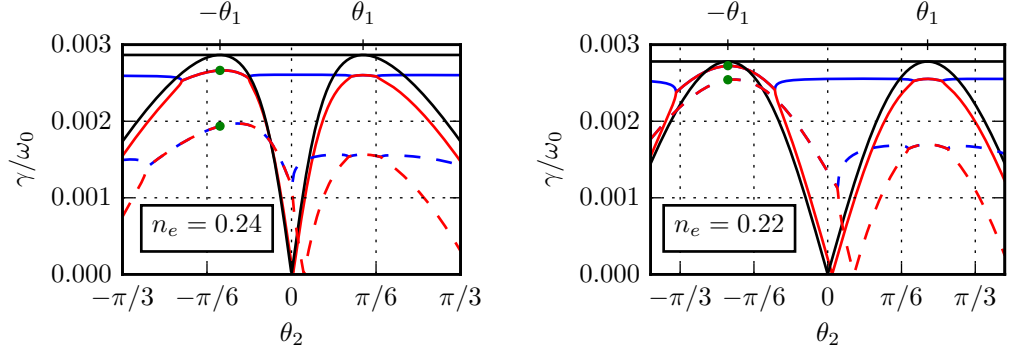


Figure 4.3: Dependence of the TPD growth rate on the location of a second TPD EPW pair coupled by density perturbations, with  $T_e = 3.5\text{keV}$ ,  $I = 2 \times 10^{15}\text{Wcm}^{-2}$  and background density indicated in the figure. The EPW pairs are parameterised by an angle made by one of their wavevectors, defined  $\tan(\theta) \equiv k_y/(k_x - \frac{k_0}{2})$ . Here the first TPD pair is located at the angle marked  $\theta_1$ , which is where peak TPD growth occurs with no density perturbation. Two growth rates are obtained, one for each pair, shown as blue and red curves corresponding to  $\mathbf{k}(\theta_1)$  and  $\mathbf{k}(\theta_2)$  respectively. Density perturbation amplitudes of  $\delta n/n_e = 0$  (black), 0.01 (solid colour) and 0.02 (dashed colour) are used. A green dot marks the growth rates corresponding to transverse density perturbations.

so that the wavenumbers can be calculated as

$$\mathbf{k}(\theta) \equiv \left[ \frac{k_0}{2} + k'(n_e, T_e) \cos(\theta) \right] \hat{\mathbf{x}} + k'(n_e, T_e) \sin(\theta) \hat{\mathbf{y}}. \quad (4.21)$$

Note that  $k'$  also has a slight dependence on  $\theta$  but this may be neglected for  $v_{th} \ll c$ . The two TPD pairs may therefore be chosen by selecting EPWs with two angles,  $\theta_1$  and  $\theta_2$ , with the IAW wavenumber then fixed at  $\mathbf{k}_{IAW} = \mathbf{k}(\theta_2) - \mathbf{k}(\theta_1)$ . The second EPW in each TPD pair has a wavenumber that is determined by the matching conditions, and is therefore at angle  $\theta - \pi$ .

In the transverse density perturbation case, the TPD EPWs were symmetric and so there was a degeneracy in the roots of equation 4.15. This meant that only one growth rate was obtained for both TPD pairs. In the general case however, there may be a separate growth rate for each TPD pair. To begin exploring this parameter space figure 4.3 shows the TPD growth rates, neglecting damping, as a function of  $\theta_2$  with  $\theta_1$  held fixed. The value for  $\theta_1$  is chosen to be the angle where maximum growth occurs for  $\delta n = 0$ . In the left panel the plasma is at  $0.24n_{cr}$ , while for the right panel it is at  $0.22n_{cr}$ . Other parameters are kept fixed (see figure caption for details). The growth rate of each TPD pair is given by the blue and



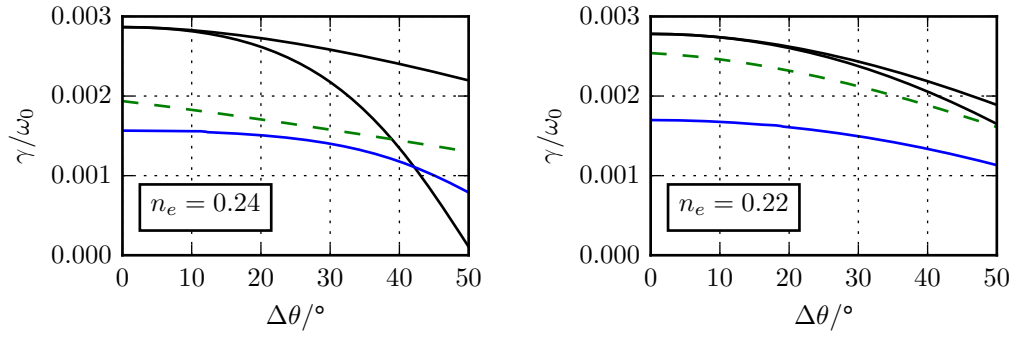


Figure 4.4: Dependence of the TPD growth rate on the separation of two TPD EPW pairs that are coupled by oblique density perturbations, with  $T_e = 3.5\text{keV}$ ,  $I = 2 \times 10^{15}\text{Wcm}^{-2}$  and background density indicated in the figure. The EPW pairs are parameterised by an angle made by one of their wavevectors, defined  $\tan(\theta) \equiv k_y/(k_x - \frac{k_0}{2})$ . Here the wavevectors are symmetrically distributed about a central angle,  $\theta_0$ , which is where peak growth occurs when no density perturbations are included. The two angles are given by  $\theta_1 = \theta_0 - \Delta\theta/2$  and  $\theta_2 = \theta_0 + \Delta\theta/2$  so that their angular separation is  $\Delta\theta$ . The growth rates of the pairs are degenerate and indicated by blue lines for  $\delta n/n_e = 0.02$ . Black lines mark the growth rates at  $\theta_1$  and  $\theta_2$  for  $\delta n = 0$ . Growth rates are also shown for equivalent transverse density perturbations (green dashed lines) where the wavevectors are located at  $\theta_1 = \theta_0 + \Delta\theta/2$  and  $\theta_2 = -\theta_1$ .

red lines, which correspond to  $\theta_1$  and  $\theta_2$  respectively, while the dashed and solid coloured lines show the solution for  $\delta n$  of 0.01 and 0.02. If no  $\delta n$  is included, the TPD pair at  $\theta_1$  is completely decoupled from that at  $\theta_2$  so that its growth rate does not vary at all (black straight line). Conversely the growth rate of the TPD pair at  $\theta_2$  depends entirely on  $\theta_2$  (this is shown by the black curve). Considering small  $\delta n/n_e$  of 0.01 (solid coloured lines), the growth rates for both TPD pairs are close to the unperturbed solutions, but show a slight reduction in growth. As expected, the line corresponding to the TPD pair at  $\theta_1$  is largely independent of  $\theta_2$ , while that at  $\theta_2$  also mostly follows the black curve. When the density perturbation is made larger at 0.02 (dashed coloured lines), there is a greater reduction in growth and a more marked deviation from the unperturbed behaviour. Both TPD pairs now show a strong dependence on the second pair's wavenumbers.

The growth rates in figure 4.3 also display degeneracy. In regions where  $\theta_2 \simeq \pm\theta_1$  the growth rates form a conjugate pair, meaning that the waves have equal growth rates and a frequency shift of opposite sign but equal value. This suggests that the coupling produced by the IAW results in the waves acting as a single parametric instability, which has a lower growth rate than the two uncoupled three-wave instabilities. The regions where  $\theta_2 \simeq \pm\theta_1$  are also the most physically relevant as these are the angles where the frequency difference of the EPWs is small and can therefore drive the required IAWs. When  $\theta_2 \simeq -\theta_1$ , the configuration of the wavenumbers is that of the transverse density perturbations (green dots mark the ‘exact’ transverse case where  $\theta_2 = -\theta_1$ ) while  $\theta_2 \simeq \theta_1$  corresponds to the oblique case. It is interesting that the ‘transverse’ and ‘oblique’ cases behave differently. At both densities shown, the range of  $\theta_2$  where growth rates are degenerate is larger for transverse density perturbations than oblique ones, and the growth rates themselves are larger. These differences suggest that the parametric instability mechanism is more effective for transverse density perturbations and therefore results in a smaller reduction in growth rate. Finally while the transverse density perturbations have a smaller effect on growth at low density, the oblique density perturbations do not appear to depend significantly on plasma density.

Another way of choosing the EPW pairs is shown in figure 4.4. Here the wavenumbers are distributed symmetrically about the angle where maximal growth occurs in the unperturbed case. Labelling this  $\theta_0$ , the wavenumber angles are given by  $\theta_1 = \theta_0 - \Delta\theta/2$  and  $\theta_2 = \theta_0 + \Delta\theta/2$  so that their angular separation is  $\Delta\theta$ . This separation is then varied up to  $50^\circ$ ; a larger angular separation would not be expected to lead to driving of large density perturbations. Swapping  $\theta_1$  and  $\theta_2$  by choosing  $\Delta\theta < 0$  produces the same growth rates, as would be expected, and so

only positive  $\Delta\theta$  is shown. Growth rates for a perturbation amplitude of  $0.02n_e$  are shown in blue, again for background densities of  $0.24n_{\text{cr}}$  and  $0.22n_{\text{cr}}$ , and with other parameters the same as figure 4.3. For reference, black curves show the growth rates at  $\theta_1$  and  $\theta_2$  for  $\delta n = 0$ , and the equivalent transverse density perturbation growth rates (with wavenumbers at  $\theta_1 = \theta_0 + \Delta\theta/2$  and  $\theta_2 = -\theta_1$ ) are shown as green dashed lines. Within this value of  $\delta n$  and range of angular separations, both the oblique and transverse density perturbations produce degenerate growth rates. Though not shown here, it is found that a larger  $\delta n$  is required to make the TPD growth rates degenerate at larger angular separations. As before, there is little difference in the curves between the low and high density cases for oblique density perturbations. The principal difference here is a greater reduction in growth at larger separations in the high density case, and is caused by one of the TPD pairs approaching the edge of the quadrant ( $\theta_0$  is smaller for this case so  $\theta_1$  approaches zero at smaller  $\Delta\theta$ ). In contrast, the curves for the transverse density perturbations differ more significantly between the two densities, indicating again that they are more effective at suppressing growth closer to  $n_{\text{cr}}/4$ .

## 4.4 Summary

The above analysis presents a general, but relatively straightforward model for the effect of ion density perturbations on TPD linear growth. Two possible configurations were described, with the IAW wavevector either large ( $\sim 2k_0$ ) and transverse to the laser propagation axis or small ( $\sim k_0/4$ ) and oblique. These cases are therefore simply labelled ‘transverse’ and ‘oblique’. While the former has previously been associated with TPD saturation and analysed both theoretically and numerically [Yan et al., 2010], the theoretical model was not published. The oblique type of density perturbation has not previously been described in the literature, however is found to play an important role in the simulations presented in subsequent chapters.

The model illustrates that both kinds of density perturbation lead to the coupling of previously independent pairs of TPD waves, whose growth rates can become degenerate so that all four EPWs act as a single parametric instability. The coupling also results in a lower growth rate for both pairs of waves, with the reduction increasing with the amplitude of the density perturbation. A threshold density perturbation therefore exists above which TPD growth is suppressed. A simple formula was derived for this threshold in the transverse case, and can be obtained for the oblique case by numerical solution of the general growth rate equation (no. 4.15).

The two types of density perturbation lead to different qualitative behaviour that may help distinguish their effects. Since the transverse density perturbations act on pairs of TPD waves with equal and opposite  $k_y$ , the amplitude reached by both  $k_y$  ‘branches’ will be equal. In contrast since the oblique density perturbations act only on waves in one  $k_y$  ‘branch’, the  $k_y$  symmetry of overall TPD growth may be broken. This asymmetry is observed in the simulations described in the next chapter. Furthermore, it was found that the transverse density perturbations become less effective at suppressing growth at lower plasma density, while in contrast the oblique density perturbations retain their effect at low plasma density.

For the present analysis the model was purposefully kept simple. It would however be of interest to extend it to more complex and physically relevant scenarios. For example, only a single density perturbation mode was included whereas in reality one would expect a broad spectrum of modes to exist. Secondly, the couplings examined were those found to be important to the two-dimensional simulations performed later. More possibilities exist, and may also be of importance. These could be additional pairings of TPD EPWs in the two-dimensional wavevector space, due for example to inhomogeneity, or couplings of waves within a three-dimensional wavevector space. Finally, the ion response was neglected, with the density perturbation having a fixed amplitude and a frequency chosen to match the frequency difference of the two EPW pairs. Including ion dynamics would result in a nonlinear system of equations and so would require a different approach, however could be used to examine the resulting long-term behaviour in a computationally inexpensive manner. This could potentially act as a simple model for the TPD behaviour observed in later chapters. Preliminary work has been performed in this vein by treating the system as a coupled set of ODEs and solving these numerically, however is currently incomplete and so has not been presented here.

## Chapter 5

# Small-scale Simulation

*This chapter contains results submitted for publication in Physics of Plasmas:*

A. G. Seaton & T. D. Arber, “Particle-in-Cell Simulations of Laser-plasma Instabilities in Long Scale-Length Plasmas Relevant to Shock-ignition”

In this chapter results are presented from a simulation of laser-plasma instabilities at shock-ignition intensities relevant to ‘small-scale’ plasma coronas. Here ‘small-scale’ refers to density scale-lengths ( $L_n \equiv (\nabla n_e/n_0)^{-1}$ ) on the order of  $150\mu\text{m}$ , which is typical of experiments at the OMEGA laser. The targets used in these experiments are of a smaller size than required for ignition-relevant designs, which is a simple consequence of the lower drive energy available on OMEGA (30kJ UV). An ignition-scale target would be expected to produce a significantly larger coronal plasma with a scale-length on the order of  $L_n \simeq 600\mu\text{m}$  [Rosenberg et al., 2018]. A simulation with ignition-relevant parameters is examined in the next chapter.

In section 5.1 the simulation setup is first described. The initial conditions are taken from a previous investigation of shock ignition in the small-scale regime [Yan et al., 2014]. A more detailed analysis of the simulation results is performed here than was presented in [Yan et al., 2014]. These are described in several sections, with the first concerning the instabilities’ linear growth and initial saturation (section 5.2). A second section then considers the ‘long-term’ nonlinear behaviour (section 5.3) in which particular focus is given to the effect of ion density perturbations. Notably, the behaviour observed is consistent with the predictions of chapter 4 in that oblique density perturbations lead to asymmetric TPD growth. These observed dynamics were not discussed in [Yan et al., 2014], and this is an aspect of TPD

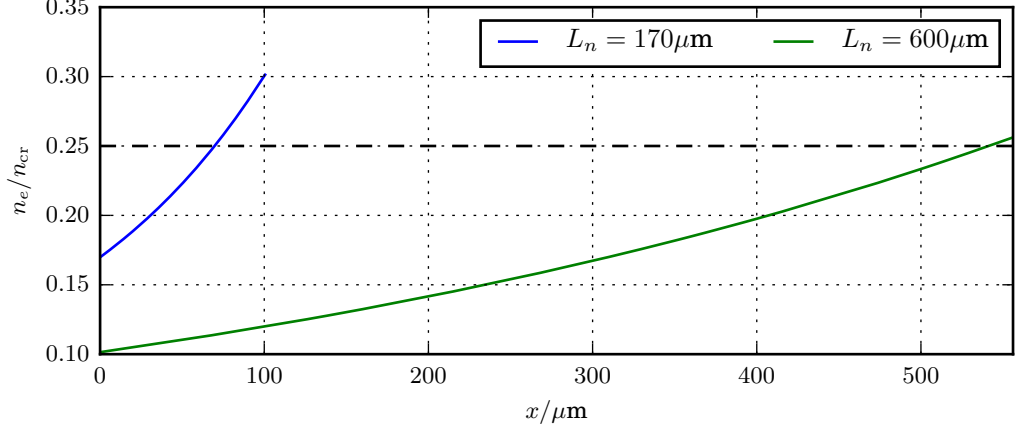


Figure 5.1: Density profiles used for the simulations presented in this and the next chapter. The large-scale profile is purely exponential (see chapter 6) while the small-scale profile, used for the simulation in this chapter, is given in [Yan et al., 2014]. The small-scale profile is a fit to the output of a hydrodynamic simulation of an experiment on the OMEGA laser [Theobald et al., 2012].

behaviour that has not previously been described elsewhere. Hot electron production is then considered in section 5.4. It is found that, contrary to the conclusions of [Yan et al., 2014], hot electrons are predominantly due to TPD. Finally, a summary of these results is given in section 5.5 where they are compared to observations from relevant experiments on the OMEGA laser.

## 5.1 Simulation Setup

As discussed above, the initial conditions chosen for this simulation are taken from [Yan et al., 2014] and match the high-temperature case described there. These parameters represent conditions found in OMEGA experiments with spherical targets [Theobald et al., 2012]. There are several motivations for choosing these parameters. First, they provide us with a ‘base’ scenario to compare larger-scale simulations against. Additionally, while the analysis presented in [Yan et al., 2014] is helpful in illuminating some aspects of the behaviour, it was a short preliminary study and does not provide us with the full dataset required when comparing detailed physics with larger-scale simulations. Finally, the simulation acts as a benchmark of our code against the OSIRIS PIC code, allowing us to ensure that the physics is consistent. While both codes are mature projects that have been extensively tested,

EPOCH has not previously been used for large-scale LPI studies of this kind and so this simulation provided a useful comparison. One important aspect in which the codes differ for these simulations is that the collision module was disabled in all simulations presented in this thesis. In contrast [Yan et al., 2014] use a collision model based on [Nanbu and Yonemura, 1998]. We were unable to use a collision model as the algorithm that was implemented in EPOCH at the time would have required an order of magnitude increase in compute time, which was not available. Having results from an otherwise identical simulation therefore allows us to assess the importance of collisions on the resulting LPI behaviour.

The simulation plasma was composed of fully ionised plastic (CH) with an equal ratio of carbon to hydrogen ions. The electron temperature was spatially uniform at 3.5keV, and the electron-ion temperature ratio was  $T_e/T_i = 2$ . This, along with the plasma composition, results in a high ion-acoustic wave damping rate. In addition the plasma had no initial bulk motion throughout. 128 particles-per-cell were used for electrons and 64 for each ion species. The domain was formed of  $10000 \times 2000$  grid cells and measured  $100 \times 20\mu\text{m}$ . Finally, the simulation was run for 9ps rather than the full 21ps simulated in [Yan et al., 2014].

Density profiles for the simulations presented in this thesis are shown in figure 5.1. Both have spatial dependence similar to  $n \sim \exp(x/L_n)$ . In the small-scale case the profile used was that specified in [Yan et al., 2014], and is based on hydrodynamic simulations of the experiments of [Theobald et al., 2012]. This spans a density range of  $0.17\text{--}0.30n_{\text{cr}}$ .

The front and rear boundaries were thermal for particles and open for fields. Thermal particle boundary conditions are intended to represent a thermal bath of particles in contact with the simulation domain. To accomplish this, particles exiting the domain are replaced by inwards-propagating particles with velocity sampled from a thermal distribution. On the transverse boundaries, periodic boundary conditions were used for both fields and particles. This can be thought of as emulating a much larger transverse extent of plasma, as would be present in an experiment.

The laser had in-plane polarisation. In this polarisation, TPD has its maximum growth rates while the SRS side-scatter growth rate is reduced. The effect of an out-of-plane laser polarisation or alternatively an investigation of the complete problem via a 3D simulation is a subject that should be examined in future work. The laser had a uniform ‘plane-wave’ spatial intensity profile, and an intensity of  $2 \times 10^{15}\text{Wcm}^{-2}$  was used; this is common to all plane wave simulations performed in this thesis. This is a relatively low intensity for shock-ignition, where intensities between  $1\text{--}10 \times 10^{15}\text{Wcm}^{-2}$  are usually encountered. It should be noted however

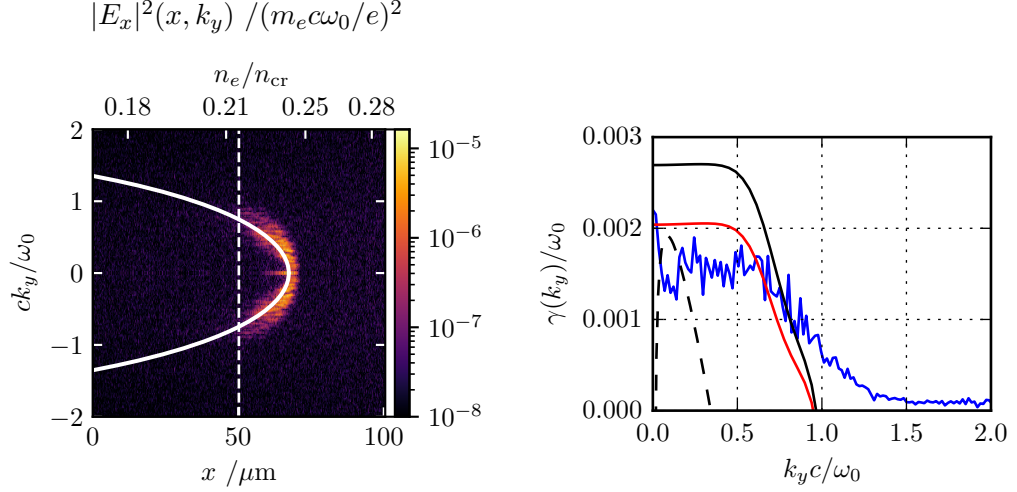


Figure 5.2: **Left:** Instantaneous  $k_y$  energy spectrum of the  $E_x$  field component during initial instability growth at  $t = 2.1\text{ps}$ . The laser wave-vector and  $\nabla n_e$  are parallel to the  $x$  axis while the laser polarisation is along the  $y$  axis. The white curve indicates where maximal linear growth of TPD is expected at each density, while the white dashed line marks TPD Landau cutoff ( $|\mathbf{k}|\lambda_D = 0.3$ ). The feature with small  $k_y$  near  $n_{\text{cr}}/4$  corresponds to absolute SRS backscatter. **Right:** Measured TPD linear growth rate (blue). Solid black and red lines indicate the theoretical convective growth rate at  $2 \times 10^{15} \text{ Wcm}^{-2}$  and  $1.2 \times 10^{15} \text{ Wcm}^{-2}$  [Yan et al., 2010], including Landau damping. Dashed line shows theoretical absolute growth rate [Simon, 1983].

that even in higher intensity shock-ignition designs, the intensity of light reaching  $n_{\text{cr}}/4$  will be reduced due to LPs such as CBET occurring at lower density. Finally the laser pulse was formed of a one-sided Gaussian temporal profile beginning at  $10^{-3}$  of the maximum field strength and, on reaching maximum intensity, followed by constant power for the remainder of the simulation. In this case the rising portion of the pulse took 2ps, as in [Yan et al., 2014].

## 5.2 Initial Behaviour

Following the propagation of the laser through the domain, a rapid series of events takes place. Discussion of these is split into two subsections. The first considers the instabilities' linear growth, while in the second we discuss the beginning of the nonlinear phase by considering effects that cause instability saturation.



### 5.2.1 Linear Growth

To examine the linear phase of instability growth a snapshot of the  $E_x$  field component during this period, Fourier transformed along the perpendicular ( $y$ ) direction, is shown in the left panel of figure 5.2. The solid white line indicates the perpendicular wavenumbers ( $k_y$ ) of the electron plasma waves (EPWs) expected to have maximum TPD linear growth rates. The corresponding features in the simulation data indicate that this instability is present during the simulation's linear phase. A white dashed line marks the TPD Landau cutoff ( $k\lambda_D = 0.3$ ), which is in good agreement with the lower density bound of TPD growth. EPWs due to SRS are also visible in figure 5.2 and may be identified as the feature with small  $k_y$  at  $n_{cr}/4$ . This corresponds to absolute SRS backscatter.

The linear growth rates of TPD were measured using these spectra to give growth as a function of the perpendicular wavenumber  $k_y$ . To accomplish this, the  $k_y$  spectrum was calculated for each snapshot in time, and integrated over the  $x$  direction. The instantaneous growth rate was then evaluated by using numerical differences to approximate the quantity

$$\gamma(k_y, t) = \frac{d}{dt} \ln[E_x(k_y, t)]. \quad (5.1)$$

A Gaussian filter was applied to  $\gamma(k_y, t)$  along both  $k_y$  and  $t$  to reduce the effect of particle noise. The period when growth was approximately linear was identified by eye, and the maximum value taken across this period in time to give the growth rates shown in the right panel of figure 5.2. Absolute growth rates from [Simon, 1983] are plotted (black dashed lines) along with the inhomogeneous convective growth rates of [Yan et al., 2010] (black solid lines). The range of wavenumbers that are observed to grow are consistent with those where convective growth is expected to occur. The measured growth rates are considerably smaller than those predicted by the theory. This is due to the slow rise-time of the laser pulse in this case, which varies significantly over the linear growth phase. Using an average intensity of  $1.2 \times 10^{15} \text{Wcm}^{-2}$  for the calculation gives better agreement with the data. The prominence of convective TPD observed is consistent with previous results for conventional direct-drive [Yan et al., 2009].

### 5.2.2 Initial Saturation Effects

Linear instability growth is rapidly arrested during an initial phase of nonlinear saturation. While several nonlinear effects come into play during this period, the one which initially causes saturation is pump depletion. This occurs due to the large

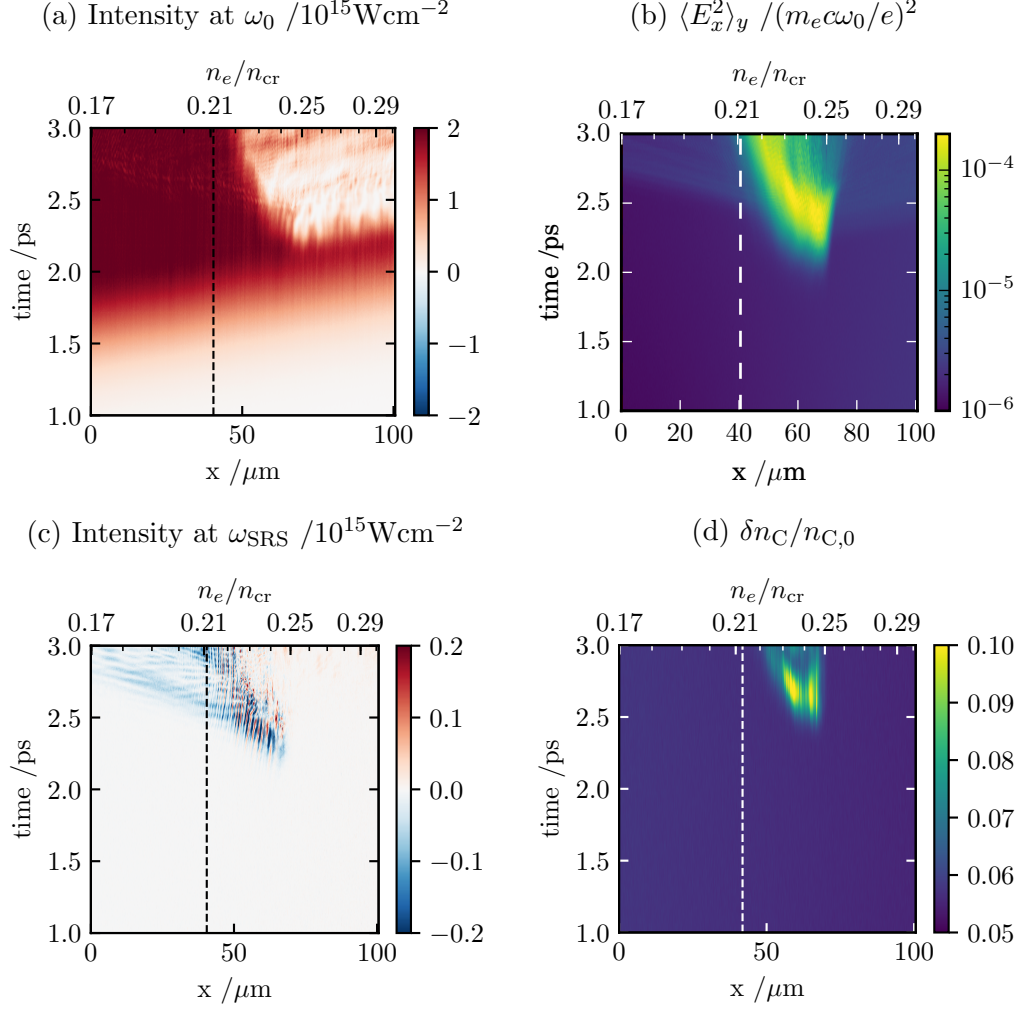


Figure 5.3: Diagnostics of initial LPI growth. **Left column:** Poynting flux diagnostics, filtered to include only waves at the laser frequency (a) or SRS scattered light frequency (c). Differing colour scales are used to allow scattered light to be seen. Positive values denote flux in the  $+\hat{x}$  direction. Striations visible in (c) correspond to the SRS backscattered light wavelength. **(b):** Transverse-averaged electrostatic wave energy. **(d):** Transverse standard deviation of carbon density fluctuations. Dashed vertical lines on all plots mark the TPD Landau cutoff ( $|\mathbf{k}|\lambda_D = 0.3$ ).

growth rate and hence inhomogeneous gain of convective TPD at this intensity. To illustrate this, figure 5.3 shows space-time maps of various important quantities. The diagnostics shown are laser Poynting flux (a), transverse-averaged electrostatic wave energy (b), SRS scattered light Poynting flux (c) and finally the transverse standard deviation density perturbation of the carbon ions (d). For this final diagnostic, the carbon ion density is chosen as it is relatively noise free compared to the hydrogen ion density. The density perturbation of a given species is then calculated as

$$\delta n(\mathbf{r}, t) \equiv \frac{n - \langle n \rangle_y}{\langle n \rangle_y}. \quad (5.2)$$

To produce figure 5.3 (d), the standard deviation of  $\delta n(\mathbf{r}, t)$  is taken across the transverse direction, as the mean would average to zero.

In all panels of figure 5.3, dashed lines mark the location of the TPD Landau cutoff ( $|\mathbf{k}|\lambda_D = 0.3$ ), and the time period shown is restricted to the initial part of the simulation. Pump depletion and ion density perturbations can both cause saturation of TPD. While both of these are observed, it is pump depletion that occurs first. This takes place at approximately 2.2ps at  $n_{cr}/4$ , while density perturbations grow to large amplitude somewhat later at 2.4ps. At lower densities where Landau damping of the TPD EPWs produces lower growth rates, TPD growth and saturation take place with a slight delay. However it is again pump-depletion that saturates the instability first.

While pump depletion is the effect which first saturates the instabilities, the density perturbations that initially grow also play an important role. As discussed in chapter 4 ion density fluctuations can be driven ponderomotively by the beating of intense TPD daughter EPWs. To show which perturbations initially grow and their effect on the TPD EPWs, the  $E_x$  and carbon density perturbation spectra at 2.2ps and 2.4ps are plotted in figure 5.4. At 2.2ps the instability has just reached saturation due to pump-depletion, and no significant density perturbations are present. The EPW spectrum at this time bears close resemblance with that predicted by linear theory (see for example the left panel of figure 2.10). Note that since these spectra are calculated from static snapshots, the direction of  $\mathbf{k}$  is ambiguous. In the EPW spectrum the direction of propagation may be inferred from the overlaid theoretical curves.

In the spectra calculated 300fs later at 2.5ps, an initial set of density perturbations  $\delta n$  have been driven. At this point in time the main feature of the  $\delta n$  spectrum is a peak corresponding to the transverse density waves described in chapter 4. Due to the range of densities present this feature is broad, spanning a range

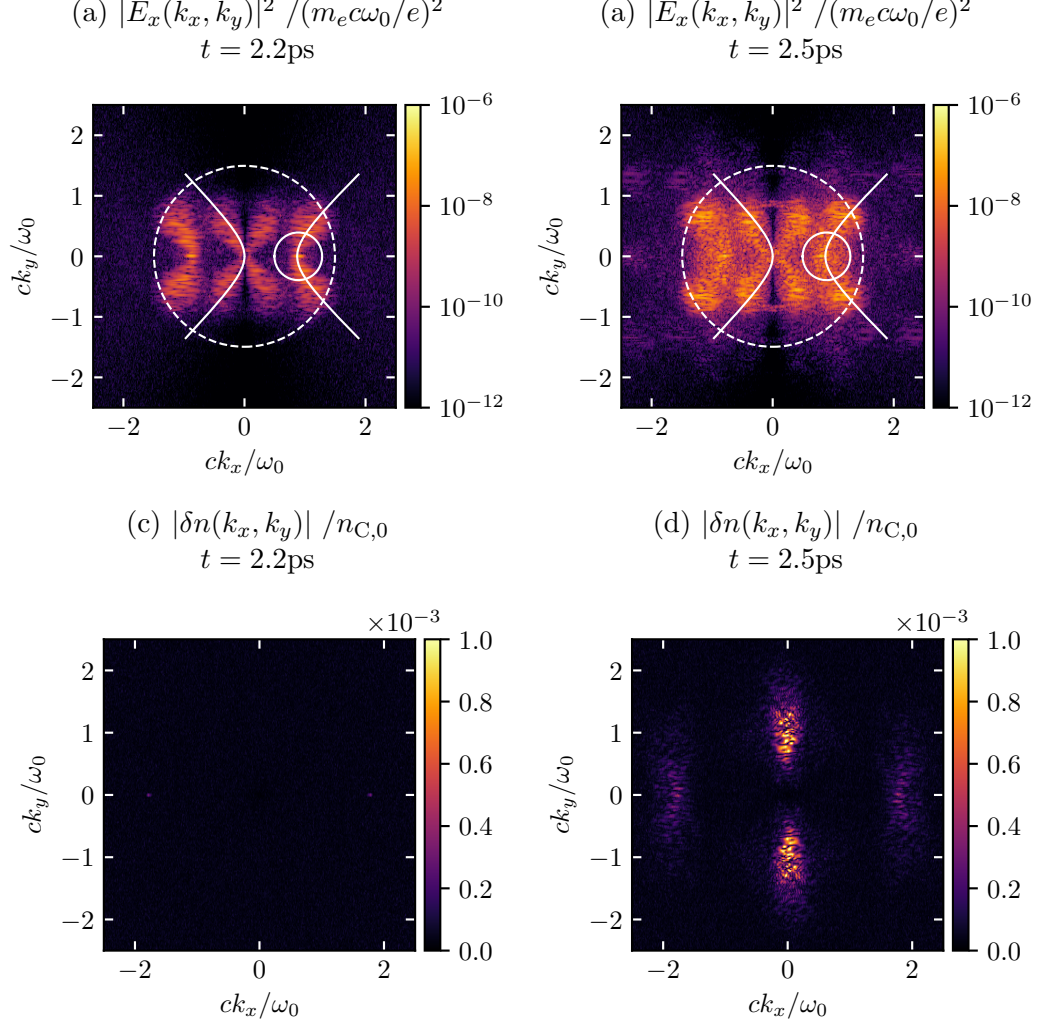


Figure 5.4: Energy spectra of electrostatic field ( $E_x$ , top) and carbon density perturbations ( $\delta n_C$ , bottom) at 2.2ps (left), and 2.5ps (right). The data used covers the entire domain. In the  $E_x$  spectra a dashed line marks the Landau cutoff ( $|\mathbf{k}| \lambda_D = 0.3$ ), the solid circle bounds possible SRS EPW wavenumbers, and solid curved lines mark the wavenumbers where TPD has its maximum linear growth rate in a homogeneous plasma. Since these spectra are calculated using instantaneous snapshots the sign of  $\mathbf{k}$  is ambiguous; forward-propagating TPD daughter waves at  $\mathbf{k} = \mathbf{k}_+$  also appear at  $\mathbf{k} = -\mathbf{k}_+$ .

up to  $k_y = 1.8\omega_0/c$  and with a width that increases with  $k_y$  up to approximately  $\Delta k_x = 0.5\omega_0/c$ . As expected the upper  $k_y$  limit is roughly double the maximum transverse wavenumber  $k_y = 0.9\omega_0/c$  of the EPW spectrum. In addition the width  $\Delta k_x$  of this feature is also in reasonable agreement with the width of the TPD EPW spectrum, which also broadens at increasing  $k_y$ . A further, lower amplitude peak in the  $\delta n$  spectrum is visible at  $\mathbf{k} \simeq (2\omega_0/c, 0)$ . This is due to the beating of forwards-propagating TPD EPWs with backwards propagating EPWs and can only occur very close to  $n_{\text{cr}}/4$  where the forwards and backwards-propagating EPWs have very small frequency difference.

The EPW spectrum at 2.5ps has significant differences from that at 2.2ps. This is largely caused by the ion density perturbations, which scatter the EPWs. The main part of the TPD spectrum has undergone significant broadening as a result, with the previously distinct components now blurred into a largely continuous spectrum. Broad peaks are also visible at high  $|\mathbf{k}|$ . These waves have very low amplitude as they are mostly far beyond the Landau cutoff and consequently subject to large Landau damping rates. Not all of the high- $|\mathbf{k}|$  modes can be explained by scattering from ion density perturbations. Some of these may be caused by beating of pairs of EPWs with large frequency difference coupling directly to other high-frequency waves, while others are harmonics of the large-amplitude EPWs.

As discussed in chapter 4, the density perturbations lead to a reduction in the linear growth rate of TPD. By the time the the density perturbations are driven the region is already pump-depleted so no growth can occur anyway, however their presence now limits any future growth when the laser re-enters.

### 5.3 Long-term Behaviour

After the initial period of rapid instability growth and saturation, the nonlinear saturated state evolves over a longer timescale. LPI activity is primarily due to TPD and effects resulting from it. While SRS is observed at a low level, it accounts for a very small fraction of absorbed energy. This can be seen in the reflectivity and transmission diagnostics shown in figure 5.5. During the initial linear growth phase, absolute SRS occurred at  $n_{\text{cr}}/4$ . This is responsible for the spike in backscattered light observed in the diagnostic at around 2.8ps. Later on in the simulation, forward and back-scattered light are observed due to convective SRS at lower density, but the total fraction of laser power delivered in these is on the order of 2%. Since the transmitted fraction of laser energy ranges between approximately 10-40%, laser absorption must be at 60-90%. Assuming half of the SRS and SBS-absorbed en-

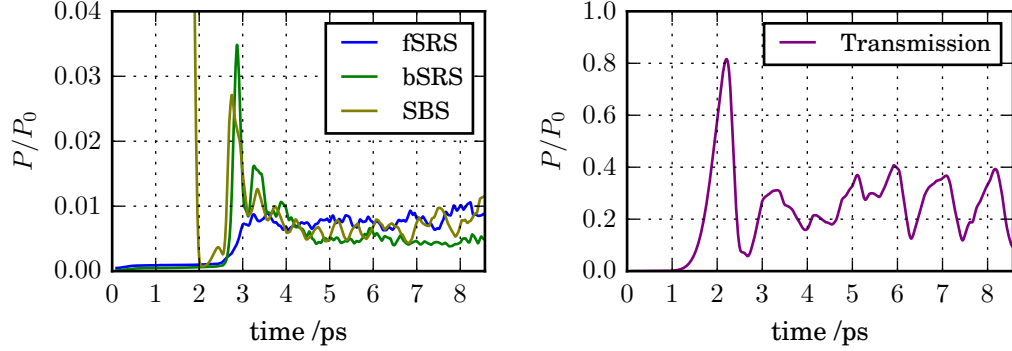


Figure 5.5: **Left:** Scattered light time-history. Green and olive lines measure SRS and SBS back-scatter detected at the laser entrance boundary, while SRS forward-scatter measured at the laser exit boundary is shown by the blue line. The SBS curve is calculated by subtracting the laser’s maximum power from the signal measured at the laser entrance boundary and negating the result. This does not account for the laser rise, leading to the apparent 100% SBS scattering before 2ps. **Right:** Transmitted light time-history. In both panels, the vertical scale is normalised to the maximum incident laser power, and a Gaussian filter has been applied to all signals to remove high-frequency noise with period shorter than 25fs.

ergy is seen as scattered light (with the remainder delivered to EPWs and IAWs), the observed activity of these scattering instabilities can only account for a small proportion of total absorption. The vast majority of absorption is instead due to TPD.

In discussing long-term instability activity, the focus of this section is therefore on the behaviour of TPD. Three effects are predominantly responsible for the observed dynamics, and these are discussed in turn in the next three subsections.

### 5.3.1 Cavitation

Near the quarter-critical surface, the intense EPWs present lead to the formation of unstable density depressions or ‘cavities’ that trap the EPWs [DuBois et al., 1995; Russell and DuBois, 2001]. Consideration of the relative strength of the plasma thermal pressure and the ponderomotive pressure of the EPWs can be used to produce a criterion for where these unstable cavities can form [Dendy, 1990]. In particular, the turbulence parameter  $\bar{W}$  of the EPWs is used to quantify the relative strength these effects and leads to the condition

$$\bar{W} \equiv \frac{\varepsilon_0 |\mathbf{E}|^2}{4n_e k_B T_e} > 3(k\lambda_D)^2. \quad (5.3)$$

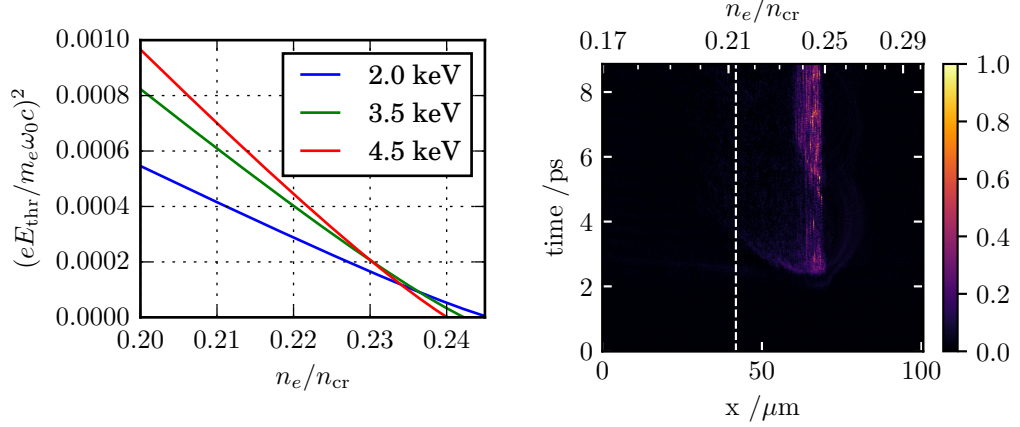


Figure 5.6: **Left:** Threshold EPW field amplitude as a function of density for TPD. The wavenumber used in the calculation is that of the backwards-propagating daughter wave as this produces the lowest threshold. **Right:** Transverse-averaged cavitation correlator as a function of space and time. Vertical dashed line marks the TPD Landau cutoff. Following initial growth, TPD EPWs cause cavitation in the region closest  $n_{\text{cr}}/4$ , as predicted by threshold calculation in left panel.

Here the electric field  $\mathbf{E}$  refers to the field amplitude of an EPW with wavenumber  $k$ . This indicates that cavitation occurs near  $n_{\text{cr}}/4$  for TPD due to the short EPW wavenumbers required in this region. In particular, the backwards-propagating TPD EPW wavenumber vanishes as  $n_e$  approaches  $n_{\text{cr}}/4$ , so the threshold is most easily satisfied in that region. To illustrate this, the left panel of figure 5.6 shows the threshold electric field energy as a function of density for the backwards-propagating TPD EPW, at three different temperatures. Additionally, the upper right panel of figure 5.7 shows the transverse-averaged electrostatic field energy. Electric field energy can be seen to be fairly uniform in time and space with a value of approximately  $(eE/m_e\omega_0c)^2 \simeq 10^{-4}$ . According to figure 5.6, cavitation should therefore occur in a narrow density region  $0.235 \lesssim n_e/n_{\text{cr}} < 0.25$ .

To determine where cavitation actually occurs, the transverse-averaged ‘cavitation correlator’ [DuBois et al., 1996] has been evaluated. This is a metric for cavitation activity, and is defined

$$C_{\delta n|E|^2} \equiv -\frac{\langle \delta n |\mathbf{E}|^2 \rangle}{\langle \delta n^2 \rangle^{1/2} \langle |\mathbf{E}|^2 \rangle}. \quad (5.4)$$

Cavitation takes place where EPWs with large electrostatic field amplitude  $|\mathbf{E}_{\text{ES}}|$  are able to drive ion density depressions  $\delta n$  that trap the EPWs. In regions where

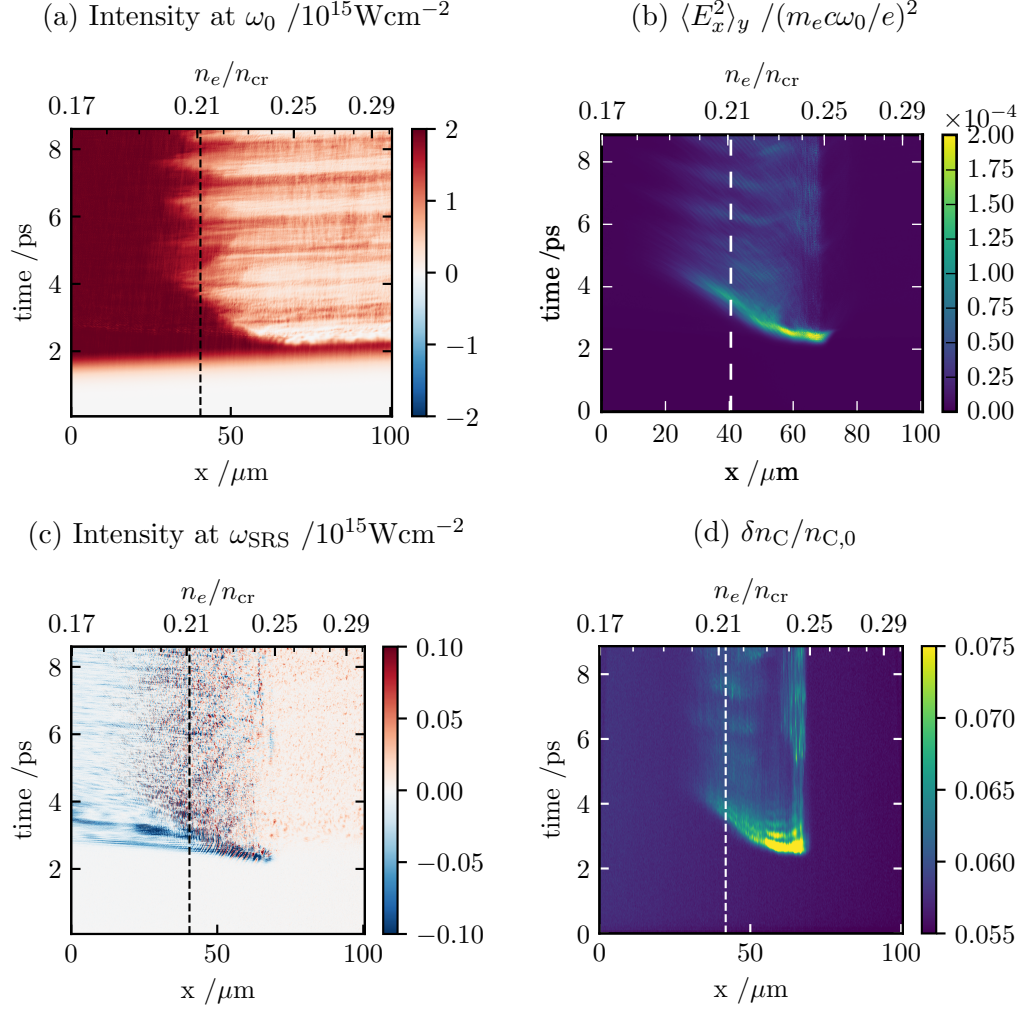


Figure 5.7: **(a)**: Poynting flux, filtered to include only EM waves at the laser frequency. **(c)**: Poynting flux filtered to include only EM waves at frequency of SRS scattered light. **(b)**: Transverse-averaged electrostatic wave energy in the  $E_x$  field component. **(d)**: Transverse standard deviation of carbon ion density perturbations. See main text for an explanation of these figures.



this occurs,  $|\mathbf{E}_{\text{ES}}|$  and  $-\delta n$  should therefore be correlated, so the statistic should have values above 0.5. Elsewhere the fluctuations due to linear EPWs and IAWs are uncorrelated and so the statistic should average to zero. The right hand panel of figure 5.6 shows this statistic for the small-scale simulation. Here it indicates that cavitation begins shortly after initial instability growth, and persists for the remainder of the simulation. The range of densities in which cavitation occurs also corresponds roughly to the same region predicted by the threshold.

Single-beam RPIC (Reduced PIC) simulations that were performed with the same laser intensity and similar plasma conditions to this simulation have also led to cavitation ([Vu et al., 2012a], section V). It is therefore unclear why it was not reported in [Yan et al., 2014], though the spectra presented in their paper display a broadened EPW spectrum near  $n_{\text{cr}}/4$  which is similar to that observed in our results. While cavitation plays a relatively limited role in our single-beam simulations, it plays a more important part in RPIC and extended Zakharov simulations of TPD driven by multiple laser beams [Myatt et al., 2012; Vu et al., 2012a,b]. In those cases it was identified as the leading source of hot electrons.

### 5.3.2 Pump Depletion & Wave Propagation

Cavitation has a less important role in this simulation as most laser energy is absorbed at densities around the TPD Landau cutoff. In this relatively low density region the threshold field amplitude for cavitation is large, and so other nonlinear effects saturate TPD instead.

Figure 5.7 shows the same set of diagnostics as figure 5.3, but now spanning the full duration of the simulation. In all plots the TPD Landau cutoff ( $|\mathbf{k}|\lambda_D = 0.3$ ) is marked with a vertical dashed line. During the initial phase of linear growth, large amplitude EPWs were produced in the plasma near  $n_{\text{cr}}/4$  where Landau damping is minimal. These can be seen in the EPW energy diagnostic (figure 5.7, upper right) as an arc spanning roughly  $45\text{--}70\mu\text{m}$ . This arc is at a slight angle from horizontal since the higher density TPD EPWs have slightly larger growth rates and so appear earlier in time. At later time this arc is seen to continue into the low density region (between approx.  $20\text{--}45\mu\text{m}$ , from  $2.5\text{--}4.5\text{ps}$ ), and notably continues past the Landau cutoff. The gradient of the arc is now significantly steeper, and in particular is close to the group velocity of the backwards-travelling TPD EPWs.

In the diagnostic of laser Poynting flux (upper left panel of figure 5.7), pump-depletion is seen to track the arc of TPD activity. This strong laser absorption indicates that further instability growth is occurring in the low density plasma. In [Yan et al., 2014], it was suggested that backwards-propagating waves from the

high-density plasma can act as large-amplitude seeds for further convective TPD near the Landau cutoff. These would not be able to undergo significant growth but might be sufficient to deplete the laser of energy. The same authors also found, in a previous work, that TPD activity at low density could be enhanced by ion density perturbations [Yan et al., 2012]. This was explained in terms of the broadening effect of the ion density perturbations on the EPW spectrum; the additional modes introduced when the spectrum becomes broadened increase the EPW seed amplitude that is then amplified by convective TPD. Interestingly it was claimed that ion density perturbations, and therefore also this mechanism, are not important to LPI in the low density region of the simulation we have reproduced [Yan et al., 2014]. In contrast, we find that TPD in this region *is* affected by density perturbations, and furthermore, it is clear from the spectra presented in [Yan et al., 2014] that they are also important there. This will be discussed in the next subsection.

In the original simulation, which was run for 21ps, TPD activity in the low density plasma diminished after 15ps [Yan et al., 2014]. A second ‘arc’ of TPD growth was then seen to propagate from  $n_{\text{cr}}/4$ . A tentative explanation was given for this. In particular it was suggested that, since pump-depletion in the low density plasma prevents growth of waves near  $n_{\text{cr}}/4$ , this could also starve the low-density TPD activity of a supply of the waves needed to support it from the high density plasma [Yan et al., 2014]. Since our simulation covers a shorter time duration this effect is not observed here.

While no second large wave of growth is observed, the behaviour seen for the remainder of the simulation involves a cyclic pattern of TPD growth in the low density plasma. These bursts of activity result in a varying degree of pump depletion, which can be seen from the laser Poynting flux diagnostic (upper left, fig. 5.7) and the time history of laser transmission (right, fig. 5.5). This illustrates that the majority of absorption continues to occur about the Landau cutoff, but that periodic reductions of activity there allow a higher laser intensity to propagate into the higher density plasma. This allows for continued TPD activity at higher density, which for example sustains the cavitation near  $n_{\text{cr}}/4$ .

### 5.3.3 Ion Density Perturbations

To explain the bursts of TPD growth described above, we examine the effect ion density fluctuations in the plasma near the TPD Landau cutoff. Figure 5.8 shows energy spectra of the electrostatic field  $E_x$  (left column) and amplitude spectra of carbon density perturbations  $\delta n_c$  (right column). These spectra are calculated at  $t = 3.8, 6.3$ , and  $7.3$ ps (top to bottom rows respectively), using data from the plasma

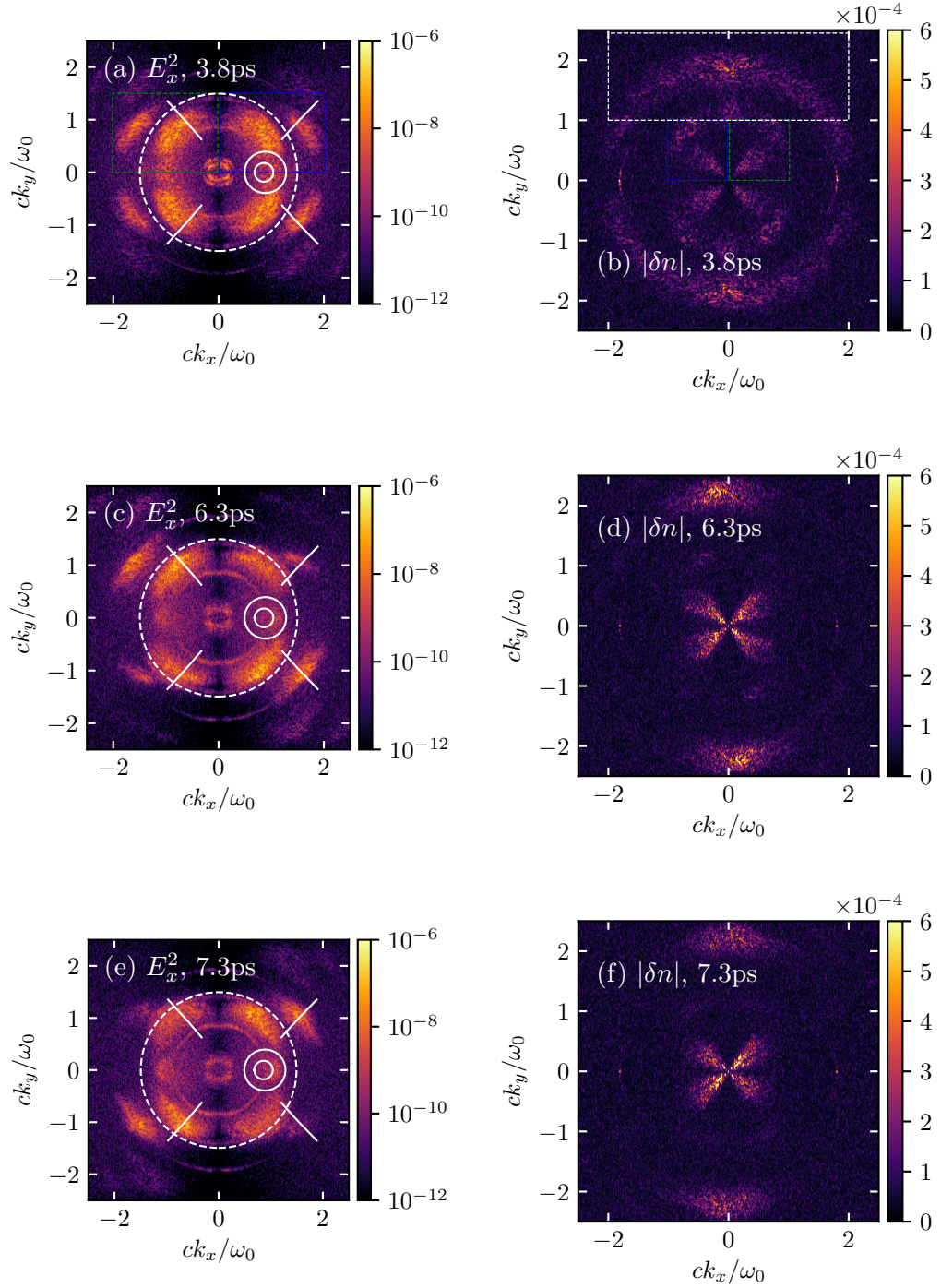


Figure 5.8: Spectra of electrostatic field ( $E_x^2$ , left) and carbon density perturbations ( $\delta n_C$ , right) at 3.8ps (top), 6.3ps (middle), and 7.3ps (bottom). Data from  $0.17-0.23n_{cr}$ . In the EPW spectra, the dashed line marks the Landau cutoff ( $|\mathbf{k}|\lambda_D = 0.3$ ), solid circles bound possible SRS EPW wavenumbers, and solid lines mark location of maximum TPD linear growth rate. Dashed boxes in (a) and (b) indicate the integration regions for figure 5.9.

at densities below the cavitation region. This spans a density range of  $0.17\text{--}0.23n_{\text{cr}}$ .

The spectra at early time (3.8ps) are calculated during the first burst of TPD when the backwards propagating EPWs have almost reached their final position. Both spectra are symmetric in  $k_y$ . The EPW spectrum is again broadened due to scattering of EPWs from the ion density perturbations. In addition, it features modes at  $\mathbf{k}$  beyond the Landau cutoff. The  $\delta n$  spectrum contains transverse density perturbations at  $\mathbf{k} \simeq (0, 1.8)\omega_0/c$  and ‘oblique’ density perturbations with  $|\mathbf{k}| < \omega_0/c$  and  $k_y \simeq \pm k_x$ . Further ion density perturbations are present in the spectrum due to additional processes.

The two later snapshots are captured at the peak of successive TPD bursts. In the  $E_x$  spectra, the most prominent difference from the spectrum at 3.8ps is the  $k_y$  asymmetry that is now apparent. The EPWs with largest amplitude correspond to a single ‘handedness’ of TPD growth – also visible in the spectra in [Yan et al., 2014] (panels (e) & (g) of figure 3). Furthermore, the handedness of the EPWs alternates between successive bursts. The IAW spectra obtained at these times display fewer features than the spectrum at 3.8ps, however the transverse and oblique density perturbations remain and indeed are at larger amplitude. At the chosen times there are some visible asymmetries in the  $\delta n$  spectra, however these are difficult to discern.

The analysis of chapter 4 suggests that the ‘oblique’ density perturbations could be responsible for the asymmetry observed in the EPW spectra. To examine whether this is consistent with the simulation data, sections of the EPW and IAW spectra are integrated to produce individual amplitudes whose time-dependence can be more easily compared. These are shown in the top two panels of figure 5.9. In the upper panel, the time histories of the averaged  $E_x$  spectra are plotted. The quantity labelled  $\mathbf{k}$  is the spectral amplitude  $|E_x(k_x, k_y)|$  averaged over the region marked by dashed blue lines in the early-time  $E_x$  spectrum of figure 5.8. Due to the ambiguity in the sign of  $\mathbf{k}$  of the static Fourier transforms used, this captures the complete set of TPD waves of one ‘handedness’. The opposing set of EPWs is labelled  $\mathbf{k}^\dagger$  and is measured by integrating the region bounded by the green dashed lines. The sum of the two TPD signals is also plotted as a solid black line, while vertical grey lines mark the main ‘bursts’ in TPD activity. In the next panel of figure 5.9, the time series of density perturbation ( $\delta n$ ) amplitudes are shown. These are colour coded according to the amplitudes they should affect in the upper panel. Transverse density perturbations are marked  $\mathbf{k}_\perp$ , calculated by averaging  $|\delta n(k_x, k_y)|$  in the region shown by the white dashed rectangle in the early-time  $\delta n$  spectrum in figure 5.8. Finally the two quantities marked  $\mathbf{k}_{\text{IAW}}$  and  $\mathbf{k}_{\text{IAW}}^\dagger$  represent oblique density perturbations and correspond to the regions bounded by blue and green

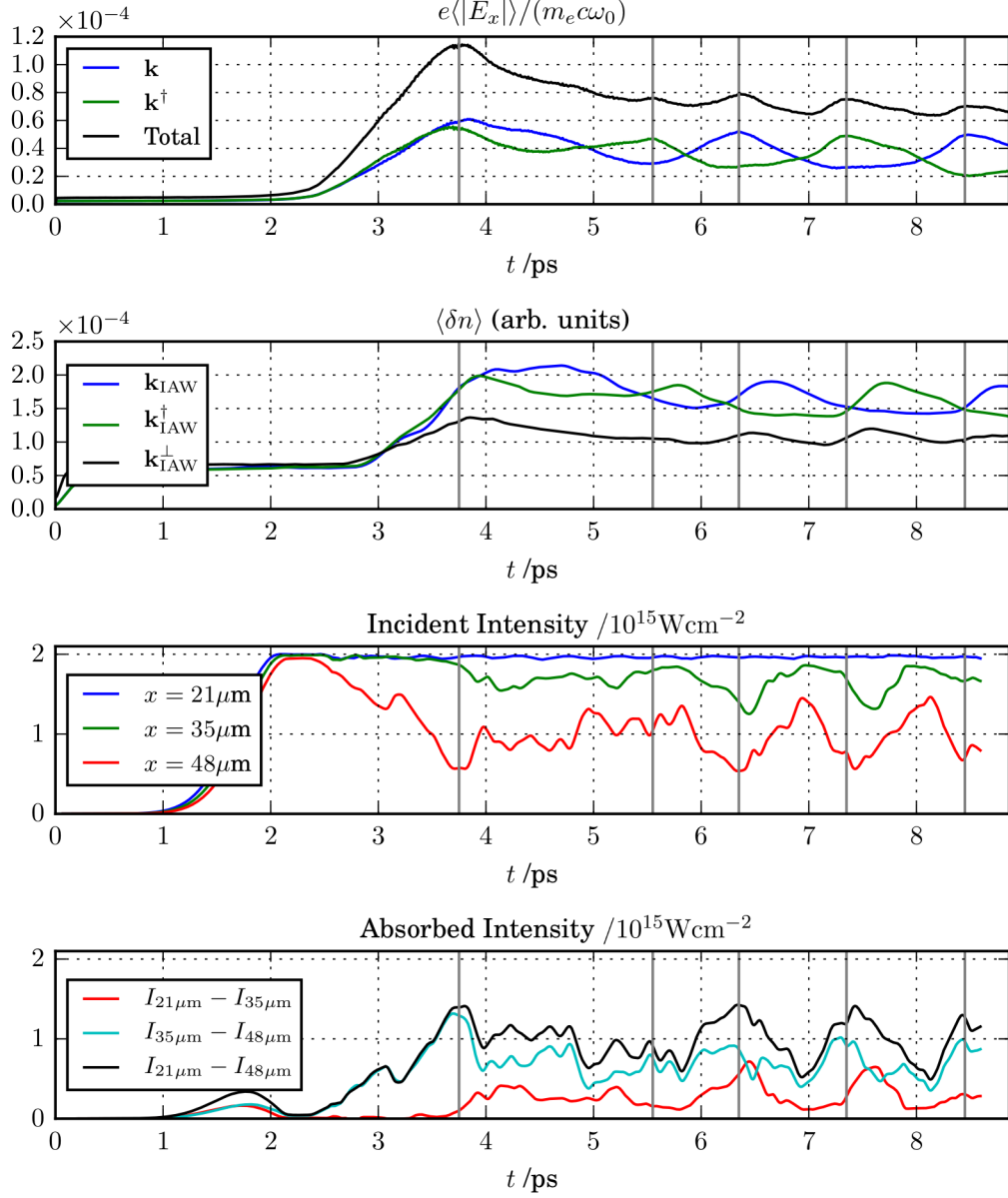


Figure 5.9: Diagnostics of ‘bursty’ TPD activity as time series. Upper panel: Coloured lines show spectral amplitude of TPD EPWs of different handedness, averaged over regions bounded by dashed lines in first  $E_x$  spectrum of fig. 5.8. Black line is the sum of coloured lines. Vertical grey lines mark the peak of each burst. Second panel: Mean spectral amplitude of density perturbations, averaged over corresponding regions of first  $\delta n$  spectrum in fig. 5.8. Third panel: Lineouts of laser intensity from laser Poynting flux diagnostic of figure 5.7 at locations indicated in legend. Final panel: Differences between the lineouts of the previous panel, indicating absorbed intensity over the respective intervals.

dashed lines respectively in the early-time  $\delta n$  spectrum.

It is clear from the time histories of the various quantities that the density perturbations and TPD EPWs are related. Each type of density perturbation responds to changes in the amplitude of the EPW waves responsible for driving it, and in a manner that is consistent with what would be expected. This is most apparent after the initial growth has occurred. Focusing for example on the blue curves, periods of rising  $\delta n$  amplitude occur when the EPWs are at high amplitude (e.g. at 6.0-6.6ps), while conversely periods of decaying  $\delta n$  amplitude occur when the EPWs are at low amplitude (e.g. 6.6-8.2ps).

The behaviour observed also appears consistent with the results of chapter 4 in that the EPWs respond to the activity of the oblique density perturbations. The EPWs undergo periods of decay in amplitude (due to Landau damping) when TPD growth is suppressed by elevated density perturbation amplitudes (e.g. 6.3-7.1ps for the blue curves).

Another effect that is apparent from the time histories is that during a burst in activity of one pair of TPD waves, the other pair does not grow. For example after the burst between 6.0-6.6ps seen in the ‘blue’ EPWs, it might be expected that another phase of growth might begin at approximately 7ps when the corresponding oblique density perturbation has dropped sufficiently in amplitude. Instead, growth does not resume until around 8ps when the opposing set of ‘green’ EPWs has itself been suppressed.

A possible explanation for this behaviour can be given in terms of pump depletion. In particular, during each burst the region where peak absorption occurs shifts to lower density. This is visible in the laser Poynting flux diagnostic (upper left panel, figure 5.7). To illustrate this effect as a time-series, lineouts have been taken from the Poynting flux diagnostic and are also plotted in figure 5.9 (panel third from top). Three locations are chosen; two bounding the region where most absorption occurs, and one located roughly in the centre. These lineouts indicate incident intensity at each point. In the final panel of figure 5.9, the differences of these intensities has been calculated; these measure the ‘absorbed intensity’ within each region. The red and cyan curves measure absorption at low and high density respectively, while the black curve measures absorption over the combined area. This calculation does not account for the propagation time between each point, however since the points are closely spaced this should be very short. For the last three bursts, marked by vertical grey lines, total absorption peaks during each burst. Additionally, during each of these three bursts absorption first rises in the high density region (cyan) before moving to the low density region (red). Interestingly



this pattern is not observed in the lineouts for the burst at 5.5ps, however this is likely due to absorption instead being centred at higher density as can be seen in the Poynting flux diagnostic.

The shift of absorption to lower density during each burst is potentially due to the convective nature of the instability. The backwards-propagating TPD wave has a significantly lower damping rate than the forwards-propagating one, leading to each burst of TPD growth occurring as an overall backwards-propagating pulse. It is possible therefore that in order for a burst to be initiated in a particular set of TPD EPWs, not only does the amplitude of corresponding oblique density perturbations have to be sufficiently low, but a large intensity is required at high density. These conditions are not both satisfied until the opposing set of TPD EPWs have diminished sufficiently to allow a larger fraction of laser energy to pass into the high density plasma.

#### 5.3.4 Summary

As we have seen, LPI in this simulation exhibits complex and dynamic behaviour. TPD is the primary instability active, and its saturation state is subject to a variety of effects. The density range in which TPD takes place can be split into two sub-regions that are distinguished by the dominant nonlinear saturation mechanisms. In the high-density region, adjacent to the quarter-critical surface, the primary effect is cavitation which has previously been observed in simulations at lower laser intensity relevant to conventional direct-drive ICF [Vu et al., 2012a,b; Myatt et al., 2012]. In the low-density region in the vicinity of the TPD Landau cutoff, TPD is instead saturated by coherent ion density perturbations. These, along with pump-depletion, lead to regular periods of EPW amplitude growth and decline, and an asymmetric EPW spectrum. Furthermore, this low-density TPD activity is found to cause efficient absorption of laser energy, in contrast with the cavitation region. That TPD is so active in this low-density region is likely a consequence of the higher laser intensity used and therefore specific to the shock-ignition regime.

### 5.4 Hot Electron Production

#### 5.4.1 Angular Distribution

In order to investigate the hot electron output of the simulation, data from suprathermal electrons leaving the domain was used to construct an inferred distribution function. The distribution of particle fluxes  $f_F(\mathbf{p})$  through a given boundary may

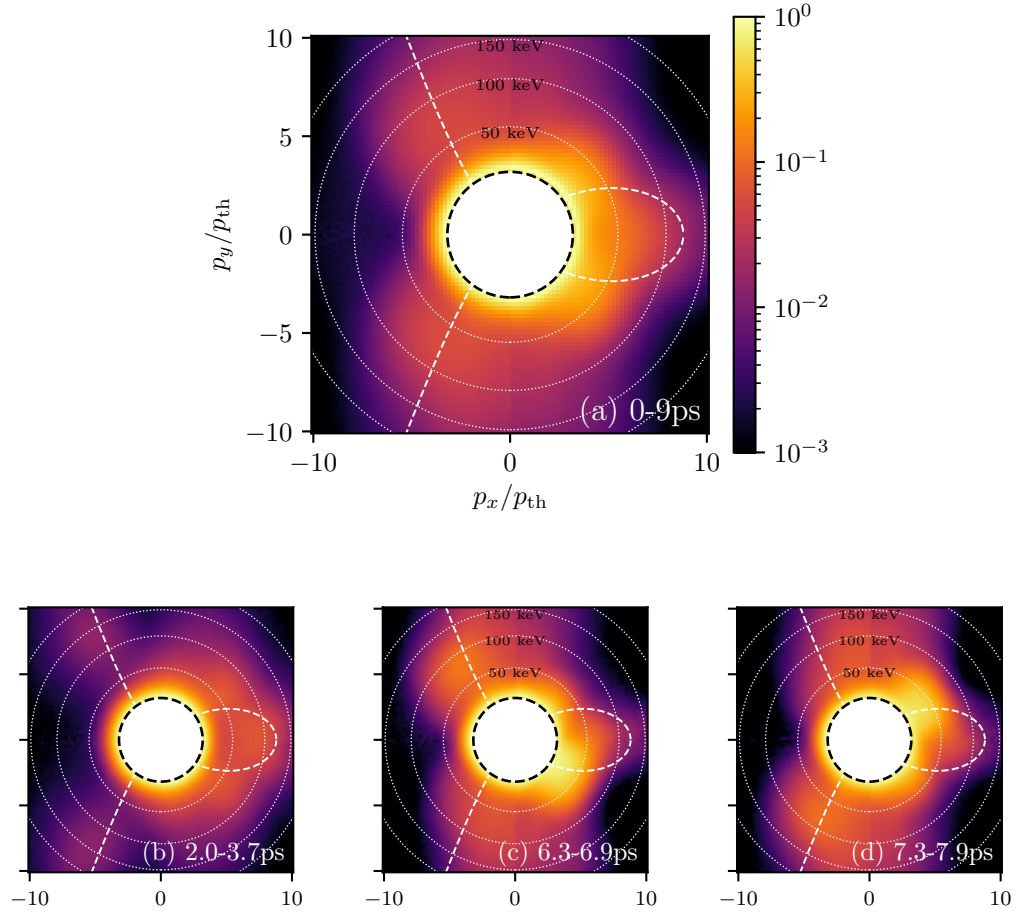


Figure 5.10: Inferred time-integrated distribution functions, calculated from outgoing hot electron data. Time integration is performed over the period indicated in each panel. Particle counts in each momentum bin have been weighted according to the energy of the bin. Histograms are each normalised to maximum of the binned values, and colour scales are shared. White dashed lines show the momenta expected of TPD-accelerated hot electrons, while the white circles indicate the particle energy at a given  $|\mathbf{p}|$ .



be written in terms of the particle distribution function  $f_B(\mathbf{v})$  as

$$f_F(\mathbf{v}) = \mathbf{v} \cdot \hat{\mathbf{n}} f_B(\mathbf{v}), \quad (5.5)$$

where  $\hat{\mathbf{n}}$  is a unit vector normal to the boundary. In this case the convention is used that  $\hat{\mathbf{n}}$  is directed out of the domain. Data from outgoing electrons was binned according to their momentum in  $x$  and  $y$ , which produces an estimate of the flux distribution. The inferred distribution function at a given boundary was then calculated from this by inverting the above equation.

The inferred distributions from each of the four simulation boundaries were then combined into a single inferred distribution, which provides an estimate for the mean hot electron distribution at a given instant in time. Given that there is significant variation in time of the hot electron production in the simulation, and that the hot electrons take varying times to reach the different boundaries, this is clearly a rather crude estimate. However, this can be mitigated by time-averaging to produce a better estimator of the hot electron population. Data from the transverse boundaries was intentionally included in this dataset, and means that when time-averaged, the hot electrons propagating oblique or perpendicular to the laser may be counted multiple times. This can be thought of as accounting for hot electron production from a much larger transverse extent of plasma.

The inferred hot electron distribution, time averaged over the entire simulation is plotted in figure 5.10 (a). Data was not collected in the core of the distribution, which is bounded by black dashed lines. White dashed lines mark the phase velocities expected of TPD waves. Note that for both TPD and SRS the EPW phase velocity increases in magnitude with density. Distinct hot electron populations can be identified in this figure, which can be associated with different instabilities. Since TPD is the most prevalent instability in the simulation, significant hot-electron populations are found to lie underneath the dashed lines that mark expected TPD phase velocities.

The inferred distribution shown in figure 5.10 (a) appears symmetric in  $p_y$ , however on a shorter timescale this is not always the case. In figures 5.10 (b), (c), and (d), inferred distributions are shown for different averaging periods, indicated in the respective figures. During the initial growth and saturation phase (figure 5.10 (b)) the hot electron distribution is symmetric in  $k_y$ , however in the distributions calculated during successive TPD bursts (figure 5.10 (c) & (d)), there is an asymmetry which reverses between the two cases. These asymmetries are clearly due to the asymmetric nature of the nonlinear saturation state of TPD.

### 5.4.2 Hot Electron Sources

The distribution function in figure 5.10 (a) also includes features that do not correspond directly to TPD. For example there are also populations propagating parallel and perpendicular to the laser. To identify the sources of these hot electrons, subsets of the electron distributions in the bulk domain were examined. In figure 5.11 (a) the  $x$ - $p_y$  phase space is shown for forwards-propagating ( $p_x > 0$ ) electrons with kinetic energy  $E_k > 50\text{keV}$  at  $t = 4.5\text{ps}$ . It was argued in [Yan et al., 2014] that features with large  $|p_y|$  correspond to TPD EPW accelerated electrons, while those with small  $|p_y|$  to electrons from SRS EPWs.

To examine the source of the small- $|p_y|$  electrons figure 5.11 (b) shows the density of electrons that have  $|p_y| < 0.1m_e c$ ,  $p_x > 0$  and  $E_k > 50\text{keV}$ . This figure shows only a small section of the domain ( $x = 46\text{--}52\mu\text{m}$  and  $y = 2\text{--}8\mu\text{m}$ ) to highlight the structures present. In particular, modulations of hot-electron density clearly show the trapping of electrons in waves' potential wells. To identify the waves responsible for this trapping, the spectrum of this component of the distribution function is shown in figure 5.11 (c), while the corresponding  $E_x$  field spectrum shown in figure 5.11 (d). Both spectra are calculated using only data from  $x < 55\mu\text{m}$  ( $n_e < 0.23n_{\text{cr}}$ ) so as to examine only the region where most hot-electron production occurs. Here two solid circles bound the wavenumbers of the electrostatic waves that could be excited by SRS, while solid lines mark wavenumbers where TPD growth rates are maximised in the linear theory. Finally, dashed lines mark the Landau cutoff. In the distribution function spectrum several distinct features are present. Those lying outside the Landau cutoff clearly correspond directly to TPD waves in the  $E_x$  spectrum, while the feature with  $\mathbf{k} \simeq 0$  represents the 'background' of particles which have been accelerated, de-trapped and subsequently de-phased. Since the hot electron density spectrum only includes forward-propagating electrons there is no feature corresponding to the backwards-propagating TPD EPWs. The remaining feature has a broad spectrum that is centred at  $\mathbf{k} = \mathbf{k}_0$ . Due to the lack of any obvious SRS features in the EPW spectrum we argue that this hot-electron population cannot be produced by SRS EPWs. Instead it is most likely due to the broad background EPW spectrum brought about by scattering of EPWs from ion perturbations, and is therefore a result of the nonlinear saturation of TPD. Indeed, as discussed previously, after the simulation's linear growth phase where absolute SRS was observed at  $n_{\text{cr}}/4$ , SRS activity is severely restricted. There is a low level of convective SRS that remains but this scatters on the order of 1% of the laser energy and is therefore insufficient to explain the hot electron production observed. Similar analysis has been performed to identify the sources of the remaining hot

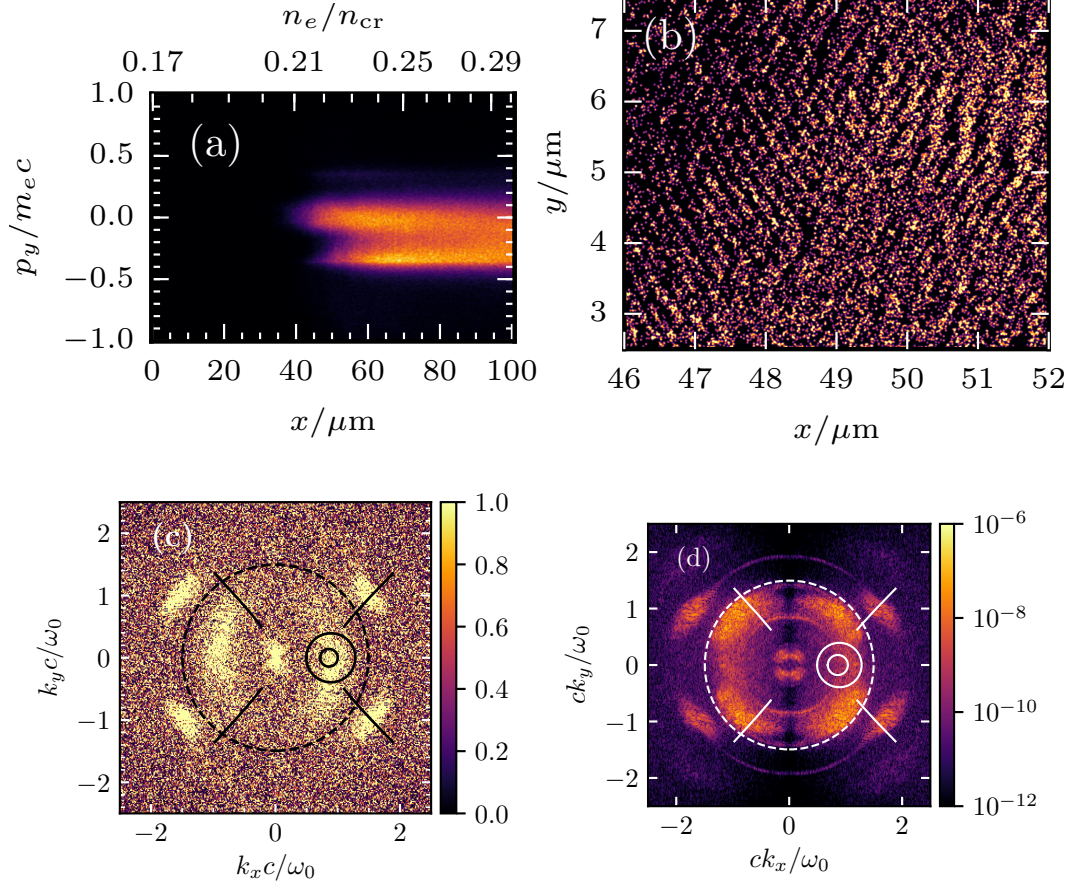


Figure 5.11: All panels from  $t = 4.5\text{ps}$ . **(a)**: Distribution of forward-propagating electrons with kinetic energy  $E_k > 50\text{keV}$  in  $x$ - $p_y$  phase space. Large  $|p_y|$  population due to Landau damping of TPD EPWs. **(b)**: Spatial distribution of small  $|p_y|$  ( $|p_y| < 0.1m_e c$ ) electrons from (a) in subsection of simulation domain, featuring striations corresponding to potential wells of EPWs, along with de-phased (uniformly distributed) electrons. **(c)**:  $k_x$ - $k_y$  spectrum of spatial modes of hot electron density (same population as in (b), but calculated over entire domain). Bright features identify EPW wavenumbers causing trapping. **(d)**: EPW spectrum from  $E_x$  field component, showing EPWs responsible for trapped electron populations in (c). Note that spectra in (c) and (d) are from static snapshots so the sign of  $\mathbf{k}$  is ambiguous. In (c) & (d) dashed circle indicates approximate Landau cutoff ( $|\mathbf{k}|\lambda_D = 0.3$ ), small solid circle indicates wavenumbers of SRS EPWs and two curved lines denote TPD wavenumbers.

electron populations, confirming that the dominant source of hot electrons is TPD.

### 5.4.3 Conversion Efficiency & Energy Distribution

To examine overall hot electron production in this simulation, two final diagnostics of the hot-electron behaviour are now discussed.

The left panel of figure 5.12 shows the time-dependent hot electron flux through the laser exit boundary. The flux of particles recorded by the diagnostic have been grouped into broad energy bins, with the vertical scale showing the fraction of laser power delivered by flux in each bin. The  $E > 50\text{keV}$  and  $E > 100\text{keV}$  bins may be used for comparison against [Yan et al., 2014, figure 2 (d)]. The time-history shown in this figure can be understood in the context of the dynamics described in the previous section. Unfortunately this is somewhat complicated as the various energy bins each have an associated time-of-flight lag that differs according to the electron energy, direction of propagation and location of initial acceleration. In general however, all of these effects are expected to contribute to the electrons in higher energy bins reaching the diagnostic faster, which to an extent is visible in their initial rise.

The initial rise is composed mainly of electrons in the  $E > 100\text{keV}$  band, and is due to growth of instabilities near  $n_{\text{cr}}/4$  that produce EPWs with large phase velocities. The flux in this high-energy band rapidly drops as pump-depletion saturates the instabilities near  $n_{\text{cr}}/4$ , and TPD at progressively lower densities takes over hot-electron production. This produces electrons of successively lower energy due to the lower phase velocity waves involved. Finally, at  $\sim 5\text{ps}$ , the simulation enters a relatively steady state in which hot electron production is mostly in the lowest energy band, and the fluxes oscillate due to the bursts of TPD. Since these involve oscillations in the density at which peak absorption occurs, the characteristic temperature of the hot electron output varies in time, which can be seen as oscillations in the relative amplitude of the different fluxes.

In the right hand panel of figure 5.12, the time-averaged energy distribution of electrons travelling through the forward boundary is shown. Here the vertical scale indicates the energy contained in each bin as a fraction of that delivered by the laser. The measured distribution is shown in black, with the contribution from the thermal bulk shown in blue. The flux diagnostic records only particles with total energy above a threshold, so no data is available for the core of the distribution. It is clear from this figure that there are at least two distinct components to the suprathermal tail of the distribution. A three-temperature fit was found to closely match the majority of the distribution, and is marked by a purple dashed

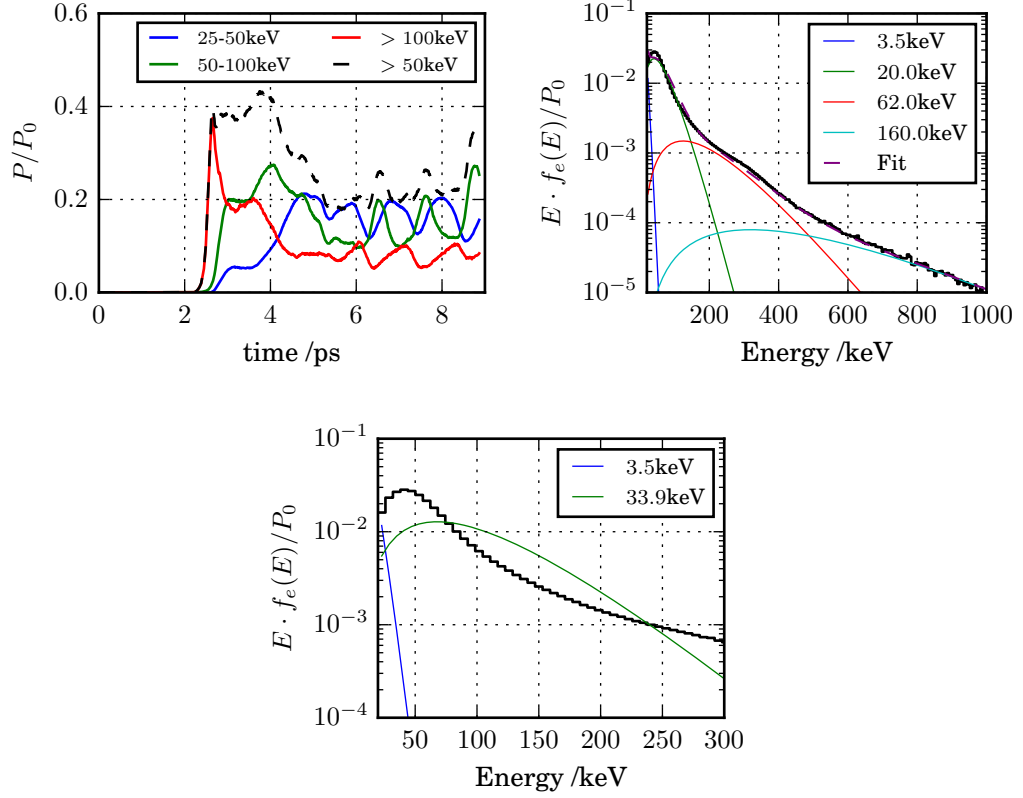


Figure 5.12: Flux of particles travelling through the laser exit boundary. **Left:** Instantaneous flux distribution integrated over different energy bins to produce time-histories of the power carried within these bins, normalised to the laser power. Flux from the bulk plasma in the lowest energy bin has been subtracted, and is negligible in higher-energy bins. **Right:** Flux distribution, time integrated over the whole simulation and weighted according to the energy of each bin. The  $y$ -axis normalisation is the total delivered laser energy. Curves plotted are simulation data (black), the expected thermal distribution (blue) and components of a multi-temperature fit to the hot-electron distribution (green, red and cyan). **Bottom:** Same as right, but showing low-energy range. Green line shows an energy-equivalent single-temperature fit to the multi-component version above.

line which is almost indistinguishable from the data. This fit was performed ‘by hand’, by first fitting the highest-energy section of the tail and adding lower-energy components in turn. The functions used for this fitting were thermal distributions, with characteristic temperatures obtained of 20keV, 62keV and 160keV. It is important to note however that these sub-populations are not truly ‘thermal’. These temperatures simply indicative of the typical energy of the electrons produced by acceleration from a given set of EPWs.

The distribution was integrated over different time intervals to identify these components. It was found that the low-temperature component only becomes prominent when TPD activity shifts to lower density, suggesting that this component is caused by TPD near the Landau cutoff. In a similar manner, the 60keV component was identified with TPD activity in the high-density plasma near  $n_{cr}/4$ . This may therefore be produced by cavitation and the turbulent, high phase-velocity EPW spectrum. The final component appears shortly after initial saturation (3-4ps) but diminishes slowly over the remainder of the simulation. Despite its high temperature, this component carries a small fraction of laser energy ( $\sim 1\%$ ). This is similar to the level of SRS scattering recorded by the reflectivity diagnostic, which suggests that it may be related to SRS, however further analysis would be required to confirm this.

To compute a single temperature that characterises the overall distribution, the temperatures  $T_i$  of the different components of the multi-temperature fit were combined into an ‘effective temperature’ using

$$T_{\text{eff}} = \frac{\sum_i F_i T_i}{\sum_i F_i}, \quad (5.6)$$

where  $F_i$  is the total energy flux of the component with  $T_i$ . This gives a temperature of  $T_{\text{ave}} \simeq 34\text{keV}$ . A hot electron population with this temperature is shown in the lower panel of figure 5.12. The size of the population shown was chosen so as to produce an equivalent energy flux to the multi-component fit and, while this calculation is in no way rigorous, produces a reasonable characterisation of the section of the distribution carrying the majority of energy. This low overall hot-electron temperature is a simple consequence of the location at which the instability is taking place; most TPD observed in the simulation occurs near the Landau cutoff where the EPW phase velocities expected from linear theory are relatively low. While the nonlinear saturation spectrum of TPD is somewhat different from what might be predicted from linear theory, these differences do not significantly alter the temperature of the resulting hot electron distributions.

## 5.5 Summary

One prominent feature of this simulation is the very high fraction of absorption, which is caused by TPD near the Landau cutoff. The time-averaged transmission fraction from 2.5ps until the end of the simulation is 23% (see figure 5.5), indicating that LPI is responsible for absorption of 77% of the laser’s energy. Since the plasma model is collisionless, energy delivered into EPWs is mostly delivered into hot electrons via Landau damping or collapse of cavities. Therefore as TPD is responsible for most absorption, a large portion of this energy should ultimately exit the domain as hot electrons, which would then mainly be seen at the forward boundary. This can be confirmed by summing and time-integrating the hot-electron fluxes measured in the left panel of figure 5.12, which indicates a hot-electron fraction of 41%.

Part of the motivation for performing this simulation was to examine the effect of collisions. A collision model was not enabled for any of the simulations performed in this project, in contrast to those performed in [Yan et al., 2014]. The results presented in that work, which otherwise bear close resemblance to ours, differ in the measured hot electron fraction. In particular the quoted energy fractions in the 50-100keV and  $> 100\text{keV}$  bins is given as 11% and 8% respectively. In our simulation these fractions are 16% and 11%; an overall increase of 45%. While this may partly be due to the longer duration over which their hot-electron fraction was measured, previous comparisons of collisional and collisionless simulations have also observed significant differences in hot-electron production. This was attributed to the partial suppression of ‘staged-acceleration’, in which individual electrons are accelerated by multiple EPWs of increasing phase velocity [Yan et al., 2012].

While it would therefore be desirable to include collisional behaviour, this was unfortunately not feasible for the simulations presented here. It is nevertheless encouraging that, while the hot-electron fraction measured is somewhat inflated, the behaviour observed in this simulation and that of [Yan et al., 2014] is otherwise consistent. If it is indeed the case that collisions lead to a reduction of staged electron acceleration, one might expect that this would lead to a reduced damping rate of the higher phase-velocity plasma waves involved. This may therefore lead to modified activity in the higher-density region of the simulation, but would not be expected to affect the low-phase velocity EPWs around the TPD Landau cutoff which are responsible for the majority of absorption.

Initial conditions for this simulation [Yan et al., 2014] were intended to reproduce those found in early OMEGA experiments investigating shock-ignition [Theobald et al., 2012]. In those experiments a series of shots was performed with

beam intensities varied between  $0.5\text{--}8 \times 10^{15} \text{Wcm}^{-2}$ . The beams were not overlapped and shots were taken with and without phase plates, though those with phase plates were only performed at an intensity of  $1.5 \times 10^{15} \text{Wcm}^{-2}$ . In the shots without phase plates, large SRS reflectivities were recorded of up to 24%, which was attributed to filamentation of the beams. Since this simulation used a uniform intensity profile, it is likely most representative of the shots with phase plates. In those, an SRS reflectivity of around 0.5% was recorded, the same as measured in the simulation (see figure 5.5), and an SBS reflectivity of  $\sim 5\%$ . The initial conditions in the simulation do not include a bulk velocity profile, which is important for modelling SRS, and the range of plasma densities simulated is smaller than those over which SRS can occur. These factors are likely why the SRS reflectivity measured in the simulation is smaller ( $\sim 1\%$ ). No  $3/2\omega$  signal (which is associated with TPD) was measured in the shots without phase plates, and a  $\sim 30\text{keV}$  hot electron temperature was recorded, consistent with absorption dominated by filamentation-driven SRS far below  $n_{\text{cr}}/4$ . In contrast, in the shots with phase plates, a  $3/2\omega$  signal was observed along with a marginally higher hot-electron temperature of  $\sim 40\text{keV}$  and a hard X-ray signal approximately twice as large as equivalent-intensity shots without phase plates. However, the diagnostic was not absolutely calibrated and so a hot electron fraction was not given. While the hot electron temperature measured is close to our effective temperature of  $34\text{keV}$ , it is unfortunate that the hot electron fraction was not recorded as this is a key prediction of the simulation.



## Chapter 6

# Ignition-scale Simulation

*This chapter contains results submitted for publication in Physics of Plasmas:*

A. G. Seaton & T. D. Arber, “Particle-in-Cell Simulations of Laser-plasma Instabilities in Long Scale-Length Plasmas Relevant to Shock-ignition”

In this chapter results are presented from a simulation in which parameters were chosen to represent ignition-scale shock-ignition (SI) experiments. Currently, igniting SI designs are expected to require a driver that can deliver energy on the order of that available at the National Ignition Facility. Unfortunately that laser system is currently configured for indirect-drive and has insufficient bandwidth to support the pulse shape required by many SI designs [Anderson et al., 2013]. Nevertheless, it is of interest to explore laser-plasma instabilities at this scale to begin to gain an understanding of their behaviour in this regime.

While there has been little work investigating LPI at SI intensities on the NIF, experiments have been performed to investigate these instabilities at lower intensities. The experiments and modelling done in this regime have found that while at smaller scale TPD was the main instability that was active, at NIF-scale SRS takes over instead [Rosenberg et al., 2018]. This was given preliminary theoretical justification in terms of the scaling of SRS and TPD absolute growth thresholds with temperature and density scale-length [Rosenberg et al., 2018]. Furthermore it was shown that absolute and convective SRS side-scatter are important [Michel et al., 2019].

The simulation examined in this section represents the first 2D simulation of LPI at shock-ignition intensities, and bears marked differences with the small-scale simulation, with SRS in particular found to play a much greater role here. Inter-

estingly, no evidence is found of  $90^\circ$  side-scatter, which is potentially a consequence of the laser polarisation chosen. This chapter is structured in a similar way to the previous chapter to aid comparison between the two. The simulation setup is first covered in section 6.1. Results are then described, again beginning with the initial growth and saturation in section 6.2. Longer-term development is described in section 6.3, where it is shown that kinetic inflation [Montgomery et al., 2002; Vu et al., 2002] plays an important role in the development of the SRS instability at these intensities. An analysis is performed of the resulting behaviour, with two mechanisms proposed to explain the dynamics that emerge. While kinetic inflation has been examined in great detail in prior large-scale studies of homogeneous indirect-drive plasmas, it has received more limited attention in a direct-drive context. This is therefore the first study in which this effect has been observed in a realistic large-scale direct-drive simulation. Finally, an analysis of hot electron production is given in section 6.4, and results are summarised in section 6.5.

## 6.1 Simulation Setup

The setup used for the NIF-scale case is similar to that used in the previous chapter. Rather than describe all of the initial conditions again, only the differences will be covered in this section. Parameters that are not mentioned here may be assumed to be the same as for the small-scale simulation and can therefore be found in section 5.1.

Plasma parameters for this case were based on reported values from direct-drive experiments on the National Ignition Facility [Rosenberg et al., 2018]. As such they may not be representative of a true shock-ignition experiment, however it is currently unclear as to how these parameters would differ from a conventional direct-drive shot. The parameters used were therefore an electron temperature of 4.5keV, along with a density scale-length of  $L_n = 600\mu\text{m}$ . Estimates of the ion temperature and bulk velocity profiles were not available so an electron-ion temperature ratio of  $T_e/T_i = 2$ , and a stationary plasma was again used.

Initial NIF-scale simulations were run that spanned a similar range of densities to the small-scale simulation in the previous chapter. Unfortunately however, spurious SRS occurred at the laser boundary and led to very little laser energy passing this point after the initial period of instability growth. This suggested that SRS from lower densities is important and that the range of densities simulated was insufficient. As a result the density range used for this case was considerably expanded by comparison to the smaller-scale simulations presented in this thesis. The

density profile chosen was a pure exponential, and spans  $0.10\text{--}0.26n_{\text{cr}}$ . This is shown in figure 5.1 along with the sub-scale cases. Due to the larger simulation domain and consequently longer time required for the laser and scattered light to traverse it, the simulation duration was 20ps to help ensure that the behaviour observed was not simply part of a transient phase.

In the small-scale case a laser rise time was used of 2ps. It was unclear what benefit this relatively lengthy rise had, so in this case the rise was shortened to 0.26ps to help reduce computational costs. All other laser parameters were kept the same.

The domain itself measured  $556 \times 19\mu\text{m}$ , and was composed of a grid of  $44200 \times 1500$  cells. This number of cells was determined by choosing the cell size to be  $1.2\lambda_{\text{D}}(n_{e,\text{max}})$  along both axes, where  $n_{e,\text{max}}$  is the maximum density encountered in the domain. This helps to avoid significant self-heating and ensures that the waves of interest are resolved. While the plasma parameters help reduce the computational cost in this regime (higher temperature results in larger  $\lambda_{\text{D}}$ , so larger cell size, and also longer time-step), the considerably larger domain size and simulation duration required made this by far the most costly simulation presented in this thesis. It was practically only possible to use around 2000 CPU cores, resulting in a total run-time of 45 days. This clearly is one of the major deficiencies in such self-consistent kinetic modelling - such simulations are unlikely to be of use for routine modelling of experiments. Furthermore there remain several sacrifices that must be made in terms of the physics modelled which mean that even these extremely detailed simulations do not capture all aspects that might be of interest. For example it would be desirable to have a fully 3D model, and to investigate much larger regions of plasma over hydrodynamic timescales ( $\delta t \sim 100\text{ps}$ ). Such modelling remains far out of reach despite recent advances in computing hardware.

## 6.2 Initial Behaviour

As in chapter 5, discussion of the initial behaviour of the simulation is split into an analysis of initial instability growth, and investigation of the initial mechanisms responsible for saturation.

### 6.2.1 Linear Growth

The left panel of figure 6.1 shows the  $k_y$  spectrum of the  $E_x$  field component during the simulation's linear growth phase, with a solid white line marking the wavenumbers for which TPD growth should be maximised. As in the small-scale case (figure

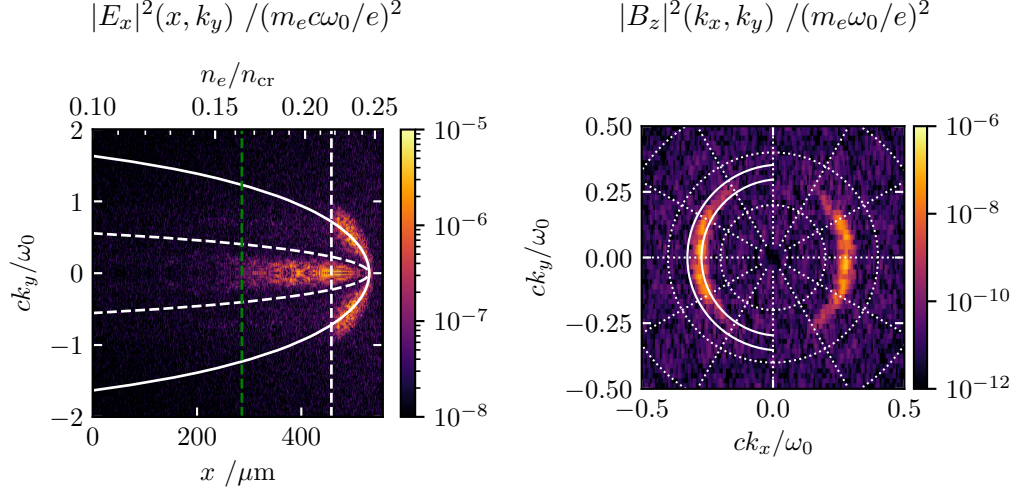


Figure 6.1: **Left:** Instantaneous  $k_y$  energy spectrum of the  $E_x$  field component during initial instability growth at 2.3ps. The laser wave-vector and  $\nabla n_e$  are parallel to the  $x$  axis while laser polarisation is along the  $y$  axis. The solid white curve indicates where maximal linear growth of TPD is expected at each density, while the dashed white curve indicates wavenumbers required for absolute  $90^\circ$  SRS side-scatter. The SRS observed has lower  $k_y$  and is therefore convective and at lower scatter angles. Dashed white and green lines mark the Landau cutoffs of TPD and SRS backscatter respectively. Both are in reasonable agreement with the data. **Right:** Instantaneous  $k_y$ - $k_x$  energy spectrum of  $B_z$  field component calculated from the same snapshot but using only data from between  $x = 350$ - $400\mu\text{m}$ . Arcs are EM waves from SRS back and side-scatter at angles of up to  $60^\circ$  from direct backscatter. Overlaid solid white curves mark bounds on the possible SRS backscatter wavenumbers for the relevant range of densities.

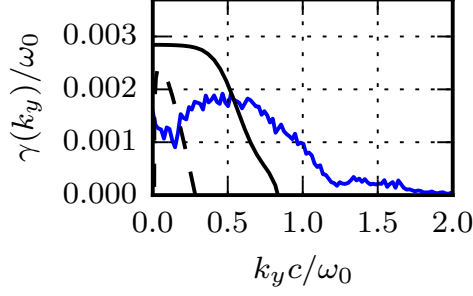


Figure 6.2: Measured TPD linear growth rate for NIF-scale simulation (blue). The solid black line indicates the theoretical inhomogeneous convective growth rate [Yan et al., 2010] including Landau damping, while the dashed black line indicates the theoretical absolute growth rates [Simon, 1983]. The observed growth shows better agreement with the range of wavenumbers where convective growth is expected to occur, but there is a large discrepancy in the values which is currently unexplained.

5.2) a feature is observed underneath this curve, indicating the presence of TPD. The dashed white line marks the TPD Landau cutoff ( $|\mathbf{k}|\lambda_D = 0.3$ ), and is in good agreement with the lower density bound of observed growth. To explore TPD growth further, its growth rates have again been measured using the method described in chapter 5, and are plotted in figure 6.2. Since the range of wavenumbers where growth occurs is again most consistent with those spanned by the convective theory (black solid line), growth is thought to be predominantly convective in nature.

The growth rates in figure 6.2 differ somewhat from the theoretical convective growth calculation. Two discrepancies are present. First, the range of wavenumbers where significant growth occurs is somewhat larger than is predicted by the theory. In particular, no growth is predicted to occur above  $0.8\omega_0/c$ , in contrast with the data where it is observed at up to  $\sim 1.25\omega_0/c$ . Note that the low amplitude signal above  $\sim 1.25\omega_0/c$  is due to noise from thermal fluctuations. A possible explanation for this is that the growth rates plotted are for the maximally growing TPD EPW wavenumbers at given  $k_y$ , and the calculation of this maximally growing wavenumber assumes no Landau damping. In fact at each density TPD grows over a spectrum of wavenumbers (as seen for example in the left panel of figure 6.1), so  $k_y$  does not uniquely determine the growth rate. Landau damping will affect regions of this wavenumber spectrum differently, so it is possible that the high  $k_y$  modes observed to grow in figure 6.2 are waves that do not lie on the maximally growing wavenumber curve and experience lower Landau damping rates. Secondly, there is also a prominent difference between the measured and predicted growth rates which

increases at small  $k_y$ . This is more difficult to explain, however it is possible that the difference is caused by relativistic effects, which might have become more important at this elevated temperature. Alternatively, there may be some interaction with SRS which has not been included. These issues are left for future investigation.

Features due to SRS are also visible in the  $k_y$  spectrum. SRS may occur as an absolute instability where the scattered EM waves are born near their turning point [Drake and Lee, 1973; Liu et al., 1974]. For backscatter ( $k_y = 0$ ) absolute instability is only possible at  $n_{\text{cr}}/4$ . At lower density, for the scattered light to be at its turning point the scatter angle must be  $90^\circ$ , requiring  $k_y \simeq (\omega_0/c)\sqrt{1 - 2\omega_{\text{pe}}/\omega_0}$ . These wavenumbers are plotted in the left panel of figure 6.1 as a dashed curve. None of the SRS activity observed in this simulation below  $n_{\text{cr}}/4$  lies on this curve, indicating that the modes excited are convective in nature. This lack of a  $90^\circ$ sidescatter signal may be due to the in-plane laser polarisation used, for which the sidescatter growth rate is minimised. A dashed green line in the electrostatic  $k_y$  spectrum in figure 6.1 marks the Landau cutoff for SRS backscatter. This is in reasonable agreement with the observed growth.

While no scattering occurs at  $90^\circ$ , the range of wavenumbers excited displays a significant spread in  $k_y$ . This is greater than would be expected for pure backscatter, and indicates that scattering occurs over a large range of angles. To examine the angular distribution of SRS scattering, the right panel of figure 6.1 shows the  $k_x$ - $k_y$  energy spectrum of the  $B_z$  field in the region  $x = 300\text{-}350\mu\text{m}$  using the same snapshot as for the  $k_y$  spectrum. Viewed on the logarithmic scale, it is evident that EM waves are present propagating at angles of up to approximately 60 degrees from  $k_x$ , though the majority of scattering is in fact at angles below  $30^\circ$ . A similar angular distribution is observed for the rest of the SRS activity in the domain at this time. Further analysis was performed to resolve the ambiguity in scattered light propagation direction, and verified that the light observed is purely backwards propagating ( $k_x < 0$ ).

### 6.2.2 Initial Saturation Effects

For TPD, saturation occurs in much the same way as was described in the small-scale case (see section 5.2.2). As before diagnostics are shown in figure 6.3 as space-time maps for the period between 1-3ps. The diagnostics shown are the laser and SRS light Poynting fluxes (left column), transverse-averaged electrostatic energy (upper right) and transverse-standard deviation of carbon ion density perturbations (lower right). Dashed lines mark the SRS backscatter and TPD Landau cutoffs, which are located at approximately  $0.16n_{\text{cr}}$  and  $0.21n_{\text{cr}}$  respectively. In the electrostatic

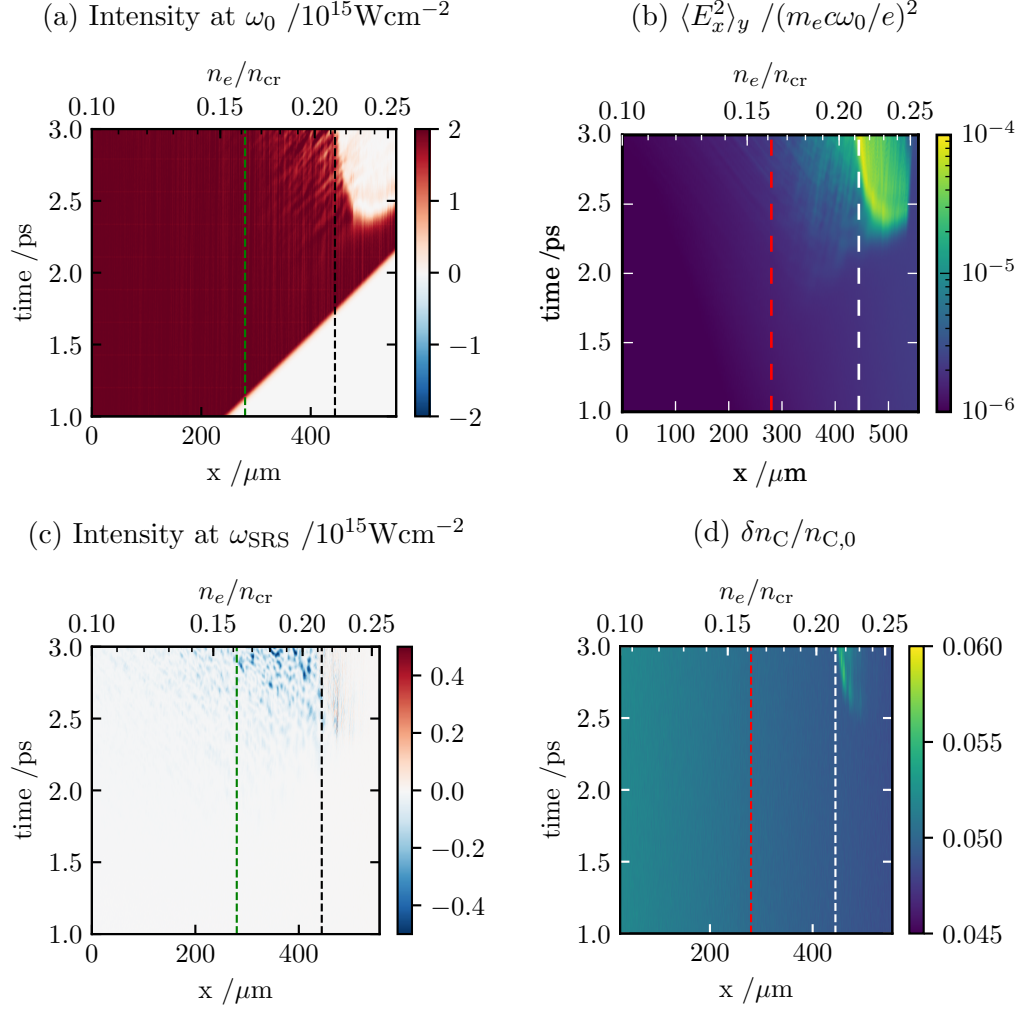


Figure 6.3: Diagnostics of initial LPI growth. **(a)**: Poynting flux filtered to include only waves at the laser frequency. **(c)**: Same, but for SRS scattered light frequencies. **(b)**: Transverse-averaged electrostatic wave energy. **(d)**: Transverse standard deviation of carbon density fluctuations.

field diagnostic, features due to TPD can be observed as the intense arc in the upper right hand corner. SRS is less prominent and produces EPWs of significantly lower amplitude; its presence can instead be discerned by the signals observed in the scattered light diagnostic.

It is clear from the Poynting flux and electrostatic field energy diagnostics that saturation of TPD is initially due to pump-depletion. The ion density perturbation diagnostic indicates that ion density perturbations are indeed driven, however as in the small-scale case these are observed to grow after the initial phase of saturation. Furthermore, close inspection of the differences in this diagnostic between figures 5.3 and 6.3 reveals that the ion density perturbations found in this case reach a lower amplitude than those driven in the small-scale case. This is partially due to the lower amplitude reached by the EPWs at saturation, but the higher thermal pressure resulting from NIF-scale parameters may also contribute. The ion density perturbations that are initially driven have a broadening effect on the EPW spectrum. This was discussed in detail in section 5.2.2; similar behaviour is observed here.

In-depth discussion of SRS behaviour is left until section 6.3.3. It is however of note that SRS activity, evident in the scattered light diagnostic of figure 6.3, develops progressively over several picoseconds. This timescale is longer than that on which SRS linear growth might be expected to occur. Additionally, while there is clearly pump-depletion occurring in the region where SRS takes place, it does not occur in the manner observed for TPD where the laser is almost completely absorbed. This suggests that pump-depletion is, at least at this stage in the simulation, less important to the saturation of SRS than other effects. Finally, the SRS activity observed is not sufficient to drive density perturbations; these are purely due to TPD.

## 6.3 Long-term Behaviour

### 6.3.1 Two-plasmon Decay

Over the course of the simulation, most laser energy is absorbed at densities below those where TPD is active ( $n < 0.19n_{\text{cr}}$ ) due to SRS and SBS activity. To examine how much energy is available to TPD, the laser Poynting flux diagnostic shown in figure 6.4 is examined. To aid in this, figure 6.5 shows lineouts taken from this



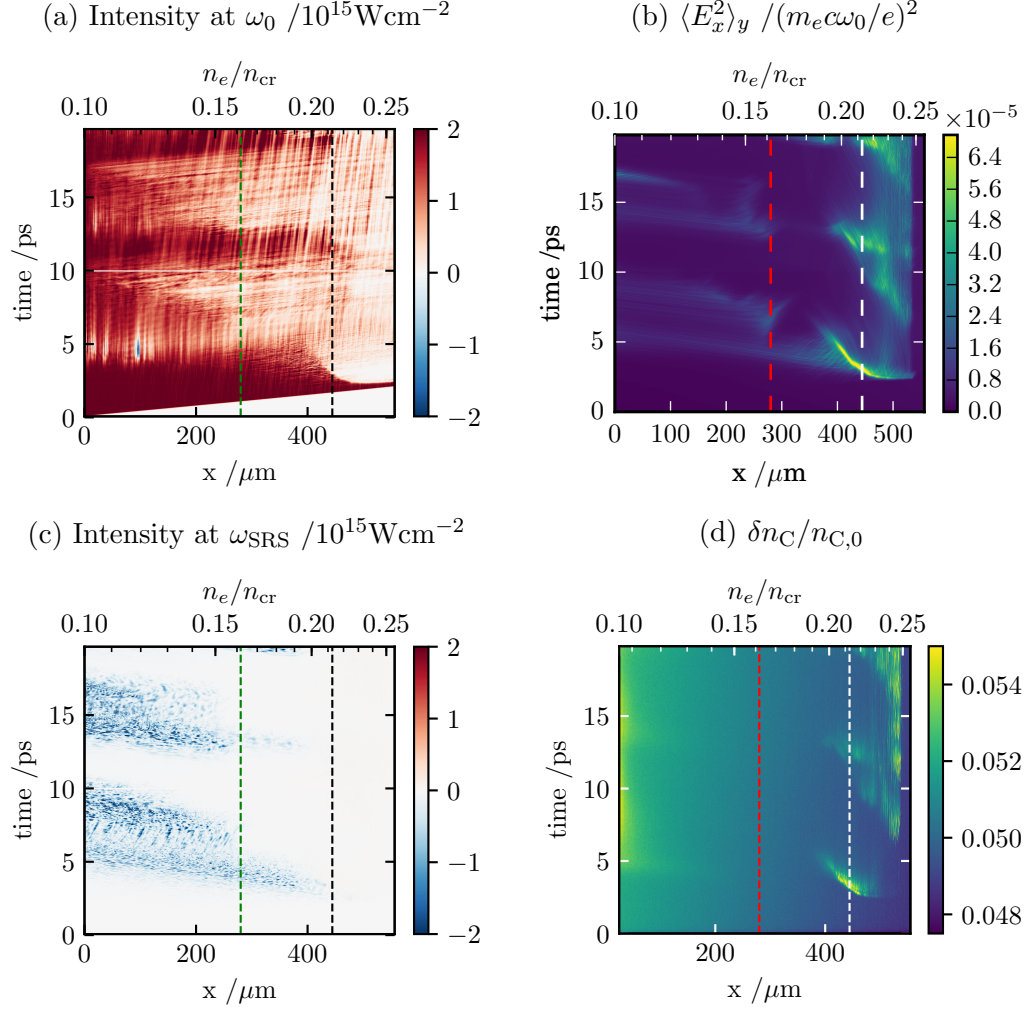


Figure 6.4: Diagnostics of initial LPI growth. **(a)**: Poynting flux along  $y = 0$ , filtered to include only waves at the laser frequency. **(c)**: Same, but for SRS scattered light frequencies. **(b)**: Transverse-averaged electrostatic wave energy. **(d)**: Transverse standard deviation of carbon density fluctuations.

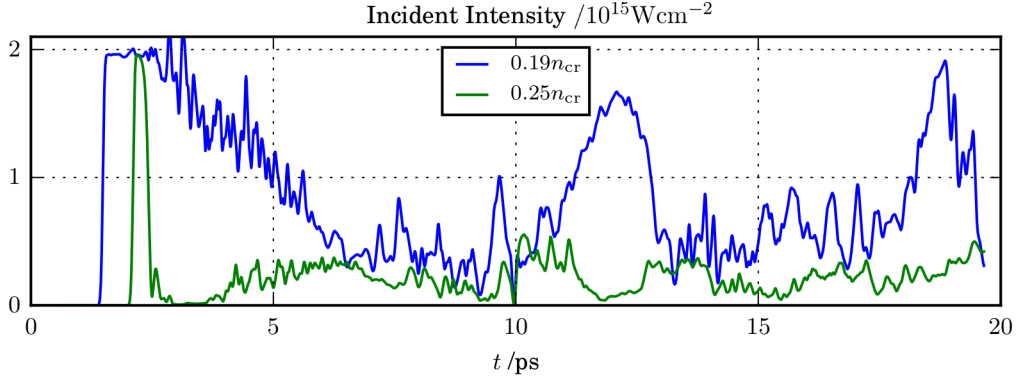


Figure 6.5: Lineouts from figure 6.4 (a) at the densities indicated. These show the incident intensity available to TPD ( $0.19n_{\text{cr}}$ ) and the remaining intensity at  $n_{\text{cr}}/4$ . Note that these intensities are measured at  $y = 0$  and so may not be representative of the intensity where  $y \neq 0$ .

diagnostic at  $0.19n_{\text{cr}}$  and  $0.25n_{\text{cr}}$  respectively<sup>1</sup>. During periods when absorption is dominated by scattering instabilities, the intensity reaching  $0.19n_{\text{cr}}$ , and therefore driving TPD, is around  $5 \times 10^{14} \text{Wcm}^{-2}$ . For reference the TPD absolute instability threshold is approximately  $1.7 \times 10^{14} \text{Wcm}^{-2}$  [Simon, 1983]. In contrast when the scattering instabilities are less active, the intensity reaching the TPD region rises significantly to  $15\text{--}19 \times 10^{14} \text{Wcm}^{-2}$ .

These swings in laser intensity lead to TPD exhibiting two distinct types of behaviour, which can be observed in the electrostatic energy diagnostic (fig. 6.4, upper right). At times when the incident intensity is low, TPD retreats to the region immediately adjacent to the quarter-critical surface where the wave damping rates are low but cavitation may occur. During lulls in the scattering instabilities' activity the incident intensity rises, and TPD becomes active over a larger region that extends down to the Landau cutoff. This latter behaviour is what defined the small-scale simulation of chapter 5.

As was previously discussed in chapter 5, EPWs produced by TPD may cause cavitation in the plasma near  $n_{\text{cr}}/4$ . This leads to a further kinetic energy dissipation mechanism when the cavities ultimately collapse and produce hot electrons. The transverse-averaged cavitation correlator was previously introduced to

<sup>1</sup>This diagnostic only measures Poynting flux at  $y = 0$ , so does not necessarily represent the intensities at other  $y$ . The transmitted power diagnostic (shown in the right panel of figure 6.8) measures intensity across the full domain width, and can be compared with the Poynting flux diagnostic lineout at  $n_{\text{cr}}/4$ .

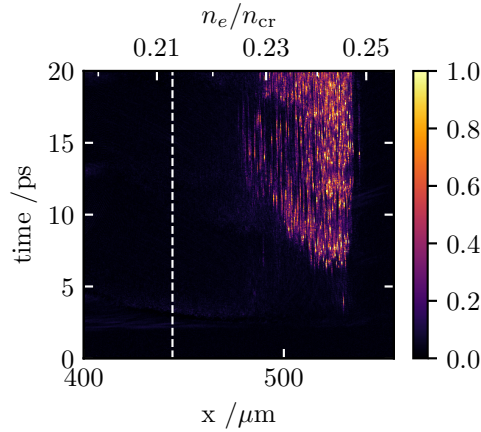


Figure 6.6: Transverse-averaged cavitation correlator. The white vertical line marks the TPD Landau cutoff. Values of the statistic that are above 0.5 indicate probable cavitation activity. Note that in this figure only a subset of the domain is shown; cavitation does not occur in the lower density plasma.

identify regions where this may be occurring, and is shown for this simulation in figure 6.6. Note that this figure only shows a section of the domain near  $n_{\text{cr}}/4$ ; the statistic is close to zero in all of the lower-density plasma. Figure 6.6 indicates that cavitation sets in relatively late in the simulation, at around 6ps. This delay is due to the almost complete pump-depletion from the initial TPD burst. Only after the conclusion of the first burst, which is itself ended by less extreme pump depletion from SRS and SBS, is a sufficient laser intensity able to reach  $n_{\text{cr}}/4$  to cause cavitation. Once this begins it persists for the remainder of the simulation, sustained by the low laser intensity reaching  $n_{\text{cr}}/4$ . From figure 6.6, cavitation activity can be seen to span a density range of approximately  $0.23\text{--}0.25n_{\text{cr}}$ .

At lower density, outside the cavitation region, ion density perturbations are also observed to grow during the bursts of TPD. These include both ‘transverse’ and ‘oblique’ spectral components. The oblique density perturbations again cause asymmetric TPD growth however the regular cycles that were observed in the previous simulation are disrupted by pump depletion from instabilities at lower density. When incident laser intensity drops, EPW energy in the vicinity of the TPD Landau cutoff also drops due to Landau damping, while persisting over a longer period in the plasma closer to  $n_{\text{cr}}/4$ .

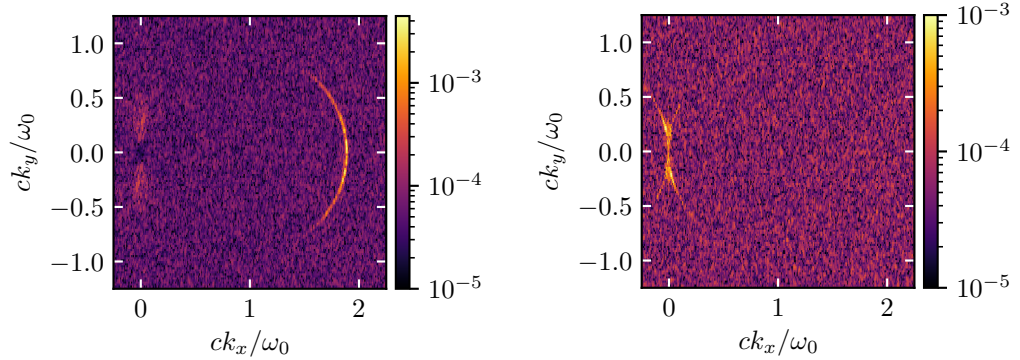


Figure 6.7: Carbon density perturbation spectra. **Left:** Evaluated between  $x = 50$ - $100\mu\text{m}$  at  $5.0\text{ps}$ . Arc visible at  $k_x \sim 1.8\omega_0/c$  is due to SBS backscatter. **Right:** Evaluated between  $x = 350$ - $400\mu\text{m}$  at  $14.0\text{ps}$ . Arc at  $\mathbf{k} \simeq \mathbf{0}$  is due to the filamentation instability; this is also visible at lower amplitude in the left panel.

### 6.3.2 Stimulated Brillouin Scattering & Filamentation

One instability which has been largely neglected in the discussion so far is SBS. This was not discussed earlier as it only becomes apparent relatively late in the simulation, some time after the laser first propagates through the domain and the other instabilities have undergone saturation. The reason for this is its slow growth rate in comparison to SRS and TPD which involve high-frequency waves. Furthermore, it is a convective instability here and therefore requires long propagation distances to cause significant energy transfer. This, in addition to high levels of pump-depletion, is likely why it was only responsible for very small scattered light fractions in the small-scale simulation.

Despite its slow onset, SBS scatters very significant fractions of the laser's energy in this simulation; a fraction which is likely to be elevated by comparison to experiments. This is due to the initial conditions used in which there is no imposed bulk plasma motion and therefore no velocity gradient. Including these more realistic initial conditions would create a spatially varying IAW Doppler shift that would act to reduce the possible convective amplification length available to SBS pulses.

SBS is difficult to diagnose as it produces light with almost no shift relative to the laser frequency, making it difficult to separate from the laser itself. Furthermore, the ion-acoustic waves it produces are largely charge-neutral and heavily damped

under these plasma conditions, so are difficult to observe in the electrostatic wave spectrum. While it is possible to see the effects of SBS indirectly through the reduction in measured Poynting flux at the laser frequency, we first confirm that it is taking place by examining the density fluctuation spectrum. This is shown in the left hand panel of figure 6.7, in which the  $k_x - k_y$  spectrum of the carbon density perturbations is plotted. This spectrum is calculated using data from  $x = 50\text{-}100\mu\text{m}$  at 5ps. An arc is visible in the spectrum that satisfies the SBS matching conditions – this is shown as the blue circle in figure 2.11. The arc is centred on  $\mathbf{k}_0 \simeq 2\omega_0/c$  which is consistent with SBS backscatter. As with the SRS observed in this simulation, SBS scatters over a wide range of angles, though the majority of scattered light energy is concentrated at relatively small angles.

The space-time map of carbon density perturbations shown in the lower right panel of figure 6.4 also shows density perturbations associated with SBS. These are visible as the diffuse bright features on the left hand side of the domain, and are particularly noticeable at the laser boundary. Unfortunately, this diagnostic only shows the largest amplitude IAWs driven by SBS; lower amplitude waves are obscured by the high level of background noise that is caused by thermal fluctuations. This issue is exacerbated by the increase of the thermal background at lower density. Nevertheless, comparison of this figure with the laser Poynting flux diagnostic (figure 6.4, upper left) indicates that SBS scatters significant fractions of the laser’s energy, particularly between 4-6ps and 13-15ps. Due to the convective nature of the instability, SBS is most effective when scattered light is able to traverse a large region of plasma. This is clear from the laser Poynting flux diagnostic since the peaks in SBS-scattered light occur after high laser intensities reach high densities ( $n > 0.2n_{\text{cr}}$ ). These initiate backwards-propagating SBS seed pulses that grow convectively as they travel back through the domain.

While diagnosing precisely where SBS occurs is difficult, it is more straightforward to measure the overall level of scattered light. This was achieved using the reflectivity diagnostic, by subtracting the injected laser power from the Poynting flux (at  $\omega_0$ ) at the laser boundary. The remaining signal must therefore be due to SBS and is shown as a function of time in figure 6.8, along with diagnostics of SRS scatter and laser transmission. This confirms that the IAW signals discussed above are indeed responsible for scattering significant fractions of the laser power, peaking at 70% and 40% during the first two bursts.

An associated effect that occurs throughout the simulation is filamentation. This may be thought of as ‘SBS forward-scatter’, and can be observed in the right hand spectrum of figure 2.11. This was evaluated using data from  $x = 350\text{-}400\mu\text{m}$

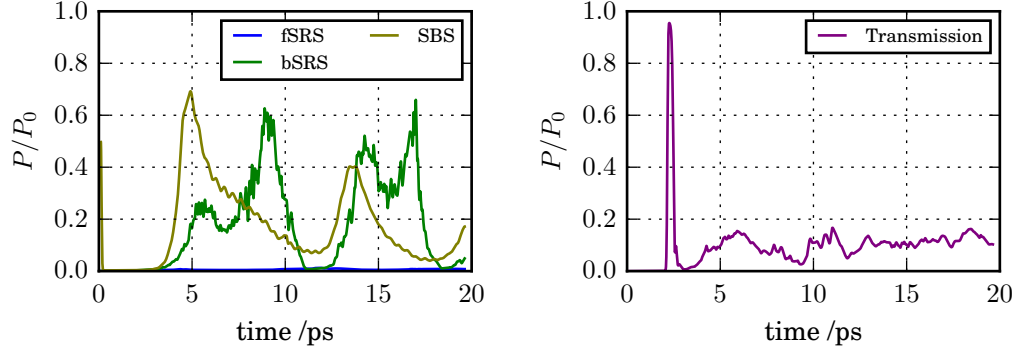


Figure 6.8: **Left:** Scattered light time-history. Green and olive lines measure SRS and SBS back-scatter detected at the laser entrance boundary. SRS forward-scatter measured at the laser exit boundary is shown by a blue line, however this remains at  $\sim 1\%$  for the duration of the simulation. **Right:** Transmitted light time-history. In both panels, the vertical scale is normalised to the maximum incident laser power, and a Gaussian filter has been applied to all signals to remove high-frequency noise with period shorter than 25fs.

at 14ps. The arc in the spectrum occurring at  $\mathbf{k} \simeq 0$  also satisfies the SBS matching conditions. In contrast with the SBS backscatter, these features grow in amplitude with increasing  $x$ . Filamentation activity is also evident in the laser Poynting flux diagnostic. In particular, it is visible as striations in the measured Poynting flux that are either stationary or move with a velocity much lower than  $c$ . The effect of filamentation is visible in this diagnostic due to the fact that it only records data along  $y = 0$ . If, as is the case for the reflectivity/transmission diagnostic, Poynting flux were averaged across the transverse extent of the domain these striations would not be seen.

Unlike SBS backscatter, filamentation is likely to be under-represented in these simulations. This is because the laser intensity profile used does not contain a laser speckle pattern. This intensity profile is found in all ICF lasers and provides the seed for filamentation, though is to some degree mitigated by temporal and polarisation smoothing. While it might be expected by the unnaturally uniform intensity profile used in the simulation that no filamentation would occur, some transverse intensity perturbations are introduced by SRS activity. This may explain the prominence of the filamentation that is observed.

### 6.3.3 Kinetic Inflation of SRS

In addition to SBS, large fractions of laser energy are scattered by SRS. This can be identified in the SRS scatter Poynting flux diagnostic (lower left, figure 6.4). Comparing this against the flux at the laser frequency (upper left, figure 6.4), it is apparent that following the bursts of SBS, pump depletion is also caused by SRS activity. This can also be seen in the reflectivity diagnostic in figure 6.8.

To identify where SRS is taking place, the electrostatic wave energy diagnostic is examined (upper right, figure 6.4). Since scattered light from SRS and SBS is emitted at oblique angles, this diagnostic also captures EM waves. These are visible as straight lines with velocity  $v_g \simeq -c$ , and propagate away from regions where SRS growth occurs. By comparing this with the SRS Poynting flux diagnostic, the regions where SRS light is emitted can be identified. This indicates that the instability is active in bursts, each of which begins at some initial density and propagates to successively lower densities. During these bursts instability growth is observed at low densities where Landau damping rates of the SRS EPW are high and significant growth would not be expected.

SRS is able to grow despite the anticipated large Landau damping rates due to the kinetic inflation process [Montgomery et al., 2002; Vu et al., 2002]. Here electron trapping in the electron plasma wave reduces its damping rate. Prior work has investigated this in great detail for the sparse, homogeneous plasmas relevant to indirect-drive experiments on the National Ignition Facility [Vu et al., 2002; Brunner and Valeo, 2004; Yin et al., 2006b,a, 2007; Vu et al., 2007; Yin et al., 2009, 2012, 2013, 2014]. In particular, it has been shown that the trapped particle population leads to the instability driving beam-acoustic modes (BAM), which have a lower damping rate and a downshift relative to EPWs [Yin et al., 2006b,a]. Following amplification, the resulting large amplitude electrostatic waves are unstable to the trapped particle modulational instability (TPMI) [Kruer et al., 1969]. This causes saturation of SRS via plasma wave break-up in 1D simulations [Brunner and Valeo, 2004], or EPW bowing and self-focusing in higher dimensions [Yin et al., 2007, 2008].

There has been more limited consideration of the kinetic inflation of SRS in inhomogeneous plasmas. Here it has been proposed that propagation of each of the daughter waves may lead to increased SRS gain. Considering the driven EPW, this would normally become detuned from three-wave resonance due to propagation into higher density plasma. However if the wave has the correct amplitude the trapped particle population it creates will allow it to retain its original wavenumber at higher density as a BAM. This process leads to ‘auto-resonant’ growth over a region larger than the Rosenbluth gain length [Chapman et al., 2010, 2012]. In

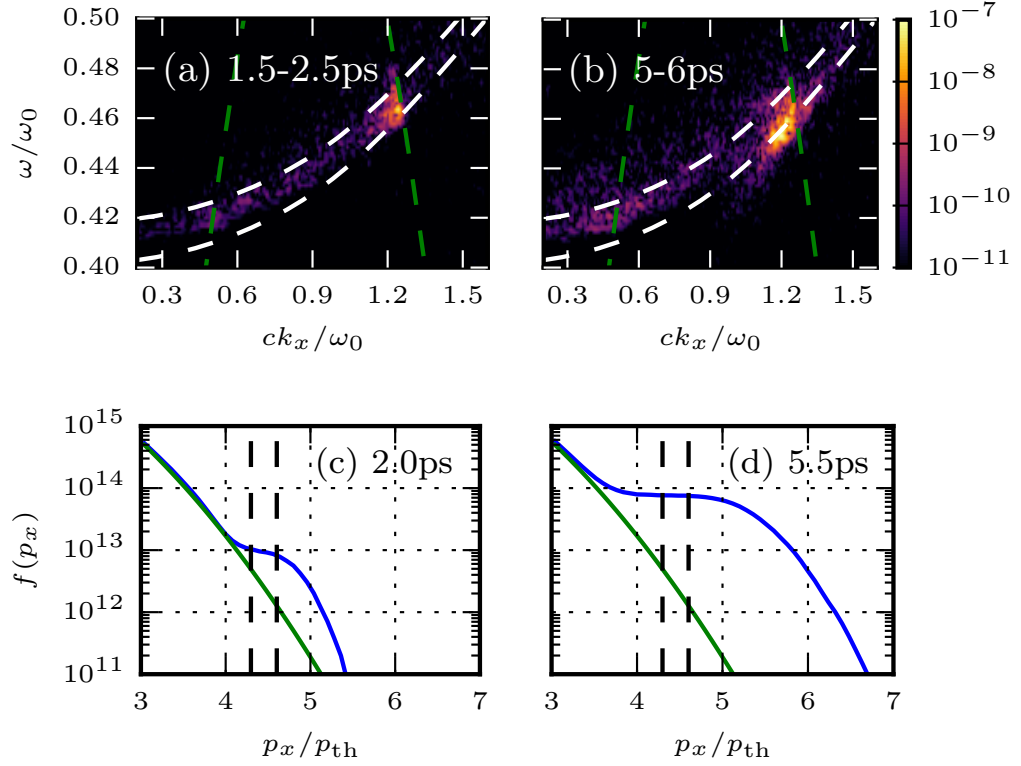


Figure 6.9: **(a)** and **(b)**:  $E_x$  field energy spectra, calculated along  $y = 0$  between 1.5-2.5ps and 5-6ps for the region  $x = 300-350\mu\text{m}$ . Colour scales are shared. White dashed lines indicate bounds on EPW wave frequencies possible within this region, while green dashed lines show the Stokes line. Instability occurs at the intersection of the Stokes line with electrostatic waves. **(c)** and **(d)**: spatially averaged electron distribution functions corresponding to each spectrum (blue lines). Range of EPW phase velocities marked by black dashed lines, distribution function at  $t = 0$  in green.

addition, propagation of backscattered light may also lead to increased SRS gain. If this is produced by scattering from BAMs then it will have a relative upshift. Therefore on propagation to lower density it may become resonant with EPWs and be further amplified [Yin et al., 2013].

To confirm that SRS here experiences inflationary growth, figure 6.9 shows data averaged over the region  $x = 300-350\mu\text{m}$  at two different times. In panels (a) and (b) the  $E_x$  field's  $\omega-k_x$  spectrum along  $y = 0$  is shown for  $t = 1.5-2.5\text{ps}$  and  $t = 5-6\text{ps}$  respectively. Dashed white lines indicate the bounding EPW frequencies for the density range within this region while dashed green lines mark the Stokes line, on which EM waves beat with the laser and ponderomotively drive electrostatic



waves. Locations where this crosses electrostatic modes are where SRS growth may occur. The corresponding spatially averaged instantaneous electron distribution functions are also shown, with the range of EPW phase velocities possible within the region indicated by vertical dashed lines. At both times considered, SRS-driven electrostatic waves have produced a suprathermal electron population. The growing size of this population, and of the flattened region of the distribution function, causes increasing deviation of the plasma's allowed electrostatic modes from those in a Maxwellian plasma. This is visible in the spectra as increases to the frequency downshift and wave amplitude, the latter of which is a consequence of the lower damping rate and hence higher attainable gain. The flattened distribution functions and downshifted SRS-driven electrostatic waves (beam-acoustic modes) are characteristic features of the kinetic inflation process [Yin et al., 2006b,a].

With reference to figure 6.4, the initial burst of SRS from  $\sim 2$ -6ps took place in plasma of density  $\sim 0.18$ - $0.22n_{\text{cr}}$ . It was prevented from occurring at higher density by the TPD-induced pump depletion. At this time there was little SRS activity at lower density plasma, despite this having had a greater period of time to grow since the laser propagated through. The burst ends when convective SRS near the laser boundary causes an additional wave of pump depletion to traverse the domain. Once the laser is able to propagate back through the domain relatively unattenuated a second burst of SRS occurs from  $\sim 6$ -9ps, however this time at significantly lower density ( $n_e \sim 0.12$ - $0.15n_{\text{cr}}$ ). Furthermore, the location of peak EPW amplitude during this second burst moves down the density profile with time. These observations suggest that SRS at lower density is somehow dependent on prior SRS activity at higher density.

Two mechanisms are identified that may be responsible for backwards motion of SRS activity. First, as discussed above, light scattered from beam-acoustic modes with an upshift relative to EPW-scattered light can act as a seed for SRS at lower density [Yin et al., 2013]. Generation of this upshifted scattered light is observed throughout the simulation. In figures 6.10 (a) and (c) the energy spectrum of the  $E_x$  field component along  $y = 0$  is shown for 2-3ps and 4-5ps respectively. Corresponding  $B_z$  energy spectra are shown in figures 6.10 (b) and (d). Assuming a Maxwellian electron distribution function, modes excited by direct back or forward-scatter SRS would grow along the dashed white and black curves respectively, with side-scatter SRS producing modes at intermediate frequencies. Over the course of the simulation no backwards-propagating scattered light is emitted with angle greater than  $\theta \simeq 60^\circ$  relative to direct backscatter; this limit is marked by red dashed lines. The small quantity of forward-propagating scattered light produced

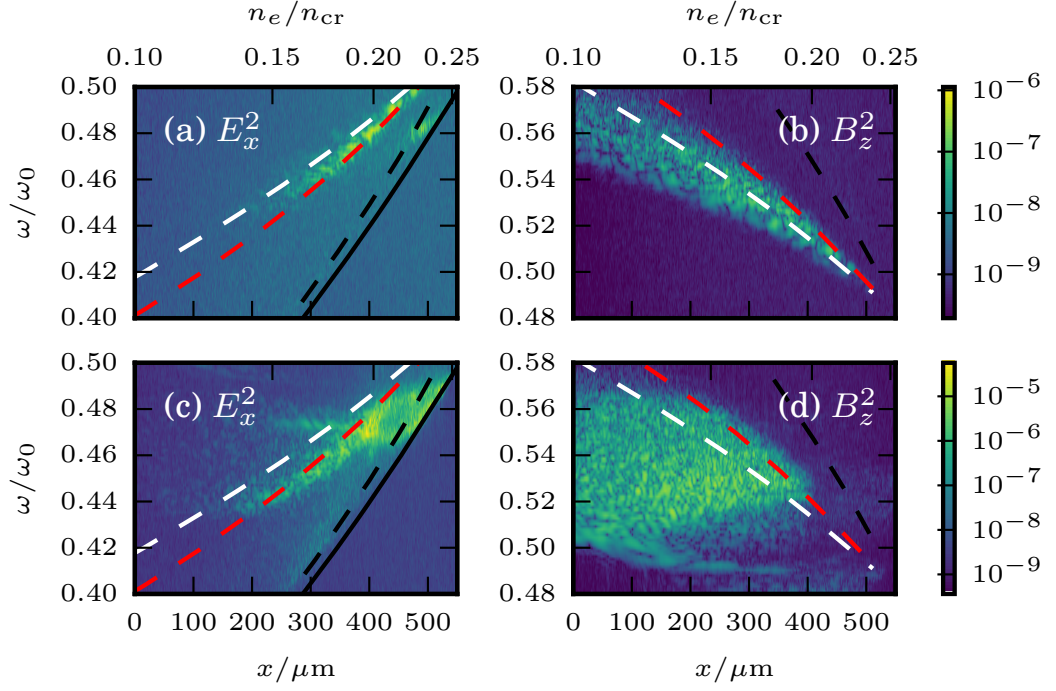


Figure 6.10:  $E_x$  (left column) and  $B_z$  (right column) field energy spectra, calculated along  $y = 0$  between 1.5-2.5ps (upper row) and 4-5ps (lower row). Colour scales are common on each row. White and black dashed lines indicate expected frequencies of EM and ES waves from back and forward-scatter SRS. Red dashed line corresponds to side-scatter at  $60^\circ$  from direct backscatter, the largest angle of scattered light relative to direct backscatter observed in the simulation. Solid black line in (a) and (c) marks  $\omega_{pe}$ . At 1.5-2.5ps, wave growth occurs between red and white dashed lines as expected. At 4-5ps, SRS electrostatic waves trap electrons leading to downshifted electrostatic waves and upshifted scattered light. Bright feature at  $x \simeq 400\mu\text{m}$  in (c) is backwards propagating TPD mode.

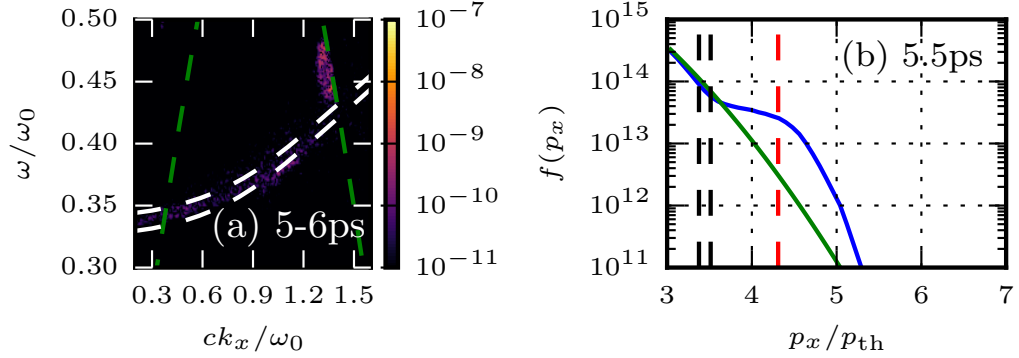


Figure 6.11: **(a)**:  $E_x$  energy spectrum along  $y = 0$  between  $t = 5$ -6ps and  $x = 50$ -100 $\mu\text{m}$ . **(b)**: Electron distribution function spatially averaged over the same region at 5.5ps. Waves visible in (a) are driven by the beating of the laser and SRS backscattered light. Beat frequencies are not natural frequencies of any electrostatic mode so are not driven to large amplitude, but are sufficient to produce the suprathermal electron population seen in (b). Black dashed lines in (b) bound possible phase velocities of SRS EPWs. Red dashed line marks largest phase velocity of waves visible in (a).

travels collinear with the laser. Therefore growth observed between the red and black dashed lines in both electrostatic and electromagnetic field components must be due to back or side-scatter SRS involving beam-acoustic modes. Immediately after the laser propagates through the domain, SRS scattered light and EPWs are produced that lie between the white and red lines (figures 6.10 (a) and (b)). Over time, the excited waves develop an increasing frequency shift due to the growing population of trapped electrons, leading to modes observed between the red and black dashed lines (figures 6.10 (c) and (d)). The resulting upshifted SRS light may be amplified further as it propagates to lower density, and may trigger further inflationary SRS growth there.

Even in the absence of a frequency upshift, backscattered light produced by SRS can trigger growth at lower density via a second nonlinear mechanism. As it propagates away from a perfect phase matching point, backscattered light beats with the laser and ponderomotively drives electrostatic waves. These have the same frequency as the initial electrostatic mode that produced the scattered light, but different wavenumber. If SRS occurs at density  $n_e$  with pump, EPW, and scattered EM wavenumbers  $k_0$ ,  $k$ , and  $k_s$  then at density  $n'_e$ , an ES wave is driven with wavenumber  $k'$  given by

$$k' = k'_0 - k'_s \simeq k \left[ 1 + \frac{\delta n_e}{n_{\text{cr}}} \frac{k_L^2}{k_0 k_s} \right], \quad (6.1)$$

where  $\delta n_e \equiv n'_e - n_e$ ,  $|\delta n_e| \ll n_{\text{cr}}$  and  $k_L \equiv \omega_0/c$ . Since  $\delta n_e < 0$  and  $k_s < 0$ , the driven ES wave has larger wavenumber ( $k' > k$ ). Figure 6.11 (a) shows the  $\omega - k_x$  spectrum of the  $E_x$  field component along  $y = 0$  between  $x = 50\text{-}100\mu\text{m}$  and  $t = 4\text{-}5\text{ps}$ . Unlike the spectra in figure 6.9, no SRS-driven EPWs are visible at the intersection of the Stokes line (green) with the EPW dispersion relation (white dashed lines). Instead, a spectral streak is visible along the stokes line at  $k \simeq 1.3\omega_0/c$  between  $\omega = 0.43\text{-}0.48\omega_0$  which corresponds to these ponderomotively driven waves. Since this frequency range is outside the allowed range for EPWs the waves are not natural modes of the plasma and so no parametric growth can occur. Nevertheless they are subject to Landau damping and produce a non-thermal electron population at their phase velocity  $v'_\phi$ . This may be approximated by

$$v'_\phi \equiv \frac{\omega'_{ek}}{k'} \simeq v_\phi \left[ 1 - \frac{\delta n_e}{n_{\text{cr}}} \frac{k_L^2}{k_0 k_s} \right], \quad (6.2)$$

where  $v_\phi \equiv \omega_{ek}/k$ . The resulting hot electron population therefore has lower velocity than the original EPW at  $n_e$ . Figure 6.11 (b) shows the electron distribution function spatially averaged over the region considered in 6.11 (a), in which this suprathermal population is clearly visible. Here dashed black lines mark the range of EPW phase velocities expected of SRS at this density, while the dashed red line indicates the maximum phase velocities of the modes in figure 6.11 (a). The accelerated electron population's velocity is therefore in good agreement with the phase velocities of the driven waves. This hot electron population will propagate up the density profile and reduce the gradient of the distribution function at  $v'_\phi$  at all higher densities. As  $v'_\phi < v_\phi$  this will match the local backscatter SRS EPW phase velocity at some intermediate density  $n''_e$  ( $n'_e < n''_e < n_e$ ), lowering its damping rate and increasing the attainable gain. Subsequent scattered light emission at  $n''_e$  may then cause the process to repeat, and lead to a cascade of SRS growth at successively lower densities.

Returning to figure 6.4 it is now possible to explain the dynamics observed. SRS back and side-scatter, along with SBS backscatter, produce intense backwards-propagating light when the laser reaches relatively high density plasma where the linear growth rates are large. SBS backscatter undergoes further convective growth as it returns to the laser boundary, and causes a wave of pump depletion to traverse the domain. Meanwhile the initial SRS undergoes kinetic inflation, producing increasingly upshifted scattered light. Following the SBS-induced pump depletion,

this SRS backscattered light causes a cascade of SRS growth at successively lower densities via the two mechanisms discussed above. At each point, the instability growth absorbs the majority of laser energy, terminating SRS and SBS growth at higher density. The ‘pulse’ of backwards propagating SRS activity is ultimately stopped, which in this simulation occurs simply due to the simulation boundary. This allows the laser to propagate to high density plasma and trigger another burst.

## 6.4 Hot Electrons

Effective energy-weighted hot electron distributions for outgoing particles were calculated using the method described in section 5.4.1. These were time-integrated over the simulation to produce figure 6.12. Compared with the equivalent figure in the small-scale case (figure 5.10), the form of the distribution is different. The four lobes produced by Landau damping of the TPD EPWs are less prominent, and a greater amount of energy is present in hot electrons propagating collinear with the laser. Both of these differences are suggestive of an increased contribution from SRS relative to that from TPD.

### 6.4.1 SRS Hot Electron Production

Identifying the sources of hot electrons is more straightforward in this case than for the small-scale simulation. This is because for the most part the instabilities take place in different locations. To determine the contribution of each instability to hot-electron production, the snapshots of particle data recorded in the bulk domain were used to calculate an inferred hot electron flux through a surface located at  $x = 350\mu\text{m}$  ( $\sim 0.18n_{\text{cr}}$ ). This data is not directly available from the standard diagnostics (discussed in section 3.3.1). This location roughly separates the regions where SRS and TPD are predominantly active, such that the forward-going hot electrons propagating through it must be due to SRS.

For ease of comparison it was desirable that this inferred data be in the same form as that output by the boundary hot electron flux diagnostic, which records the data associated with each particle crossing a surface over the output time interval ( $\Delta t_{\text{out}}$ ). To construct such a dataset, the particle data from the bulk domain at each output time  $t_{\text{out},i}$  was taken and advected over the output interval  $\Delta t_{\text{out}}$ . The data for particles found to cross the diagnostic surface during this period was then recorded as if it were the output from the particle flux diagnostic at time  $t_{\text{out},i+1}$ . In order to ensure that the output of this calculation is reasonable, the procedure was performed with a surface placed at  $x = 550\mu\text{m}$ , which is close to the laser exit

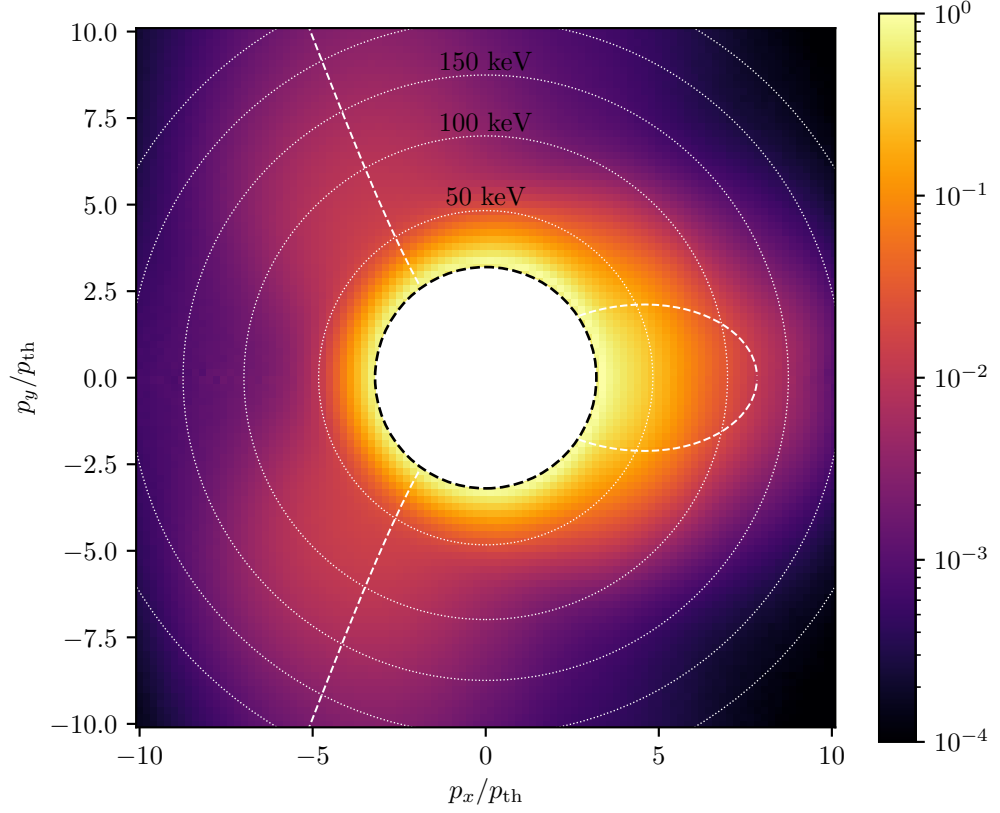


Figure 6.12: Inferred time-integrated distribution function, calculated from outgoing hot electron data using the method described in section 5.4.1. Time integration is performed over the entire simulation. Particle counts in each momentum bin have been weighted according to the energy of the bin. White dashed lines show the momenta expected of TPD-accelerated hot electrons, while the white circles indicate the particle energy at a given  $|\mathbf{p}|$ .

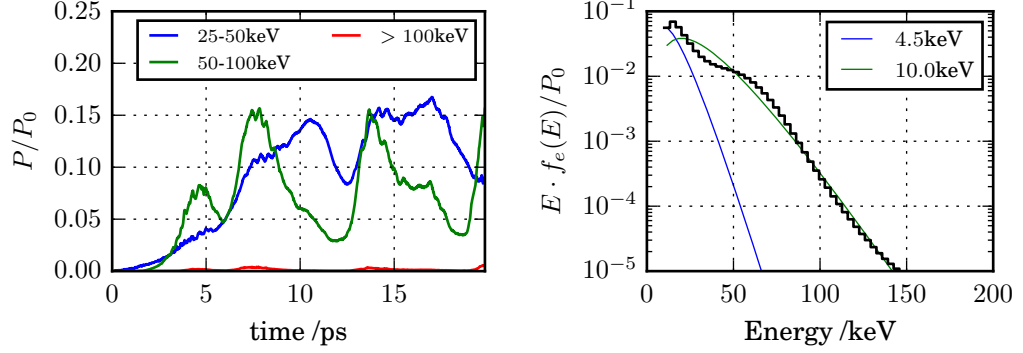


Figure 6.13: Flux of particles travelling in the forwards ( $+\hat{\mathbf{x}}$ ) direction through a surface at  $x = 350\mu\text{m}$  ( $\sim 0.18n_{\text{cr}}$ ), inferred from snapshots of high-energy electrons in the bulk plasma. These must be produced by SRS as TPD does not occur left of this surface. **Left:** Instantaneous flux distribution integrated over different energy bins to produce time-histories of the power carried within these bins, normalised to the laser power. Flux from the bulk plasma in the lowest energy bin has been subtracted, and is negligible in higher-energy bins. **Right:** Flux distribution, time integrated over the simulation and weighted according to the energy of each bin. The  $y$ -axis normalisation is the total delivered laser energy. Curves plotted are simulation data (black), the expected thermal distribution (blue) and a single-temperature fit to the hot-electron distribution (green).

boundary. Since acceleration by the EM fields is neglected in this calculation, one might expect there to be a significant error, however the output was found to closely match that of the boundary flux diagnostic. This is perhaps not surprising as at the laser exit boundary there tend not to be large electrostatic fields that might modify the fluxes. This is also true of the surface at  $x = 350\mu\text{m}$ . Furthermore, it might also be expected that while acceleration by the fields occurs on a very fast timescale of order  $\omega_{\text{pe}}$ , at most times in the simulation the hot electron population will have quickly reached a steady state and so varies over a longer timescale.

Figure 6.13 shows the analysis of the output of the calculation. The left hand panel shows the instantaneous flux from particles in different energy ranges, as a function of time and as a fraction of laser power. This matches the behaviour discussed in previous sections. In particular, there is notable correlation between the particle fluxes and the SRS reflectivity diagnostic (figure 6.8, green line). Additionally, at the start of each burst of SRS activity, the flux of electrons in the 25-50keV bin and 50-100keV bins rise together. Later in the burst, as the location of peak SRS emission moves to lower density, the 25-50keV flux remains approximately constant while that in the 50-100keV bin drops rapidly. It would be expected that, as

SRS activity shifts to lower density, the energy of the accelerated electrons would decrease in accordance with the phase velocity of the EPWs. The behaviour of the fluxes in these two energy bins is consistent with a hot electron temperature that reduces over the course of each burst.

The right hand panel of figure 6.13 shows the energy distribution of the particles within this dataset, time integrated over the duration of the simulation. The bins are weighted according to their energy, with the time-integrated laser power (i.e. total delivered laser energy) used to normalise the vertical axis. The simulation data is plotted in black, with the expected thermal component in blue and a fit to the suprathermal component shown as the green curve. While the fitted curve cannot be expected to precisely match the data, and indeed does deviate slightly, the hot electron output of the SRS activity matches remarkably well. The fit indicates a temperature of 10keV, which is close to that of the thermal bulk. This reflects the fact that the instability is active well below the Landau cutoff.

#### 6.4.2 TPD Hot Electron Production

Figure 6.14 shows analysis of the output of the particle flux diagnostic at the laser exit boundary. This includes fluxes from the regions in which SRS and TPD take place. Since the SRS hot electron flux has already been measured, it is tempting to simply subtract this from the total in order to isolate the TPD component. Careful comparison of the left panel of figures 6.13 & 6.14 (note the differing scales) shows that this would not give an accurate result. As a specific example of this, the inferred hot electron flux due to SRS at  $x = 350\mu\text{m}$  in the 25-50keV bin is at approximately  $0.15P_0$  between 13-17.5ps. The flux leaving the domain (at  $x \simeq 550\mu\text{m}$ ) is  $0.1P_0$  between 15-19ps, leaving a  $0.05P_0$  discrepancy. Some of this may be explained by the different time-of-flight delay of the electrons within the bin; 25keV and 50keV electrons would take 2.2ps and 1.6ps respectively to traverse the intermediate  $200\mu\text{m}$  (assuming purely  $x$ -directed momenta). However, it is also possible that this discrepancy is partially caused by further acceleration of some of these hot-electrons by the TPD EPWs in the high density region, many of which have phase velocities comparable to electrons of this energy.

Despite these complications it is nevertheless clear that, relative to the hot-electron flux at  $x = 350\mu\text{m}$ , TPD is responsible for producing a sizeable portion of the hot-electron population that leaves the domain. It is particularly noticeable from the time-integrated energy distributions that the overall temperature of the hot electrons is considerably increased at the exit boundary compared to  $x = 350\mu\text{m}$ . As with the small-scale case, the distribution of the electrons leaving the domain (right



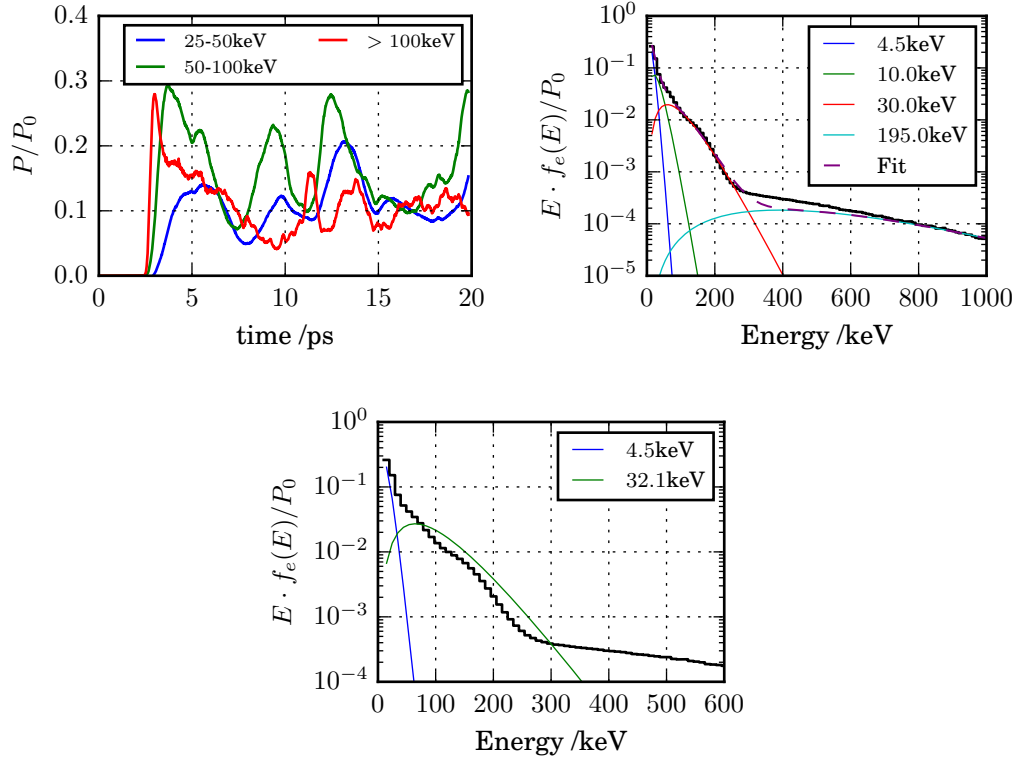


Figure 6.14: Flux of particles through the laser exit boundary. **Left:** Instantaneous flux distribution integrated over different energy bins to produce time-histories of the power carried within these bins, normalised to the laser power. Flux from the thermal component in the lowest energy bin has been subtracted, and is negligible in higher-energy bins. **Right:** Flux distribution, time integrated over the simulation duration and weighted according to the energy of each bin. The  $y$ -axis normalisation is the total delivered laser energy. Curves plotted are simulation data (black), the expected thermal distribution (blue) and a three-temperature fit to the suprathermal distribution (purple), along with the three separate components (green, red and cyan). **Bottom:** Same as right panel, but with a single-temperature fit used instead.

panel, figure 6.14) contains at least two distinct populations. A three-temperature fit has again been applied (purple, with components shown in green, red, and cyan lines) and indicates temperatures of 10keV, 30keV, and  $\sim 200\text{keV}$ . The lower-temperature component is most likely that observed at  $x = 350\mu\text{m}$  and generated by SRS, as this was the temperature identified for the SRS hot electrons. The 30keV component is due to TPD occurring near its Landau cutoff and, when the distribution is integrated over shorter periods, is found to be correlated with TPD activity. It is again unclear what is responsible for the hot 200keV component. Given that it is only observed in the particle fluxes at the laser exit, and not in those at  $x = 350\mu\text{m}$ , it cannot be caused by the backscatter SRS at lower density. It may therefore be a consequence of TPD or due to SRS forward-scatter, which is observed at low levels in the simulation. As in the small-scale case, this component accounts for  $\sim 1\%$  of laser power.

The effective temperature defined in chapter 5 was again calculated using the temperatures from the three-component fit. This results in a value of  $T_{\text{eff}} = 32\text{keV}$ , which is close to the value calculated for the small-scale case (34keV). A hot-electron distribution with equivalent hot electron energy flux as the original fit is shown in the lower panel of figure 6.14. This again produces a reasonable characterisation of the overall hot-electron distribution.

## 6.5 Summary

The results presented in this chapter are, to our knowledge, the first multi-dimensional kinetic simulations performed of LPI with parameters relevant to shock-ignition on the National Ignition Facility. They therefore provide a first indication of the type of behaviour that may be expected from experiments investigating this scheme. The analysis presented suggests that both the SRS and TPD instabilities could be important in this regime, in contrast with the results of the previous section. Despite this, both simulations produce similar hot-electron fluxes and effective hot-electron temperatures which are essentially the same (34keV and 32keV for the small and ignition-scale cases respectively). This is likely a reflection of the fact that TPD near its Landau cutoff is responsible for a significant fraction of hot electron production in both cases. Both instabilities that are active display a wide range of nonlinear effects which make the resulting behaviour highly complex and deserve further study.

The role of kinetic effects in the development of SRS in particular warrants further investigation. It was found here that the instability exhibits bursty behaviour. During each burst, SRS activity was seen to shift to lower density, with

the two possible mechanisms described that may be responsible for this. Both of these depend on backwards propagation of scattered light, which suggests that this behaviour could be sensitive to the beam’s speckle pattern, as has been found in simulations of indirect-drive plasmas [Yin et al., 2012]. Additionally, one of the characteristic features of this instability, at least in homogeneous plasmas, is the existence of a threshold intensity above which inflation occurs [Montgomery et al., 2002]. If this type of behaviour occurs for inhomogeneous plasmas then it could prove problematic for shock-ignition schemes, where such a threshold would likely be exceeded.

Several aspects of the initial conditions neglect effects that may be important, and motivate further investigation. The laser polarisation, which in this case was chosen to be in the simulation plane, results in a lower growth rate for sidescatter than the out of plane case. Since sidescatter has been found to be important in experiments at lower intensity [Michel et al., 2019], this may also have a prominent role at shock-ignition intensities. This could potentially reduce the intensity of light reaching  $n_{\text{cr}}/4$  and therefore the activity of TPD. Additionally, the ions were initialised without a bulk velocity (and therefore no velocity gradient), which resulted in high levels of SBS. Modelling SBS in a more realistic manner should therefore be a priority for future simulations. It would also be of interest to examine CBET, although the geometry required for this would necessitate a significant extension of the domain in (at least) the transverse direction. This would add significantly to the computational expense.

## Chapter 7

# Conclusion

The aim of this project was to investigate the behaviour of laser-plasma instabilities (LPis) in the context of shock ignition, and in particular how this changes at different target scales. Two large-scale PIC simulations are presented in this thesis. The first of these used plasma parameters representative of the small target scales that can be accessed on the OMEGA laser, while the second used parameters expected of ignition-relevant designs that require a megajoule-class laser such as the National Ignition Facility (NIF).

The ‘small-scale’ simulation was discussed in chapter 5 and had initial conditions identical to the ‘high-temperature’ case of [Yan et al., 2014], which are intended to model the well-diagnosed experiments of [Theobald et al., 2012]. The analysis presented in [Yan et al., 2014] was focused on long-term dynamics and did not explore details of LPI behaviour in great depth. Revisiting this case therefore provided a valuable opportunity for benchmarking our simulation code while improving on the understanding in this regime. The data presented in chapter 5 is largely in agreement with that of [Yan et al., 2014], which confirms that our simulation model is accurate. One aspect in which the results differ however is in the hot-electron fraction, which was found to be 45% larger in our simulation, despite having a very similar time-dependence and energy distribution. This discrepancy is likely caused by the omission of a collision module in our case, which has previously been found to suppress ‘staged-acceleration’ of electrons by multiple electron-plasma waves (EPWs) [Yan et al., 2012].

A comprehensive study of the LPI activity in the small-scale simulation was performed. This identified nonlinear effects that had not previously been reported. The simulation was characterised by high levels of LPI absorption, with only 23% of the laser’s energy transmitted through the domain. The two-plasmon-decay (TPD)

was found to be instability primarily responsible for this, while scattering instabilities (stimulated Raman scattering & stimulated Brillouin scattering) were together responsible for scattering only  $\sim 2\%$  of laser energy. Absorption due to TPD occurred primarily in the low-density region near the TPD Landau damping cutoff. TPD was also active closer to  $n_{\text{cr}}/4$ , where it was found to result in cavitating Langmuir turbulence. In the low density region near the TPD Landau cutoff the threshold amplitude for TPD EPWs to undergo cavitation is much larger. Dynamics there were instead found to be strongly influenced by coherent ion-acoustic waves (IAWs). The spectrum of IAWs was found to be composed of two features, having wavevectors either transverse to the laser wavevector (‘transverse density perturbations’) or oblique to it (‘oblique density perturbations’). The transverse waves have previously been associated with TPD saturation [Langdon et al., 1979; Yan et al., 2010], however the oblique waves have not been discussed in the literature in any detail. This latter type was identified as causing asymmetric EPW activity in the transverse direction, which should otherwise remain symmetric.

The effect of these coherent IAWs on TPD growth was investigated in chapter 4 via an analysis of the linear growth rates of the pairs of TPD waves that they couple. It was found that the coupling of pairs of TPD EPWs via IAWs leads each EPW pair to have a reduced growth rate. Above a threshold density perturbation amplitude no growth can occur. This type of analysis has previously been performed by Yan explain behaviour in simulations investigating TPD at lower intensities [Yan et al., 2010]. However, only transverse density perturbations were considered and the theory itself was not published. The calculations in chapter 4 are in agreement with the numerical values quoted in that prior work, and a simple expression is given to treat that case. However, this theory also permits calculation of the growth rate and therefore threshold density perturbation amplitude for an arbitrary pairing of TPD EPWs. These growth rates were explored for different special cases, including the oblique density perturbations discussed above. This indicated that, while transverse density perturbations become less effective in reducing TPD growth at lower density, the threshold density perturbation amplitude does not vary significantly for the oblique density perturbations.

The second simulation presented was analysed in chapter 6. This had parameters representative of recent direct-drive experiments on the NIF [Rosenberg et al., 2018]. At these larger scales it was found that scattering instabilities such as SRS and SBS become more prominent, and are able to disrupt TPD via pump-depletion. Despite this, TPD remained active in this case, and exhibited similar behaviour as was observed in the small-scale simulation. This included cavitation

in the region near  $n_{\text{cr}}/4$  and asymmetric growth in the low-density plasma near the Landau cutoff. It was found that the variation in laser intensity reaching the TPD region caused it to occur in bursts, in which its activity would expand to include the Landau cutoff. Periods of low laser intensity resulted in the instability retreating from this region since convective modes near the Landau cutoff require a large intensity to be sustained.

SRS activity in the ignition-scale simulation was found to involve kinetic inflation [Montgomery et al., 2002], allowing it to occur at densities well below the Landau cutoff. This has previously been found important for the largely homogeneous plasmas encountered in indirect-drive experiments, but has not been observed in direct-drive experiments. Its observation here suggests that it may be an issue for future shock-ignition designs using megajoule-scale lasers. Examination of the details of this inflationary SRS activity found that it occurred in bursts. These were initiated near the Landau cutoff and subsequently spread to progressively lower density before terminating at the laser entrance boundary. Backwards propagation of inflationary SRS activity has previously been described [Yin et al., 2012], however this occurred in homogeneous plasmas where the backwards-propagating scattered light remains close to the SRS resonant frequency as it propagates. In an inhomogeneous plasma the locally resonant frequency varies with density, so backwards propagating light may only be amplified by a fixed amplification factor over a limited range of densities [Rosenbluth, 1972]. Two possible mechanisms were invoked here to explain the backwards-propagating SRS activity. In the first mechanism, originally proposed by Yin [Yin et al., 2013], EPWs are downshifted due to electron trapping and produce upshifted backscattered light that can become resonant with plasma at a lower density. In the second mechanism, proposed by us, scattered light drives off-resonant electrostatic modes along its path. These produce small hot electron populations that can reduce the Landau damping rate experienced by SRS EPWs.

In both of the simulations presented hot electron production was dominated by instabilities occurring near their respective Landau cutoffs. Due to the phase velocity of the electron plasma waves at these densities this produced a hot-electron distribution composed mostly of low-energy hot electrons, though higher-energy populations from denser plasma were also present. This distribution could be characterised overall by an effective temperature in both cases; 34keV for the small-scale simulation and 32keV at NIF-scale. Similar hot electron temperatures have been measured in sub-scale experiments on the OMEGA laser [Theobald et al., 2012]. These relatively low temperature hot-electron distributions may be of benefit to

shock-ignition because the portion of the distribution with energy below  $\sim 100\text{keV}$  can be stopped in the dense shell behind the ignitor shock, which has been shown to strengthen it [Nora et al., 2015; Theobald et al., 2015]. However, despite the relatively low hot-electron temperature, there remained a significant amount of energy carried by electrons with energy greater than  $100\text{keV}$  ( $\sim 10\%$  of laser energy). Electrons with such energies can potentially pre-heat the target ahead of the ignitor shock, which would reduce its effectiveness.

Several routes are available for further investigation. While the initial conditions used here were chosen so as to be representative of as large a class of experiments as possible, we primarily examined the effect of target scale on LPI behaviour. It would therefore be of interest to determine whether the behaviour identified here is generic, or whether it is sensitive to the choice of other aspects of the initial conditions used. Experiments on the OMEGA laser have observed that SRS reflectivity and hot-electron fractions are affected by ablator material [Theobald et al., 2017]. In our simulations we found that the saturated state of the TPD instability is strongly influenced by IAWs, whose damping rate is sensitive to ablator material and the electron-ion temperature ratio. This suggests that an understanding of the effect of varying the IAW damping rate is an important avenue for further research. Of course, this is by no means the only parameter that can be varied; a high-dimensional parameter space remains to be explored.

Future studies could also improve on the realism of the modelling, though many of these improvements are unfortunately computationally expensive. From the small-scale case, which reproduced the high-temperature case from [Yan et al., 2014], it is clear that inclusion of collisional physics is important to hot-electron production – at least in terms of the hot-electron fraction. For realistic modelling of SBS it would be necessary to include bulk ion motion with a velocity gradient. Our modelling of the laser was purposefully simplistic so as to be generic, however one could model a laser speckle pattern, include laser temporal smoothing, and the effect of oblique laser incidence and beam overlap. Finally, it would be desirable to perform three-dimensional simulations, though this would require considerably greater computing resources than were available for this study.

In a different vein, an important aspect of this work is what impact the laser-plasma instabilities would have on a shock-ignition design. To determine this, one would need to perform radiation-hydrodynamic simulations of a shock-ignition implosion where a model was included that captures the instability behaviour identified here. This could then be used to ascertain what level of hot-electron induced target preheat may be tolerated, and how this varies with the strength of the ignitor

shock. A further issue is the high level of inflationary SRS backscatter identified in the NIF-scale case, and whether this is of net benefit. While the backscattered light itself represents a loss of energy, the particularly low-energy hot-electrons produced are likely to strengthen the ignitor shock. It is also possible that absorption by inflationary SRS backscatter in the low density plasma avoids TPD occurring near the quarter-critical density surface, that has the potential to produce hotter electrons that may contribute to target preheat.



## Appendix A

# The Coupled Mode Equations

*The derivation presented here was performed in collaboration with B. C. G. Reman.*

Here the coupled mode equations (equations 2.48-2.50) are solved for the specific case of a homogeneous medium and assuming no damping or depletion of the pump wave. Discussion of the result can be found in section 2.5.2.

### A.1 Derivation of The General Solution

We begin with the coupled mode equations neglecting damping and inhomogeneity:

$$[\partial_t + V_1 \partial_x] a_1(x, t) = \gamma_0 a_2^*(x, t)$$

$$[\partial_t + V_2 \partial_x] a_2^*(x, t) = \gamma_0 a_1(x, t)$$

First  $a_2^*$  is eliminated to give an equation reminiscent of the wave equation

$$[\partial_t + V_1 \partial_x] [\partial_t + V_2 \partial_x] a_1(x, t) = \gamma_0^2 a_1(x, t).$$

Applying the method of characteristics, or simply by noting that solutions to the coupled mode equations when  $\gamma_0 = 0$  are  $a_1(x, t) = F(x - V_1 t)$  and  $a_2^*(x, t) = G(x - V_2 t)$ , the following change of variables is used

$$u = x - V_1 t,$$

$$v = x - V_2 t.$$

Writing partial derivatives in terms of the new variables reduces the equation to

$$\partial_{u,v}a_1(u,v) = -\frac{\gamma_0^2}{4V_D^2}a_1(u,v), \quad (\text{A.1})$$

where  $V_D \equiv \frac{1}{2}(V_2 - V_1)$ . Assuming a separable solution of the form  $a_1(u,v) \equiv A(u)B(v)$  we find

$$\frac{\partial_u A}{A(u)} \frac{\partial_v B}{B(v)} = -\bar{\gamma}^2, \quad (\text{A.2})$$

where  $\bar{\gamma} = \gamma_0/2V_D$  and we ensure that  $V_2 > V_1$ . This means that without loss of generality

$$\frac{\partial_u A}{A(u)} = i\lambda\bar{\gamma}, \quad (\text{A.3})$$

$$\frac{\partial_v B}{B(v)} = \frac{i}{\lambda}\bar{\gamma}, \quad (\text{A.4})$$

where  $\lambda$  is an arbitrary constant. These ordinary differential equations may be solved to give

$$A(u) = C_1 e^{i\lambda\bar{\gamma}u}, \quad (\text{A.5})$$

$$B(v) = C_2 e^{\frac{i}{\lambda}\bar{\gamma}v}, \quad (\text{A.6})$$

with  $C_1$  and  $C_2$  constants of integration. This gives us the solution of equation A.1:

$$a_1(u,v) = C e^{i\bar{\gamma}[\lambda u + \frac{1}{\lambda}v]}. \quad (\text{A.7})$$

Returning to the original variables we now have

$$a_1(x,t) = C e^{i\bar{\gamma}[(\lambda + \frac{1}{\lambda})x - (V_1\lambda + V_2\frac{1}{\lambda})t]}. \quad (\text{A.8})$$

To find particular solutions to the PDE, linear combinations of this function must be used to construct the initial conditions at  $t = 0$ , i.e.  $a_1(x,0)$  and  $\partial_t a_1(x,0)$ . In general this needs to be done via a weighted integral over  $\lambda$  with  $C = C(\lambda)$ . This may be written in more conventional form by making the substitution  $k = \bar{\gamma}(\lambda + 1/\lambda)$  and noting that

$$\bar{\gamma}\lambda = \frac{k}{2} \pm \sqrt{\frac{k^2}{4} - 1}, \quad (\text{A.9})$$

$$\frac{\bar{\gamma}}{\lambda} = \frac{k}{2} \mp \sqrt{\frac{k^2}{4} - 1}. \quad (\text{A.10})$$

With this substitution the following two integrals are obtained

$$a_{1\pm}(x, t) = \int_{-\infty}^{\infty} e^{ikx} C_{\pm}(k) e^{-ikV_T t} e^{\pm t\sqrt{\gamma_0^2 - k^2 V_D^2}} dk, \quad (\text{A.11})$$

where  $V_T \equiv \frac{1}{2}(V_1 + V_2)$ . Combining these we then arrive at

$$a_1(x, t) = \int_{-\infty}^{\infty} e^{ikx} e^{-ikV_T t} \left[ C(k) \cosh \left( t\sqrt{\gamma_0^2 - k^2 V_D^2} \right) + S(k) \sinh \left( t\sqrt{\gamma_0^2 - k^2 V_D^2} \right) \right] dk, \quad (\text{A.12})$$

which evidently is an inverse Fourier transform. Specifying initial conditions as  $a_1(x, 0) = f(x)$  and  $\partial_t a_1(x, 0) = g(x)$  we then use their spatial Fourier transforms  $\hat{f}(k)$  and  $\hat{g}(k)$  to determine the weighting functions  $C(k)$  and  $S(k)$  as

$$C(k) = \hat{f}(k), \quad (\text{A.13})$$

$$S(k) = \frac{ikV_T \hat{f}(k) + \hat{g}(k)}{\sqrt{\gamma_0^2 - k^2 V_D^2}}. \quad (\text{A.14})$$

Given equations A.12–A.14, we can now produce particular solutions to the coupled mode equations however this still requires an integration to be performed. One simplification that may be made is to apply the convolution theorem

$$a_1(x, t) = \delta(x - V_T t) * \int_{-\infty}^{\infty} e^{ikx} \left[ C(k) \cosh \left( t\sqrt{\gamma_0^2 - k^2 V_D^2} \right) + S(k) \sinh \left( t\sqrt{\gamma_0^2 - k^2 V_D^2} \right) \right] dk, \quad (\text{A.15})$$

which suggests that the solution is composed of a pulse travelling at the mean group velocity of the two waves. Furthermore, the hyperbolic functions are both even in  $k$  so, depending on the parity of the functions  $\hat{f}(k)$  and  $\hat{g}(k)$  further deductions can

be made as to the parity of the result of the remaining integral.

## A.2 Solution for Delta Function Initial Conditions

To make further progress an initial condition is specified of  $f(x) = A_1\delta(x)$  and  $g(x) = -A_1V_1\delta(x)$  which represents an initial perturbation of the wave mode that has group velocity  $V_1$ . This gives  $C(k) = A_1$  and  $S(k) = ikA_1V_D/\sqrt{\gamma_0^2 - k^2V_D^2}$ . The solution now becomes

$$a_1(x, t) = A_1\delta(x - V_T t) * \int_{-\infty}^{\infty} e^{ikx} \left[ \cosh \left( t\sqrt{\gamma_0^2 - k^2V_D^2} \right) + \frac{ikV_D}{\sqrt{\gamma_0^2 - k^2V_D^2}} \sinh \left( t\sqrt{\gamma_0^2 - k^2V_D^2} \right) \right] dk, \quad (\text{A.16})$$

We now focus on the integral and write

$$I_c(x, t) = \int_{-\infty}^{\infty} e^{ikx} \cosh \left( t\sqrt{\gamma_0^2 - k^2V_D^2} \right) dk, \quad (\text{A.17})$$

$$I_s(x, t) = \int_{-\infty}^{\infty} e^{ikx} \frac{ikV_D}{\sqrt{\gamma_0^2 - k^2V_D^2}} \sinh \left( t\sqrt{\gamma_0^2 - k^2V_D^2} \right) dk. \quad (\text{A.18})$$

Normalising lengths to  $V_D/\gamma_0$  and times to  $\gamma_0^{-1}$  these become

$$\eta_c(X, T) = \int_{-\infty}^{\infty} e^{iKX} \cosh \left( T\sqrt{1 - K^2} \right) dK, \quad (\text{A.19})$$

$$\eta_s(X, T) = \int_{-\infty}^{\infty} e^{iKX} \frac{iK}{\sqrt{1 - K^2}} \sinh \left( T\sqrt{1 - K^2} \right) dK, \quad (\text{A.20})$$

where  $X$ ,  $K$  and  $T$  are the new dimensionless variables and  $\eta_j(X, T) \equiv I_j V_d / \gamma_0$  new functions. At this point we note that the function that is being inverse-transformed in  $\eta_s$  is proportional to the  $K$ -derivative of that in  $\eta_c$ . Applying the Fourier transform derivative identity this means that  $\eta_s = (X/T)\eta_c$ . Turning to  $\eta_c$  we split this into three separate integrals

$$\begin{aligned}
\eta_c(X, T) &= \int_{-\infty}^{-1} e^{iKX} \cos\left(T\sqrt{K^2-1}\right) dK \\
&\quad + \int_{-1}^1 e^{iKX} \cosh\left(T\sqrt{1-K^2}\right) dK \\
&\quad + \int_1^{\infty} e^{iKX} \cos\left(T\sqrt{K^2-1}\right) dK.
\end{aligned} \tag{A.21}$$

The first and last of these may be combined by using the substitution  $K' = -K$  in the first

$$\begin{aligned}
\eta_c(X, T) &= \int_{-1}^1 e^{iKX} \cosh\left(T\sqrt{1-K^2}\right) dK \\
&\quad + 2 \int_1^{\infty} \cos(KX) \cos\left(T\sqrt{K^2-1}\right) dK.
\end{aligned} \tag{A.22}$$

Then using the substitutions  $K = \cos \theta$  and  $K = \cosh \theta$  for the first and second integral we arrive at

$$\begin{aligned}
\eta_c(X, T) &= \int_0^{\pi} e^{iX \cos \theta} \cosh(T \sin \theta) \sin \theta d\theta \\
&\quad + 2 \int_0^{\infty} \cos(X \cosh \theta) \cosh(T \sinh \theta) \sinh \theta d\theta.
\end{aligned} \tag{A.23}$$

The above integrals can be written in terms of Hankel functions. To show this we start with the following formulae [NIS, Eq. 10.9.13-14]:

$$\begin{aligned}
\left(\frac{z+\zeta}{z-\zeta}\right)^{\frac{1}{2}\nu} J_{\nu}\left((z^2-\zeta^2)^{\frac{1}{2}}\right) &= \frac{1}{\pi} \int_0^{\pi} e^{\zeta \cos \theta} \cos(z \sin \theta - \nu \theta) d\theta \\
&\quad - \frac{\sin(\nu\pi)}{\pi} \int_0^{\infty} e^{-\zeta \cosh \theta - z \sinh \theta - \nu \theta} d\theta,
\end{aligned} \tag{A.24}$$

$$\begin{aligned}
\left(\frac{z+\zeta}{z-\zeta}\right)^{\frac{1}{2}\nu} Y_{\nu}\left((z^2-\zeta^2)^{\frac{1}{2}}\right) &= \frac{1}{\pi} \int_0^{\pi} e^{\zeta \cos \theta} \sin(z \sin \theta - \nu \theta) d\theta \\
&\quad - \frac{1}{\pi} \int_0^{\infty} \left(e^{\nu \theta + \zeta \cosh \theta} + e^{-\nu \theta - \zeta \cosh \theta} \cos(\nu \pi)\right) e^{-z \sinh \theta} d\theta.
\end{aligned} \tag{A.25}$$

Note that for convergence of the integrals with infinite limits  $\Re(z \pm \zeta) > 0$ . Defining the left or right hand sides of the equations as  $X_{J,\nu}(\zeta, z)$  and  $X_{Y,\nu}(\zeta, z)$ , we specialise to the case of  $\nu = 2\mu + 1; \mu \in \mathbb{Z}$  and find the quantity  $Z_\nu(\zeta, z) = \pi(X_{J,\nu} + iX_{Y,\nu})$ :

$$Z_\nu = \int_0^\pi e^{\zeta \cos \theta} e^{iz \sin \theta} e^{-i\nu\theta} d\theta - i \int_0^\infty e^{-z \sinh \theta} \left( e^{\nu\theta + \zeta \cosh \theta} - e^{-\nu\theta - \zeta \cosh \theta} \right) d\theta. \quad (\text{A.26})$$

Then to construct e.g. the  $\sin \theta$  component of the first integral in eq. A.23 take  $(Z_{-1} - Z_1)/2i$

$$\begin{aligned} \frac{Z_{-1} - Z_1}{2i} &= \int_0^\pi e^{\zeta \cos \theta} e^{iz \sin \theta} \sin \theta d\theta \\ &+ 2 \int_0^\infty \cosh(\zeta \cosh \theta) e^{-z \sinh \theta} \sinh \theta d\theta. \end{aligned} \quad (\text{A.27})$$

Now, choosing  $\zeta = iX$ ,  $z = \pm iT + \delta$ ,  $\delta \in \mathbb{R}$  and  $\delta > 0$ , we find that

$$\begin{aligned} \eta_c(X, T) &= \frac{1}{4i} \lim_{\delta \rightarrow 0} [(Z_{-1}(iX, -iT + \delta) - Z_1(iX, -iT + \delta)) \\ &+ (Z_{-1}(iX, iT + \delta) - Z_1(iX, iT + \delta))]. \end{aligned} \quad (\text{A.28})$$

The parameter  $\delta$  in the limit is necessary to ensure that the correct branch of the  $Z_\nu(\zeta, z)$  function is taken and that the integral is convergent. We now write this in terms of Hankel functions by using the LHS of equations A.24 & A.25. Using the definition of the Hankel function of the first kind  $H_\nu^{(1)}(\xi) \equiv J_\nu(\xi) + iY_\nu(\xi)$ , the function  $Z_\nu(\zeta, z)$  becomes

$$Z_\nu(\zeta, z) = \pi \left( \frac{z + \zeta}{z - \zeta} \right)^{\frac{1}{2}\nu} H_\nu^{(1)} \left( (z^2 - \zeta^2)^{\frac{1}{2}} \right). \quad (\text{A.29})$$

So

$$Z_\nu(iX, \pm iT + \delta) = \pi \left( \frac{T \pm (X - i\delta)}{T \mp (X + i\delta)} \right)^{\frac{1}{2}\nu} H_\nu^{(1)} \left( (X^2 - T^2 + \delta^2 \pm 2i\delta T)^{\frac{1}{2}} \right). \quad (\text{A.30})$$

Then taking the limit of  $\delta \rightarrow 0^+$

$$\lim_{\delta \rightarrow 0} Z_\nu(iX, \pm iT + \delta) = \begin{cases} i\pi \operatorname{sgn}(\nu X) \left(-\frac{T \pm X}{T \mp X}\right)^{\frac{1}{2}\nu} H_\nu^{(1)}\left((X^2 - T^2)^{\frac{1}{2}}\right), & |X| > |T| \\ \pi \left(\frac{T \pm X}{T \mp X}\right)^{\frac{1}{2}\nu} H_\nu^{(1)}\left(\pm i \operatorname{sgn}(T)(T^2 - X^2)^{\frac{1}{2}}\right), & |X| < |T|. \end{cases} \quad (\text{A.31})$$

Beginning with the case where  $|X| > |T|$  and for brevity writing  $Q_\pm \equiv -\frac{T \pm X}{T \mp X}$  and  $D \equiv \sqrt{X^2 - T^2}$  (note that  $Q_\pm$  and  $D$  are real and positive here), we substitute the expression into A.28:

$$\eta_c(X, T) = -\operatorname{sgn}(X) \frac{\pi}{4} \left[ \left( Q_-^{-\frac{1}{2}} H_{-1}^{(1)}(D) + Q_-^{\frac{1}{2}} H_1^{(1)}(D) \right) + \left( Q_+^{-\frac{1}{2}} H_{-1}^{(1)}(D) + Q_+^{\frac{1}{2}} H_1^{(1)}(D) \right) \right].$$

Noting that  $Q_\pm^{-\frac{1}{2}} = Q_\mp^{\frac{1}{2}}$  this can then be factorised

$$\eta_c(X, T) = -\operatorname{sgn}(X) \frac{\pi}{4} \left( Q_+^{\frac{1}{2}} + Q_-^{\frac{1}{2}} \right) \left( H_{-1}^{(1)}(D) + H_1^{(1)}(D) \right),$$

and applying the identity  $H_{\nu-1}^{(1)}(z) + H_{\nu+1}^{(1)}(z) = (2\nu/z)H_\nu^{(1)}(z)$  we find, somewhat anticlimactically, that

$$\eta_c(X, T) = 0, \quad |X| > |T|.$$

This result is expected from a physical standpoint as if the function were non-zero in the region where  $|X| > |T|$  it would violate causality.

For the case where  $|X| < |T|$ , taking  $P_\pm \equiv -Q_\pm = \frac{T \pm X}{T \mp X}$ ,  $\Delta \equiv \operatorname{sgn}(T)\sqrt{T^2 - X^2}$  and substituting the corresponding expression from A.31 into A.28

$$\eta_c(X, T) = \frac{\pi}{4i} \left[ \left( P_-^{-\frac{1}{2}} H_{-1}^{(1)}(-i\Delta) - P_-^{\frac{1}{2}} H_1^{(1)}(-i\Delta) \right) + \left( P_+^{-\frac{1}{2}} H_{-1}^{(1)}(i\Delta) - P_+^{\frac{1}{2}} H_1^{(1)}(i\Delta) \right) \right].$$

This can then be simplified using  $P_\pm^{-\frac{1}{2}} = P_\mp^{\frac{1}{2}}$  and the identity  $H_{-1}^{(1)}(z) = -H_1^{(1)}(z)$  to give

$$\eta_c(X, T) = i\pi \left( P_+^{\frac{1}{2}} + P_-^{\frac{1}{2}} \right) \left( H_1^{(1)}(-i\Delta) + H_1^{(1)}(i\Delta) \right), \quad |X| < |T|. \quad (\text{A.32})$$

Finally returning to our initial expression (equation A.16) and performing the convolution we may write the end result in terms of this function as

$$a_1(x, t) = \begin{cases} 0, & |X'| > |T|. \\ A_1 \frac{\gamma_0}{V_D} \left( 1 + \frac{X'}{T} \right) \eta_c(X', T), & |X'| < |T|. \end{cases} \quad (\text{A.33})$$

where for convenience the various quantities are defined:

$$X'(x, t) \equiv \frac{\gamma_0}{V_D} (x - V_T t), \quad (\text{A.34})$$

$$T(t) \equiv \gamma_0 t, \quad (\text{A.35})$$

$$P_{\pm}(X, T) \equiv \frac{T \pm X}{T \mp X}, \quad (\text{A.36})$$

$$\Delta(X, T) \equiv \sqrt{T^2 - X^2}. \quad (\text{A.37})$$



# Bibliography

- NIST Digital Library of Mathematical Functions. <http://dlmf.nist.gov/>, Release 1.0.23 of 2019-06-15. URL <http://dlmf.nist.gov/>.
- B. B. Afeyan and E. A. Williams. Stimulated Raman sidescattering with the effects of oblique incidence. *Physics of Fluids*, 28(11):3397, 1985. ISSN 00319171. doi: 10.1063/1.865340. URL <https://aip.scitation.org/doi/10.1063/1.865340>.
- Bedros B. Afeyan and Edward A. Williams. A variational approach to parametric instabilities in inhomogeneous plasmas III: Two-plasmon decay. *Physics of Plasmas*, 4(11):3827–3844, nov 1997a. ISSN 1070-664X. doi: 10.1063/1.872506. URL <http://aip.scitation.org/doi/10.1063/1.872507><http://aip.scitation.org/doi/10.1063/1.872506>.
- Bedros B. Afeyan and Edward A. Williams. A variational approach to parametric instabilities in inhomogeneous plasmas II: Stimulated Raman scattering. *Physics of Plasmas*, 4(11):3803–3826, nov 1997b. ISSN 1070-664X. doi: 10.1063/1.872505. URL <http://aip.scitation.org/doi/10.1063/1.872507><http://aip.scitation.org/doi/10.1063/1.872505>.
- K. S. Anderson, R. Betti, P. W. McKenty, T. J B Collins, M. Hohenberger, W. Theobald, R. S. Craxton, J. A. Delettrez, M. Lafon, J. A. Marozas, R. Nora, S. Skupsky, and A. Shvydky. A polar-drive shock-ignition design for the National Ignition Facility. *Physics of Plasmas*, 20(5):056312, 2013. ISSN 1070664X. doi: 10.1063/1.4804635. URL <http://scitation.aip.org/content/aip/journal/pop/20/5/10.1063/1.4804635>.
- T D Arber, K Bennett, C S Brady, A Lawrence-Douglas, M G Ramsay, N J Sircombe, P Gillies, R G Evans, H Schmitz, A R Bell, and C P Ridgers. Contemporary particle-in-cell approach to laser-plasma modelling. *Plasma Physics and Controlled Fusion*, 57(11):113001, 2015. ISSN 0741-3335. doi: 10.1088/

0741-3335/57/11/113001. URL <http://stacks.iop.org/0741-3335/57/i=11/a=113001?key=crossref.907aa156b73b99b125b1a0ae886c4c22>.

Stefano Atzeni and Jürgen Meyer-ter Vehn. *The Physics of Inertial Fusion*. Oxford University Press, jun 2004. ISBN 9780198562641. doi: 10.1093/acprof:oso/9780198562641.001.0001. URL <http://www.oxfordscholarship.com/view/10.1093/acprof:oso/9780198562641.001.0001/acprof-9780198562641>.

D. Batani, G. Malka, G. Schurtz, X. Ribeyre, E. Lebel, L. Giuffrida, V. Tikhonchuk, L. Volpe, A. Patria, P. Koester, L. Labate, L. A. Gizzi, L. Antonelli, M. Richetta, J. Nejd, M. Sawicka, D. Margarone, M. Krus, E. Krousky, J. Skala, R. Dudzak, A. Velyhan, J. Ullshmid, O. Renner, M. Smid, O. Klimo, S. Atzeni, A. Marocchino, A. Schiavi, C. Spindloe, T. O'Dell, T. Vinci, J. Wolowski, J. Badziak, T. Pysarcizck, M. Rosinski, Z. Kalinowska, and T. Chodukowski. Preliminary results from recent experiments and future roadmap to shock ignition of fusion targets. *Journal of Physics: Conference Series*, 399(Spig):1–8, 2012. ISSN 17426596. doi: 10.1088/1742-6596/399/1/012005.

D Batani, L Antonelli, S Atzeni, J Badziak, F Baffigi, T Chodukowski, F Consoli, G Cristoforetti, R. De Angelis, R Dudzak, G Folpini, L Giuffrida, L A Gizzi, Z Kalinowska, P Koester, E Krousky, M Krus, L. Labate, T Levato, Y Maheut, G Malka, D Margarone, A Marocchino, J Nejd, Ph Nicolai, T. O'Dell, T. Pisarczyk, O Renner, Y J Rhee, X Ribeyre, M Richetta, M Rosinski, M Sawicka, A Schiavi, J Skala, M. Smid, Ch Spindloe, J Ullschmied, A Velyhan, and T Vinci. Generation of high pressure shocks relevant to the shock-ignition intensity regime. *Physics of Plasmas*, 21(3):032710, mar 2014. ISSN 1070-664X. doi: 10.1063/1.4869715. URL <http://aip.scitation.org/doi/10.1063/1.4869715>.

D Batani, L Antonelli, F Barbato, G Boutoux, A. Colaitis, J.-L. Feugeas, G. Folpini, D. Mancelli, Ph. Nicolai, J. Santos, J. Trela, V. Tikhonchuk, J. Badziak, T. Chodukowski, K. Jakubowska, Z. Kalinowska, T. Pisarczyk, M. Rosinski, M. Sawicka, F. Baffigi, G. Cristoforetti, F. D'Amato, P. Koester, L.A. Gizzi, S. Viciani, S. Atzeni, A. Schiavi, M. Skoric, S. Gus'kov, J. Honrubia, J. Limpouch, O. Klimo, J. Skala, Y.J. Gu, E. Krousky, O. Renner, M. Smid, S. Weber, R. Dudzak, M. Krus, and J. Ullschmied. Progress in understanding the role of hot electrons for the shock ignition approach to inertial confinement fusion. *Nuclear Fusion*, 59(3):032012, mar 2019. ISSN 0029-5515. doi: 10.1088/1741-4326/aaf0ed. URL <http://stacks.iop.org/0029-5515/59/i=3/a=032012?key=crossref.d8b5eee3ab11e94e45fbd2a418e5fb50>.

- S. D. Baton, M. Koenig, E. Brambrink, H. P. Schlenvoigt, C. Rousseaux, G. Debras, S. Laffite, P. Loiseau, F. Philippe, X. Ribeyre, and G. Schurtz. Experiment in planar geometry for shock ignition studies. *Physical Review Letters*, 108(19):1–5, 2012. ISSN 00319007. doi: 10.1103/PhysRevLett.108.195002.
- S. D. Baton, E. Le Bel, S. Brygoo, X. Ribeyre, C. Rousseaux, J. Breil, M. Koenig, D. Batani, and D. Raffestin. Shock generation comparison with planar and hemispherical targets in shock ignition relevant experiment. *Physics of Plasmas*, 24(9):092708, 2017. ISSN 1070-664X. doi: 10.1063/1.4989525. URL <http://aip.scitation.org/doi/10.1063/1.4989525>.
- Ira B. Bernstein, John M. Greene, and Martin D. Kruskal. Exact Nonlinear Plasma Oscillations. *Physical Review*, 108(3):546–550, nov 1957. ISSN 0031-899X. doi: 10.1103/PhysRev.108.546. URL <https://link.aps.org/doi/10.1103/PhysRev.108.546>.
- R. Betti and O. A. Hurricane. Inertial-confinement fusion with lasers. *Nature Physics*, 12(May):435–448, 2016. ISSN 1745-2473. doi: 10.1038/nphys3736. URL <http://dx.doi.org/10.1038/nphys3736>.
- R. Betti, C. D. Zhou, K. S. Anderson, L. J. Perkins, W. Theobald, and A. A. Solodov. Shock ignition of thermonuclear fuel with high areal density. *Physical Review Letters*, 98(15):1–4, 2007. ISSN 00319007. doi: 10.1103/PhysRevLett.98.155001.
- R. Betti, W. Theobald, C. D. Zhou, K. S. Anderson, P. W. McKenty, S. Skupsky, D. Shvarts, V. N. Goncharov, J. A. Delettrez, P. B. Radha, T. C. Sangster, C. Stoeckl, and D. D. Meyerhofer. Shock ignition of thermonuclear fuel with high areal densities. *Journal of Physics: Conference Series*, 112(2):022024, may 2008. ISSN 1742-6596. doi: 10.1088/1742-6596/112/2/022024. URL <http://stacks.iop.org/1742-6596/112/i=2/a=022024?key=crossref.f469a4e2f6ca098fe38799883513c62a>.
- C. K. Birdsall and A. B. Langdon. *Plasma Physics via Computer Simulation*. Taylor and Francis, 1991. ISBN 9780750310253.
- T. R. Boehly, V. A. Smalyuk, D. D. Meyerhofer, J. P. Knauer, D. K. Bradley, R. S. Craxton, M. J. Guardalben, S. Skupsky, and T. J. Kessler. Reduction of laser imprinting using polarization smoothing on a solid-state fusion laser. *Journal of Applied Physics*, 85(7):3444–3447, apr 1999. ISSN 0021-8979. doi: 10.1063/1.369702. URL <http://aip.scitation.org/doi/10.1063/1.369702>.

- David Book. *NRL Plasma Formulary*. Naval Research Laboratory, 2018.
- J P Boris. Fourth conference on numerical simulation of plasmas. In *Numerical Simulation of Plasma*, number July, page 3, 1971.
- H.-S Bosch and G.M Hale. Improved formulas for fusion cross-sections and thermal reactivities. *Nuclear Fusion*, 32(4):611–631, apr 1992. ISSN 0029-5515. doi: 10.1088/0029-5515/32/4/I07. URL <http://stacks.iop.org/0029-5515/32/i=4/a=I07?key=crossref.499a5e49f8dde53d266bf4090e2da6c1>.
- S. I. Braginskii. Transport processes in a plasma. *Reviews of Plasma Physics*, 1: 205, 1965.
- Richard J. Briggs. *Electron-stream interaction with plasmas*. MIT Press, Cambridge, Mass., 1964. ISBN 9780262020114.
- S. Brunner and E. J. Valeo. Trapped-particle instability leading to bursting in stimulated Raman scattering simulations. *Physical Review Letters*, 93(14):2–5, 2004. ISSN 00319007. doi: 10.1103/PhysRevLett.93.145003.
- R. A. Cairns. The effect of wave reflection on induced Raman scattering in an inhomogeneous plasma. *Journal of Plasma Physics*, 12(01):169, aug 1974. ISSN 0022-3778. doi: 10.1017/S0022377800025009. URL [http://www.journals.cambridge.org/abstract/\\_S0022377800025009](http://www.journals.cambridge.org/abstract/_S0022377800025009).
- R. A. Cairns. *Plasma Physics*. Blackie & Son Ltd., 1985. ISBN 0-216-91779-4.
- K.M Case. Plasma oscillations. *Annals of Physics*, 7(3):349–364, jul 1959. ISSN 00034916. doi: 10.1016/0003-4916(59)90029-6. URL <https://linkinghub.elsevier.com/retrieve/pii/0003491659900296>.
- T. Chapman, S. Hüller, P. E. Masson-Laborde, W. Rozmus, and D. Pesme. Spatially autoresonant stimulated Raman scattering in inhomogeneous plasmas in the kinetic regime. *Physics of Plasmas*, 17(12):122317, dec 2010. ISSN 1070-664X. doi: 10.1063/1.3529362. URL <http://aip.scitation.org/doi/10.1063/1.3529362>.
- T. Chapman, S. Hüller, P. E. Masson-Laborde, A. Heron, D. Pesme, and W. Rozmus. Driven Spatially Autoresonant Stimulated Raman Scattering in the Kinetic Regime. *Physical Review Letters*, 108(14):145003, apr 2012. ISSN 0031-9007. doi: 10.1103/PhysRevLett.108.145003. URL <https://link.aps.org/doi/10.1103/PhysRevLett.108.145003>.

- D. S. Clark, C. R. Weber, J. L. Milovich, J. D. Salmonson, A. L. Kritcher, S. W. Haan, B. A. Hammel, D. E. Hinkel, O. A. Hurricane, O. S. Jones, M. M. Marinak, P. K. Patel, H. F. Robey, S. M. Sepke, and M. J. Edwards. Three-dimensional simulations of low foot and high foot implosion experiments on the National Ignition Facility. *Physics of Plasmas*, 23(5):056302, may 2016. ISSN 1070-664X. doi: 10.1063/1.4943527. URL <http://aip.scitation.org/doi/10.1063/1.4943527>.
- T. P. Coffey. Breaking of Large Amplitude Plasma Oscillations, 1971. ISSN 00319171. URL <http://scitation.aip.org/content/aip/journal/pof1/14/7/10.1063/1.1693620>.
- G Cristoforetti, A Colatis, L Antonelli, S Atzeni, F Baffigi, D Batani, F Barbato, G Boutoux, R Dudzak, P Koester, E Krousky, L Labate, Ph Nicola, O Renner, M Skoric, V Tikhonchuk, and L A Gizzi. Experimental observation of parametric instabilities at laser intensities relevant for shock ignition. *EPL*, 117, 2017.
- G. Cristoforetti, L. Antonelli, S. Atzeni, F. Baffigi, F. Barbato, D. Batani, G. Boutoux, A. Colaitis, J. Dostal, R. Dudzak, L. Juha, P. Koester, A. Marocchino, D. Mancelli, Ph Nicolai, O. Renner, J. J. Santos, A. Schiavi, M. M. Skoric, M. Smid, P. Straka, and L. A. Gizzi. Measurements of parametric instabilities at laser intensities relevant to strong shock generation. *Physics of Plasmas*, 25(1):012702, jan 2018. ISSN 1070-664X. doi: 10.1063/1.5006021. URL <http://aip.scitation.org/doi/10.1063/1.5006021>.
- J. M. Dawson and R. Shanny. Some Investigations of Nonlinear Behavior in One-Dimensional Plasmas. *Physics of Fluids*, 11(7):1506, 1968. ISSN 00319171. doi: 10.1063/1.1692136. URL <https://aip.scitation.org/doi/10.1063/1.1692136>.
- John M. Dawson. Nonlinear Electron Oscillations in a Cold Plasma. *Physical Review*, 113(2):383–387, jan 1959. ISSN 0031-899X. doi: 10.1103/PhysRev.113.383. URL <https://link.aps.org/doi/10.1103/PhysRev.113.383>.
- R. O. Dendy. *Plasma Dynamics*. Oxford University Press, 1990. ISBN 0-19-851991-5.
- T. R. Dittrich, O. A. Hurricane, D. A. Callahan, E. L. Dewald, T. Döppner, D. E. Hinkel, L. F. Berzak Hopkins, S. Le Pape, T. Ma, J. L. Milovich, J. C. Moreno, P. K. Patel, H. S. Park, B. A. Remington, J. D. Salmonson, and J. L. Kline. Design of a high-foot high-adiabat ICF capsule for the national ignition facility. *Physical*

*Review Letters*, 112(5):1–5, 2014. ISSN 00319007. doi: 10.1103/PhysRevLett.112.055002.

J. F. Drake and Y. C. Lee. Temporally Growing Raman Backscattering Instabilities in an Inhomogeneous Plasma. *Physical Review Letters*, 31(19):1197–1200, nov 1973. ISSN 0031-9007. doi: 10.1103/PhysRevLett.31.1197. URL <https://link.aps.org/doi/10.1103/PhysRevLett.31.1197>.

D. F. DuBois, D. A. Russell, and Harvey A. Rose. Saturation Spectra of the Two-Plasmon Decay Instability. *Physical Review Letters*, 74(20):3983–3986, may 1995. ISSN 0031-9007. doi: 10.1103/PhysRevLett.74.3983. URL <https://link.aps.org/doi/10.1103/PhysRevLett.74.3983>.

D F DuBois, Harvey A Rose, and David Russell. Saturation of radiation-induced parametric instabilities by excitation of Langmuir turbulence. *Physica Scripta*, T63(1):16–27, jan 1996. ISSN 0031-8949. doi: 10.1088/0031-8949/1996/T63/002. URL <http://iopscience.iop.org/1402-4896/1996/T63/002><http://stacks.iop.org/1402-4896/1996/i=T63/a=002?key=crossref.55a218e984718da11de054069968dddf>.

T.Zh. Esirkepov. Exact charge conservation scheme for Particle-in-Cell simulation with an arbitrary form-factor. *Computer Physics Communications*, 135(2):144–153, apr 2001. ISSN 00104655. doi: 10.1016/S0010-4655(00)00228-9. URL <http://www.sciencedirect.com/science/article/pii/S0010465500002289>[http://www.sciencedirect.com/science?\\_ob=ImageURL&\\_cid=271575&\\_user=1553416&\\_pii=S0010465500002289&\\_check=y&\\_origin=&\\_coverDate=01-Apr-2001&view=c&wchp=dGLbVlS-zSkzV&md5=e6d6965007](http://www.sciencedirect.com/science?_ob=ImageURL&_cid=271575&_user=1553416&_pii=S0010465500002289&_check=y&_origin=&_coverDate=01-Apr-2001&view=c&wchp=dGLbVlS-zSkzV&md5=e6d6965007).

Henry E. Fettis, James C Caslin, and Kenneth R Cramer. Complex Zeros of the Error Function and of the Complementary Error Function. *Mathematics of Computation*, 27(122):401, apr 1973. ISSN 00255718. doi: 10.2307/2005630. URL <http://www.jstor.org/stable/2005630><https://www.jstor.org/stable/2005630?origin=crossref>.

D. W. Forslund, J. M. Kindel, and E. L. Lindman. Theory of stimulated scattering processes in laser-irradiated plasmas. *Physics of Fluids*, 18(8):1002, feb 1975. ISSN 00319171. doi: 10.1063/1.861248. URL <http://dx.doi.org/10.1063/1.861248><http://scitation.aip.org/content/aip/journal/pof1/18/8?ver=pdfcov><http://aip.scitation.org/doi/10.1063/1.1658762><http://scitation.aip.org/content/aip/journal/pof1/18/8/10.1063/1.861248>.

- Burton D. Fried and Samuel D. Conte. *The Plasma Dispersion Function*. Academic Press, 1961.
- D. H. Froula, B. Yaakobi, S. X. Hu, P-Y. Chang, R. S. Craxton, D. H. Edgell, R. Follitt, D. T. Michel, J. F. Myatt, W. Seka, R. W. Short, A. Solodov, and C. Stoeckl. Saturation of the Two-Plasmon Decay Instability in Long-Scale-Length Plasmas Relevant to Direct-Drive Inertial Confinement Fusion. *Physical Review Letters*, 108(16):165003, apr 2012. ISSN 0031-9007. doi: 10.1103/PhysRevLett.108.165003. URL <https://link.aps.org/doi/10.1103/PhysRevLett.108.165003>.
- Martin V Goldman. Parametric plasmon-photon interactions. *Annals of Physics*, 38(1):117–169, jun 1966. ISSN 00034916. doi: 10.1016/0003-4916(66)90253-3. URL <http://linkinghub.elsevier.com/retrieve/pii/0003491666902533>.
- D. E. Hinkel, L. F. Berzak Hopkins, T. Ma, J. E. Ralph, F. Albert, L. R. Benedetti, P. M. Celliers, T. Döppner, C. S. Goyon, N. Izumi, L. C. Jarrott, S. F. Khan, J. L. Kline, A. L. Kritcher, G. A. Kyrala, S. R. Nagel, A. E. Pak, P. Patel, M. D. Rosen, J. R. Rygg, M. B. Schneider, D. P. Turnbull, C. B. Yeaman, D. A. Callahan, and O. A. Hurricane. Development of Improved Radiation Drive Environment for High Foot Implosions at the National Ignition Facility. *Physical Review Letters*, 117(22):225002, nov 2016. ISSN 0031-9007. doi: 10.1103/PhysRevLett.117.225002. URL <https://link.aps.org/doi/10.1103/PhysRevLett.117.225002>.
- M. Hohenberger, W. Theobald, S. X. Hu, K. S. Anderson, R. Betti, T. R. Boehly, A. Casner, D. E. Fratanduono, M. Lafon, D. D. Meyerhofer, R. Nora, X. Ribeyre, T. C. Sangster, G. Schurtz, W. Seka, C. Stoeckl, and B. Yaakobi. Shock-ignition relevant experiments with planar targets on OMEGA. *Physics of Plasmas*, 21(2):022702, feb 2014. ISSN 1070-664X. doi: 10.1063/1.4865373. URL <http://aip.scitation.org/doi/10.1063/1.4865373>.
- W.J. Huang, G. Audi, Meng Wang, F. G. Kondev, S. Naimi, and Xing Xu. The AME2016 atomic mass evaluation (I). Evaluation of input data; and adjustment procedures. *Chinese Physics C*, 41(3):030002, mar 2017. ISSN 1674-1137. doi: 10.1088/1674-1137/41/3/030002. URL <http://stacks.iop.org/1674-1137/41/i=3/a=030002?key=crossref.c5ac715502743b64b763cf8c555c73d2>.
- O. A. Hurricane, D. A. Callahan, D. T. Casey, P. M. Celliers, C. Cerjan, E. L. Dewald, T. R. Dittrich, T. Döppner, D. E. Hinkel, L. F. Berzak Hopkins, J. L. Kline, S. Le Pape, T. Ma, A. G. MacPhee, J. L. Milovich, A. Pak, H.-S. Park, P. K. Patel, B. A. Remington, J. D. Salmonson, P. T. Springer, and R. Tommasini.

Fuel gain exceeding unity in an inertially confined fusion implosion. *Nature*, 506 (7488):343–348, feb 2014. ISSN 0028-0836. doi: 10.1038/nature13008. URL <http://www.nature.com/articles/nature13008>.

O. A. Hurricane, P. T. Springer, P. K. Patel, D. A. Callahan, K. Baker, D. T. Casey, L. Divol, T. Döppner, D. E. Hinkel, M. Hohenberger, L. F. Berzak Hopkins, C. Jarrott, A. Kritcher, S. Le Pape, S. Maclaren, L. Masse, A. Pak, J. Ralph, C. Thomas, P. Volegov, and A. Zylstra. Approaching a burning plasma on the NIF. *Physics of Plasmas*, 26(5):052704, 2019. ISSN 1070-664X. doi: 10.1063/1.5087256. URL <http://aip.scitation.org/doi/10.1063/1.5087256>.

E. Atlee Jackson. Parametric effects of radiation on a plasma. *Physical Review*, 153 (1):235–244, 1967. ISSN 0031899X. doi: 10.1103/PhysRev.153.235.

Eric Jones, Travis Oliphant, and Pearu Peterson. SciPy: Open Source Scientific Tools for Python, 2001. URL <http://www.scipy.org/>.

Y. Kato, K. Mima, N. Miyanaga, S. Arinaga, Y. Kitagawa, M. Nakatsuka, and C. Yamanaka. Random Phasing of High-Power Lasers for Uniform Target Acceleration and Plasma-Instability Suppression. *Physical Review Letters*, 53(11): 1057–1060, sep 1984. ISSN 0031-9007. doi: 10.1103/PhysRevLett.53.1057. URL <https://link.aps.org/doi/10.1103/PhysRevLett.53.1057>.

O Klimo, J Psikal, V T Tikhonchuk, and S Weber. Two-dimensional simulations of laser-plasma interaction and hot electron generation in the context of shock-ignition research. *Plasma Physics and Controlled Fusion*, 56(5):055010, may 2014. ISSN 0741-3335. doi: 10.1088/0741-3335/56/5/055010. URL <http://stacks.iop.org/0741-3335/56/i=5/a=055010?key=crossref.aa51f60b6b1ab2e137f3972039a116da>.

A. L. Kritcher, D. E. Hinkel, D. A. Callahan, O. A. Hurricane, D. Clark, D. T. Casey, E. L. Dewald, T. R. Dittrich, T. Döppner, M. A. Barrios Garcia, S. Haan, L. F. Berzak Hopkins, O. Jones, O. Landen, T. Ma, N. Meezan, J. L. Milovich, A. E. Pak, H.-S. Park, P. K. Patel, J. Ralph, H. F. Robey, J. D. Salmonson, S. Sepke, B. Spears, P. T. Springer, C. A. Thomas, R. Town, P. M. Celliers, and M. J. Edwards. Integrated modeling of cryogenic layered highfoot experiments at the NIF. *Physics of Plasmas*, 23(5):052709, may 2016. ISSN 1070-664X. doi: 10.1063/1.4949351. URL <http://aip.scitation.org/doi/10.1063/1.4949351>.

W. L. Kruer, J. M. Dawson, and R. N. Sudan. Trapped-Particle Instability. *Physical Review Letters*, 23(15):838–841, oct 1969. ISSN 0031-9007. doi: 10.1103/



PhysRevLett.23.838. URL <https://link.aps.org/doi/10.1103/PhysRevLett.23.838>.

William L. Kruer. *The Physics of Laser Plasma Interactions*. Westview Press, 2003. ISBN 0-8133-4083-7.

L. D. Landau. ON THE VIBRATIONS OF THE ELECTRONIC PLASMA. *Journal of Physics of the USSR*, 10:25, 1946.

A. Bruce Langdon, Barbara F. Lasinski, and William L. Kruer. Nonlinear saturation and recurrence of the two-plasmon decay instability. *Physical Review Letters*, 43(2):133–136, 1979. ISSN 00319007. doi: 10.1103/PhysRevLett.43.133.

Y. C. Lee and P. K. Kaw. Temporal Electrostatic Instabilities in Inhomogeneous Plasmas. *Physical Review Letters*, 32(4):135–138, jan 1974. ISSN 0031-9007. doi: 10.1103/PhysRevLett.32.135. URL <https://link.aps.org/doi/10.1103/PhysRevLett.32.135>.

C. S. Liu. Raman and Brillouin scattering of electromagnetic waves in inhomogeneous plasmas, 1974. ISSN 00319171. URL <http://scitation.aip.org/content/aip/journal/pof1/17/6/10.1063/1.1694867>.

C. S. Liu and Marshall N. Rosenbluth. Parametric decay of electromagnetic waves into two plasmons and its consequences. *Physics of Fluids*, 19(7):967, 1976. ISSN 00319171. doi: 10.1063/1.861591. URL <https://aip.scitation.org/doi/10.1063/1.861591>.

C. S. Liu, Marshall N. Rosenbluth, and R. B. White. Raman and Brillouin scattering of electromagnetic waves in inhomogeneous plasmas. *Physics of Fluids*, 17(6):1211, 1974. ISSN 00319171. doi: 10.1063/1.1694867. URL <http://scitation.aip.org/content/aip/journal/pof1/17/6/10.1063/1.1694867><https://aip.scitation.org/doi/10.1063/1.1694867>.

N B Meezan, M J Edwards, O A Hurricane, P K Patel, D A Callahan, W W Hsing, R P J Town, F Albert, P A Amendt, L F Berzak Hopkins, D K Bradley, D T Casey, D S Clark, E L Dewald, T R Dittrich, L Divol, T Döppner, J E Field, S W Haan, G N Hall, B A Hammel, D E Hinkel, D D Ho, M Hohenberger, N Izumi, O S Jones, S F Khan, J L Kline, A L Kritcher, O L Landen, S LePape, T Ma, A J MacKinnon, A G MacPhee, L Masse, J L Milovich, A Nikroo, A Pak, H-S Park, J L Peterson, H F Robey, J S Ross, J D Salmonson, V A Smalyuk, B K Spears, M Stadermann, L J Suter, C A Thomas, R Tommasini, D P Turnbull,

and C R Weber. Indirect drive ignition at the National Ignition Facility. *Plasma Physics and Controlled Fusion*, 59(1):014021, 2017. ISSN 0741-3335. doi: 10.1088/0741-3335/59/1/014021. URL <http://stacks.iop.org/0741-3335/59/i=1/a=014021?key=crossref.77bc2339bef47d7ce55411860b791dcc>.

P. Michel, M. J. Rosenberg, W. Seka, A. A. Solodov, R. W. Short, T. Chapman, C. Goyon, N. Lemos, M. Hohenberger, J. D. Moody, S. P. Regan, and J. F. Myatt. Theory and measurements of convective Raman side scatter in inertial confinement fusion experiments. *Physical Review E*, 99(3):033203, mar 2019. ISSN 2470-0045. doi: 10.1103/PhysRevE.99.033203. URL <https://link.aps.org/doi/10.1103/PhysRevE.99.033203>.

D. S. Montgomery, J. A. Cobble, J. C. Fernández, R. J. Focia, R. P. Johnson, N. Renard-Legalloudec, H. A. Rose, and D. A. Russell. Recent Trident single hot spot experiments: Evidence for kinetic effects, and observation of Langmuir decay instability cascade. *Physics of Plasmas*, 9(5):2311–2320, 2002. ISSN 1070664X. doi: 10.1063/1.1468857.

G. J. Morales and T. M. O’Neil. Nonlinear Frequency Shift of an Electron Plasma Wave. *Physical Review Letters*, 28(7):417–420, feb 1972. ISSN 0031-9007. doi: 10.1103/PhysRevLett.28.417. URL <http://link.aps.org/doi/10.1103/PhysRevLett.28.417><https://link.aps.org/doi/10.1103/PhysRevLett.28.417>.

E. I. Moses, R. N. Boyd, B. A. Remington, C. J. Keane, and R. Al-Ayat. The National Ignition Facility: Ushering in a new age for high energy density science. *Physics of Plasmas*, 16(4):041006, apr 2009. ISSN 1070-664X. doi: 10.1063/1.3116505. URL <http://aip.scitation.org/doi/10.1063/1.3116505>.

J. F. Myatt, J. Zhang, J. A. Delettrez, A. V. Maximov, R. W. Short, W. Seka, D. H. Edgell, D. F. Dubois, D. A. Russell, and H. X. Vu. The dynamics of hot-electron heating in direct-drive-implosion experiments caused by two-plasmon-decay instability. *Physics of Plasmas*, 19(2):1–12, 2012. ISSN 1070664X. doi: 10.1063/1.3683004.

J. F. Myatt, J. Zhang, R. W. Short, A. V. Maximov, W. Seka, D. H. Froula, D. H. Edgell, D. T. Michel, I. V. Igumenshchev, D E Hinkel, P Michel, and J D Moody. Multiple-beam laser-plasma interactions in inertial confinement fusion. *Physics of Plasmas*, 21(5):055501, may 2014. ISSN 1070-664X. doi: 10.1063/1.4878623. URL <http://aip.scitation.org/doi/10.1063/1.4878623>.

- K. Nanbu and S. Yonemura. Weighted Particles in Coulomb Collision Simulations Based on the Theory of a Cumulative Scattering Angle. *Journal of Computational Physics*, 145(2):639–654, 1998. ISSN 00219991. doi: 10.1006/jcph.1998.6049.
- Kyoji Nishikawa. Parametric Excitation of Coupled Waves. II. Parametric Plasmon-Photon Interaction. *Journal of the Physical Society of Japan*, 24(5):1152–1158, may 1968. ISSN 0031-9015. doi: 10.1143/JPSJ.24.1152. URL <http://journals.jps.jp/doi/10.1143/JPSJ.24.1152>.
- R. Nora, W. Theobald, R. Betti, F. J. Marshall, D. T. Michel, W. Seka, B. Yaakobi, M. Lafon, C. Stoeckl, J. Delettrez, A. A. Solodov, A. Casner, C. Reverdin, X. Ribeyre, A. Vallet, J. Peebles, F. N. Beg, and M. S. Wei. Gigabar spherical shock generation on the OMEGA laser. *Physical Review Letters*, 114(4):1–5, 2015. ISSN 10797114. doi: 10.1103/PhysRevLett.114.045001.
- John Nuckolls, Lowell Wood, Albert Thiessen, and George Zimmerman. Laser Compression of Matter to Super-High Densities: Thermonuclear (CTR) Applications. *Nature*, 239(5368):139–142, sep 1972. ISSN 0028-0836. doi: 10.1038/239139a0. URL <http://www.nature.com/doi/10.1038/239139a0><http://www.nature.com/articles/239139a0>.
- Thomas O’Neil. Collisionless Damping of Nonlinear Plasma Oscillations. *Physics of Fluids*, 8(12):2255, jun 1965. ISSN 00319171. doi: 10.1063/1.1761193. URL <http://link.aip.org/link/?PFL/8/2255/1><http://scitation.aip.org/content/aip/journal/pof1/8/12/10.1063/1.1761193><http://linkinghub.elsevier.com/retrieve/pii/0003491666902533><https://aip.scitation.org/doi/10.1063/1.1761193>.
- S. Le Pape. Fusion energy output greater than the kinetic energy of an imploding shell at the National Ignition Facility. *Physical Review Letters*, 245003:1–6, 2018. doi: 10.1103/PhysRevLett.120.245003.
- H. S. Park, O. A. Hurricane, D. A. Callahan, D. T. Casey, E. L. Dewald, T. R. Dittrich, T. Döppner, D. E. Hinkel, L. F. Berzak Hopkins, S. Le Pape, T. Ma, P. K. Patel, B. A. Remington, H. F. Robey, J. D. Salmonson, and J. L. Kline. High-adiabat high-foot inertial confinement fusion implosion experiments on the national ignition facility. *Physical Review Letters*, 112(5):1–5, 2014. ISSN 00319007. doi: 10.1103/PhysRevLett.112.055001.
- J. L. Peebles, S. X. Hu, W. Theobald, V. N. Goncharov, N. Whiting, P. M. Celliers, S. J. Ali, G. Duchateau, E. M. Campbell, T. R. Boehly, and S. P. Regan.

Direct-drive measurements of laser-imprint-induced shock velocity nonuniformities. *Physical Review E*, 99(6):063208, jun 2019. ISSN 2470-0045. doi: 10.1103/PhysRevE.99.063208. URL <https://link.aps.org/doi/10.1103/PhysRevE.99.063208>.

F. Pegoraro and F. Porcelli. Equation of state for relativistic plasma waves. *Physics of Fluids*, 27(7):1665, 1984. ISSN 00319171. doi: 10.1063/1.864820. URL <https://aip.scitation.org/doi/10.1063/1.864820>.

M. J. Rosenberg, A. A. Solodov, J. F. Myatt, W. Seka, P. Michel, M. Hohenberger, R. W. Short, R. Epstein, S. P. Regan, E. M. Campbell, T. Chapman, C. Goyon, J. E. Ralph, M. A. Barrios, J. D. Moody, and J. W. Bates. Origins and Scaling of Hot-Electron Preheat in Ignition-Scale Direct-Drive Inertial Confinement Fusion Experiments. *Physical Review Letters*, 120(5):055001, 2018. ISSN 0031-9007. doi: 10.1103/PhysRevLett.120.055001. URL <https://link.aps.org/doi/10.1103/PhysRevLett.120.055001>.

M. N. Rosenbluth, R. B. White, and C. S. Liu. Temporal Evolution of a Three-Wave Parametric Instability. *Physical Review Letters*, 31(19):1190–1193, nov 1973. ISSN 0031-9007. doi: 10.1103/PhysRevLett.31.1190. URL <https://link.aps.org/doi/10.1103/PhysRevLett.31.1190>.

Marshall N. Rosenbluth. Parametric Instabilities in Inhomogeneous Media. *Physical Review Letters*, 29(9):565–567, aug 1972. ISSN 0031-9007. doi: 10.1103/PhysRevLett.29.565. URL <https://link.aps.org/doi/10.1103/PhysRevLett.29.565>.

D. A. Russell and D. F. DuBois.  $3\omega/2$  Radiation from the Laser-Driven Two-Plasmon Decay Instability in an Inhomogeneous Plasma. *Physical Review Letters*, 86(3):428–431, jan 2001. ISSN 0031-9007. doi: 10.1103/PhysRevLett.86.428. URL <https://link.aps.org/doi/10.1103/PhysRevLett.86.428>.

W. Seka, D. H. Edgell, J. F. Myatt, A. V. Maximov, R. W. Short, V. N. Goncharov, and H. A. Baldis. Two-plasmon-decay instability in direct-drive inertial confinement fusion experiments. *Physics of Plasmas*, 16(5), 2009. ISSN 1070664X. doi: 10.1063/1.3125242.

W. L. Shang, R. Betti, S. X. Hu, K. Woo, L. Hao, C. Ren, A. R. Christopher, A. Bose, and W. Theobald. Electron Shock Ignition of Inertial Fusion Targets. *Physical Review Letters*, 119(19):195001, 2017. ISSN 0031-9007. doi:

10.1103/PhysRevLett.119.195001. URL <https://link.aps.org/doi/10.1103/PhysRevLett.119.195001>.

A. Simon. On the inhomogeneous two-plasmon instability. *Physics of Fluids*, 26(10):3107, 1983. ISSN 00319171. doi: 10.1063/1.864037. URL <http://scitation.aip.org/content/aip/journal/pof1/26/10/10.1063/1.864037><https://aip.scitation.org/doi/10.1063/1.864037>.

S. Skupsky, R. W. Short, T. Kessler, R. S. Craxton, S. Letzring, and J. M. Soures. Improved laser-beam uniformity using the angular dispersion of frequency-modulated light. *Journal of Applied Physics*, 66(8):3456–3462, oct 1989. ISSN 0021-8979. doi: 10.1063/1.344101. URL <http://aip.scitation.org/doi/10.1063/1.344101>.

Donna Strickland and Gerard Mourou. Compression of amplified chirped optical pulses. *Optics Communications*, 55(6):447–449, oct 1985. ISSN 00304018. doi: 10.1016/0030-4018(85)90151-8. URL <https://linkinghub.elsevier.com/retrieve/pii/0030401885901518>.

W. Theobald, R. Betti, C. Stoeckl, K. S. Anderson, J. A. Delettrez, V. Yu Glebov, V. N. Goncharov, F. J. Marshall, D. N. Maywar, R. L. McCrory, D. D. Meyerhofer, P. B. Radha, T. C. Sangster, W. Seka, D. Shvarts, V. A. Smalyuk, A. A. Solodov, B. Yaakobi, C. D. Zhou, J. A. Frenje, C. K. Li, F. H. Séguin, R. D. Petrasso, and L. J. Perkins. Initial experiments on the shock-ignition inertial confinement fusion concept. *Physics of Plasmas*, 15(5):056306, may 2008. ISSN 1070-664X. doi: 10.1063/1.2885197. URL <http://aip.scitation.org/doi/10.1063/1.2885197>.

W. Theobald, R. Nora, M. Lafon, A. Casner, X. Ribeyre, K. S. Anderson, R. Betti, J. A. Delettrez, J. A. Frenje, V. Yu Glebov, O. V. Gotchev, M. Hohenberger, S. X. Hu, F. J. Marshall, D. D. Meyerhofer, T. C. Sangster, G. Schurtz, W. Seka, V. A. Smalyuk, C. Stoeckl, and B. Yaakobi. Spherical shock-ignition experiments with the 40 20-beam configuration on OMEGA. *Physics of Plasmas*, 19(10):102706, oct 2012. ISSN 1070664X. doi: 10.1063/1.4763556. URL <http://aip.scitation.org/doi/10.1063/1.4763556>.

W. Theobald, R. Nora, W. Seka, M. Lafon, K. S. Anderson, M. Hohenberger, F. J. Marshall, D. T. Michel, A. A. Solodov, C. Stoeckl, D. H. Edgell, B. Yaakobi, A. Casner, C. Reverdin, X. Ribeyre, A. Shvydsky, A. Vallet, J. Peebles, F. N. Beg, M. S. Wei, and R. Betti. Spherical strong-shock generation for shock-ignition inertial fusion. *Physics of Plasmas*, 22(5):056310, may 2015. ISSN 1070-664X. doi:

10.1063/1.4920956. URL <http://scitation.aip.org/content/aip/journal/pop/22/5/10.1063/1.4920956>.

W Theobald, A Bose, R Yan, R Betti, M Lafon, D Mangino, A R Christopherson, C Stoeckl, W Seka, W Shang, D T Michel, C Ren, R C Nora, A Casner, J Peebles, F N Beg, X Ribeyre, E. Llor Aisa, A. Colaitis, V. Tikhonchuk, and M. S. Wei. Enhanced hot-electron production and strong-shock generation in hydrogen-rich ablaters for shock ignition. *Physics of Plasmas*, 24(12):120702, dec 2017. ISSN 1070-664X. doi: 10.1063/1.4986797. URL <http://aip.scitation.org/doi/10.1063/1.4986797>.

J Trela, W Theobald, K S Anderson, D Batani, R Betti, A Casner, J A Delettrez, J A Frenje, V Yu Glebov, X Ribeyre, A A Solodov, M. Stoeckl, and C. Stoeckl. The control of hot-electron preheat in shock-ignition implosions. *Physics of Plasmas*, 25(5):052707, may 2018. ISSN 1070-664X. doi: 10.1063/1.5020981. URL <http://aip.scitation.org/doi/10.1063/1.5020981>.

N.G. Van Kampen. On the theory of stationary waves in plasmas. *Physica*, 21(6-10): 949–963, jan 1955. ISSN 00318914. doi: 10.1016/S0031-8914(55)93068-8. URL <http://linkinghub.elsevier.com/retrieve/pii/S0031891455930688><https://linkinghub.elsevier.com/retrieve/pii/S0031891455930688>.

A. A. Vlasov. On the Kinetic Theory of an Assembly of Particles with Collective Interaction. *Journal of Physics of the USSR*, 9:22–40, 1945.

H. X. Vu, D. F. DuBois, and B. Bezzerides. Kinetic inflation of stimulated Raman backscatter in regimes of high linear Landau damping. *Physics of Plasmas*, 9(5): 1745, 2002. ISSN 1070664X. doi: 10.1063/1.1471235.

H. X. Vu, D. F. DuBois, and B. Bezzerides. Inflation threshold: A nonlinear trapping-induced threshold for the rapid onset of stimulated Raman scattering from a single laser speckle. *Physics of Plasmas*, 14(1):012702, jan 2007. ISSN 1070664X. doi: 10.1063/1.2426918. URL <http://aip.scitation.org/doi/10.1063/1.2426918>.

H. X. Vu, D. F. DuBois, J. F. Myatt, and D. A. Russell. Hot-electron production and suprathermal heat flux scaling with laser intensity from the two-plasmon-decay instability. *Physics of Plasmas*, 19(10): 102703, oct 2012a. ISSN 1070-664X. doi: 10.1063/1.4757978. URL <http://aip.scitation.org/doi/10.1063/1.4757978><http://scitation.aip.org/content/aip/journal/pop/19/10/10.1063/1.4757978>.

- H. X. Vu, D. F. Dubois, D. A. Russell, and J. F. Myatt. Hot-electron generation by "cavitating" Langmuir turbulence in the nonlinear stage of the two-plasmon-decay instability. *Physics of Plasmas*, 19(10):1–10, 2012b. ISSN 1070664X. doi: 10.1063/1.4764075.
- S. Weber, C. Riconda, O. Klimo, A. Héron, and V. T. Tikhonchuk. Fast saturation of the two-plasmon-decay instability for shock-ignition conditions. *Physical Review E - Statistical, Nonlinear, and Soft Matter Physics*, 85(1):1–6, 2012. ISSN 15393755. doi: 10.1103/PhysRevE.85.016403.
- E. A. Williams and T. W. Johnston. Phase-inflection parametric instability behavior near threshold with application to laser-plasma stimulated Raman scattering (SRS) instabilities in exploding foils. *Physics of Fluids B: Plasma Physics*, 1(1):188–194, jan 1989. ISSN 0899-8221. doi: 10.1063/1.859086. URL <http://aip.scitation.org/doi/10.1063/1.859086>.
- E. A. Williams, R. L. Berger, R. P. Drake, A. M. Rubenchik, B. S. Bauer, D. D. Meyerhofer, A. C. Gaeris, and T. W. Johnston. The frequency and damping of ion acoustic waves in hydrocarbon (CH) and two-ion-species plasmas. *Physics of Plasmas*, 2(1):129–138, jan 1995. ISSN 1070-664X. doi: 10.1063/1.871101. URL <http://aip.scitation.org/doi/10.1063/1.871101>.
- B. J. Winjum, J. Fahlen, and W. B. Mori. The relative importance of fluid and kinetic frequency shifts of an electron plasma wave. *Physics of Plasmas*, 14(10), 2007. ISSN 1070664X. doi: 10.1063/1.2790385.
- R. Yan, A. V. Maximov, C. Ren, and F. S. Tsung. Growth and Saturation of Convective Modes of the Two-Plasmon Decay Instability in Inertial Confinement Fusion. *Physical Review Letters*, 103(17):6–9, 2009. ISSN 00319007. doi: 10.1103/PhysRevLett.103.175002.
- R. Yan, A. V. Maximov, and C. Ren. The linear regime of the two-plasmon decay instability in inhomogeneous plasmas. *Physics of Plasmas*, 17(5):1–7, 2010. ISSN 1070664X. doi: 10.1063/1.3414350.
- R. Yan, C. Ren, J. Li, A. V. Maximov, W. B. Mori, Z. M. Sheng, and F. S. Tsung. Generating energetic electrons through staged acceleration in the two-plasmon-decay instability in inertial confinement fusion. *Physical Review Letters*, 108(17):1–5, 2012. ISSN 00319007. doi: 10.1103/PhysRevLett.108.175002.

- R. Yan, J. Li, and C. Ren. Intermittent laser-plasma interactions and hot electron generation in shock ignition. *Physics of Plasmas*, 21(6):062705, jun 2014. ISSN 1070-664X. doi: 10.1063/1.4882682. URL <http://aip.scitation.org/doi/10.1063/1.4882682>.
- Kane S. Yee. Numerical solution of initial boundary value problems involving maxwell's equations in isotropic media. *IEEE Transactions on Antennas and Propagation*, 14(3):302–307, may 1966. ISSN 0018-926X. doi: 10.1109/TAP.1966.1138693. URL <http://citeseerx.ist.psu.edu/viewdoc/download;jsessionid=B8E201B2B537605E0A60FDFA766FFF03?doi=10.1.1.172.6957{&}rep=rep1{&}type=pdfhttp://ieeexplore.ieee.org/document/1138693/>.
- L. Yin, W. Daughton, B. J. Albright, B. Bezzerides, D. F. Dubois, J. M. Kindel, and H. X. Vu. Nonlinear development of stimulated Raman scattering from electrostatic modes excited by self-consistent non-Maxwellian velocity distributions. *Physical Review E - Statistical, Nonlinear, and Soft Matter Physics*, 73(2):3–6, 2006a. ISSN 15393755. doi: 10.1103/PhysRevE.73.025401.
- L. Yin, W. Daughton, B. J. Albright, K. J. Bowers, D. S. Montgomery, J. L. Kline, J. C. Fernández, and Q. Roper. Nonlinear backward stimulated Raman scattering from electron beam acoustic modes in the kinetic regime. *Physics of Plasmas*, 13(7), 2006b. ISSN 1070664X. doi: 10.1063/1.2210929.
- L. Yin, B. J. Albright, K. J. Bowers, W. Daughton, and H. A. Rose. Saturation of backward stimulated scattering of a laser beam in the kinetic regime. *Physical Review Letters*, 99(26):1–4, 2007. ISSN 00319007. doi: 10.1103/PhysRevLett.99.265004.
- L. Yin, B. J. Albright, K. J. Bowers, W. Daughton, and H. A. Rose. Saturation of backward stimulated scattering of laser in kinetic regime: Wavefront bowing, trapped particle modulational instability, and trapped particle self-focusing of plasma waves. *Physics of Plasmas*, 15(1), 2008. ISSN 1070664X. doi: 10.1063/1.2825663.
- L. Yin, B. J. Albright, H. A. Rose, K. J. Bowers, B. Bergen, D. S. Montgomery, J. L. Kline, and J. C. Fernández. Onset and saturation of backward stimulated Raman scattering of laser in trapping regime in three spatial dimensions. *Physics of Plasmas*, 16(11):113101, 2009. ISSN 1070664X. doi: 10.1063/1.3250928.



- L. Yin, B. J. Albright, H. A. Rose, K. J. Bowers, B. Bergen, and R. K. Kirkwood. Self-organized bursts of coherent stimulated Raman scattering and hot electron transport in speckled laser plasma media. *Physical Review Letters*, 108(24):10–14, 2012. ISSN 00319007. doi: 10.1103/PhysRevLett.108.245004.
- L. Yin, B. J. Albright, H. A. Rose, D. S. Montgomery, J. L. Kline, R. K. Kirkwood, P. Michel, K. J. Bowers, and B. Bergen. Self-organized coherent bursts of stimulated Raman scattering and speckle interaction in multi-speckled laser beams. *Physics of Plasmas*, 20(1):1–13, 2013. ISSN 1070664X. doi: 10.1063/1.4774964.
- L. Yin, B. J. Albright, H. A. Rose, D. S. Montgomery, J. L. Kline, R. K. Kirkwood, J. Milovich, S. M. Finnegan, B. Bergen, and K. J. Bowers. Stimulated scattering in laser driven fusion and high energy density physics experiments. *Physics of Plasmas*, 21(9):092707, sep 2014. ISSN 1070-664X. doi: 10.1063/1.4895504. URL <http://aip.scitation.org/doi/10.1063/1.4895504>.